LEONARDO's PARADOX

Path and Shape Instabilities of Particles and Bubbles

Samenstelling promotiecommissie:

Prof. dr. ir. A. Bliek, voorzitter	Universiteit Twente
Prof. dr. rer. nat. D. Lohse, promotor	Universiteit Twente
Prof. dr. ir. L. van Wijngaarden, promotor	Universiteit Twente
Dr. ir. A. Biesheuvel, assistent-promotor	Universiteit Twente
Prof. dr. J. Magnaudet	Institut de Mécanique des Fluides de Toulouse
Prof. dr. ir. G.J.F. van Heijst	Technische Universiteit Eindhoven
Prof. dr. A. Prosperetti	Universiteit Twente
Dr. ir. R. Hagmeijer	Universiteit Twente

The research described in this thesis is part of the research program of the ”Stichting voor Fundamenteel Onderzoek der Materie” (FOM), which is financially supported by the ”Nederlandse Organisatie voor Wetenschappelijk Onderzoek” (NWO). It was carried out at the Physics of Fluids research group of the faculty of Science and Technology of the University of Twente.

Nederlandse titel:
Leonardo’s paradox: Pad- en vorminstabiliteiten van deeltjes en bellen

Publisher:
Christian Veldhuis, Physics of Fluids, University of Twente,
P.O. Box 217, 7500 AE Enschede, The Netherlands
pof.tnw.utwente.nl

Cover design: Christian Veldhuis
Back cover illustration: Rising sphere with its wake, see chapter 3
Print: Gildeprint B.V., Enschede

ISBN 90-365-2446-6

LEONARDO'S PARADOX

PATH AND SHAPE INSTABILITIES OF PARTICLES AND BUBBLES

PROEFSCHRIFT

ter verkrijging van
de graad van doctor aan de Universiteit Twente,
op gezag van de rector magnificus,
prof. dr. W. H. M. Zijm,
volgens besluit van het College voor Promoties
in het openbaar te verdedigen
op woensdag 7 februari 2007 om 15.00 uur

door

Christian Hendrikus Johannes Veldhuis
geboren op 21 februari 1978

te Hengelo

Dit proefschrift is goedgekeurd door de promotoren:

prof. dr. rer. nat. D. Lohse
prof. dr. ir. L. van Wijngaarden

en de assistent-promotor:

dr. ir. A. Biesheuvel

Contents

Chapter 1

Introduction

This chapter will give a brief introduction to the motion of a single solid sphere and a bubble in a liquid. At the beginning of each one of the next chapters the introduction will be extended with the particular aspects discussed in that chapter. At the end of this chapter a guide through this thesis will be given.

1.1 Sphere and bubble motion

Bubble and particle laden flows can be found in a wide range of industrial and geophysical processes. They play an important role in mixing in chemical reactors, heat exchangers, atmospheric and oceanic flows. This broad application field stimulated bubbly and particles laden flow research. It addresses many questions in a broad range of Reynolds numbers. In the upper limit the research focuses on dense, highly laden flows. This research provides the overall statistical properties of such flows. In the lower limit the research addresses the problem of single bubble or particle behavior, providing a more fundamental knowledge of the hydrodynamic forces acting on these bodies. This thesis focuses on these fundamental aspects. It studies the behavior of single, rising or ascending, solid spherical particles and rising bubbles in a quiescent Newtonian liquid.

The driving force on a sphere or bubble moving through a quiescent liquid is buoyancy. Therefore one might expect an axi-symmetric body to move along a vertical path through the liquid. This is indeed true for small Reynolds numbers. But that this idea does not always hold is shown by Leonardo da Vinci (1452-1519) [23, 25]. He was the first who reported on the peculiar path a rising bubble follows through stagnant water. Figure 1.1 shows a sketch of one of his observations in which the bubble is rising along a helicoidal path.

Figure 1.1: Leonardo da Vinci's sketch of a spiraling bubble. Reproduced from [23].

Similar observations are made for spheres moving in air. In 1726 Sir Isaac Newton reported on experiments done in 1719 by Dr. Desaguliers. Desaguliers measured the sphere drag by timing the fall of spherically shaped inflated hog bladders. He found that *"the inflated bladders did not always fall directly down, but sometimes fluttered a little in the air and waved to and fro as they were descending"*. The reason for this fluttering is the unsteady wake behind the sphere causing fluctuating forces and moments acting on it when it moves freely through the fluid [29].

The wake behind solid spheres has been a research topic for quite some years. Already in 1927 Ermisch [6] reported on unsteady wakes behind fixed spheres. Later more numerical and experimental studies followed [7, 11, 15, 22, 24, 26]. Only recently the wakes of freely moving spheres have been analyzed [10, 17]. These wake structures are important to understand the motion of spheres moving freely through a liquid. The inertia of these spheres, and therefore the sphere-fluid density ratio, is also of great importance when the motion is unsteady. It might have an important influence on the wake of the sphere. Therefore a more extensive research into the wake structures of spheres in a wide range of Reynolds numbers and sphere-fluid density ratios is necessary.

Related to the drag experiments by Desaguliers are the findings of Karamanev and co-workers [12–14]. They state that at Reynolds numbers larger than about 130 the drag experienced by light spheres (sphere-fluid density ratio smaller than 0.3) is considerably larger than the drag experienced by heavy spheres. Recalling the previous discussion it might be expected that these observations are connected with changes in the wake structures. Therefore this light sphere motion will be investigated more thoroughly. Analysis of the forces acting on the spheres must help us to explain Karamanev's findings.

More recently (2004) Dušek and co-workers [10] published excellent numerical work on sphere motion in a Newtonian fluid. They found that indeed the motion of the sphere is not symmetric about a sphere-fluid density ratio of one as one can conclude from the work by Karamanev and co-workers. Several regimes of sphere motion (e.g. straight, zigzagging, chaotic) have been found for different sphere-fluid density ratios and sphere diameters. Their work gives answers to many problems encountered in research related to freely moving spheres, but it also raises several new questions related to wake structures behind those spheres. By verifying their numerical work with an experimental study some of these questions will be addressed.

From solid spheres moving in liquids some links can be made to bubbles rising in liquids, but some important differences remain. Firstly, bubbles and solid spheres have a different boundary condition; solid spheres have a no-slip condition at their surface, while on bubble surfaces slip is allowed and a no-shear condition is imposed, when the bubble moves through a sufficiently clean liquid. Secondly, because of the small density of the bubbles compared to that of the liquid, the inertia in the system is almost entirely due to accelerated or decelerated liquid. Therefore, the liquid inertia plays an important role in the analysis of the hydrodynamic forces predicting bubble motion. Thirdly, the bubble shape is not fixed; local pressures around the bubble will cause local curvatures, leading to bubble shapes which are non-spherical. For larger bubbles shape oscillations set in, causing inertia effects which play an important role in the prediction of bubble motion.

Lindt [16] gives a nice overview of bubble motion for a wide range of bubble diameters. Small bubbles rise rectilinearly, for somewhat larger ones the path is a zigzag or spiral. Still larger bubbles start to experience shape oscillations. Finally, the bubble assumes a so-called spherical cap shape and rises rectilinearly.

For bubbles performing path oscillations, without shape oscillations, the literature provides much information on results of the path followed by the bubble [1, 2, 8, 9, 19]. In recent studies more extensive research has been done to explain this bubble motion in terms of the flow field behind the bubble [3–5, 17, 20, 28]. Up to now only recent numerical work of Mougin & Magnaudet [21] really quantifies the forces and torques acting on bubbles of fixed ellipsoidal shape related to its wake. They state: ”*...the present paper focuses on a description of the forces and torques experienced by the bubble along its path. Achieving an equivalent determination of forces and torques through a laboratory experiment is very challenging; only partial answers have yet been provided (Ellingsen & Risso 2001)...*” To provide more conclusive answers the regime of fixed shaped bubbles performing path oscillations will be investigated thoroughly. The wake visualizations of De Vries [27, 28] will be repeated to have a more detailed knowledge of the wake structures. The forces and torques will be calculated to be able to reveal their relation with the bubble wake and to understand the bubble motion in general.

In the regime of larger bubbles with shape oscillations, before the regime with spherical caps sets in, the literature is less extensive. Lunde & Perkins [18] discussed the effect of shape oscillations on the bubble motion. Other researchers [4, 17] provide some information on wake structures behind such bubbles in contaminated water. But detailed knowledge of their wakes and the relation to bubble dynamics, especially shape oscillations, in this regime is not available. Analysis of the oscillations in path, shape, and wake have to be done in order to reveal new relations between these three aspects and understand bubble motion in this regime.

This introduction addressed several research topics to be dealt with in this thesis. The next section will provide an overview of the chapters in which these topics will be discussed.

1.2 A guide through the chapters

The introduction stressed the necessity for an adequate understanding of the wake behind solid spheres and bubbles. In chapter 2 the experimental setup to analyze the wake structures of spheres and bubbles will be introduced. Thereafter the thesis is divided into two main parts: one part on the motion of particles (chapter 3,4, and 5) and one part on the motion of bubbles (chapter 6,7, and 8).

Chapter 3 discusses general features of wake structures behind spheres rising or falling in quiescent water at Reynolds numbers ranging between 205 and 4623. Chapter 4 is inspired by the work by Karamanev and co-workers [12–14]. It gives a extensive discussion on the motion of very light spheres, with a sphere-fluid density ratio of 0.02. It addresses the question why the drag experienced by these spheres is considerably larger than the drag experienced by heavy spheres at Reynolds numbers larger than about 130. Chapter 5 is a reaction on the numerical work by Dušek and co-workers [10]. In their numerical study they found several regimes of sphere motion which have not been reported in literature before. Their numerical results are verified by approaching this problem experimentally.

Chapter 6 gives the general aspects of single bubble motion. It reports on bubble dynamics starting with small rectilinearly rising bubbles, continuing with bubbles performing path oscillations and ending with bubbles performing path and shape oscillations. This chapter is an introduction to the last two chapters. Chapter 7 discusses the dynamics of oblate ellipsoidal bubbles of fixed shape. It carries on on the work of Ellingsen & Risso [5]. Forces and torques are calculated and visualizations of the wake structures are used to model drag and lift experienced by these bubbles. Chapter 8 elaborates on the work by Lunde & Perkins [18]. It discusses larger bubbles which also perform shape oscillations and addresses the question what the relation is between the bubble path, shape and wake.

Chapter 9 is left to conclusions and recommendations for future research.

References

[1] Aybers, N.M. & Tapucu, A. 1969 The motion of gas bubbles rising through stagnant liquid. *Wärm- und Stoffübertragung* **2**, 118–228.

[2] Aybers, N.M. & Tapucu, A. 1969 Studies on the drag and shape of gas bubbles rising through a stagnant liquid. *Wärm- und Stoffübertragung* **2**, 171–177.

[3] Blanco, A. & Magnaudet, J. 1995 The structure of high Reynolds number flow around an ellipsoidal bubble of fixed shape. *Phys. Fluids* **7**, 1265–1274.

[4] Brücker, C. 1999 Structure and dynamics of the wake of bubbles and its relevance for bubble interaction. *Phys. Fluids* **11**, 1781–1796.

[5] Ellingsen, K. & Risso, F. 2001 On the rise of an ellipsoidal bubble in water: oscillatory paths and liquid-induced velocity. *J. Fluid Mech.* **440**, 235–268.

[6] Ermisch, H. 1927 Strömungsverlauf und Druckverteilung and Widerstandskörpern in Abhängigkeit von der Kennzahl. *Abh. Aero. Inst. Aachen* **6**, 18–50.

[7] Ghidersa, B. & Dušek, J. 2000 Breaking of axisymmetry and onset of unsteadiness in the wake of a sphere. *J. Fluid Mech.* **423**, 33–69.

[8] Haberman, W.L. & Morton, R.K. 1954 An experimental study of bubble moving in liquids. *Trans. ASCE* **387**, 227–252.

[9] Hartunian, R.A. & Sears, W.R. 1957 On the instability of small gas bubbles moving uniformly in various liquids. *J. Fluid Mech.* **3**, 27–47.

[10] Jenny, M., Dušek, J. & Bouchet, G. 2004 Instabilities and transition of a sphere falling or ascending freely in a Newtonian fluid. *J. Fluid Mech.* **508**, 201–239.

[11] Johnson, T.A. & Patel, V.C. 1999 Flow past a sphere up to a Reynolds number of 300. *J. Fluid Mech.* **378**, 19–70.

[12] Karamanev, D.G. 2001 The study of free rise of buoyant spheres in gas reveals the universal behaviour of free rising rigid spheres in fluid in general. *Int. J. Multiphase Flow* **27**, 1479–1486.

[13] KARAMANEV, D.G., CHAVARIE, C. & MAYER, R.C. 1996 Dynamics of the free rise of a light solid sphere in liquid. *AIChE J.* **42**, 1789–1792.

[14] KARAMANEV, D.G. & NIKOLOV, L.N. 1992 Free rising spheres do not obey Newton's law for free settling. *AIChE J.* **38**, 1843–1846.

[15] LEE, S. 2000 A numerical study of the unsteady wake behind a sphere in a uniform flow at moderate Reynolds numbers. *Comput. Fluids* **29**, 639–667.

[16] LINDT, J.T. 1972 On the periodic nature of the drag of a rising bubble. *Chem. Eng. Sci.* **27**, 1775–1781.

[17] LUNDE, K. & PERKINS, R.J. 1997 Observations on wakes behind spheroidal bubbles and particles. , vol. FEDSM97, p. 3530.

[18] LUNDE, K. & PERKINS, R.J. 1998 Shape oscillations of rising bubbles. *Appl. Sci. Res.* **58**, 387–408.

[19] MERCIER, J., LYRIO, A. & FROSLUND, R. 1973 Three-dimensional study of the nonrectilinear trajectory of air bubbles in water. *Trans. ASME, J. Appl. Mech.* **40**, 650–654.

[20] MOUGIN, G. & MAGNAUDET, J. 2002 Path instability of a rising bubble. *Phys. Rev. Letters* **88**, 014502.

[21] MOUGIN, G. & MAGNAUDET, J. 2006 Wake-induced forces and torques on a zigzagging/spiralling bubble. *J. Fluid Mech.* **567**, 185–194.

[22] NAKAMURA, I. 1976 Steady wake behind a sphere. *Phys. Fluids* **19**, 5–8.

[23] OHL, C.D., TIJINK, A. & PROSPERETTI, A. 2003 The added mass of an expanding bubble. *J. Fluid Mech.* **482**, 271–290.

[24] PLOUMHANS, P., WINCKELMANS, G.S., SALMON, J.K., LEONARD, A. & WARREN, M.S. 2002 Vortex methods for direct numerical simulation of three-dimensional bluff body flows: Application to the sphere at Re = 300, 500, and 1000. *J. Comput. Phys.* **178**, 427–463.

[25] PROSPERETTI, A. 2004 Bubbles. *Phys. Fluids* **16**, 1852–1865.

[26] SCHOUVEILER, L. & PROVANSAL, M. 2002 Self-sustained oscillations in the wake of a sphere. *Phys. Fluids* **14**, 3846–3854.

[27] DE VRIES, A.W.G. 2001 Path and wake of a rising bubble. PhD thesis, University of Twente, Enschede, the Netherlands.

[28] DE VRIES, A.W.G., BIESHEUVEL, A. & VAN WIJNGAARDEN, L. 2002 Notes on the path and wake of a gas bubble rising in pure water. *Int. J. Multiphase Flow* **28**, 1823–1835.

[29] WILLMARTH, W.W. & ENLOW, R.L. 1969 Aerodynamic lift and moment fluctuations on a sphere. *J. Fluid Mech.* **36**, 417–432.

Chapter 2

The thermographic Schlieren setup [‡]

This chapter presents the stereoscopic and thermographic Schlieren setup used for wake visualization behind rising and falling spheres and rising bubbles in water. The Schlieren method has advantages over other methods like PIV and dye injection, because it is able to visualize the entire 3D flow field without contaminating the fluid. De Vries [11] was one of the first to report on wake visualizations behind rising bubbles using a Schlieren setup. His setup has been improved for higher sensitivity to capture more details in the Schlieren images.

2.1 Introduction

The Schlieren technique is a well-known technique to visualize density differences in a transparent medium [9]. Density differences cause a change in light refraction index of the medium. Light travelling through the medium will be refracted differently depending on the local density of the medium. A technique similar to the Schlieren technique is the shadowgraph technique. Whereas the Schlieren technique visualizes the spacial derivative of the refraction index, the shadowgraph visualizes the second spatial derivative of the refraction index. Therefore, in most cases, Schlieren is much more sensitive than shadowgraphy. A famous shadowgraph image is the blurry view an automobile driver has, looking through the heated

---

[‡] adapted from: C.H.J. Veldhuis, M. Versluis, & C.D. Ohl, *Notes on a thermographic Schlieren setup*, to be submitted to Exp. Fluids (2007)

air just above a sun heated road or if one looks through the hot air rising above a candle.

Both Schlieren and shadowgraphy are broadly used in compressible flows, in which pressure fluctuations and therefore density differences are common. We want to visualize wake structures behind freely rising and falling spheres and rising bubbles in quiescent water. De Vries [11] was one of the first to report on wake visualizations behind rising spheres using a Schlieren setup. His setup has been improved for higher sensitivity to capture more details in the Schlieren images.

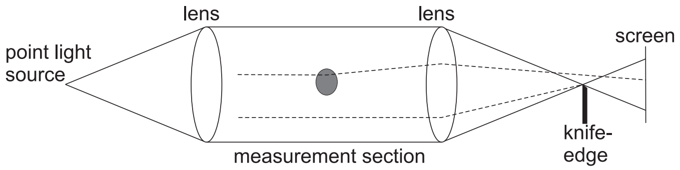

Figure 2.1: Basic idea of a Schlieren setup. The dark spot in the measurement section resembles a density difference. The dotted lines resemble light rays.

The basic idea of a Schlieren setup is shown in figure 2.1. A point light source is positioned in the focal point of a positive lens, generating a parallel bundle of light behind the lens. A second positive lens focuses the light into its focal point, where a knife edge is used to cut off the light. Any light ray not affected by a density difference in the measurement section will be cut off by the knife edge. Light rays which are bend by density differences will be projected onto the screen.

In reality the light source is not a perfect point light source. Figure 2.2 shows a sketch of a Schlieren setup with an extended light source. More information can be found in [4], on which part of this discussion is based.

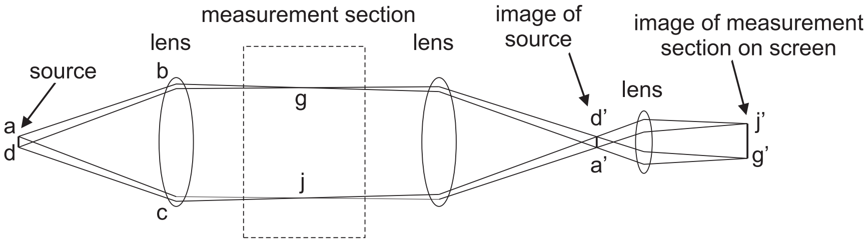

Figure 2.2: Basic idea of a Schlieren setup with an extended light source.

A point a in the source emits a light bundle abc which focuses on a' in the source-image plane, which is located in the focal plane of the second lens. Other points in the source are focused similarly and form the image $d'a'$ of the source. Notice that each light bundle, such as abc, completely fills the measurement section. Therefore every point in the image of the source receives light from every part of the measurement section.

Now consider light reaching point g in the measurement section. This light comes from the source ad, passes the image $d'a'$ of the source, and finally is focused onto the screen in point g'. Hence, all light passing point g completely fills the image $d'a'$ of the source. This is also true for other points (e.g. j) in the measurement section. Only one plane, consisting of points g and j can be focused onto the screen precisely. Depending on the focal depth other parts of the measurement section will also be sufficiently sharp.

Now we understand, that by cutting off a part of the light in the source-image plane the light intensity in the entire image, which is focused onto the screen, is evenly decreased. The only effect of the cut off is the direction in which the density differences are visualized. If a straight knife edge is used to cut off the light only density differences perpendicular to the edge can be visualized; therefore a circular cut off (a dot) will be used to visualize density differences in all directions within the measurement plane.

The basic aspects of Schlieren are introduced and it is shown that the Schlieren technique does not alter the flow, it only uses optical techniques to visualize the flow. In the next section two standard techniques will be discussed: PIV and dye injection, which are both widely used in the literature to visualize wake structures behind bodies. This is followed by a section on the Schlieren setup and a section in which some experimental results will be presented and comparisons of those results with the literature will be made. The last section is left to conclusions.

2.2 Flow visualization methods

Two common techniques used in the field of wake visualization in water are Particle Image Velocimetry (PIV) and dye injection. PIV uses thin light sheets which lighten small particles, which are added to the water. These particles have the same density as the surrounding water. By following these particles the local flow structures can be reconstructed for the flow captured in the light sheet. For the dye injection method one injects dye just behind the an object. The flow will carry on this dye and the flow structures will be visualized. Because the spheres and bubbles are rising freely both techniques have their disadvantages.

PIV limits the measurement section. Because the light sheets only have a limited thickness they do not provide a 3D view of the flow field. Furthermore, the spheres and bubbles rising through water at the Reynolds numbers we are interested in hardly move straight through the water. This problem was also encountered by Brücker [1] who used PIV for the visualization of wake structures behind bubbles. Hence, the chance to capture a sphere or bubble in the light sheet is low and once captured it will soon continue its path outside the light sheet. Although PIV can provide quantitative data on velocities around moving spheres or bubbles the time resolution of images with the actual sphere or bubble captured is low.

Dye injection techniques are commonly used for flow visualization behind fixed objects. Schouveiler & Provansal [8] obtained beautiful pictures from dye injection experiments to visualize the wake instabilities behind fixed spheres. A major problem in their experiments was the position where dye is injected. Vorticity generated at the sphere surface leaves the surface at specific locations in vortex threads. When dye is injected outside these vortex threads there is a chance that the flow is not entirely visualized. Furthermore, downstream of the sphere secondary vortices may be induced by the vortices leaving the sphere surface, as has been reported by Johnson & Patel [3] in their numerical study on wake structures behind spheres. Schouveiler & Provansal discuss this problem and note that they are not able to visualize these induced wake vortices, because the dye remains in the vortex threads generated at the sphere surface.

Dye injection has also been used by Magarvey & Bishop for visualization of both freely moving sphere and bubble wakes [5–7]. Here a second problem appears. The dye introduces contaminants in the water. For solid spheres this is not a problem, because the no slip boundary condition is not affected by contaminants. For bubbles contaminants can change the bubble boundary condition from no shear in clean water to no slip in contaminated water, changing the bubble dynamics substantially. Not only the amount of vorticity generated at the bubble surface changes, but also the shape of the bubble is affected by the contaminants. PIV introduces similar contamination problems, but here one might still think of micro bubble PIV instead of using micro particles for flow visualization.

The Schlieren technique introduces no contaminants in the fluid and is therefore in particular interesting for bubble experiments. This was also the main interest of De Vries [11]. The field of view is not limited to a sheet or places where dye is injected, it provides flow information in the entire measurement section. In the next section the Schlieren setup will be introduced.

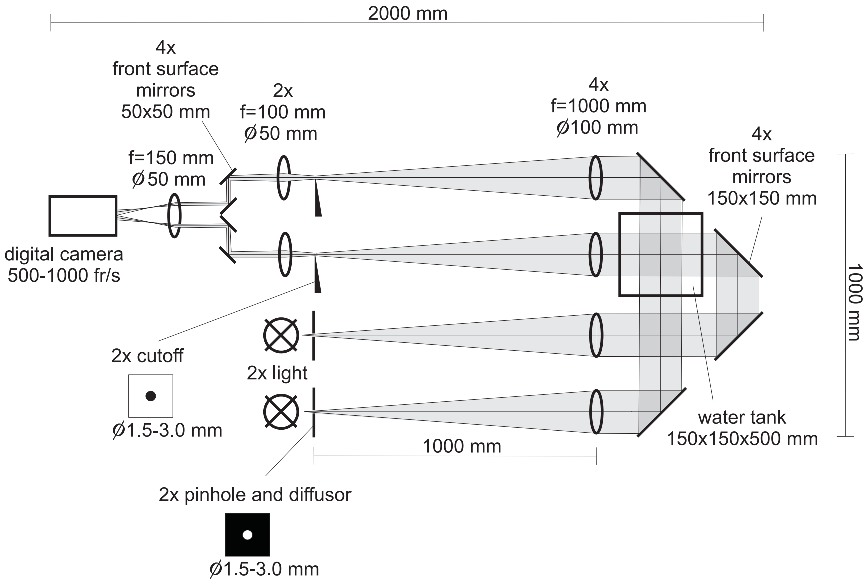

Figure 2.3: Schematic top view of the stereoscopic Schlieren setup. Grey areas indicate the light bundles

2.3 Schlieren setup

2.3.1 The optical components

Figure 2.3 shows the schematic top view of the Schlieren setup. In the center the water tank (15x15x50cm) is positioned in which the spheres and bubbles are released. Two light sources are used: either two Light Emitting Diodes (0.12W) or two halogen lamps (50W). The pinhole (diameter 1.5-3.0 mm) with diffusor creates a perfect point light source. A thin milk white plastic plate is used as diffusor. Typical path oscillations of spheres and bubbles moving through water have a wavelength around 50 mm. To capture an oscillation period properly, the vertical field of view is 70 mm. Therefore the two light bundles are collimated by the first two positive lenses (f=1000 mm, ø100 mm) into two non-diverging light bundles (ø100 mm). Four front surface mirrors (150x150 mm) direct the two light bundles perpendicular to each other through the water tank. Two positive lenses (f=1000 mm, ø100 mm) focus the light bundles after passage through the water tank onto the cutoff plate, with a circular cutoff of 1.5-3.0 mm, depending on the used pinhole. The circular cutoff is simply produced by printing dots on a transparent plastic sheet. After the cutoff two positive lenses (f=100 mm, ø50 mm), a positive lens (f=150 mm, ø50 mm) and four front surface mirrors (40x40 mm) are used to direct the light bundle directly onto the high speed camera which is: either a Kodak CR2000 with frame rates varying between 500-1000 fr/s and 384x512 pixels or a PCO at 640 fr/s with 1024x1280 pixels, resulting in resolutions of 0.21 and 0.078 mm/pixel, respectively. The outer rim of the 100 mm light bundles might be distorted by abberations; therefore the actual field of view is limited to 70 mm. The system is calibrated using a dotted grid (dot diameter 3 mm, spacing 5 mm) positioned vertically, diagonally in the water tank before and after a series of experiments. The last three lenses are used to adjust the focus and magnification factor. In the post-processing a background image is subtracted from all recorded images to provide a smooth background in each image. Finally, we end up with an image with two projections of a sphere or bubble with its wake structure.

2.3.2 The thermographic Schlieren method

Density differences in the water created by the motion of spheres and bubbles are too small to detect. Therefore, a vertical temperature gradient is imposed on the quiescent water in the water tank. A heating lamp is positioned on top of the water tank, creating a constant vertical temperature gradient of 1.0 Kcm^{-1}. An array of temperature sensors (one every 50 mm) is positioned vertically in the water tank to constantly measure the water temperature with an accuracy of ± 0.2 K. Experiments are conducted with temperatures between 25 to 32^{o}C in the measurement section. The spheres and bubbles drag along water of different density, creating a local change in density which can be visualized with the Schlieren technique.

The temperature gradient has a negative side effect; it changes the water viscosity (up to 14%). Especially for time resolved reconstruction of forces acting on these bodies, this viscosity change has to be taken into account. This can easily be done once the temperature is known from the temperature sensors. The temperature changes give rise to a change of the surface tension of only 1.5%. Hence, locally, on the bubble surface, this change can be neglected.

The next section will give the results with respect to flow visualizations behind spheres and bubbles. These results will be compared with experimental results in the literature.

2.4 Experimental results

Two examples of flow visualizations will be discussed. One on the wake behind a bubble, which is compared to work of De Vries [11]. The other on the wake

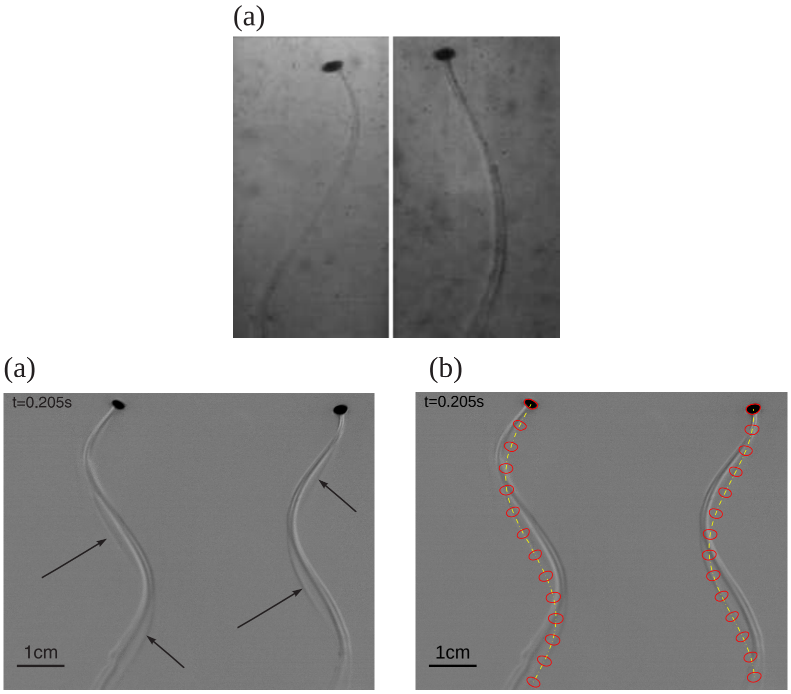

Figure 2.4: Stereoscopic Schlieren images of wake structure behind a spiraling rising bubble. (*a*) Image taken from De Vries [11]. (*b*) Image made with the Schlieren setup with two halogen lights. Black arrows indicate a weaker wake structure not visible in figure (*a*). (*c*) Same image as in figure (*b*), but now with path and bubble shapes included. The bubble shapes are plotted every 10 frames, giving a time interval of 0.64 s between the bubble shapes. The elapsed time after the bubble has entered the field of view is given in the upper left corner.

structure behind a falling sphere, which will be compared with dye injections experiments by Schouveiler & Provansal [8].

2.4.1 The wake behind a rising bubble

Figure 2.4(*a*) shows a visualization of the wake behind a spiraling bubble made by De Vries [11]. He used a stereoscopic Schlieren setup with two 500W Mercury lights and recorded the experiments with a NAC high speed camera at 500 fr/s. The well-known double vortex threads are clearly visible. With the Schlieren setup similar experiments were carried out at 640 fr/s (figures 2.4(*b*) and (*c*))). Comparison of figures (*a*) and (*b*) show an improvement in contrast and sharpness. More de-

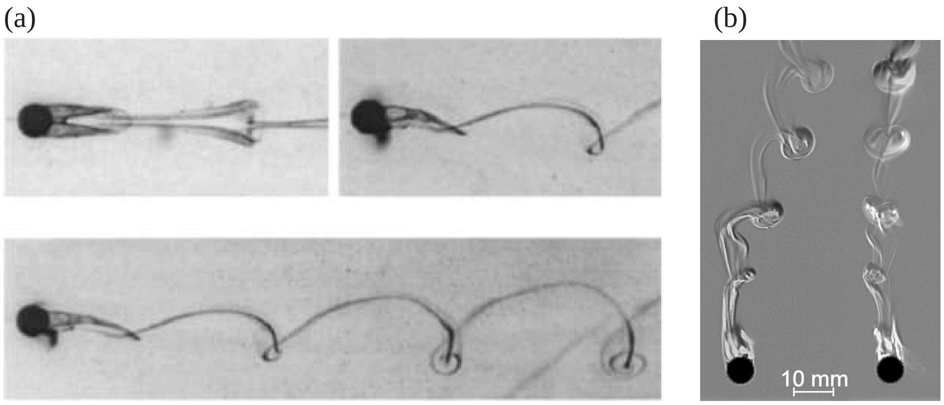

Figure 2.5: (*a*) Wake behind a fixed sphere visualized with dye injection. Taken from [8]. (*b*) Wake behind a freely falling sphere visualized with the Schlieren setup with two LED's.

tails are visible in figure (*b*), where a third weaker vortex structure becomes visible indicated by the black arrows. Comparison with figure (*c*) shows that this distortion is positioned on the bubble path. This observation agrees with an remark by Ellingsen & Risso [2] on the wake behind rising bubbles. They state that the wake consists of two vortex threads and a weaker axisymmetric wake straight behind the bubble. With the setup of De Vries it was not possible to detect this weaker wake structure. A reason for this might be that his camera provided less contrast or the mirrors and lenses he used were of lower quality, which can introduce distortions in the image. More information on the wake behind rising bubbles can be found in chapters 7 and 8.

2.4.2 The wake behind a falling sphere

Schouveiler & Provansal [8] visualized wake structures behind fixed spheres, using dye injection (figure 2.5(*a*)). The periodic vortex shedding in hairpin vortices is clearly visible. In the present setup spheres are released that are heavier than water, resulting in similar wake structures (figure 2.5(*b*)). The sphere is now allowed to move freely through the liquid, but still the details of the hairpin vortex shedding is captured nicely. Although the Schlieren technique averages over the horizontal depth in the field of view, the vortex structures are so localized that they can be captured in much detail. More on the wake structures behind freely rising and falling solid spheres can be found in [10] and chapter 3.

2.5 Conclusion

By using an artificial temperature gradient in water the Schlieren technique can be used for flow visualizations in water at low Mach numbers. The Schlieren setup of De Vries [11] is improved, resulting in sharper images with more contrast. It is shown that the use of LED or halogen light sources is still sufficient to properly visualize the wakes of freely rising or falling solid sphere and rising bubbles in quiescent water.

The Schlieren technique has some advantages over the established techniques as PIV and dye injection. It captures flow structures in the entire measurement section, making it suitable for freely moving objects. Furthermore, it does not introduce contaminants to the water making it specifically suitable for flow visualization of bubbles rising in purified water.

References

[1] BRÜCKER, C. 1999 Structure and dynamics of the wake of bubbles and its relevance for bubble interaction. *Phys. Fluids* **11**, 1781–1796.

[2] ELLINGSEN, K. & RISSO, F. 2001 On the rise of an ellipsoidal bubble in water: oscillatory paths and liquid-induced velocity. *J. Fluid Mech.* **440**, 235–268.

[3] JOHNSON, T.A. & PATEL, V.C. 1999 Flow past a sphere up to a Reynolds number of 300. *J. Fluid Mech.* **378**, 19–70.

[4] LIEPMANN, H.W. & ROSHKO, A. 1965 *Elements of gasdynamics*, 6th edn. John Wiley & Sons, New York, USA.

[5] MAGARVEY, R.H. & BISHOP, R.L. 1961 Transition ranges for three-dimensional wakes. *Can. J. Phys.* **39**, 1418–1422.

[6] MAGARVEY, R.H. & BISHOP, R.L. 1961 Wakes in liquid-liquid systems. *Phys. Fluids* **4**, 800–805.

[7] MAGARVEY, R.H. & MACLATCHY, C.S. 1965 Vortices in sphere wakes. *Can. J. Phys.* **43**, 1649–1656.

[8] SCHOUVEILER, L. & PROVANSAL, M. 2002 Self-sustained oscillations in the wake of a sphere. *Phys. Fluids* **14**, 3846–3854.

[9] SETTLES, G.S. 2001 *Schlieren and Shadowgraph Techniques*. Springer-Verlag, Berlin Heidelberg New York.

[10] VELDHUIS, C.H.J., BIESHEUVEL, A., VAN WIJNGAARDEN, L. & LOHSE, D. 2005 Motion and wake structure of spherical particles. *Nonlinearity* **18**, C1–C8.

[11] DE VRIES, A.W.G. 2001 Path and wake of a rising bubble. PhD thesis, University of Twente, Enschede, the Netherlands.

Chapter 3

Motion and wake structure of spherical particles [‡]

This paper presents results from a flow visualization study of the wake structures behind solid spheres rising or falling freely in liquids under the action of gravity. These show remarkable differences to the wake structures observed behind spheres held fixed. The two parameters controlling the rise or fall velocity (i.e., the Reynolds number) are the density ratio between sphere and liquid and the Galileo number.

3.1 Introduction

In the past years extensive numerical investigations [3, 7, 8, 15, 17] have established how the wake of a sphere held *fixed* in a uniform flow undergoes a series of transitions as the Reynolds number $Re = Ud/\nu$ is increased. Here U is the free stream velocity, d the diameter of the sphere, and ν the kinematic viscosity of the water. It was found that the wake is axially symmetric up to $Re = 212$. Above this value a planar-symmetric wake is found that consists of two steady counter-rotating threads. At $Re \approx 270$ there is a further transition and the planar-symmetric flow becomes time-dependent: opposite-signed streamwise vortices then form a series of loops that resemble hairpin vortices. As the Reynolds number is further increased, the flow gradually becomes more irregular and finally turbulent. The Digital Particle Image Velocimetry (DPIV) measurements by Brücker [2] and the

---

[‡] C.H.J. Veldhuis, A. Biesheuvel, L. Van Wijngaarden, & D. Lohse, *Motion and wake structure of spherical particles*, Nonlinearity **18**, pp. C1-C8 (2005)

flow visualization studies by Schouveiler & Provansal [16] have confirmed most of these numerical results and have further elucidated the sequence of transitions.

For *freely* moving spheres the Reynolds number is defined by the measured *mean* velocity of rise or fall of the sphere U_T and the corresponding 'Reynolds number' becomes $Re_T = \langle U_T \rangle d/\nu$. The *mean* velocity is the time averaged velocity of the sphere, not including the acceleration of the sphere from rest. The flow looses its axial symmetry at a critical Reynolds number which is not significantly affected by the density ratio ρ_s/ρ [5]: Re_{cr}=211.9 for $\rho_s/\rho \rightarrow \infty$ (i.e. sphere held fixed), $Re_{cr} = 206.3$ for $\rho_s/\rho = 0.5$ and $Re_{cr} = 205.8$ for $\rho_s/\rho = 0.0$. This is in good agreement with, for example, the experimental results on solid spheres [13], on surface-contaminated gas bubbles [4], and on wake visualizations in experiments with drops of tetrachloride and chlorobenzene falling in water [10–12]. As pointed out by Natarajan & Acrivos [14], these drops must have behaved effectively as solid spheres due to presence of surface-active impurities, and these visualizations have therefore often served as a basis of comparison with numerical studies on fixed spheres.

What happens for *freely* falling or rising spheres at higher Reynolds number, which is more common in multiphase flow applications? How are the wake structures and transitions observed for the fixed sphere case modified? Is there a (clear) difference in wake structure between rising and falling spheres? In this paper we present flow visualizations of the wakes behind freely moving solid spheres at large Reynolds number ($Re = 450 - 4623$) for which the density ratio ρ_s/ρ is in the range 0.50 to 2.63.

3.2 Experimental details

The flow visualizations of the sphere wakes were carried out in a transparent tank (0.15 x 0.15 x 0.5 m^3) filled with decalcified water. Smooth plastic spheres with diameters between 1.5 mm and 10 mm and densities between 500 kg/m^3 and 2781 kg/m^3 were released from rest. By means of an optical system consisting of two LED-lights, pinholes, lenses and mirrors, two perpendicular images of the particle and its wake were created and recorded at 500 frames/s with a CCD-camera (figure 3.1). Hence, each image consists of two perpendicular views of the same sphere. The images are taken at a position in the transparent tank where the spheres do not accelerate anymore. The wake was visualized using the Schlieren technique. To this end a small vertical temperature gradient in the water was maintained (1 K/cm.). The *mean* water temperature at the measurement section was 302 K, with corresponding values of the density ($\langle \rho \rangle$) and viscosity ($\langle \nu \rangle$) of 996 kg/m^3 and $0.802 \cdot 10^{-6}$ m^2/s, respectively. Hence, the Reynolds number is based on the *mean*

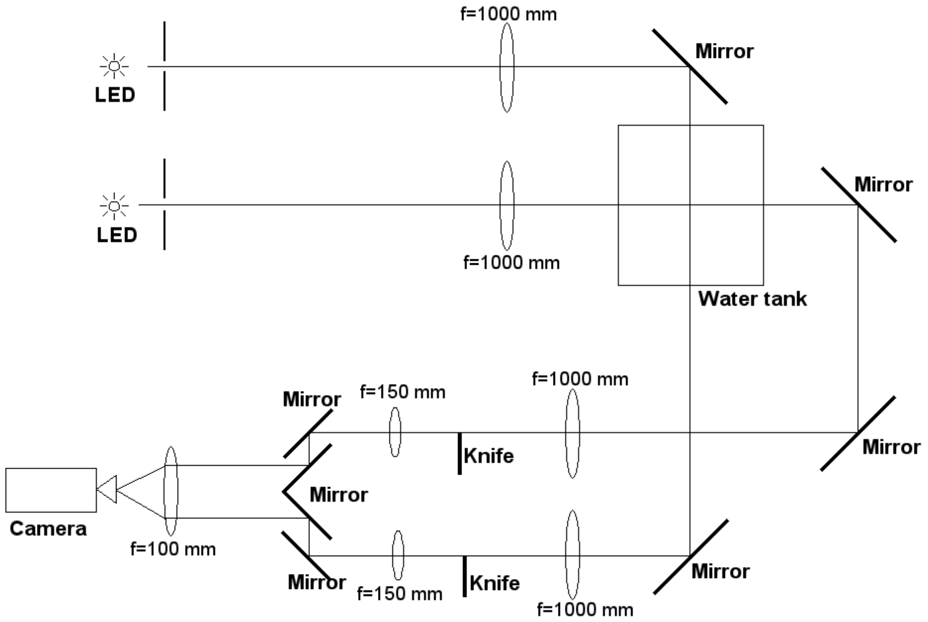

Figure 3.1: Top view of the Schlieren set-up used to visualize the sphere wakes.

viscosity and is defined as $Re_T = \langle U_T \rangle d / \langle \nu \rangle$. It turned out to be difficult to keep a constant temperature gradient. Therefore the error in the *mean* water temperature at the measurement section is about 3 K, leading to a relative error in the viscosity of 10 %. As opposed to the fixed-sphere problem, the Reynolds number for freely moving spheres is not an independent parameter. Following Jenny *et al.* [5] we choose as independent dimensionless variables the ratio $\rho_s / \langle \rho \rangle$ of the densities and the Galileo number

$$G = \frac{(|(\rho_s/\langle \rho \rangle - 1)|g)^{1/2} d^{3/2}}{\langle \nu \rangle}. \tag{3.1}$$

Since $(|(\rho_s/\langle \rho \rangle - 1)|gd)^{1/2}$ can be considered as a velocity scale, G plays a similar dynamical role as the free-stream Reynolds number in the case of fixed sphere. The parameter values for which we made the flow visualizations are summarized in Table 1.

	Number	d	ρ_s	$\rho_s/\langle\rho\rangle$	G	Re_T	Figure
falling	1	3.2	1028	1.03	121	205	Figure 3.8
	2	4.0	1058	1.06	239	325	Figure 3.8
	3	1.5	2781	2.79	304	450	Figure 3.8
	4	6.0	1035	1.04	359	546	Figure 3.2
	5	6.0	1043	1.05	394	608	Figure 3.2
	6	4.0	2629	2.63	1261	1970	Figure 3.8
rising	7	3.2	965	0.97	121	210	Figure 3.6
	8	5.0	950	0.95	297	450	Figure 3.3
	9	5.0	947	0.95	306	475	Figure 3.3
	10	4.0	873	0.88	334	565	Figure 3.6
	11	10.0	988	0.99	350	576	Figure 3.4
	12	8.0	982	0.99	331	602	Figure 3.6
	13	6.0	958	0.96	355	647	Figure 3.2
	14	6.0	950	0.95	390	656	Figure 3.2
	15	6.4	925	0.93	534	920	Figure 3.6
	16	6.4	864	0.87	728	1180	Figure 3.7
	17	7.9	925	0.93	732	1350	Figure 3.7
	18	6.4	650	0.65	1160	1965	Figure 3.7
	19	9.5	500	0.50	2548	4623	Figure 3.7

Table 3.1: Parameter values in our visualizations: d in mm, ρ_s in kg/m^3. G is defined by equation (3.1) and Re_T is the *mean* Reynolds number ($Re_T = \langle U_T\rangle d/\langle\nu\rangle$).

3.3 Observations

Figure 3.2 shows stereoscopic images of the wake structure behind falling spheres with densities approximately 4% (fig. 3.2*a*) and 5% (fig. 3.2*b*) higher than that of the surrounding liquid, and, for comparison, that behind rising spheres with densities that are approximately 4% (fig. 3.2*c*) and 5% (fig. 3.2*d*) lower. In all these examples the sphere diameter is 6 mm, so that the parameter G is roughly identical in cases (*a*) and (*c*), and in cases (*b*) and (*d*). The lighter spheres have a slightly higher vertical velocity than the heavier spheres, as indicated by Re_T

in table 3.1. The wakes of the falling spheres appear to have a more ‘irregular’ structure, and the path followed by these spheres shows much larger deviations from a straight vertical line. These pictures illustrate that the density ratio $\rho_s/\langle\rho\rangle$ matters, even at values close to 1.

Figures 3.3*a* and 3.3*b* give examples of a phenomenon that we believe to be characteristic for spheres following a zigzag path, namely that the two counter-rotating threads in the wake cross at the centerline of the zigzag (indicated by ‘1’ in fig. 3.3*a*). The presence of these threads of opposite-signed streamwise vorticity implies that the sphere experiences a lift force. As a consequence of the periodic crossing of the threads this force is always directed towards the zigzag center-line (see the sketch in fig.3.3*c*). A similar observation was made by De Vries *et al.* [18] on the wake behind zigzagging gas bubbles.

Schouveiler & Provansal [16] remark that for a fixed sphere “the dynamics of the two opposite-sign streamwise vortices ... presents a striking similarity with the long-wavelength (or Crow) instability of a pair of counter-rotating parallel vortices” and further “such a vortex pair instability could be responsible of the appearance of unsteadiness in the sphere wake”. Figure 3.3 suggests that the situation is slightly different for freely moving spheres. Here it appears that close to the sphere each of the vortices first develop a ‘kink’ (indicated by ‘2’ in fig. 3.3*a*), a process in which the curvature of the vortices presumably plays an important role [1]. As the kinks develop further downstream of the sphere they come near each other and finally combine into what resembles a hairpin vortex (indicated by ‘3’). This sequence of events can be seen in the flow visualizations presented in figure 3.4, see also figure 6 of ref. [11].

As the kinks develop and hairpin-like vortices are formed further downstream, a pattern results. Lunde & Perkins [9] interpreted this pattern as a series of hairpin vortices of alternating sign, shed periodically by the spheres at the extremes of the zigzag path. Our visualizations suggest instead that the streamwise vorticity produced at the surface of the sphere does not change sign; the legs of the like-signed hairpin vortices cross at the centerline of the zigzag.

Figure 3.2*b* is an example in which more than one kink develops in a half-period of the zigzag. We have not yet been able to determine the conditions (in terms of the parameters $\rho_s/\langle\rho\rangle$, G, or Re_T) that select the number of kinks that are formed. What is remarkable is that the development of the kinks and the subsequent formation of the hairpin vortices do not seem to affect the trajectory of the sphere. This corroborates the opinion that at high Reynolds numbers the details of the vorticity distribution very close to a body basically determine the forces that it experiences.

We will now turn to experiments with density ratios more different from one.

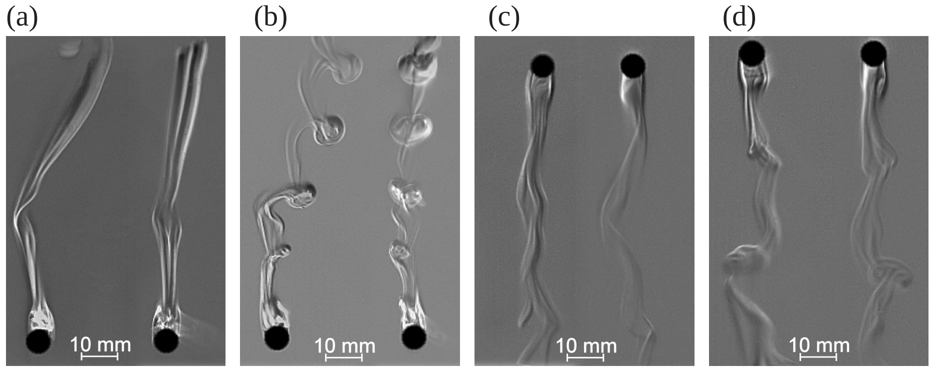

Figure 3.2: Stereoscopic views of falling and rising spheres and their wakes. The left part of each frame shows the xz-plane and the right part the yz-plane. In each case the sphere diameter is 6 mm. The values of the parameters $\rho_s/\langle\rho\rangle$, G, and Re_T are, respectively: (*a*) 1.04, 359, 546; (*b*) 1.05, 394, 608; (*c*) 0.96, 355, 647; (*d*) 0.95, 390, 656.

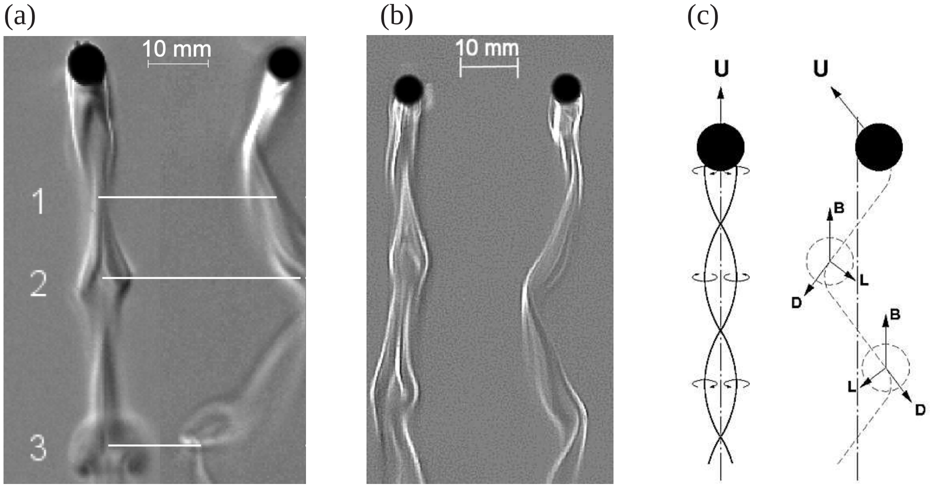

Figure 3.3: Stereoscopic views of rising zigzagging spheres and their wakes. The left part of each frame shows the xz-plane and the right part the yz-plane. The views illustrate the crossing at the center-line of the zigzag path of the two counter-rotating threads of the wake (‘1’), the occurrence of kinks (‘2’) at the extremes of the path, and the formation of hairpin-like vortices (‘3’) as two neighbouring kinks connect. Values of the parameters d, $\rho_s/\langle\rho\rangle$, G and Re_T are, respectively: (*a*) 5 mm, 0.95, 297, 450; (*b*) 5 mm, 0.95, 306, 475. As shown in (*c*) the crossing of the vortex threads results in a lift force L that is always directed towards the center-line of the zigzag path. D shows the direction of the drag force and B the one of the buoyancy.

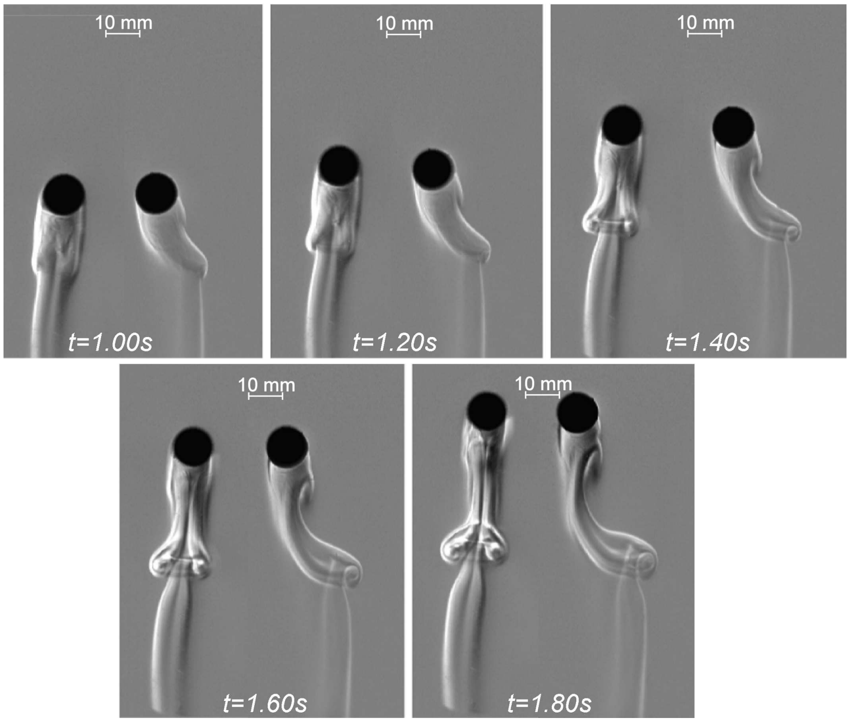

Figure 3.4: Sequence of stereoscopic views of a rising sphere and its wake. The left part of each frame shows the xz-plane and the right part the yz-plane. The views illustrate the process of formation of a hairpin-like vortex ($d = 10$ mm, $\rho_s/\langle\rho\rangle = 0.99$, $G = 350$ and $Re_T = 576$).

Recently Jenny *et al.* [6] reported on their numerical work on freely moving spheres in a Newtonian fluid. They focussed on the frequencies in the wake and the path of the sphere in the parameter space spanned up by the density ratio and the Galileo number. Figure 3.5 reproduces their phase diagram. The numbers in the diagram refer to the numbers of the experiments given in table 3.1. A lot of our experiments are outside their investigated region and new experiments should be done in the interesting regions around a Galileo number of 200. Further experiments should focus more on the frequencies in the wake of the sphere and compare this to the frequencies given by Jenny *et al.* (see caption of figure 3.5). Furthermore, we must stress that wake visualizations with the Schlieren method demand a temperature gradient in the water. Hence the density and viscosity of the water are not constant through the entire flow field and the local Galileo number will not be constant. The differences between the *mean* Galileo number and the local Galileo number can reach 10 % and must be taken into account when analyzing figure 3.5.

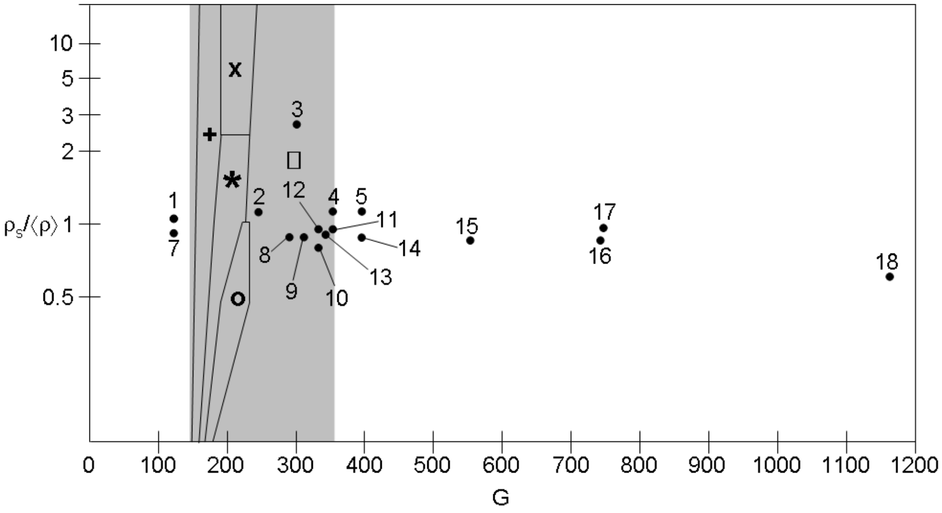

Figure 3.5: Phase diagram: density ratio $\rho_s/\langle\rho\rangle$ versus Galileo number. The grey box is the regime analysed by Jenny *et al.* [5]. They find in the most left region an axisymmetric wake. The symbols, directly taken from [5], denote: $+$ steady and oblique, $*$ oblique and oscillating regime with low frequency ($0.045 \leq f \leq 0.068$), $\times$ oblique and oscillating regime with high frequencies ($f = 0.180$), O zigzagging periodic regime ($0.023 \leq f \leq 0.035$) and $\square$ chaotic regime. The numbers denote the number of our experiment in table 1. Experiments 6 and 19 fall outside the diagram.

A striking difference between our experimental data and the numerical data of Jenny *et al.* is the behavior of falling spheres with a density ratio close to one. From figures 3.2 and 3.8 it can be seen that these falling spheres can also fall in a non-vertical path. This contradicts Jenny *et al.* who claim that only rising spheres can go in a zigzagging motion (the circles in the phase diagram figure 3.5).

From our experiments one concludes that for increasing Reynolds number the wake becomes more irregular (figures 3.6 to 3.8). The two-threaded wake structure is also present for higher Reynolds numbers. Is the double threaded wake structure also present in the case of the highest Reynolds numbers, where the wake structure has a turbulent structure? If so, do instabilities in the wake cause kinking of the vortex threads which leads to this turbulent wake structure? Further research will address these questions in order to get a better understanding of the boundary layer separation from spheres at high Reynolds numbers as shown on this year's cover.

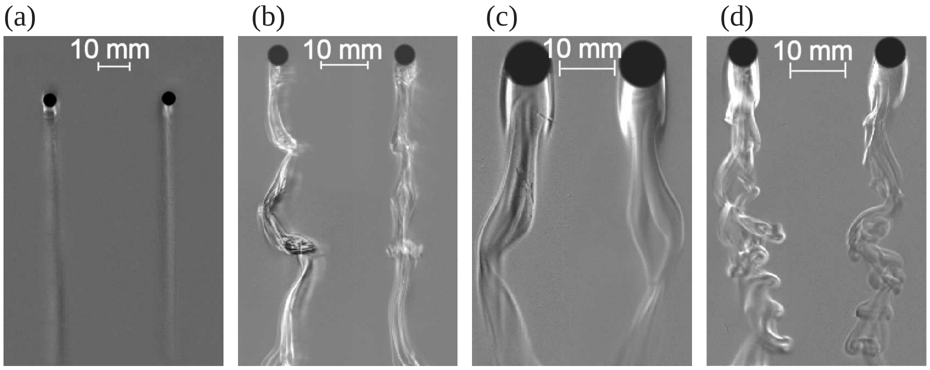

Figure 3.6: Stereoscopic views of rising spheres and their wake structures observed at several Reynolds numbers (Reynolds number increases from a to d and continues in figure 3.7). The left part of each frame shows the xz-plane and the right part the yz-plane. Values of the parameters d, $\rho_s/\langle\rho\rangle$, G and Re_T are, respectively: (*a*) 3.2 mm, 0.97, 121, 210; (*b*) 4.0 mm, 0.88, 334, 565; (*c*) 8.0 mm, 0.99, 331, 602; (*d*) 6.4 mm, 0.93, 534, 920.

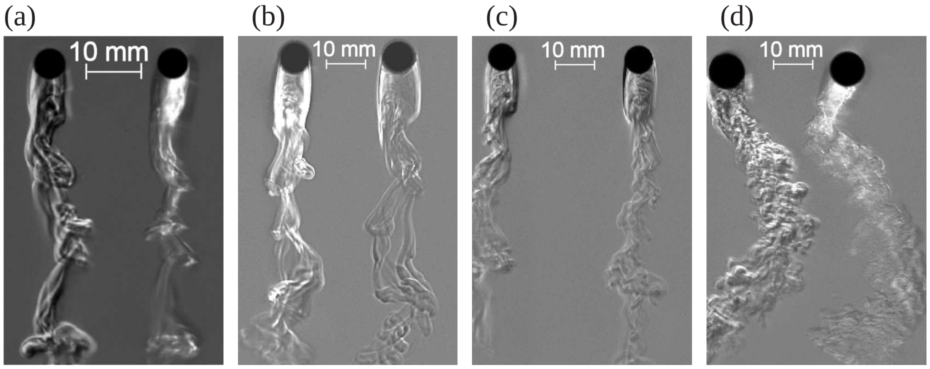

Figure 3.7: Stereoscopic views of rising spheres and their wake structures observed at several Reynolds numbers (Reynolds number increases from a to d). The left part of each frame shows the xz-plane and the right part the yz-plane. Values of the parameters d, $\rho_s/\langle\rho\rangle$, G and Re_T are, respectively: (*a*) 6.4mm, 0.87, 728, 1180; (*b*) 7.9 mm, 0.93, 732, 1350; (*c*) 6.4 mm, 0.65, 1160, 1965; (*d*) 9.5 mm, 0.50, 2548, 4623.

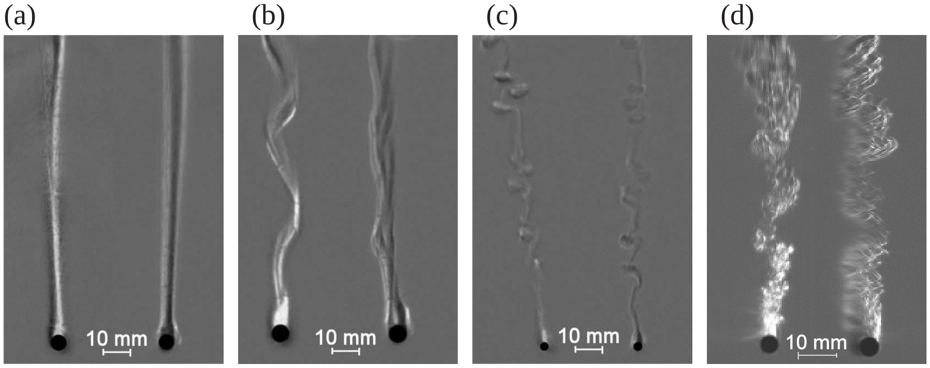

Figure 3.8: Stereoscopic views of falling spheres and their wake structures observed at several Reynolds numbers (Reynolds number increases from a to d). The left part of each frame shows the xz-plane and the right part the yz-plane. Values of the parameters d, $\rho_s/\langle\rho\rangle$, G and Re_T are, respectively: (*a*) 3.2mm, 1.03, 121, 205; (*b*) 4.0 mm, 1.06, 239, 325; (*c*) 1.5 mm, 2.79, 304, 450; (*d*) 4.0 mm, 2.63, 1261, 1970.

3.4 Conclusions

Flow visualizations of the wakes behind solid spheres moving under the action of gravity reveal remarkable differences with the wakes behind spheres held fixed: the crossing of threads of opposite-signed vorticity, the formation of kinks on these threads that develop into hairpin vortices. The ratio between the densities of the sphere and that of the surrounding fluid appears to be important. Our experiments clearly show the difference in path and wake structure between rising and falling spheres with the same Galileo number. Furthermore, the double threaded wake structure seems to be a basic feature, even for large Reynolds numbers. This should be investigated thoroughly in future research.

References

[1] BETCHOV, R. 1965 On the curvature and torsion of an isolated vortex filament. *J. Fluid Mech.* **22**, 471–479.

[2] BRÜCKER, C. 2001 Spatio-temporal reconstruction of vortex dynamics in axisymmetric wakes. *J. Fluids Struct.* **15**, 543–554.

[3] GHIDERSA, B. & DUŠEK, J. 2000 Breaking of axisymmetry and onset of unsteadiness in the wake of a sphere. *J. Fluid Mech.* **423**, 33–69.

[4] HARTUNIAN, R.A. & SEARS, W.R. 1957 On the instability of small gas bubbles moving uniformly in various liquids. *J. Fluid Mech.* **3**, 27–47.

[5] JENNY, M., BOUCHET, G. & DUŠEK, J. 2003 Nonvertical ascension or fall of a free sphere in a Newtonian fluid. *Phys. Fluids* **15**, L9–L12.

[6] JENNY, M., DUŠEK, J. & BOUCHET, G. 2004 Instabilities and transition of a sphere falling or ascending freely in a Newtonian fluid. *J. Fluid Mech.* **508**, 201–239.

[7] JOHNSON, T.A. & PATEL, V.C. 1999 Flow past a sphere up to a Reynolds number of 300. *J. Fluid Mech.* **378**, 19–70.

[8] LEE, S. 2000 A numerical study of the unsteady wake behind a sphere in a uniform flow at moderate Reynolds numbers. *Comput. Fluids* **29**, 639–667.

[9] LUNDE, K. & PERKINS, R.J. 1997 Observations on wakes behind spheroidal bubbles and particles. , vol. FEDSM97, p. 3530.

[10] MAGARVEY, R.H. & BISHOP, R.L. 1961 Transition ranges for three-dimensional wakes. *Can. J. Phys.* **39**, 1418–1422.

[11] MAGARVEY, R.H. & BISHOP, R.L. 1961 Wakes in liquid-liquid systems. *Phys. Fluids* **4**, 800–805.

[12] MAGARVEY, R.H. & MACLATCHY, C.S. 1965 Vortices in sphere wakes. *Can. J. Phys.* **43**, 1649–1656.

[13] NAKAMURA, I. 1976 Steady wake behind a sphere. *Phys. Fluids* **19**, 5–8.

[14] NATARAJAN, R. & ACRIVOS, A. 1993 The instability of the steady flow past spheres and disks. *J. Fluid Mech.* **254**, 323–344.

[15] PLOUMHANS, P., WINCKELMANS, G.S., SALMON, J.K., LEONARD, A. & WARREN, M.S. 2002 Vortex methods for direct numerical simulation of three-dimensional bluff body flows: Application to the sphere at Re = 300, 500, and 1000. *J. Comput. Phys.* **178**, 427–463.

[16] SCHOUVEILER, L. & PROVANSAL, M. 2002 Self-sustained oscillations in the wake of a sphere. *Phys. Fluids* **14**, 3846–3854.

[17] TOMBOULIDES, A.G. & ORZAG, S.A. 2000 Numerical investigation of transitional and weak turbulent flow past a sphere. *J. Fluid Mech.* **416**, 45–73.

[18] DE VRIES, A.W.G., BIESHEUVEL, A. & VAN WIJNGAARDEN, L. 2002 Notes on the path and wake of a gas bubble rising in pure water. *Int. J. Multiphase Flow* **28**, 1823–1835.

Chapter 4

Freely rising light solid spheres[‡]

This paper examines the remarkable observations of Karamanev and co-workers [8–10] on the behavior of spheres rising freely in a Newtonian fluid when the ratio between the density of the spheres and that of the surrounding fluid is less than 0.3. For these light spheres Karamanev & Nikolov have proposed to replace the standard relation for the drag coefficient C_D as a function of the Reynolds number Re by $C_D = 0.95$ for $Re > 130$. We have performed detailed experiments with spheres with density ratio of about 0.02. High-speed imaging is used to reconstruct three-dimensional trajectories of the rising spheres. From the analysis of the trajectories the magnitudes of the drag and lift forces exerted by the surrounding fluid are deduced. It turns out that the Karamanev & Nikolov proposal is not supported by our experiments. It is argued that the two main contributions to the drag force are (i) a viscous drag that may be estimated from the standard drag curve by evaluating the Reynolds number using the actual value of the velocity, and (ii) an inertial drag that arises essentially by the same mechanisms that cause the lift-induced drag familiar from wing theory. Estimates of both contributions, the latter using visualizations of the wakes of the spheres, give a favorable agreement with the measured drag forces.

4.1 Introduction

The mean velocity of single solid spheres, rising or falling freely in an infinite fluid, is of interest in numerous fields, including chemical, mechanical, and environmen-

---

[‡] C.H.J. Veldhuis, A. Biesheuvel, & D. Lohse, *Freely rising light solid spheres*, submitted to J. Fluid Mech. (2006)

tal engineering. This velocity may be determined from a balance between the net gravitational force and the mean drag on the sphere,

$$\tfrac{1}{6}\pi d^3\,|\rho_s-\rho|g=\tfrac{1}{8}\pi d^2\,\rho\,U_T^2\,C_D, \tag{4.1}$$

together with a relation for the drag coefficient C_D as a function of the Reynolds number $Re = U_T d/\nu$. Here ρ_s, d, and U_T denotes the density, diameter, and mean velocity of the sphere, respectively, ρ and ν are the density and the kinematic viscosity of the surrounding fluid, and g is the gravitational acceleration. A simple and well-known relation for the drag coefficient is that of Turton & Levenspiel [14],

$$C_D=\frac{24(1+0.173Re^{0.657})}{Re}+\frac{0.413}{1+16300Re^{-1.09}}; \tag{4.2}$$

a discussion of this relation and of others, together with a proposal for an alternative

$$C_D=\frac{24}{Re}(1+0.150Re^{0.681})+\frac{0.407}{1+8710Re^{-1}}, \tag{4.3}$$

is given in Brown & Lawler [2]. Both relations are applicable for $Re < 2\times10^5$.

The data used to construct these relations appear to not have included cases in which the density ratio ρ_s/ρ is small. Karamanev and co-workers have pointed out, referring to their experiments with ‘light’ solid spheres rising in water [9, 10] and soap bubbles filled with helium or hydrogen rising in air [8], that these relations do not apply if $\rho_s/\rho < 0.3$. They suggest that for $Re > 130$ the constant value $C_D = 0.95$ is more appropriate. This may be compared with the much smaller limiting value for high Reynolds numbers following from eqs. (4.2) and (4.3), namely $C_D = 0.413$ and $C_D = 0.407$, respectively, that is found for heavy spheres. (Karamanev & Nikolov mention “Newton’s law” in the title of their 1992 paper which states that $C_D \simeq 0.5$.)

The conclusion must be [cf. 8] that the dynamics of a heavy and a light sphere are quite different even though they have the same diameter, the same absolute value of particle-fluid density difference and are placed in the same fluid, so that the driving force due to gravity has the same magnitude but only a different direction, namely, upwards or downwards. The explanation, as put forward first in [10] and repeated in the two later papers by Karamanev’s group, lies in, as they call, ”the effect of turbulence on the particle”. On page 1845 of their paper Karamanev & Nikolov state:

”As Re increases above 130, a wake shedding begins. Periodic pulsations of the fluid around the sphere are observed; hence the flow streamlines are not axisymmetric in this region. This causes an imbalance of the forces applied to the sphere in nonvertical direction. The main force (along with that of fluid viscosity)

opposing these nonvertical forces is that of mechanical inertia of the spherical particle. The main difference among a light and a heavy particle with the same driving force ... is that the light particle is less inert because of the smaller density and therefore smaller mass".

This explanation is not fully convincing. Firstly, it ignores the inertia of the fluid surrounding the spheres. This may be thought of as adding a contribution $\frac{1}{2}(\rho/\rho_s)M\,\mathbf{U}$ to the inertia $M\,\mathbf{U}$ of the sphere. Here M is its mass and $\mathbf{U}$ its vector velocity. The fluid inertia is clearly not negligible. It may even be dominant for the light spheres considered here. Secondly, the phrase "the effect of turbulence" bears with it a notion of randomness that is at odds with the phrase "periodic pulsations of the fluid around the sphere". Moreover, all the spheres studied by Karamanev and colleagues are claimed to have risen along helical paths which suggests that the spheres have experienced a force of constant magnitude and direction, associated with some underlying structure in the flow.

To examine the questions raised by the work of Karamanev's group, we have carried out further experiments on the behavior of light ascending solid spheres. A brief description of the materials and methods is given in $\S$ 2, followed by a discussion of the drag relation in $\S$ 3. Recordings of the trajectories of the light spheres ($\rho_s/\rho \approxeq 0.02$) have been analyzed to deduce the forces exerted by the surrounding fluid. The results are presented in $\S$ 4, together with a simple model for the drag experienced by the spheres. The paper ends with conclusions.

4.2 Materials and methods

For the experiments we used a plexiglass tank with a height of 0.50 m and a cross-section of 0.15 m × 0.15 m, filled with decarbonated tap water. The temperature was maintained at a temperature of 21 $^{\mathrm{o}}$C, giving a fluid density of 998 kg m^{-3} and a kinematic viscosity of 0.96·10^{-6} m^2 s^{-1}. A total of 31 experiments with light solid spheres were conducted. We used expanded-polystyrene (EPS) spheres, density $\rho_s = 18.5$ kg m^{-3}, each with a different diameter in a range between 3.5 and 5.6 mm. In addition, to see any differences in their dynamics, experiments with ascending and falling spheres with larger density were carried out. These included spheres of the following materials and properties: polypropylene ($\rho_s = 850$ kg m^{-3}, $d = 3.97$ mm); low-density polyethylene ($\rho_s = 925$ kg m^{-3}, $d = 6.35$ mm and $d = 7.94$ mm); polystyrene ($\rho_s = 1058$ kg m^{-3}, $d = 3.97$ mm); polyamide-imide ($\rho_s = 1410$ kg m^{-3}, $d = 3.18$ mm and $d = 3.97$mm); and glass ($\rho_s = 2472$ kg m^{-3}, $d = 2.50$ mm; $\rho_s = 2629$ kg m^{-3}, $d = 4.00$ mm).

With the help of mirrors two mutually perpendicular views of the moving spheres were recorded with a Kodak CR 2000 camera at 500 or 1000 frames per second. Standard image analysis techniques then resulted in a three-dimensional reconstruction of the paths.

In a second series of experiments the water was heated from above. This resulted in a small temperature gradient of 1.0 K/cm, which allows to use a Schlieren optics technique to visualize the wakes of the spheres. This technique was originally developed to obtain information on the wakes behind gas bubbles [16]. Details of the improved set-up used here may be found in Veldhuis *et al.* [15].

4.3 The drag relation

The data for the dimensionless mean velocity U_T, i.e. the Reynolds number

$$Re = \frac{U_T d}{\nu}, \tag{4.4}$$

and the drag coefficient as defined by equation (1),

$$C_D = \tfrac{4}{3}|\rho_s/\rho - 1|gd/U_T^2. \tag{4.5}$$

have been compiled in Figure 4.1. The 'light' ascending spheres ($\rho_s/\rho \approxeq 0.02$) are distinguished from the 'heavy' ascending spheres ($0.3 \lesssim \rho_s/\rho < 1.0$) and the data for settling spheres ($\rho_s/\rho > 1.0$) by the use of the gray values. The errorbars represent estimates of the uncertainty in the determination of the physical parameters in each individual experiment. The solid curve is the relation (4.2) proposed by Turton & Levenspiel [14] and the dashed line is the relation for light spheres, $C_D = 0.95$ for $Re > 130$, proposed by Karamanev & Nikolov [10].

The figure confirms what was observed by Karamanev's group, namely that as the density ratio ρ_s/ρ is sufficiently small, and the Reynolds number is sufficiently high, there are significant deviations from the standard drag relation. However, the measured values of the drag coefficient for our light spheres, all for Reynolds numbers much higher than 130, are lower than the proposed value $C_D = 0.95$.

Jenny *et al.* [5] have recently shown by numerical analysis that the critical Reynolds number Re_{cr} at which the flow around a 'free' massless solid sphere looses axial symmetry is 205.8, a value that is only slightly lower than the well-known critical value $Re_{cr} = 211.9$ for the flow around a fixed sphere (in other words, an extremely heavy 'free' sphere). This suggests that the Karamanev & Nikolov's 'critical' Reynolds number of 130 is merely the value of the Reynolds number for which the Turton-Levenspiel relation gives $C_D(Re) = 0.95$. So it seems that the Karamanev-Nikolov relation is too simple.

Formally, the problem is characterized by two dimensionless parameters, which, following Jenny *et al.* [5], may be chosen as the density ratio ρ_s/ρ and the Galileo

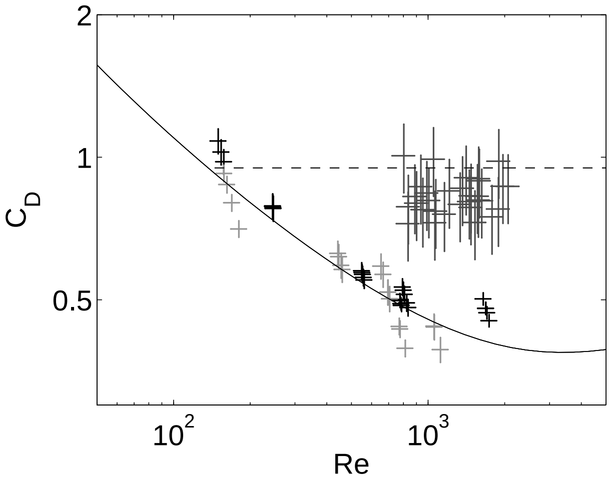

Figure 4.1: The drag coefficient C_D, defined by (4.5), as a function of the Reynolds number Re, based on the mean velocity of rise U_T. Solid curve: Turton-Levenspiel relation for heavy spheres ($\rho_s/\rho > 0.3$). Dashed line: Karamanev-Nikolov relation for light spheres ($\rho_s/\rho < 0.3$). Experimental data with small error bar close to relation of Turton-Levenspiel in black: $\rho_s/\rho > 1.0$, and light gray: $0.3 < \rho_s/\rho < 1.0$. Experimental data with large error bar (group at $C_D \approx$ 0.85): $\rho_s/\rho = 0.02$.

number

$$G = \frac{\sqrt{|\rho_s/\rho - 1|gd^3}}{\nu}. \tag{4.6}$$

Since $(|\rho_s/\rho - 1|gd)^{\frac{1}{2}}$ can be considered as a velocity scale, the Galileo number plays a similar dynamical role as the Reynolds number. With definition (4.5) one can express C_D in terms of G and Re

$$C_D = \tfrac{4}{3}(G/Re)^2. \tag{4.7}$$

The Karamanev-Nikolov relation for $C_D(Re)$ should be replaced by a *family* of curves* $C_D(Re, \rho_s/\rho)$ parameterized by the density ratio ρ_s/ρ. Each curve coincides with the standard drag curve up to some Reynolds number between $Re = 205.8$ and $Re = 211.9$, but then bends upwards. The data of Karamanev and coworkers suggest that for very small density ratios and at sufficiently high Reynolds

---

*Rather than taking Re and ρ_s/ρ as parameters, one could also take Re and G or G and ρ_s/ρ, employing the relations (4.4) – (4.7) between C_D, Re, G, and ρ_s/ρ.

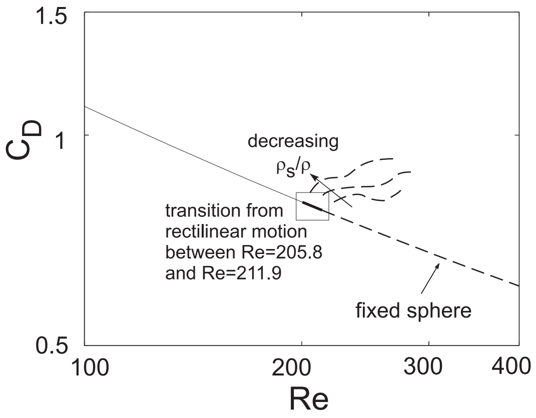

Figure 4.2: Sketch of the parametrization of the drag curve with the density ratio. For a density ratio of infinity (sphere held fixed) the drag curve is the standard drag curve Turton & Levenspiel [14]. For density ratios other than infinity the drag curve leaves the standard drag curve between $Re = 205.8$ and 211.9 [5].

numbers the curves approach $C_D \simeq 0.95$. However, for larger density ratios the curves would hardly deviate from the standard drag curve. Figure 4.2 shows a sketch clarifying this idea.

The construction of the family of curves $C_D(Re, \rho_s/\rho)$ (by using spheres with different diameters and densities) will require a considerable effort. The first steps in a related spirit were taken by Karamanev *et al.* [9] when they used a collection of spheres with different diameters, varied the Reynolds number for a sphere of given diameter by modifying its density, and thus obtained curves of $C_D(Re)$ parameterized by the sphere diameter. It may be noted that substantial deviations from the proposal $C_D = 0.95$ for $Re > 130$ were also found in these experiments [8].

We note that the large scatter in our data for spheres with a density ratio of approximately 0.02 raises doubts on the feasibility and the practical value of measuring the full family of curves $C_D(Re, \rho_s/\rho)$. The reason for this scatter will be discussed in the next section.

4.4 The motion of the spheres

4.4.1 Trajectories followed by the spheres

The recordings of the motion of the spheres from two perpendicular side-views were used to construct the curves they traced out in three-dimensional space. Six examples are shown in figure 4.3, all for a density ratio $\rho_s/\rho \simeq 0.02$ and with diameters ranging from 3.4 mm to 5.8 mm, so that the Galileo number G took values between 615 and 1712. The Reynolds number based on the mean velocity of rise was found to increase from 889 to 1982; detailed information is given in the caption of the figure. The character of these trajectories is revealed more clearly by a projection on a horizontal plane, i.e. as if the spheres were observed from above. These views are given in figure 4.4.

In figures 4.3 and 4.4 gray values are used to indicate the tangential velocity of the spheres, the numbers next to the gray value giving the corresponding value in m s^{-1}. The velocity appears to have the highest values where the path is most strongly curved. Ignoring the somewhat erratic path shown in case (*f*), the variations in the velocity are largest when the path is close to a perfect zigzag (see the gray value codes), and least when the path is nearly a pure spiral (spheres following a perfect helicoidal path do this at a constant velocity).

Karamanev and co-workers mention that in their experiments all the light spheres ascended along a spiral trajectory. In our experiments, even in repeated trials with spheres of the same diameter, no preferred type of path was observed. Each different path gave a different value for the mean rise velocity, which is the reason for the large scatter in our data for $C_D(Re)$. This result is a little puzzling. Karamanev's group used a tank with a height of 1.90 m; hence, it is possible that our tank, with a height of 0.50 m, was too short, and that if the spheres were allowed to rise over a much longer distance they would eventually end-up following helicoidal paths. The true explanation may be more complicated, however. Jenny *et al.* [6] have recently shown by numerical simulations that the $(G, \rho_s/\rho)$ parameter space may be divided into 'regimes', with distinct characteristics of the 'asymptotic states'. These asymptotic states refer to non-transient paths, i.e., pathes of spheres that have been rising for a sufficiently long time. Our experiments correspond to positions in this parameter space which all lie well within the 'chaotic regime'. Chaotic trajectories are characterized by periods with vigorous excursions in random directions, interrupted by periods in which the motion is seemingly 'smooth' or 'well-behaved'. Yet, with the exception of case (*f*) perhaps, the examples shown in figures 4.3 and 4.4 do not give the impression of being chaotic. It cannot be ruled out that, by coincidence, these examples represent such periods of calm behavior, but it is more likely that in this part of the chaotic regime various asymptotic states co-exist, most of which characterized by smooth paths over considerable lengths of time. Whatever is the case, using a tube of longer height should not make a difference, and measurements of the mean velocity of rise and the associated drag coefficient would appear as poorly reproducible; unless perhaps, averages were taken over a rather long time.

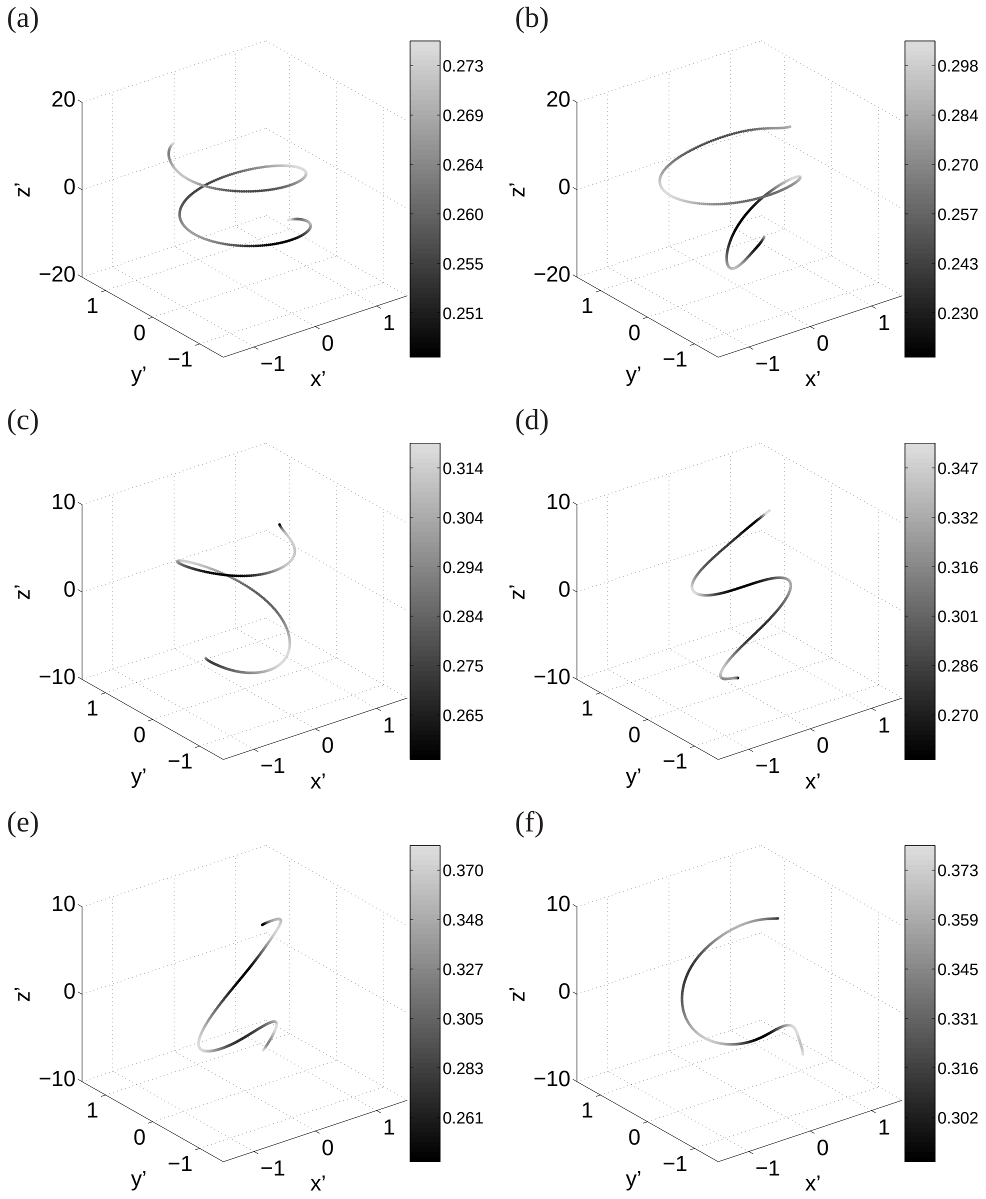

Figure 4.3: Measured trajectories of spheres rising in water. The gray values represent the tangential velocity of the spheres, with the numbers next to the gray value codes giving the corresponding value in m s^{-1}. Spatial coordinates have been non-dimensionalized with the diameter of the spheres. In all cases $\rho_s/\rho \simeq 0.02$. (*a*) $d = 3.4$ mm, $G = 615$; (*b*) $d = 3.9$ mm, $G = 756$; (*c*) $d = 4.3$ mm, $G = 875$; (*d*) $d = 4.8$ mm, $G = 1032$; (*e*) $d = 5.4$ mm, $G = 1231$; (*f*) $d = 5.7$ mm, $G = 1335$.

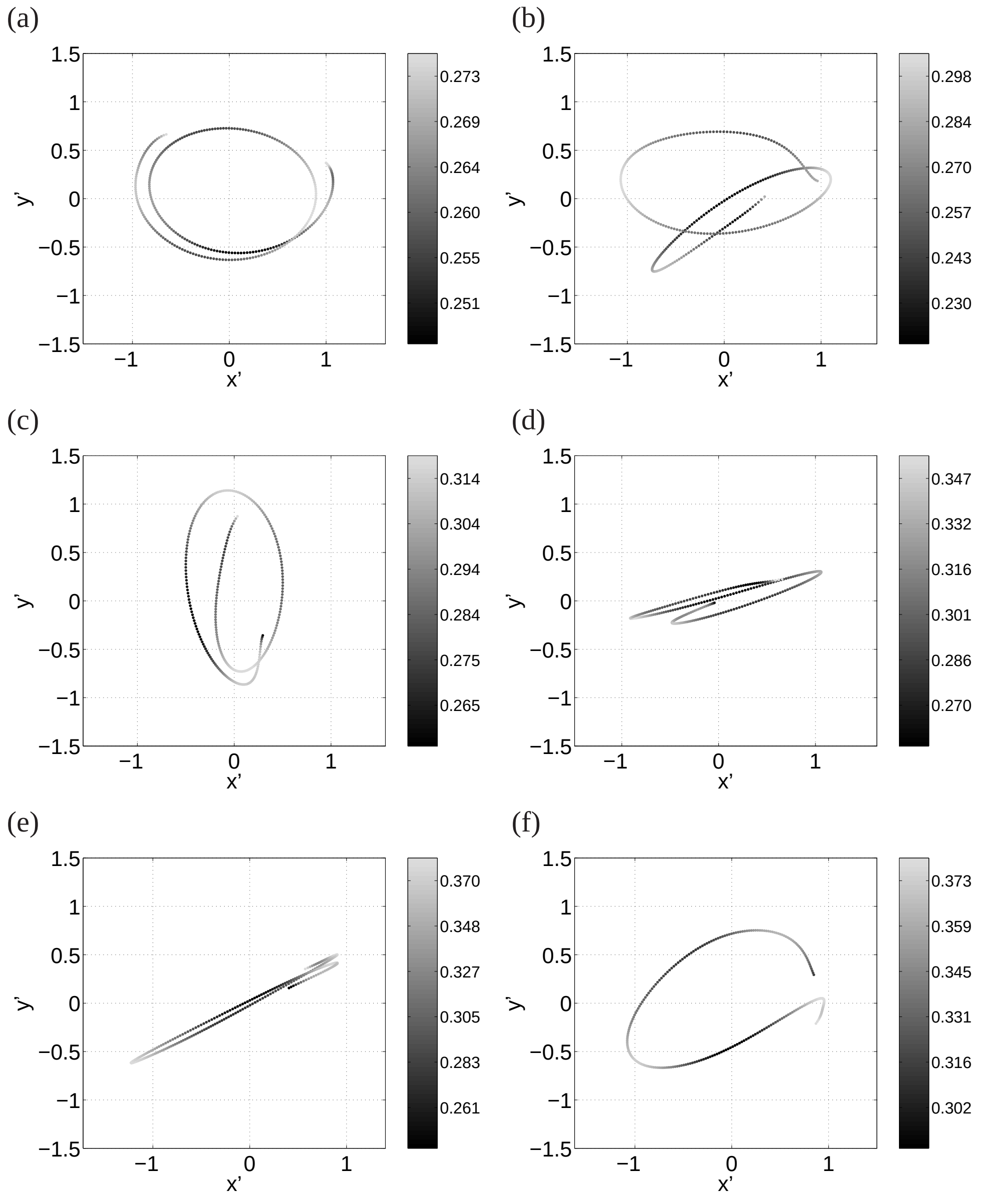

Figure 4.4: Projection of the six measured sphere trajectories of figure 4.3 on the XY-plane. Further details are given in the caption of figure 4.3.

4.4.2 Drag and lift forces

Determination

To determine the forces that have acted on the spheres as they traced out the curves exemplified in figures 4.3 and 4.4, it is helpful to use a Frenet reference frame, i.e. a moving orthogonal frame with the tangent to the curve $\mathbf{t}$, the normal to the curve $\mathbf{n}$, and the binormal $\mathbf{b}$ as unit vectors. Let $\mathbf{r}(t)$ denote the time-dependent position vector of the center of the sphere with respect to a fixed reference frame and let $s(t)$ measure the distance traveled along the curve from some arbitrary initial instant. Then the unit vectors are defined as

$$\mathbf{t} = \frac{\mathrm{d}\mathbf{r}}{\mathrm{d}s}, \quad \mathbf{n} = \frac{\mathrm{d}\mathbf{t}}{\mathrm{d}s} \Big/ \left|\frac{\mathrm{d}\mathbf{t}}{\mathrm{d}s}\right|, \quad \mathbf{b} = \mathbf{t} \times \mathbf{n}, \tag{4.8}$$

while the variation of these unit vectors along the curve is given by the Frenet-Serret formulae

$$\frac{\mathrm{d}\mathbf{t}}{\mathrm{d}s} = \kappa\mathbf{n}, \quad \frac{\mathrm{d}\mathbf{n}}{\mathrm{d}s} = -\kappa\mathbf{t} + \tau\mathbf{b}, \quad \frac{\mathrm{d}\mathbf{b}}{\mathrm{d}s} = -\tau\mathbf{n}. \tag{4.9}$$

Here κ is the curvature and τ is the torsion of the curve. An instructive, alternative formulation is obtained on introducing the Darboux vector

$$\mathbf{d} = -\tau\mathbf{t} + \kappa\mathbf{b}, \tag{4.10}$$

by which the Frenet-Serret formulae become

$$\frac{\mathrm{d}\mathbf{t}}{\mathrm{d}s} = \mathbf{d} \times \mathbf{t}, \quad \frac{\mathrm{d}\mathbf{n}}{\mathrm{d}s} = \mathbf{d} \times \mathbf{n}, \quad \frac{\mathrm{d}\mathbf{b}}{\mathrm{d}s} = \mathbf{d} \times \mathbf{b}. \tag{4.11}$$

Hence, the variation of the unit vectors consists of a rotation around the instantaneous tangent and binormal at rates $-\tau$ and κ, respectively.

Two closely related methods may now be used to determine the forces. Firstly, with respect to a rectangular coordinate system $OXYZ$ fixed to the laboratory, conservation of linear momentum of a body with mass M is expressed by the equation

$$\frac{\mathrm{d}\mathbf{I}}{\mathrm{d}t} = \{1 - (\rho/\rho_s)\}\, M\,\mathbf{g} + \mathbf{F}, \tag{4.12}$$

Here $\mathbf{I}$ is the virtual momentum of the body, i.e. the sum of the actual momentum of the body and the impulse of the irrotational fluid motion that would result if the motion of the body would be generated instantaneously from a state of rest. For a sphere the virtual momentum takes the simple form

$$\mathbf{I} = \left\{1 + \tfrac{1}{2}(\rho/\rho_s)\right\} M\,\mathbf{U}, \tag{4.13}$$

where $\mathbf{U} = (U_X, U_Y, U_Z)$ is the instantaneous velocity of the center of the sphere. The first term on the right-hand side of (4.12) is the gravitational force. The 'extraneous' force $\mathbf{F}$ is what Lighthill [12] calls 'the vortex-flow force', i.e. that part of the force which the fluid exerts on the body due to the presence of 'additional vorticity' in the flow. The precise form of this vortex-flow force does not need to concern us here, but it may be noted that expressions in terms of the *actual* vorticity distribution in the flow have been given by Kambe [7] and Howe [4]; connections with earlier work of J. M. Burgers are discussed in a paper by Biesheuvel & Hagmeijer [1]. The components of the vortex flow force (F_X, F_Y, F_Z) may be determined from the experimental data on the trajectory $\mathbf{r}(t)$, and may subsequently be projected on the Frenet frame to obtain (F_t, F_n, F_b). The drag force on the sphere is $\mathbf{F}_D = -F_t\mathbf{t}$ and the lift force is given by $\mathbf{F}_L = F_n\mathbf{n} + F_b\mathbf{b}$.

In an alternative method conservation of linear momentum of the body is expressed directly with respect to the Frenet frame, the motion of which is described by the translational velocity

$$\mathbf{U} = \frac{\mathrm{d}s}{\mathrm{d}t}\,\mathbf{t} \tag{4.14}$$

of the origin, and the angular velocity

$$\mathbf{\Omega} = \frac{\mathrm{d}s}{\mathrm{d}t}\,(-\tau\mathbf{t} + \kappa\mathbf{b}) \tag{4.15}$$

about the instantaneous position of its axes. The momentum equation of the body now reads

$$\left(\frac{\mathrm{d}\mathbf{I}}{\mathrm{d}t}\right)_F + \mathbf{\Omega} \times \mathbf{I} = \{1 - (\rho/\rho_s)\}\, M\,\mathbf{g} + \mathbf{F}, \tag{4.16}$$

where the first term on the left-hand side is the vector formed by the rates of change of the components of the virtual momentum of the body with respect to the Frenet reference frame. In this case

$$\left(\frac{\mathrm{d}\mathbf{I}}{\mathrm{d}t}\right)_F = \left\{1 + \tfrac{1}{2}(\rho/\rho_s)\right\} M\,\frac{\mathrm{d}^2 s}{\mathrm{d}t^2}\,\mathbf{t}. \tag{4.17}$$

Hence, conservation of linear momentum of the body is described with respect to a Frenet reference frame by the three equations

$$\left\{1 + \tfrac{1}{2}(\rho/\rho_s)\right\} M\,\frac{\mathrm{d}^2 s}{\mathrm{d}t^2} - \{1 - (\rho/\rho_s)\}\, M\,g_t = F_t, \tag{4.18}$$

$$\left\{1 + \tfrac{1}{2}(\rho/\rho_s)\right\} M\,\kappa\left(\frac{\mathrm{d}s}{\mathrm{d}t}\right)^2 - \{1 - (\rho/\rho_s)\}\, M\,g_n = F_n, \tag{4.19}$$

$$-\{1 - (\rho/\rho_s)\}\, M\,g_b = F_b. \tag{4.20}$$

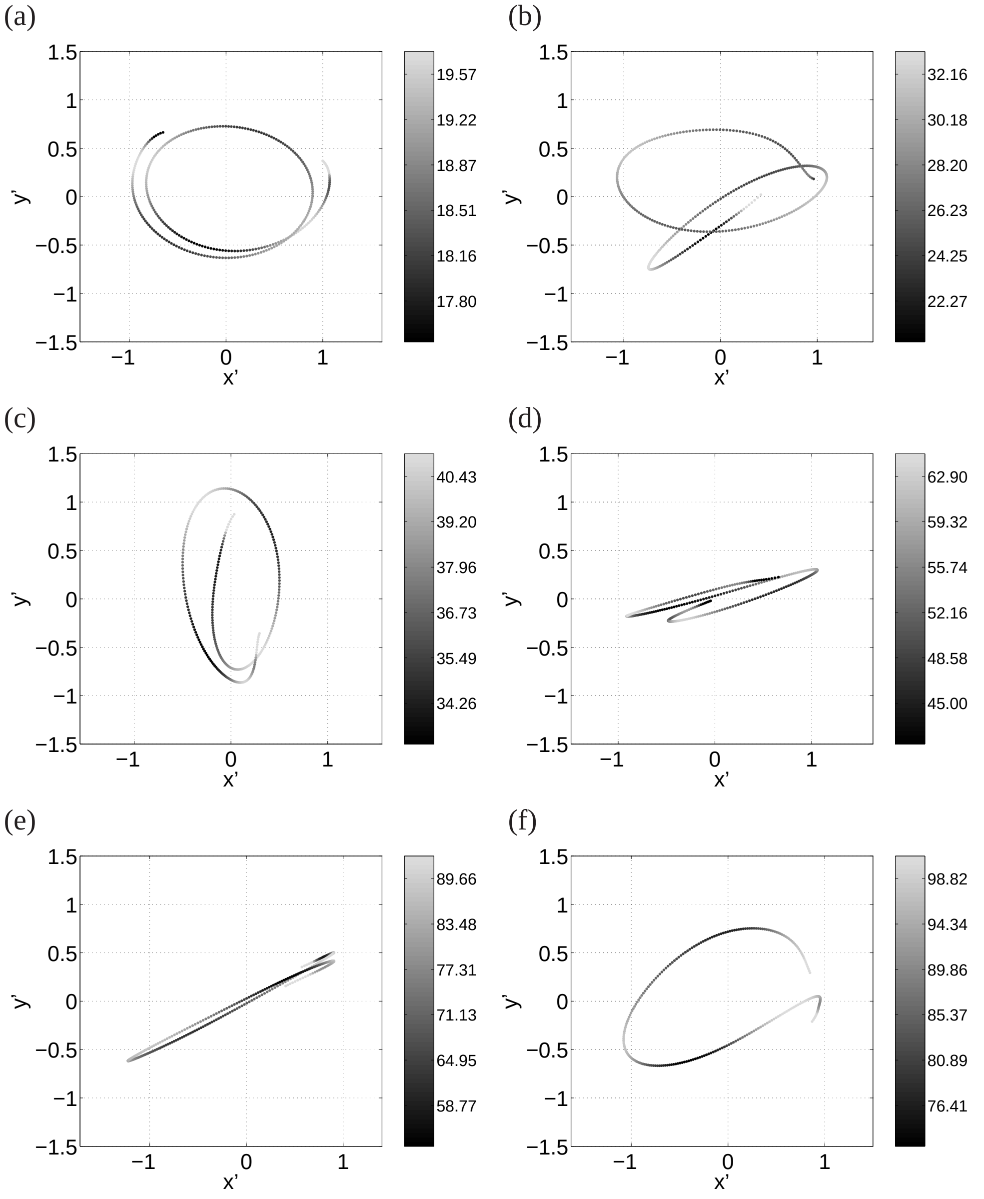

Figure 4.5: The drag force experienced by the spheres; the unit of the gray value code is 10^{-5} N. Further details are given in the caption of figure 4.3.

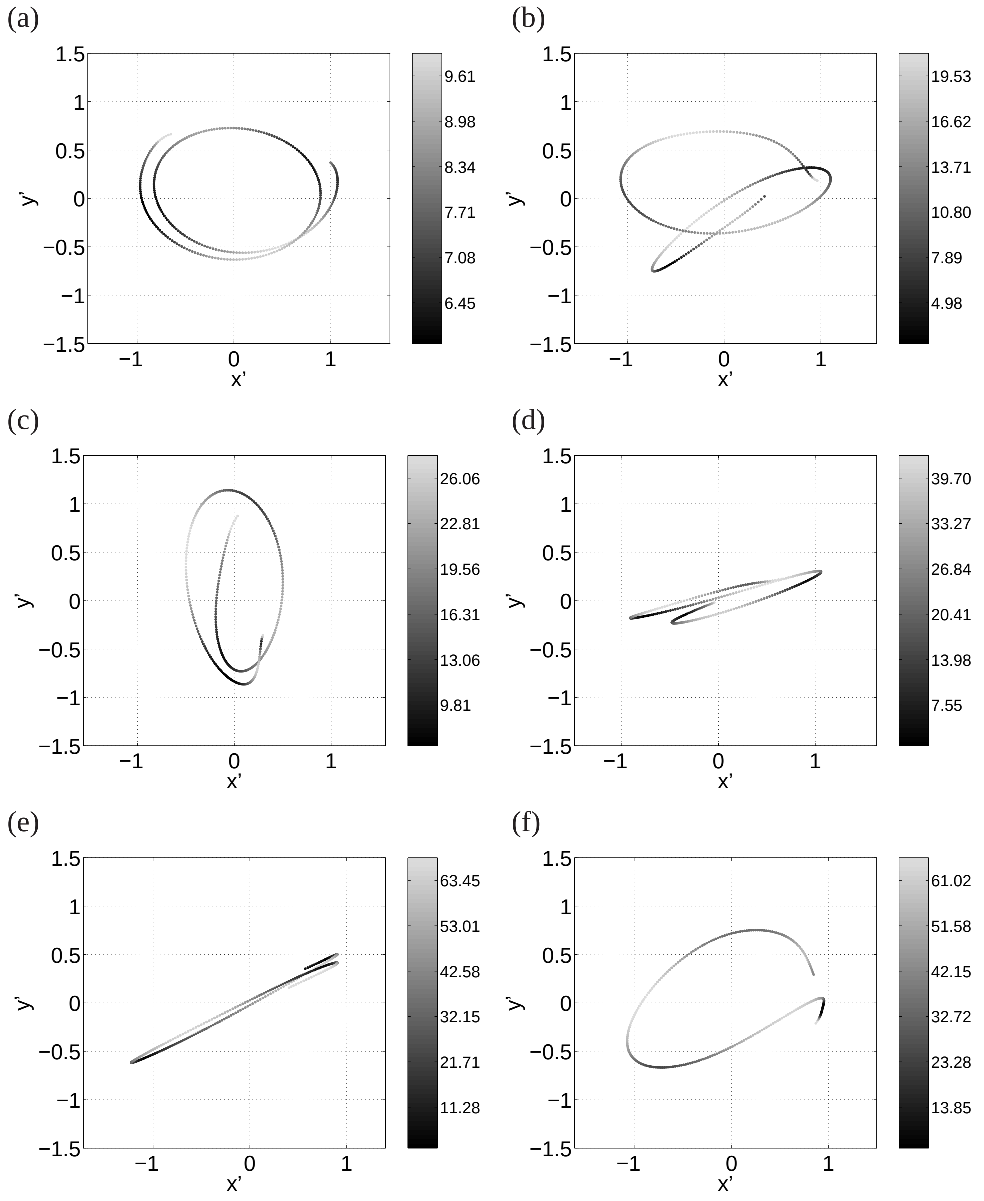

Figure 4.6: The magnitude of the lift force experienced by the spheres; the unit of the gray value code is 10^{-5} N. Further details are given in the caption of figure 4.3.

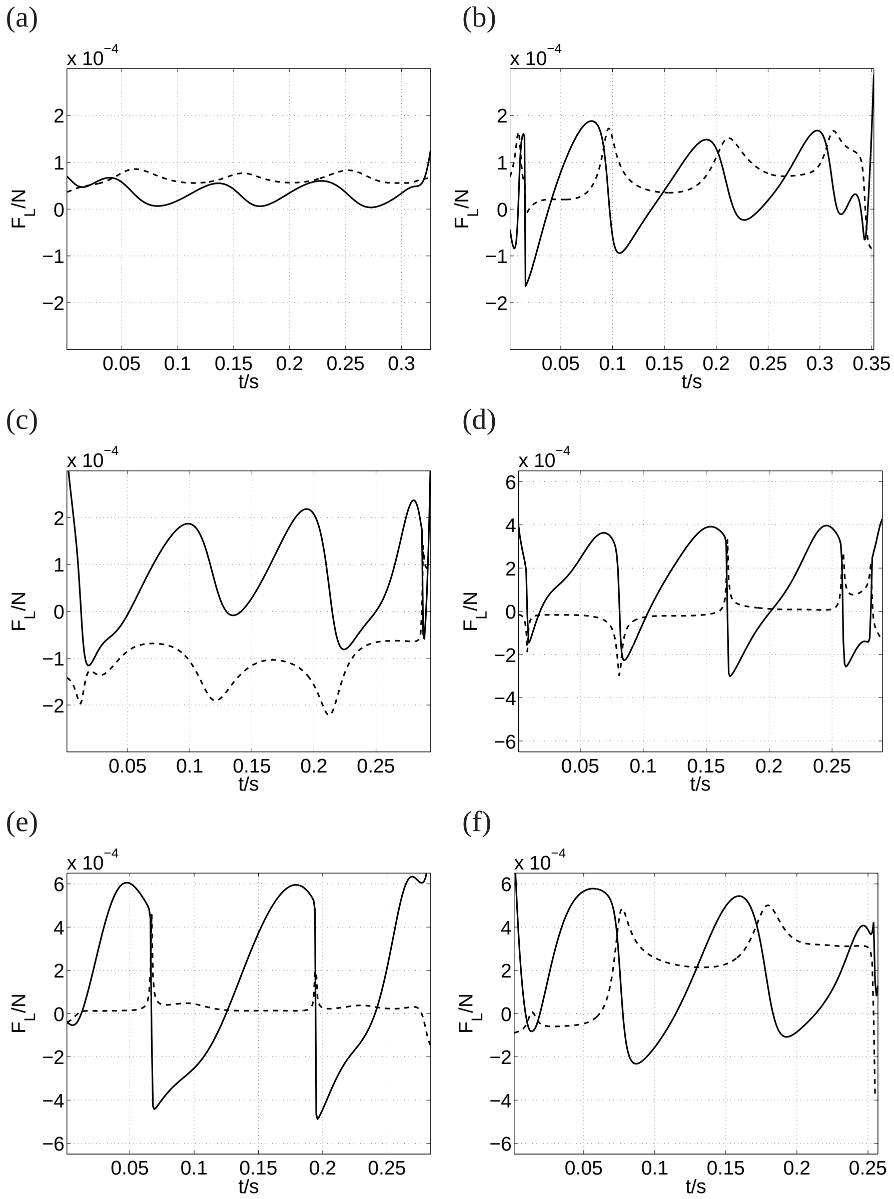

Figure 4.7: The components of the lift force acting on the spheres. Solid line: component in the direction of the normal to the curve (F_n). Dashed line: component in the direction of the binormal to the curve (F_b). Further details as in the caption of figure 4.3.

Both of the above approaches have been used to determine the drag and lift forces experienced by the spheres, with virtually identical results. These are presented in figures 4.5 and 4.6 in views from above of the same sphere trajectories shown in figures 4.3 and 4.4. Figure 4.5 gives the drag force and figure 4.6 the *magnitude* (not the direction) of the lift force. In all cases the numbers next to the gray value code give the corresponding value of the force in 10^{-5} N. In addition, time traces of the components (F_n, F_b) of the lift force are shown in figure 4.7, negative values of F_n indicating that this component is directed away from the center of curvature.

Interpretation

When comparing figures 4.4, 4.5, and 4.6 it is found that points of maximum tangential velocity do not coincide with the points at which the drag force and the lift force on the spheres take their largest value, an observation that will be discussed further below.

In figure 4.8 we present all relevant data, including path curvature and torsion, in one figure. We do this for two experiments: the spiraling sphere of case (*a*) and the zigzagging sphere of case (*e*). It is clear that for the spiral the motion is nearly steady. For the zigzag the motion is highly unsteady and the time-shift between velocity, lift and drag is clearly visible. At the point where the sphere passes the zigzag centerline the normal and the binormal vectors rotate 180^o, resulting is a sudden peak in the torsion τ. The curvature κ is smallest at the zigzag centerline indicating that the path is almost straight. The last two figures give estimates for the vortex angle ψ which will be introduced in the next paragraph.

For what concerns the lift forces, the origin of a force transverse to the direction of motion of the spheres is obviously the *generation* of a vorticity distribution in the fluid with a hydrodynamic impulse that has a component normal to the direction of the flow. Visualizations of the wakes of solid spheres by Veldhuis *et al.* [15] provided clear evidence of the continuous generation of such vorticity distributions with a structure which in the near wake consists of two parallel vortex threads, each with a strong axial component of vorticity (in opposite directions). Zigzagging and spiralling bubbles also have such a ‘bifid wake’, as shown in de Vries *et al.* [16]. Similar vortex structures are found some distance behind the wings of an airplane. At relatively low Reynolds numbers this bifid wake structure may extend a considerable distance downstream of the solid spheres (or bubbles). The threads may develop kinks and connect at fairly regularly spaced positions. At higher Reynolds numbers the wake becomes unstable and even turbulent already close to the body. These instabilities may involve a vigorous redistribution of the vorticity already

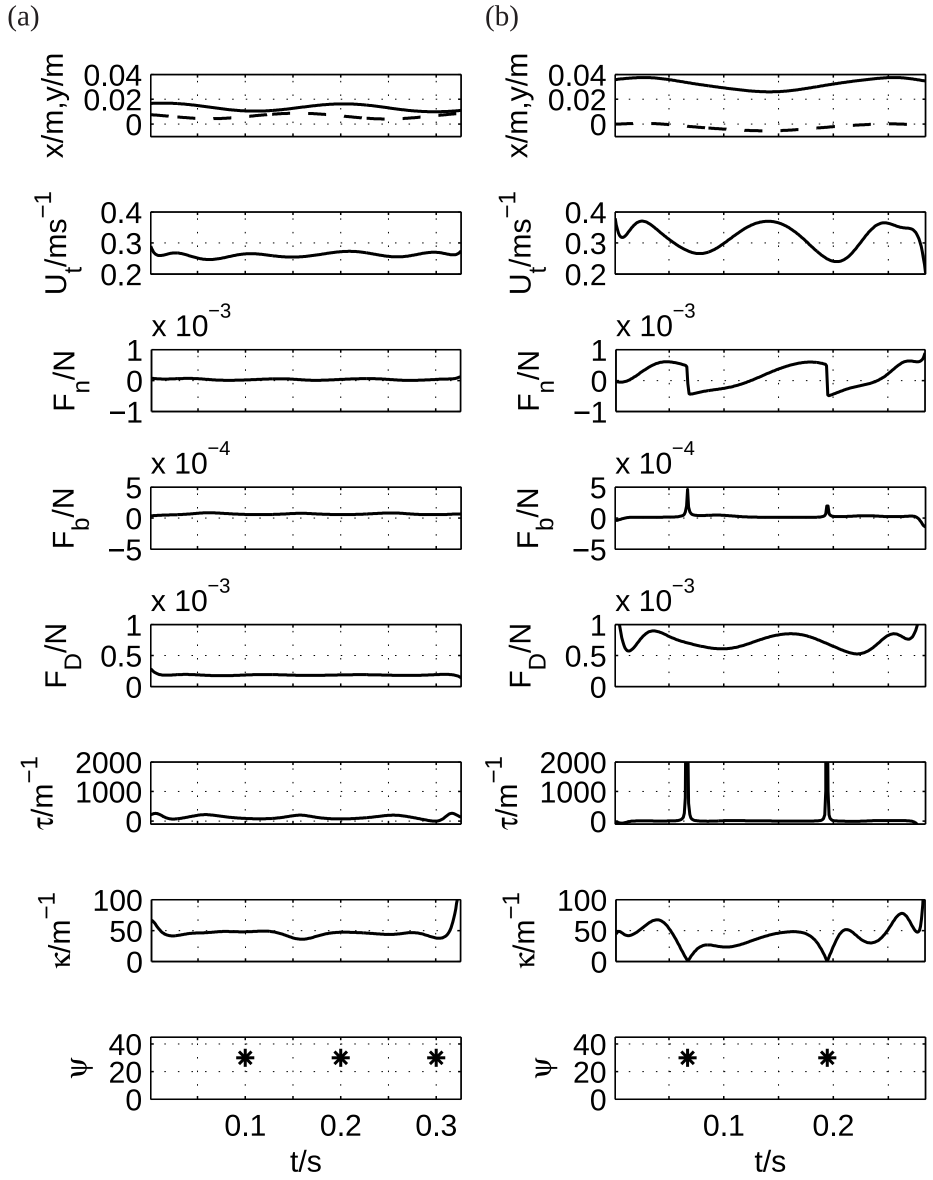

Figure 4.8: Data for case (*a*) (figure (*a*)) and case (*e*) (figure (*b*)), respectively. From top to bottom: Displacement in X and Y direction (solid and dashed line, respectively), tangential velocity U_t, lift in normal direction F_n , lift in binormal direction F_b, drag F_D, path curvature κ, path torsion τ, and vortex plane angle ψ. Further details as in the caption of figure 4.3.

present in the flow, yet the generation of new vorticity, i.e., the addition of hydrodynamic impulse transverse to the direction of motion of the body, varies much more smoothly, as evidenced by the results of the present experiments.

Another deduction made in de Vries *et al.* [16] and Veldhuis *et al.* [15], namely, that a pure zigzagging motion of a bubble or a solid sphere is accompanied by a wake that consists of two vortex threads which merge at the centerline of the zigzag and subsequently reappear with reversed direction of the vorticity within the threads, needs correction however. In figure 4.7(*e*) it may be seen how the normal component of the lift force on a zigzagging sphere suddenly jumps from a positive value to a negative value, while the magnitude remains the same. The reason for this behavior is that the normal to the path in the Frenet reference frame is directed towards the center of curvature. This forces the normal to change direction; the lift force does not change, it merely changes direction with respect to the normal to the curve. In other words, along the zigzag path points of zero curvature do not correspond to points where the lift force vanishes and changes direction.

De Vries *et al.* [16] and Veldhuis *et al.* [15] assumed that a pure zigzagging motion of a bubble or a solid sphere is accompanied by a wake that consists of two vortex threads which merge at the centerline of the zigzag. At the instant that the vortex threads merge no lift is generated, and since the curvature of the path vanishes at the centerline of the zigzag, this would imply a violation of equation (4.19), because the first term on the left hand side and the term on the right hand side are zero. What really happens is that at the centerline of the zigzag lift is produced to balance the gravitational force in the direction normal to the zigzag path, while the merging of the threads and the vanishing of the lift occurs some distance away from the centerline. Equation (4.19) shows that the value of the gravitational force depends on the density ratio. A density ratio close to one implies a small gravitational force, hence a small lift force. The experiments presented in Veldhuis *et al.* [15] used solid spheres with a density close to that of the surrounding fluid, so the error was difficult to detect. But it becomes clear immediately from figure 4.7(*e*), and some hindsight should have been provided by inspection of figure 2 of de Vries *et al.* [16] of a zigzagging gas bubble.

4.4.3 The nature of the drag

A simple method to estimate the drag forces experienced by the spheres is to use the Turton-Levenspiel relation (4.2) with the Reynolds number based on the instantaneous velocity $U(t)$ of the spheres; in other words, to write equation (4.18)

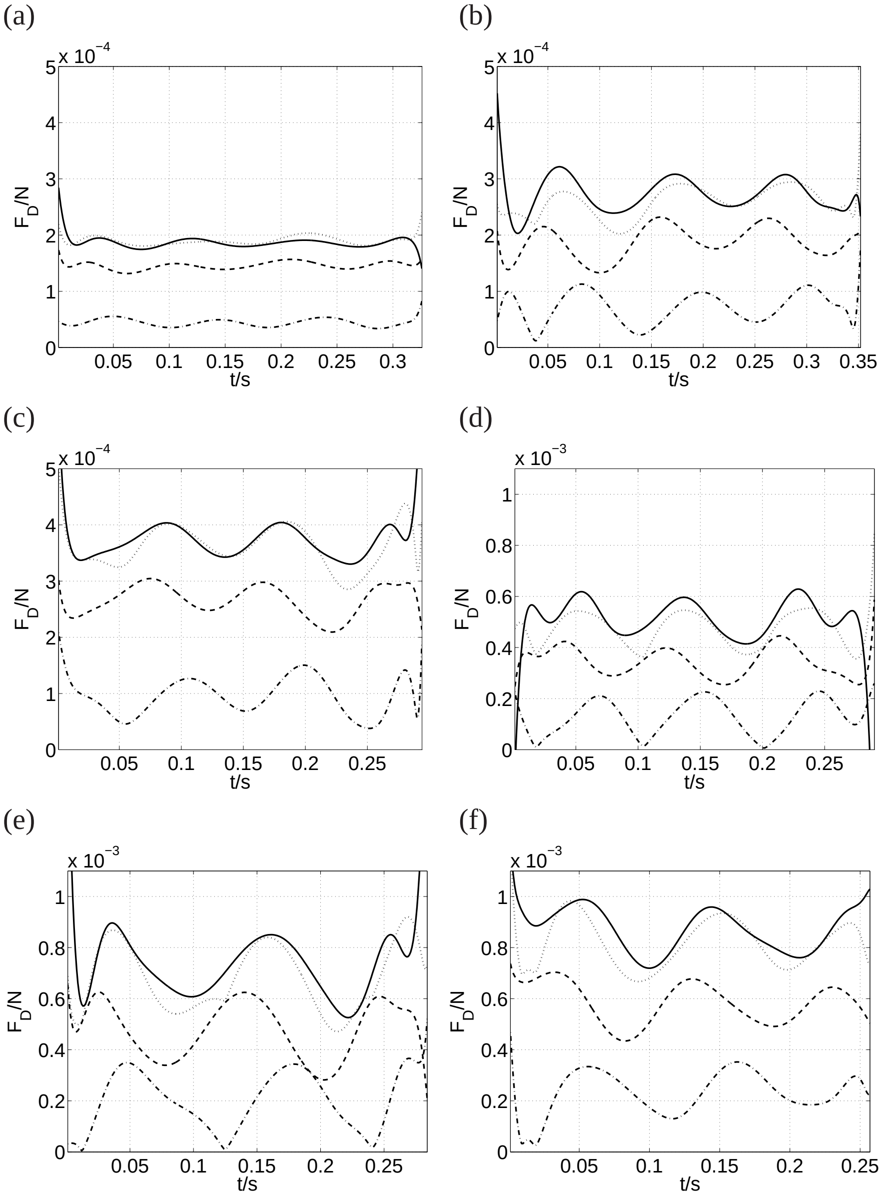

Figure 4.9: Analysis of the drag forces acting on spheres. Solid curves: measured drag force; dashed curves: viscous drag as given by the Turton-Levenspiel relation with the Reynolds number based on the instantaneous velocity; dashed-dotted curves: estimates of the lift induced drag; dotted curves: drag force as a combination of viscous drag and lift-induced drag. Parameters as given in the caption of figure 4.3.

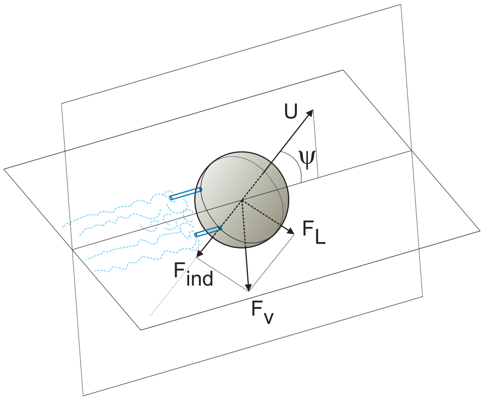

Figure 4.10: Because of the continuous generation of new vorticity, which close to the body consists of two parallel vortex threads, each with a strong axial component of vorticity but in opposite directions, a sphere experiences a vortex-flow force F_v at right angles to a plane through the two vortex threads. This force may be decomposed in a lift force F_L normal to the direction of motion and a lift-induced drag F_{ind} opposite to the direction of motion of the sphere.

as

$$\left\{1 + \tfrac{1}{2}(\rho/\rho_s)\right\} M \,\frac{\mathrm{d}U}{\mathrm{d}t} - \{1 - (\rho/\rho_s)\}\, M\, g_t = \tfrac{1}{8}\pi d^2 \,\rho\, U^2\, C_D(Re), \qquad (4.21)$$

where $Re = Ud/\nu$. This procedure is similar to that suggested by Lighthill in [12]. It leads to rather unsatisfactory results, as may be seen from figure 4.9, which shows time-traces of both the actual drag (the solid curve) and the drag calculated in this way (the dashed curve): the actual drag is not only larger, but also shows a time-lag with respect to the calculated drag. A possibly remedy, proposed, for example, by Sarpkaya [13], is to modify the added mass coefficient $\frac{1}{2}(\rho/\rho_s)M$ on the grounds that this potential-flow concept needs adjustment to reflect the presence of vorticity in the flow and/or the action of viscosity. This approach is not appealing considering the nature of the vortex-flow force, as was explained clearly by Lighthill [12] and more recently by Leonard & Roshko [11].

A better alternative, we believe, is to view the expression on the right-hand side of (4.21) as giving a good estimate of the viscous contribution to the vortex-flow force, while an estimate of the true drag follows from adding a (predominantly inertial) contribution, which in wing theory is referred to as the ‘lift-induced drag’. This contribution, as illustrated in figure 4.10, arises essentially because the instantaneous force, $\mathbf{F}_v$ say, associated with the generation of a vorticity structure which near the body consists of two vortex threads with oppositely directed axial vorticity, as described in § 4.4.2, is not at right angles with the instantaneous direction of motion of the sphere. To phrase it differently: The lift-induced drag arise because the instantaneous direction of motion is not parallel to the plane through the two threads at the place of origin of these threads. Hence, if the angle between the velocity vector and that plane is ψ, then the true force that results from the generation of the vortex threads is directed normal to that plane and has magnitude

$$(F_n^2 + F_b^2)^{\frac{1}{2}} / \cos\psi.$$

It may be decomposed into components in the directions $\mathbf{n}$ and $\mathbf{b}$ with magnitudes F_n and F_b, respectively, which have been determined experimentally, and a further component in the direction opposite to the tangent $\mathbf{t}$ with magnitude

$$F_{ind} = (F_n^2 + F_b^2)^{\frac{1}{2}} \tan\psi. \tag{4.22}$$

We have tried to obtain information on the time-variation of the angle ψ from flow visualizations made with our Schlieren-optics set-up. Let ψ_t be the angle between the tangent to the trajectory and the horizontal plane, and similarly let ψ_v be the angle between the 'vortex-plane' and the horizontal plane. Hence the angle ψ between the velocity vector and the vortex-plane is given by

$$\psi = \psi_v - \psi_t. \tag{4.23}$$

We now define the angle between the vector $\mathbf{a}$ and the horizontal XY-plane as ψ_a, see figure 4.11. The angles with the horizontal in projections on the XZ-plane and YZ-plane are called ψ_{aX} and ψ_{aY}, respectively. From elementary geometry one then obtains

$$\frac{1}{\tan^2\psi_a} = \frac{1}{\tan^2\psi_{aX}} + \frac{1}{\tan^2\psi_{aY}}. \tag{4.24}$$

Two examples of Schlieren visualizations of the wakes of rising solid spheres are shown in figure 4.12, in which we have indicated the angles ψ_{tX}, ψ_{vX}, ψ_{tY}, and ψ_{vY}; the values of ρ_s/ρ and G are based on the measured temperature at the center of the field-of-view. Obviously, this procedure can only yield rough estimates of ψ_{vX} and ψ_{vY}, because the turbulence in the wake makes the pictures 'blurry' and the wakes are highly 'curved'. Furthermore, the angle ψ is best calculated when the sphere crosses the centerline of the zigzag, where the path is (almost) straight. Now the vorticity structure is also straight, enabling a good prediction of the angle ψ. For a typical Schlieren experiment this results in two or three measurement points per experiments for the angle ψ, approximately one every 0.1 s. On using equations (4.23) and (4.24) we obtain $\psi = 26.1^o \pm 1$ for the case shown in figure 4.12*(a)*

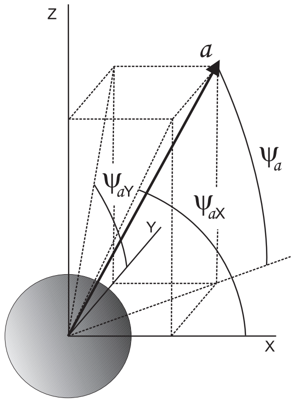

Figure 4.11: The angle between the vector $\mathbf{a}$ and the horizontal XY-plane is called ψ_a. The angles with the horizontal in projections on the XZ-plane and YZ-plane are ψ_{aX} and ψ_{aY}, respectively. Eq. (4.24) gives a relation between these three angles.

and $\psi = 37.5^o \pm 1$ for that in figure 4.12*(b)*. From a whole range of visualizations for values of G between 600 and 1800 it appears that along the sphere trajectories the angle ψ varies roughly between 25^o to 38^o. Given the uncertainty in determining the variation of ψ with time, and in order to have some definite value, we chose a fixed angle $\psi = 30^o$ and used this to evaluate expression (4.22). This procedure gives the dashed-dotted curves shown in figure 4.9 (which in this case is just $\frac{1}{3}\sqrt{3}$ times the magnitude of the lift force). Finally, adding the lift-induced contribution to the viscous contribution as estimated from the expression on the right-hand side of (4.21), resulted in an estimate of the drag experienced by the spheres that is presented in figure 4.9 as the dotted curves. The agreement with the measured drag (the solid curves) turns out to be excellent. While this supports our view of the mechanisms that govern the generation of flow-induced forces on the spheres, it also suggests that any variations in the viscous contribution to the drag associated with the building-up of the vorticity field by diffusion and convection are negligible at high Reynolds numbers. This contrast the situation at low Reynolds numbers, where they are important.

Note that we used the angle ψ extracted from Schlieren experiments as input for non-Schlieren experiments. Hence, the actual angle ψ remains unknown. If we had evaluated the Schlieren experiments as detailed as the non-Schlieren experiments, larger uncertainties would have emerged, as the image analysis cannot clearly distinguish between the sphere and its wake. Therefore the sphere position is not properly detected, resulting in errors in path, curvature, velocity, and there-

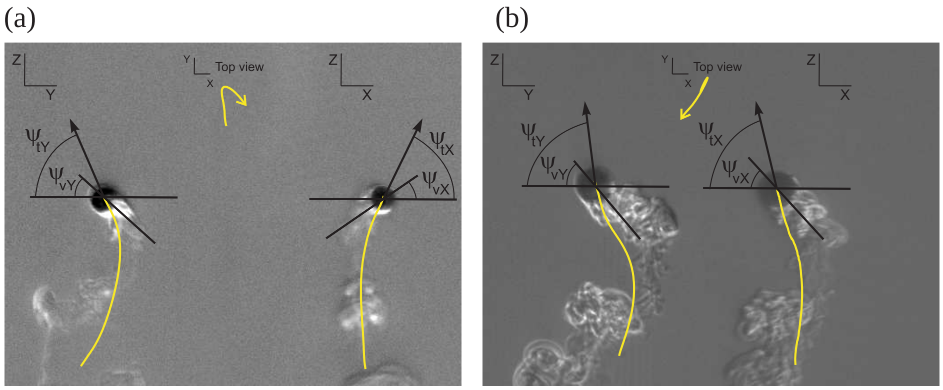

Figure 4.12: Schlieren visualizations of the wake of rising spheres, viewed from two orthogonal directions. The solid curved line indicates the path followed by the sphere during the time interval t between the moment of entering the field-of-view and the moment that the picture was taken. The angles ψ_{tX} and ψ_{tY} are the angles between the direction of motion and the horizontal as observed in projections on the XZ-plane and YZ-plane; similarly, ψ_{vX} and ψ_{vY} are the estimated angles between the horizontal and the plane containing the two vortex threads. *(a)* $\rho_s/\rho \simeq 0.02$, $d = 3.7$ mm, $G \simeq 775$, $t = 0.125$ s; *(b)* $\rho_s/\rho \simeq 0.02$, $d = 5.8$ mm, $G \simeq 1712$, $t = 0.110$ s. With time t the time passed from the moment the sphere path is plotted.

fore the forces of the sphere. However, the previous discussion showed that the use of Schlieren data for non-Schlieren experiments is justified and provides excellent agreement between theory and experiment.

4.5 Conclusions

In this paper we examined the proposal, given originally by Karamanev & Nikolov [10], to replace for spheres with a density ratio $\rho_s/\rho < 0.3$ the standard drag relation by $C_D(Re) = 0.95$ for $Re > 130$. Our experiments with spheres with $\rho_s/\rho \approxeq 0.02$ showed a rather poor agreement with this proposal, consistent with our view that it is more appropriate to replace the standard drag curve by a series of curves parameterized by the value of ρ_s/ρ, each of these curves starting off from the standard drag curve at a higher Reynolds number than 130, namely between $Re = 205.8$ and $Re = 211.9$. It was argued however, that for any individual case a substantial difference may be found between the measured mean velocity and that calculated from a balance between the net gravitational force and the mean drag as given by these relations. The reason is that for Reynolds numbers beyond about 250 light spheres do not rise along any preferred path.

By image analysis of stereoscopic recordings of the motion of the spheres three-dimensional reconstructions of the trajectories were made, which on further analysis yielded the drag and lift forces experienced by the spheres. It was proposed that the drag force consists of (i) a viscous contribution that may be estimated from the standard drag curve by evaluating the Reynolds number using the actual value of the velocity, and (ii) an inertial contribution that arises essentially by the same mechanisms that cause the lift-induced drag on airplane wings. Estimates of both contributions, the latter using visualizations of the wakes of the spheres, give a favorable agreement with the measurements.

There is obviously a connection of our study on freely rising spheres with work done on vortex-induced vibrations, as already exemplified by references to the papers of Lighthill [12], Leonard & Roshko [11] and Sarpkaya [13]. This connection is most intimate, perhaps, with studies of the motion of elastically mounted and tethered spheres, an example of which is given by Govardhan & Williamson [3]. Their description of the origin of the lift force on the spheres is essentially similar to what has been put forward by our group in the context of freely rising gas bubbles and solid spheres. It would be interesting to try to combine their beautiful visualizations and DPIV measurements of the sphere wakes with the simple model of the drag force given in § 4.4.3. Given the great detail with which the vorticity distributions was characterized, it may even be possible to estimate the vortex-flow forces experienced by the spheres on using the expressions derived by Kambe [7] and Howe [4].

References

[1] BIESHEUVEL, A. & HAGMEIJER, R. 2006 On the force on a body moving in a fluid. *Fluid Dyn. Res.* **38**, 716–742.

[2] BROWN, P.P. & LAWLER, D.F. 2003 Sphere drag and settling velocity revisited. *J. Environm. Engng* **129**, 222–231.

[3] GOVARDHAN, R.N. & WILLIAMSON, C.H.K. 2005 Vortex-induced vibration of a sphere. *J. Fluid Mech.* **53**, 11–47.

[4] HOWE, M.S. 1995 On the force and moment on a body in an incompressible fluid, with application to rigid bodies and bubbles at high and low Reynolds numbers. *Q. J. Mech. Appl.* **48**, 401–426.

[5] JENNY, M., BOUCHET, G. & DUŠEK, J. 2003 Nonvertical ascension or fall of a free sphere in a Newtonian fluid. *Phys. Fluids* **15**, L9–L12.

[6] JENNY, M., DUŠEK, J. & BOUCHET, G. 2004 Instabilities and transition of a sphere falling or ascending freely in a Newtonian fluid. *J. Fluid Mech.* **508**, 201–239.

[7] KAMBE, T. 1987 A new expression of the force on a body in viscous vortex flow and asymptotic pressure field. *Fluid Dyn. Res.* **2**, 15–23.

[8] KARAMANEV, D.G. 2001 The study of free rise of buoyant spheres in gas reveals the universal behaviour of free rising rigid spheres in fluid in general. *Int. J. Multiphase Flow* **27**, 1479–1486.

[9] KARAMANEV, D.G., CHAVARIE, C. & MAYER, R.C. 1996 Dynamics of the free rise of a light solid sphere in liquid. *AIChE J.* **42**, 1789–1792.

[10] KARAMANEV, D.G. & NIKOLOV, L.N. 1992 Free rising spheres do not obey Newton's law for free settling. *AIChE J.* **38**, 1843–1846.

[11] LEONARD, A. & ROSHKO, A. 2001 Aspects of flow-induced vibration. *J. Fluids Struct.* **15**, 415–425.

[12] LIGHTHILL, J. 1986 Fundamentals concerning wave loading on offshore structures. *J. Fluid Mech.* **173**, 667–681.

[13] SARPKAYA, T. 2001 On the force decompositions of Lighthill and Morison. *J. Fluids Struct.* **15**, 227–233.

[14] TURTON, R. & LEVENSPIEL, O. 1986 A short note on the drag correlation for spheres. *Powder Technol.* **47**, 83–86.

[15] VELDHUIS, C.H.J., BIESHEUVEL, A., VAN WIJNGAARDEN, L. & LOHSE, D. 2005 Motion and wake structure of spherical particles. *Nonlinearity* **18**, C1–C8.

[16] DE VRIES, A.W.G., BIESHEUVEL, A. & VAN WIJNGAARDEN, L. 2002 Notes on the path and wake of a gas bubble rising in pure water. *Int. J. Multiphase Flow* **28**, 1823–1835.

Chapter 5

Phase diagram for sphere motion‡

This paper presents the results of an experimental investigation aimed at verifying some of the interesting conclusions of the numerical study by Jenny, Dušek & Bouchet [3] concerning the instability and the transition of the motion of solid spheres falling or ascending freely in a Newtonian fluid. The phenomenon is governed by two dimensionsless parameters: the Galileo number G*, and the ratio of the density of the spheres to that of the surrounding fluid* ρ_s/ρ*. Jenny, Dušek & Bouchet showed that the* $(G, \rho_s/\rho)$ *parameter space may be divided into regions with distinct features of the trajectories followed eventually by the spheres after their release from rest. The characteristics of these 'regimes of motion' as described by Jenny, Dušek & Bouchet, agree well with what was observed in our experiments. However, flow visualizations of the wakes of the spheres using a Schlieren optics technique, raise doubts about another conclusion of Jenny, Dušek & Bouchet, namely the absence of a bifid wake structure.*

5.1 Introduction

Detailed numerical investigations (Kim & Pearlstein [7]; Natarajan & Acrivos [13]; Johnson & Patel [4]; Ghidersa & Dušek [1]; Lee [8]; Tomboulides & Orszag [17]) have revealed the various wake structures that may be found behind a solid sphere held fixed in a uniform flow, and have unraveled the mechanisms by which these

---

‡C.H.J. Veldhuis & A. Biesheuvel, *An experimental study of the regimes of motion of spheres falling or ascending freely in a Newtonian fluid*, submitted to Int. J. Multiphase Flow (2006)

flows loose stability. Experiments by Ormières & Provansal [14] and Schouveiler & Provansal [16] have confirmed many of the conclusions of these numerical studies. A related flow problem of practical importance, namely that of instability and transition of the flow around solid spheres falling or ascending freely in an infinite fluid, has recently been analyzed by Jenny, Bouchet & Dušek [2] and Jenny, Dušek & Bouchet [3] (referred to as JDB in what follows). Although $\S$ 3.2 of JBD presents some 'preliminary experimental observations' of the motion of the spheres, and although numerous flow visualization studies of the wakes of falling spheres have already been published – the beautiful photographs of Magarvey & Bishop [9, 10] and Magarvey & MacLatchy [11] should be noted especially –, it seems that an experimental verification of the results found by Dušek's group has not yet been given. Our paper aims at providing such a verification.

The problem is characterized by two nondimensional parameters, which may chosen as ρ_s/ρ, the ratio of the density of the solid sphere, ρ_s, to that of the surrounding fluid, ρ, and the Galileo number G, defined as

$$G = \frac{\sqrt{|\rho_s/\rho - 1|gd^3}}{\nu}. \tag{5.1}$$

Here d denotes the sphere diameter, ν is the kinematic viscosity of the fluid, and g is the gravitational acceleration. The two parameters G and ρ_s/ρ together define a parameter space. The numerical simulations of JDB show that the spheres, after having been released from rest, reach different 'asymptotic states': their trajectories eventually will have special characteristics that are typical of certain regions of the $(G, \rho_s/\rho)$ parameter space. A diagram indicating these 'regimes' is figure 29 of JDB, which is reproduced here in figure 5.1. JDB's description of their characteristics may be summarized as follows:

For values of G less than about 156 the spheres fall or ascend along a straight, vertical path. The axisymmetric flow around the spheres becomes unstable at a value of G which weakly depends on the value of the density ratio ρ_s/ρ. For example, Jenny *et al.* (2003) give critical values of $G = 155.8$ for massless spheres, $G = 156.1$ for $\rho_s/\rho = 0.5$, and $G = 159.3$ for spheres that are inhibited to move in a horizontal plane (which effectively means that the mass of the spheres is infinite). At higher values than this first critical value of G, i.e. for parameter values pertaining to the regime indicated by + in figure 5.1, the spheres move at a constant speed along a straight, oblique path; in others words, in a direction not perpendicular to the horizontal plane. The flow around the spheres is steady, but now only planar-symmetric.

At a second critical value of G, which depends much more strongly on the value of ρ_s/ρ, a waviness of the wakes behind the spheres sets in. For parameter values within the regions indicated in figure 5.1 by $\times$ and $*$, the spheres follow a path that

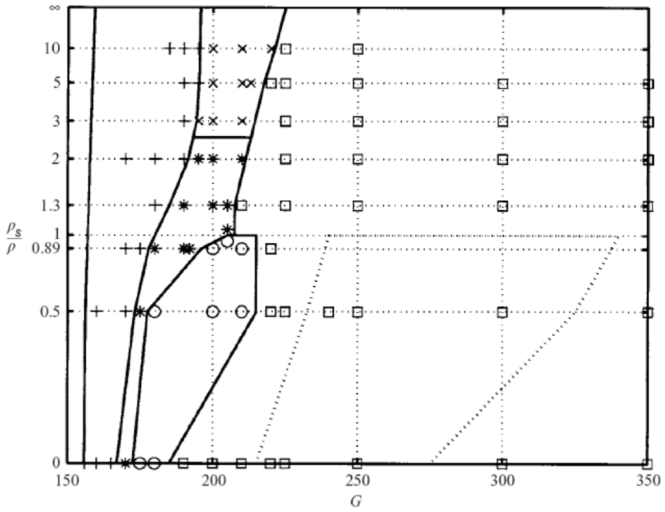

Figure 5.1: The different regimes of sphere trajectories in $(G, \rho_s/\rho)$-parameter space, as identified by Jenny, Dušek & Bouchet [3]: +, steady oblique; $*$, oblique with periodic fluctuations of low frequency; $\times$, oblique with periodic fluctuations of high frequency; $\circ$, zigzag; $\Box$, chaotic, with the domain of chaotic and zigzag motion delimited by the dotted line. (Reprinted from the *Journal of Fluid Mechanics*)

in the mean is straight and oblique, but involves small periodic excursions in a fixed plane through this oblique path. It appears that two dimensionless frequencies f, defined as

$$f = \frac{f'}{\sqrt{|\rho_s/\rho - 1|g/d}}, \tag{5.2}$$

with f' the frequency in Hz, may be associated with these excursions: a 'high' frequency $f \approx 0.180$ in regime $\times$ and a 'low' frequency $0.045 \leq f \leq 0.068$ in regime $*$; the borderline between the two regimes is the density ratio $\rho_s/\rho \approx 2.5$.

Actually, for 'light' spheres ($\rho_s/\rho < 0.5$, say) this 'oblique and oscillating regime' of rise $*$ only pertains to a narrow range of Galileo numbers: above a third critical value of G of approximately 175 the spheres ascend along a zigzag path, with a characteristic fundamental frequency $0.023 \leq f \leq 0.035$, while a strong third harmonic is also present. This 'zigzagging periodic regime' is indicated in figure 5.1 by $\circ$. The figure also shows that for $\rho_s/\rho > 0.5$ the oblique and oscillating regime extends to larger values of G and, interestingly, that the zigzagging periodic motion is *not* observed for spheres with densities larger than that of the surrounding fluid ($\rho_s/\rho > 1.0$).

Finally, in the regime indicated by □ the sphere trajectories are 'chaotic'. For spheres with a density higher than that of the surrounding fluid this means that superposed on the seemingly smooth trajectories are small random excursions, without any apparent dominant frequency. This may be contrasted with the chaotic motion of spheres with a density less than that of the fluid, which is characterized by high velocity fluctuations for which the Fourier transforms of the horizontal components show a definite peak at $f \approx 0.14$. In addition, the wandering motion may be interrupted by periods in which the spheres are zigzagging regularly at a much lower frequency; JDB give an example (see their figure 25) in which this 'low' frequency $f \approx 0.038$, i.e. comparable to the characteristic frequencies of the zigzagging periodic regime (○). JDB also point at the possibility that for $\rho_s/\rho < 1$ there is a special subdomain of the chaotic regime: in the region delimited by the dotted line in figure 5.1 special initial conditions (cf. JDB's figures 26, 27 and 28) may result also in a periodic zigzagging motion; but now the characteristic frequency is the above-mentioned 'high' value $f \approx 0.14$.

After a brief description in § 2 of the materials and methods used, we present in § 3 an overview of the sphere trajectories that were observed in the experiments. The values of the dimensionless parameters ρ_s/ρ and G cover most of the regimes described above. A puzzling result of the numerical simulations by JDB is the absence of a 'bifid wake' behind the spheres. Flow visualization studies by Magarvey & Bishop [9, 10], Magarvey & MacLatchy [11] and, much more recently, by our group (Veldhuis *et al.* [18]), have revealed the presence of two counter-rotating vortices. Some new flow visualizations, which corroborate what was found in the earlier studies, are presented in § 4. The paper ends with conclusions.

5.2 Materials and methods

The experimental set-up used to study the trajectories of the spheres is a perspex tube with height 220 cm and diameter 16 cm. At the bottom or the top (depending on whether the spheres would rise or fall) it is equipped with a special device to introduce the spheres. The measurement section (at the opposite end) is enclosed by a rectangular tank filled with tap water, to match the refraction index of the perspex and to minimize optical distortions. A halogen lamp behind a diffusive plate illuminates the measure section. By the use of mirrors a stereoscopic view from the sides is obtained, which is recorded with a Kodak CR 2000 camera at a frame rate of 500 or 1000 per second; image processing then yields the three-

	Material	d	ρ_s	%	ν	ρ_s/ρ	G
A	Glass	2.47	2470	31.0	2.54	2.31±0.05	176±11
B	HDPE	6.35	630	51.0	6.34	0.56±0.03	166±15
C	Glass	2.47	2470	28.0	2.27	2.32±0.05	198±12
D	Torlon	3.96	1410	28.0	2.27	1.32±0.04	195±13
E	Glass	2.47	2470	26.0	2.13	2.33±0.05	212±13
F	HDPE	6.35	630	47.5	5.28	0.56±0.03	198±17
G	HDPE	6.35	630	45.5	4.80	0.57±0.03	218±19

Table 5.1: Values of the physical parameters and the dimensionless numbers in the series of experiments A to G, where the capitals A to G correspond to the rectangular regions within parameter space indicated in figure 5.2. Given are the material of the spheres (HDPE: high-density polyethylene; Torlon: polyamide-imide), their diameter d in mm and density ρ_s in kg m^{-3}, the mass percentage of glycerine (%) of the mixtures and their kinematic viscosity ν in 10^{-6} m^2 s^{-1}, the density ratio ρ_s/ρ and the Galileo number G as defined in (5.1). The last two columns include estimates of the uncertainty of the given values.

dimensional positions of the spheres. To ensure a good resolution the field of view is limited to 15 cm × 15 cm × 27 cm.

The density ratio ρ_s/ρ and the Galileo number G, as defined in equation (5.1) were varied by using different fluids, tap water and mixtures of water and glycerine, and by using different spheres. The temperature was set at 20 $^{\mathrm{o}}$C. The selection of results presented below is based on experiments glass spheres ($d = 2.47 \pm 0.03$ mm, $\rho_s = 2470 \pm 30$ kg m^{-3}), polyamide-imide spheres (Torlon: $d = 3.96 \pm 0.01$ mm, $\rho_s = 1410 \pm 20$ kg m^{-3}), and with hollow spheres of high-density poly-ethylene (HDPE: $d = 6.35 \pm 0.01$ mm, $\rho_s = 920 \pm 20$ kg m^{-3}). The mass fraction of glycerine of the fluid ranged between 28 to 51 %. The viscosity of the fluids was calculated from this mass fraction using the *Handbook of Chemistry and Physics* (Weast [20]). This results in a possible error in the viscosity of less than 3.5 %. Further, a Haake RS 600 rheometer was used to verify these calculations. Detailed information on the values of the physical parameters and the dimensionless numbers ρ_s/ρ and G is given in table 1; here the labels A to G refer to the rectangular regions of parameter space indicated in figure 5.2.

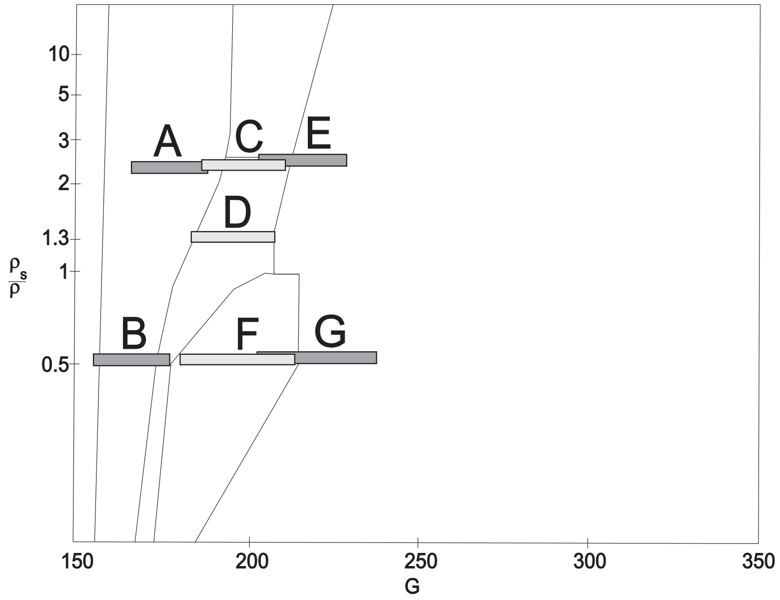

Figure 5.2: The investigated regions of the $(G, \rho_s/\rho)$ parameter space. Information on the values of the physical parameters and the dimensionless numbers is given in table 1. The size of the rectangular regions corresponds to the estimated uncertainty in the values of G and ρ_s/ρ. The lines separating the parameter space are taken from figure 5.1.

In a second experiment the flow behind the spheres was visualized using a Schlieren optics technique, which was originally developed to study the wakes of gas bubbles (de Vries, Biesheuvel & van Wijngaarden [19]). Details of the set-up used in the present study are given in Veldhuis *et al.* [18], a paper which also includes a large number of Schlieren images of sphere wakes for density ratios close to unity ($0.93 < \rho_s/\rho < 1.05$) and Galileo numbers between 306 and 732, i.e. well within the chaotic regime. The Schlieren technique relies on creating a slight temperature gradient in the fluid, of about 1.0 K cm^{-1}, by heating the fluid from above. This, of course, limits the size of the tank: here we used a rectangular glass container of 15 cm × 15 cm × 50 cm. The field of view is set by the diameters of the lenses just behind and in front of the tank, in this case 10 cm. The conditions were chosen such that in the center of the field of view the fluid properties have the values given in table 1. The visualizations of the wakes behind the spheres discussed in § 4 concern the regions of parameter space labelled B, C and F in figure 5.2; however, the spheres may not yet have reached the 'asympotic state'.

5.3 The motion of the spheres

We will now discuss the various paths along which the spheres were observed to rise up or fall down the long perspex tube. It is convenient to do this using views from above, which were reconstructed from the stereoscopic recordings made from the sides. For each of the cases A to G a series of paths will be shown (the left column of figures 5.3, 5.4, and 5.6). The recorded paths have been shifted so that they all start at the same position in the figure; each path has been given a number to simplify the discussion. Next to the views from above a ‘three-dimensional reconstruction’ of one of the paths is shown (the right column of figures 5.3, 5.4, and 5.6), thus providing an example that represents well the regime identified by JDB.

5.3.1 Steady and oblique regime: Cases A and B

JDB find that for Galileo numbers a little higher than the critical value for the primary instability, the spheres move steadily along a straight non-vertical path. Although there a few exceptions, the majority of the paths of the falling glass spheres shown in figure 5.3(*a*), case A, is consistent with the predictions of JDB. The slight curvature of the paths found in experiments 2, 4, and 9 may be due to a slight non-sphericity of the particles. Presumably, the sudden change of direction in experiment 8 indicates that the sphere has hit the wall of the tank.

Most of the paths shown in figure 5.3(*c*), case B, are also slightly curved, but not to the extent that JDB’s prediction must be considered as falsified. In these experiments hollow high-density poly-amide (HDPA) spheres were used, and a density distribution that is not perfectly spherically symmetric may be the reason that the paths are not straight. We have no explanation for the somewhat wriggly paths found in experiments 4 and 7. It may be noted that there is a resemblance with the paths found in the experiments of case F, see figure 5.6(*c*). Hollow HDPA spheres were also used in that case, but with slightly larger diameter, which suggests that we may have made a mistake during the experiments.

The existence of the steady oblique regime, which even includes solid spheres of negligible mass, may be a little surprising for those who are more familiar with the behavior of gas bubbles. The primary instability of the flow around gas bubbles eventually leads to a zigzagging or spiralling motion (something that was known already to Leonardo da Vinci; cf. Prosperetti [15]). That this is not what is observed for massless solid spheres suggests that the very different behavior of gas bubbles is due to their ability to deform easily.

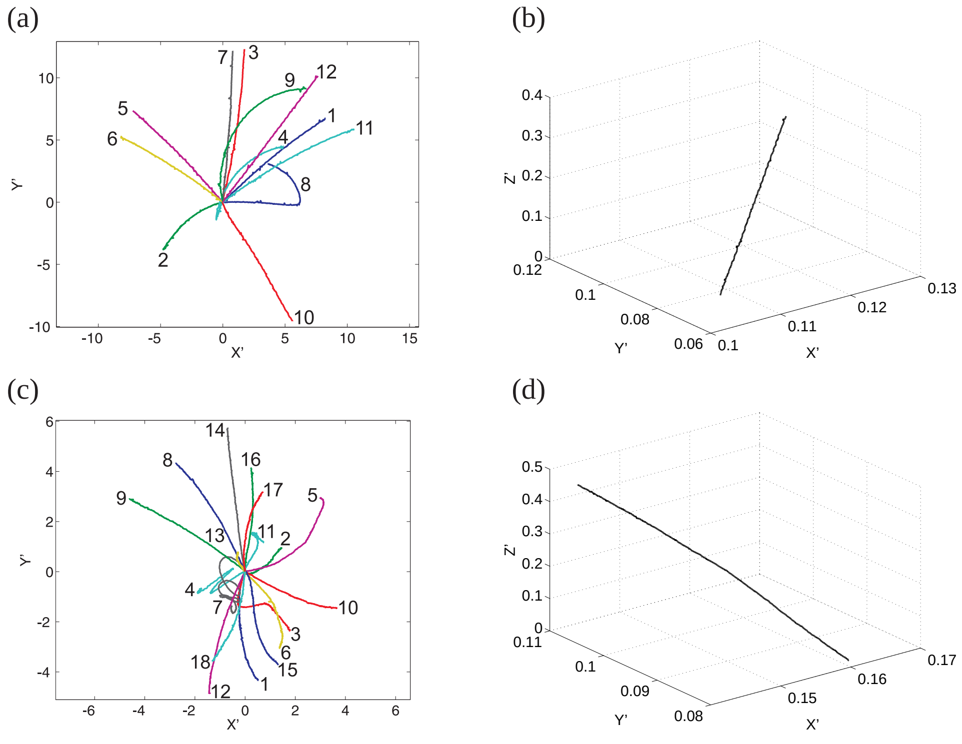

Figure 5.3: Left column: Top views of observed particle trajectories in the steady and oblique regime: (*a*) case A, (*c*) case B. Right column: 3D reconstruction of one of the paths shown on the left; (*b*) experiment 12, (*d*) experiment 8. Distances have been nondimensionalized by the diameters of the spheres.

5.3.2 Oblique and oscillating regime: Cases C and D

In the experiments of case C the same glass spheres were used as in the experiments of case A, but the fluid properties where adjusted - this changes the value of G, but hardly affects the value of ρ_s/ρ - so that the parameter values would correspond to what JDB specify as the periodic oblique regime. In fact, the value 2.32 of the density ratio ρ_s/ρ in case C is just below 2.5, which JBD estimate as the value which divides the periodic oblique regime into two parts: one with high-frequency velocity fluctuations ($\rho_s/\rho > 2.5$) and another with low-frequency velocity fluctuations ($\rho_s/\rho < 2.5$). The experiments of case D should correspond to the low-frequency periodic oblique regime and were conducted with polyamide-imide (Torlon) spheres.

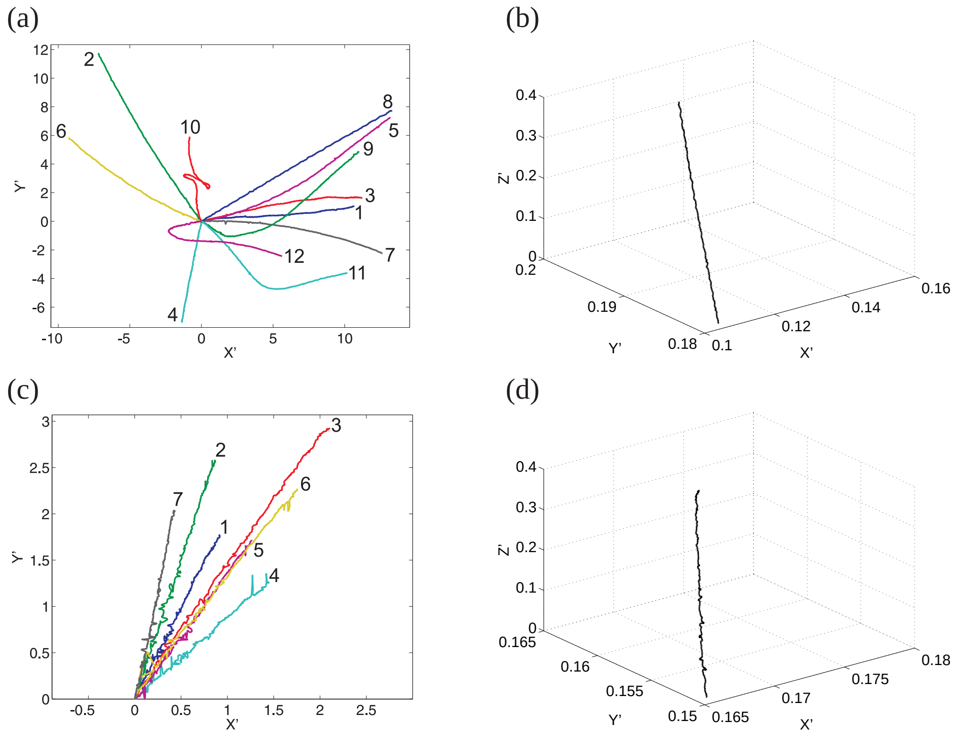

Figure 5.4: Left column: Top views of observed particle trajectories in the oblique and oscillating regime: (*a*) case C, (*c*) case D. Right column: 3D reconstruction of one of the paths shown on the left; (*b*) experiment 8, (*d*) experiment 2. Distances have been nondimensionalized by the diameters of the spheres.

For what concerns case C, most of trajectories shown in figure 5.4(*a*) are oblique and deviate little from a straight line. Exceptions are the experiments 9 to 12, in which the strong curvature of the path is presumably due to interactions with the wall. While a Fourier analysis of the components of the horizontal velocity fluctuations in cases A and B does not yield anything significant, a similar analysis of case C shows that dominant non-dimensional frequencies f of approximately 0.06 and 0.19 (see figure 5.5(*a*)) are clearly present. The first frequency is within the range of $0.045 \leq f \leq 0.068$ mentioned by JDB as typical of the low-frequency oblique and oscillating regime, while the second frequency seems to agree with the value $f \approx 0.18$, which according to JDB characterizes the high-frequency oblique and oscillating regime. Hence, it appears that there is a region of parameter space in which there is smooth transition between the two regions that

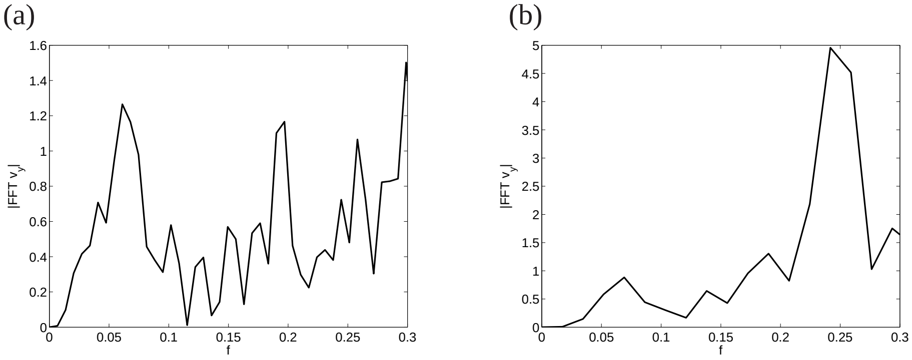

Figure 5.5: Fourier transforms of one of the horizontal velocity components in the oblique and oscillating regime. (*a*) case C, experiment 3; (*b*) case D, experiment 1. The frequency has been nondimensionalized as indicated by equation (5.2).

constitute the oblique and oscillating regime identified by JDB.

The trajectories observed for case D, with the polyamide-imide spheres, are presented in figure 5.4(*c*). Ignoring the minor deviations, these are indeed perfectly straight oblique paths. Fourier analysis of one of the horizontal velocity components in experiment 1 reveals (see figure 5.5(*b*)) a dominant non-dimensional frequency f of approximately 0.245. This value is well outside the range of $0.045 \leq f \leq 0.068$ mentioned by JDB. Peaks at frequencies $f \approx 0.25$ are also found in the horizontal velocity spectra of all the other experiments of case D. In some of the spectra broad, but much smaller, peaks may be observed at frequencies between 0.06 and 0.14 (as in figure 5.5(*b*)), yet it must be concluded that the resemblance with what was found by JDB is rather poor.

5.3.3 Zigzagging periodic and chaotic regime: Cases E, F and G

In the experiments of case E the same glass spheres were used as in those of cases A and C. By adjusting the fluid properties a region of parameter space was selected which according to JDB should lie at the border, but just within, the chaotic regime. Some of the observed trajectories are shown in figure 5.6(*a*). They differ from the trajectories of case C (the oblique and oscillating regime) shown in figure 5.4(*a*) by having much stronger variations in curvature. There is a clear resemblance with the trajectory shown in figure 20 of JDB, calculated for $\rho_s/\rho = 5$ and $G = 250$; however, because of the limited field of view it was not possible to detect the slow helicoidal motion visible in that figure. Fourier analysis of the components of the projection of the velocity vector did not reveal the presence of any dominant

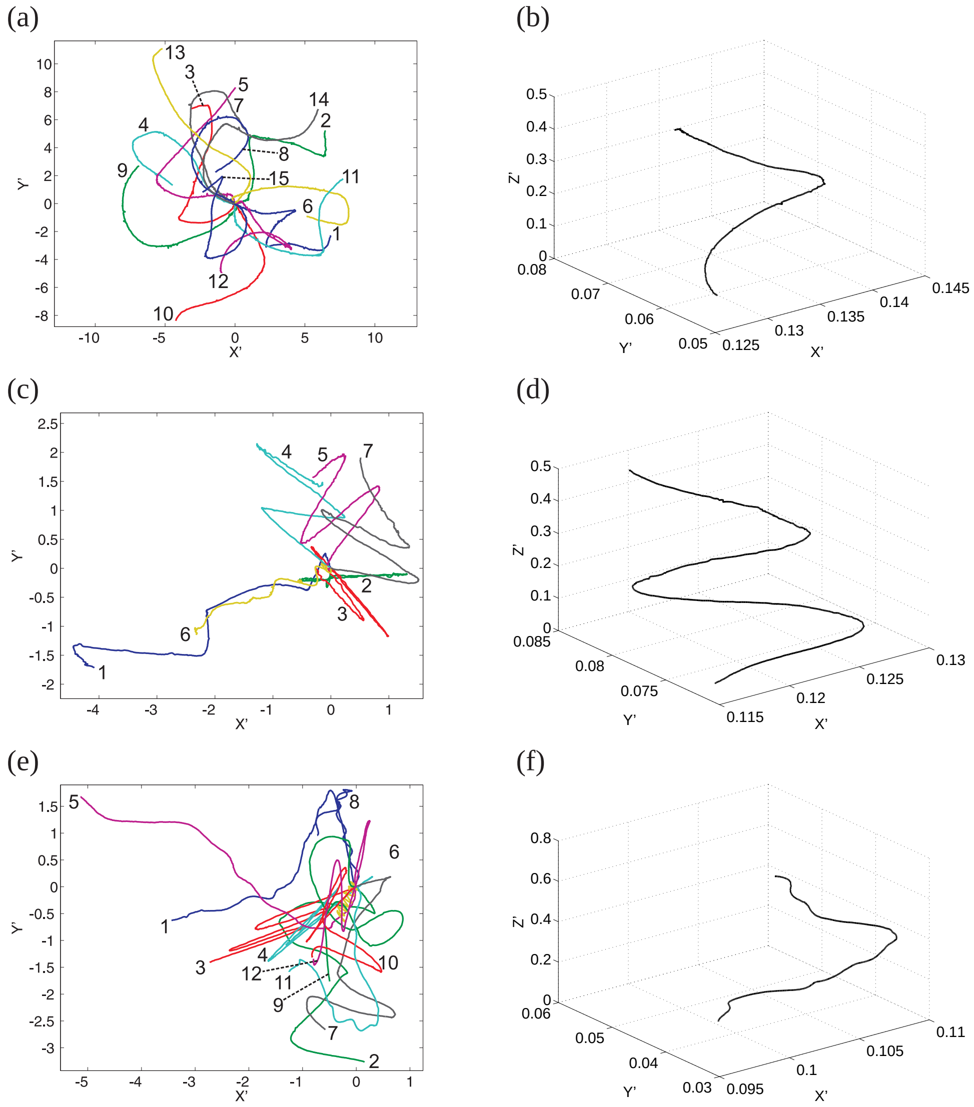

Figure 5.6: Left column: Top views of observed particle trajectories in the zigzagging periodic regime and the chaotic regime: (*a*) case E, (*c*) case F, (*e*) case G. Right column: 3D reconstruction of one of the paths shown on the left; (*b*) experiment 12, (*d*) experiment 7, (*f*) experiment 11. Distances have been nondimensionalized by the diameters of the spheres.

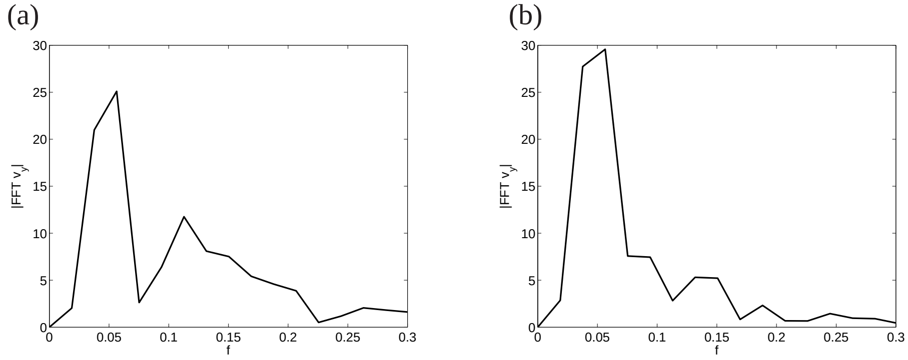

Figure 5.7: Fourier transforms of one of the horizontal velocity components. (*a*) zigzagging periodic regime: case F, experiment 9; (*b*) chaotic regime: case G, experiment 3. The frequency has been nondimensionalized as indicated by equation (5.2)

frequencies, and qualifying this regime of parameter space as chaotic seems to be justified.

The trajectories found in the experiments of cases F and G are shown in figures 5.6(*c*) and 5.6(*e*). According to JDB's classification case F belongs to the zigzagging periodic regime and case G to the chaotic regime. Yet, the trajectories have a similar appearance: in each of these cases a zigzagging is found occasionally, but more often the spheres follow a jagged path. These experiments were conducted with hollow HDPE spheres, and, as was argued above, the density distributions of many of these may not have been perfectly spherically symmetric. It seems that the observations of case F agree with the discussion in § 10 of JDB, where it is shown that slight inhomogeneities are sufficient to destroy the zigzagging periodic regime (cf. also their figure 31). Hence, in both cases F and G the motion of the spheres must be considered as chaotic, the zigzag paths being instances of the special character of the chaotic regime for ascending spheres as identified by JDB (see their figures 25 and 27); namely, that the erratic motion may be interrupted by short periods in which the spheres move along a zigzag.

Further support for these conclusions may be found by looking at the Fourier transform of a horizontal velocity component of a zigzagging particle, such as shown in figure 5.7(*a*) for experiment 9 of case F, and in figure 5.7(*b*) for experiment 3 of case G. Both spectra show a large peak at a dimensionless frequency f of about 0.052. We have no explanation for the appearance of this frequency, but it is certainly much higher than the fundamental frequency of the zigzagging periodic regime, which according to JDB should lie within the range $0.023 \leq f \leq 0.035$.

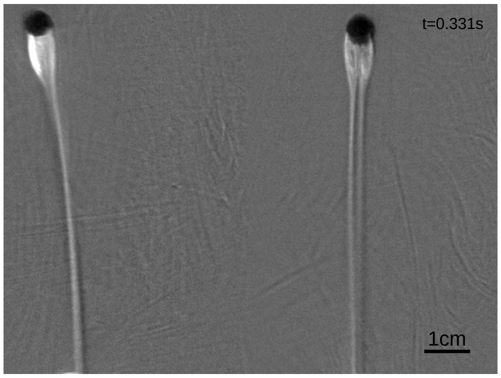

Figure 5.8: Stereoscopic Schlieren image of the wake of a rising sphere in the steady and oblique regime (case B). The picture was taken $t = 0.331$ seconds after the sphere had entered completely the field of view.

It may be noted that also a further characteristic of the zigzagging periodic regime, i.e. a strong third harmonic, is absent from figure 5.7(*a*). Instead, broad peaks are observed at dimensionless frequencies of approximately 0.12 in figure 5.7(*a*) and 0.14 in figure 5.7(*b*), values that agree very well with the value of $f = 0.14$ mentioned by JDB as characteristic of the ‘zigzagging spots’ within the chaotic trajectories.

To conclude this section, it may be noted that, on comparing figure 5.6(*a*) with figures 5.6(*c*) and 5.6(*e*), the behavior of the light, ascending, HDPE spheres differs considerably from that of the heavy, falling, glass spheres. This supports the conclusions of Karamanev & Nikolov [6] and Karamanev, Chavarie & Mayer [5]; namely, that the motion of ‘light’ spheres (which they associate with a density ratio $\rho_s/\rho < 0.3$) is truly different from that of heavy spheres; the upshot being that the standard drag correlation $C_D(Re)$, with the Reynolds number Re and the drag coefficient C_D based on the mean vertical velocity, does not apply for these light spheres. The motion of rising light solid spheres at high values of G has been studied in chapter 4.

5.4 The wakes of the spheres

It was already mentioned that for values of G slightly higher than that for which the axially symmetric flow around a gas bubble rising in clean water becomes unstable, the bubble will follow a zigzag or helicoidal path. The wake of such a bubble consists of two counter-rotating vortices, as was established by the numerical work

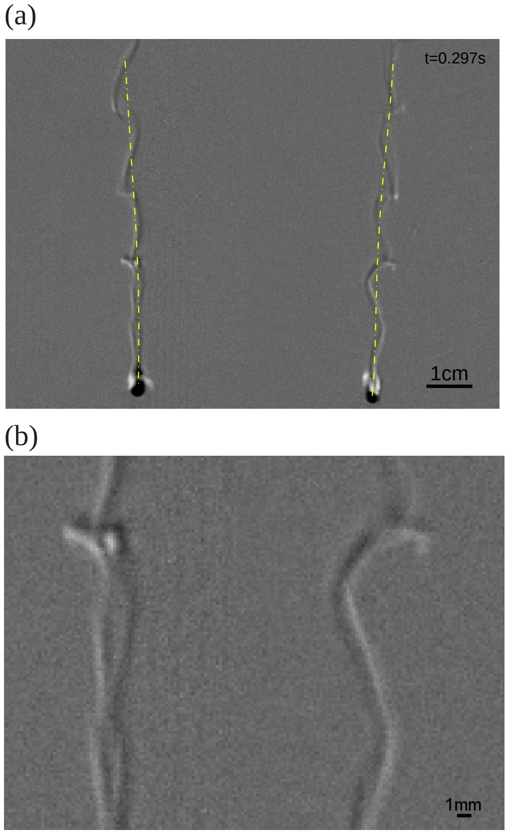

Figure 5.9: (*a*) Stereoscopic Schlieren image of the wake of a falling sphere in the oblique and oscillating regime (case C). The dash-dotted line indicates the path followed by the sphere after it completely entered the field of view $t = 0.297$ seconds earlier; this is also the starting point of the line.). (*b*) Enlarged view of a detail of (*a*).

of Mougin & Magnaudet [12] and the flow visualizations of de Vries *et al.* [19]. This behavior is quite different, as shown first by JDB and confirmed by our study, from that of solid spheres, which in the analogous situation rise or fall along a straight non-vertical path. JDB also find that the wakes behind these particles do not have a bifid structure. Figure 5.8 shows a stereoscopic Schlieren image of the wake of a falling sphere in the steady and oblique regime (case B). In our opinion, this picture proves that the wake consists of two counter-rotating vorticies, just like the wakes of zigzagging or spiralling bubbles and the wakes of solid spheres held fixed in a uniform flow (cf. Schouveiler & Provansal [16]); this contradicts the

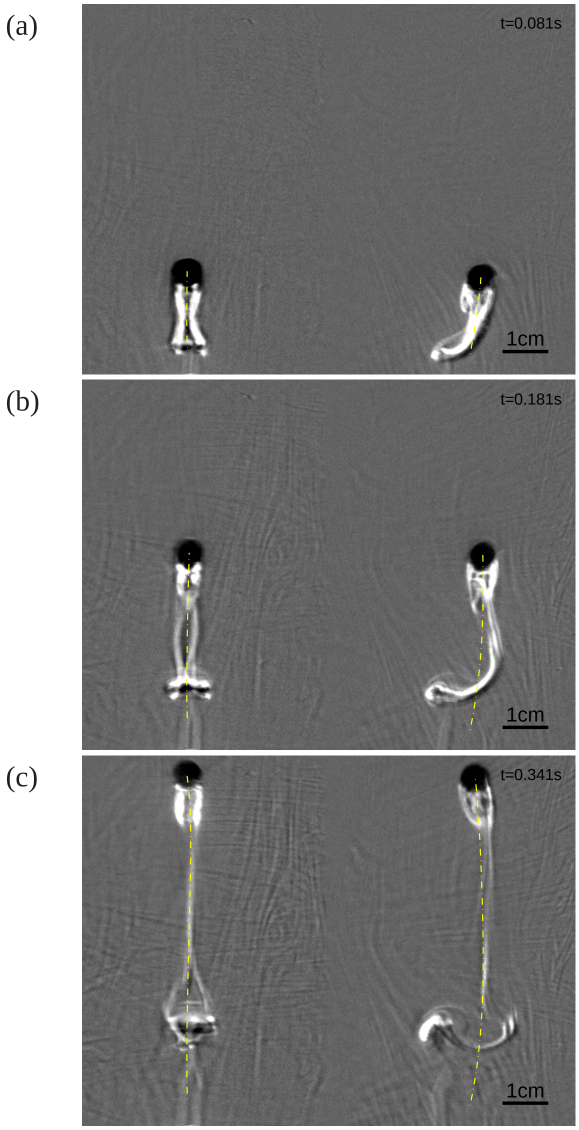

Figure 5.10: Schlieren images of the wake of a rising sphere in the ‘destroyed’ zigzagging periodic regime (case F), showing how the double-threaded wake evolves into a hairpin-like vortex structure. The pictures were taken t seconds after the sphere had entered completely the field of view. (*a*) $t = 0.081$ s, (*b*) $t = 0.181$ s, (*c*) $t = 0.341$ s.

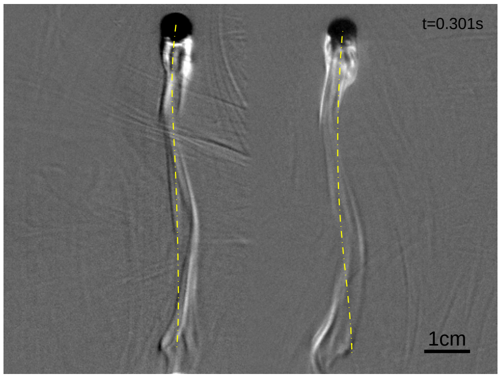

Figure 5.11: Stereoscopic Schlieren image of the wake of a rising sphere in the 'destroyed' zigzagging periodic regime (case F). The picture was taken $t = 0.301$ seconds after the sphere had entered completely the field of view. Note the different character of the wake as compared to that shown in figure 5.10.

findings of JDB.

A stereoscopic Schlieren image of the wake of a falling solid sphere in the oblique and oscillating regime (case C) is shown in figure 5.9(*a*). Here the path followed by the sphere between the moment that it entered completely the field of view and the moment that the picture was taken is visualized by the dash-dotted yellow line. The wake does not coincide with the trajectory of the sphere, which indicates that the oscillatory wake structure has evolved by a redistribution of the vorticity generated by the sphere. The enlarged view of the wake just behind the sphere, figure 5.9(*b*), supports the description of this process, as given earlier by Veldhuis *et al.* ([18]; see also their figure 3): the two counter-rotating vortices kink, through which they locally get close together (see the region just below the center of figure 5.9(*b*)), and subsequently the two threads of vorticity bend and connect (see the structure near the top of the figure). The smooth sphere trajectory of figure 5.9(*a*) also suggests that this process of redistribution of wake vorticity hardly affects the 'overall' motion of the spheres. Yet, it may lead to small fluctuations in the velocity. This becomes evident by associating a 'frequency' with the pattern observed in figure 5.9(*a*). This frequency, made dimensionless in the manner of equation (5.2), is estimated as 0.19; a value which indeed coincides with one of the peaks in the Fourier spectrum of a horizontal velocity component, such as shown in figure 5.5(*a*).

A further illustration of the evolution of the unstable bifid wake is given in the Schlieren visualizations presented in figure 5.10. This concerns a rising solid sphere in what JDB classify as the zigzagging periodic regime (case F), but which here turned out to be chaotic, as a consequence of a lack of spherical symmetry in the density distribution of the hollow HDPE spheres that were used. That the wake of rising spheres in this 'destroyed' zigzagging periodic regime may also have a somewhat different structure is exemplified in figure 5.11. Figures 5.10 and 5.11 confirm what was mentioned earlier; namely, that the overall motion of the spheres is not affected significantly by the redistribution of the vorticity in the flow. Here again, a dimensionless frequency may be associated with the wake patterns: its value is estimated as between 0.11 and 0.15 for the wake shown in figure 5.10, and between 0.15 and 0.19 for that in figure 5.11. For the case of figure 5.10 this values agrees well with the broad peak observed in the velocity spectrum shown in figure 5.7(*a*). Unfortunately, the limited field of view did not allow us to look for other details of the flow, which might explain the high peak at $f \approx 0.05$ in figure 5.7(*a*).

5.5 Conclusions

To the best of our knowledge, the work of Dušek and colleagues (JDB) is the first to give a detailed analysis of the instabilities and transitions in the motion of spheres moving freely under the action of gravity. Our experiments do not give information on the mechanisms involved in these instabilities and transitions. However, our observations agree very well with JDB's description of the main features of the motion of the spheres and how these may be associated with various regimes: regions of the $(G, \rho_s/\rho)$ parameter space for which the motion of the spheres have quite distinct characteristics. Discrepancies found in the experiments with hollow high-density poly-ethylene spheres (case B) may presumably be attributed to a lack of spherical symmetry in the density distribution of these spheres. This is supported by the fact that on using these spheres no evidence could be found for the existence of JDB's zigzagging periodic regime. JDB show that a slight mismatch in the positions of the center of volume and the center of mass of the spheres destroys this regime; the motion of the spheres is then best described as chaotic. This agrees with what was observed in our case F.

We also found some differences with JDB's description of the 'details' of the motion of the spheres. These concern the values given by JDB of the dominant frequencies that may be observed in the spectra of one of the horizontal velocity components. In particular, our experiments suggest that the oblique and oscillating regime, divided by JDB into two sub-regimes, one with a 'low' characteristic frequency and one with a 'high' characteristic frequency, must include a third sub-regime (case C) in which both of these characteristic frequencies are present. Furthermore, the observed velocity spectra of ascending spheres in the chaotic regime (cases F and G) show broad peaks at a dimensionless frequency that agrees fairly well with the characteristic frequency mentioned by JDB; yet, both these spectra also have a distinct peak at a much lower frequency ($f \approx 0.05$), a phenomenon not found by JDB.

Finally, our flow visualizations disprove a remarkable assertion of JDB, namely, the absence of a bifid wake behind the spheres. In all our pictures the wake consists, entirely or in part, of two counter-rotating vortices.

References

[1] GHIDERSA, B. & DUŠEK, J. 2000 Breaking of axisymmetry and onset of unsteadiness in the wake of a sphere. *J. Fluid Mech.* **423**, 33–69.

[2] JENNY, M., BOUCHET, G. & DUŠEK, J. 2003 Nonvertical ascension or fall of a free sphere in a Newtonian fluid. *Phys. Fluids* **15**, L9–L12.

[3] JENNY, M., DUŠEK, J. & BOUCHET, G. 2004 Instabilities and transition of a sphere falling or ascending freely in a Newtonian fluid. *J. Fluid Mech.* **508**, 201–239.

[4] JOHNSON, T.A. & PATEL, V.C. 1999 Flow past a sphere up to a Reynolds number of 300. *J. Fluid Mech.* **378**, 19–70.

[5] KARAMANEV, D.G., CHAVARIE, C. & MAYER, R.C. 1996 Dynamics of the free rise of a light solid sphere in liquid. *AIChE J.* **42**, 1789–1792.

[6] KARAMANEV, D.G. & NIKOLOV, L.N. 1992 Free rising spheres do not obey Newton's law for free settling. *AIChE J.* **38**, 1843–1846.

[7] KIM, I. & PEARLSTEIN, A.J. 1990 Stability of the flow past a sphere. *J. Fluid Mech.* **211**, 73–93.

[8] LEE, S. 2000 A numerical study of the unsteady wake behind a sphere in a uniform flow at moderate Reynolds numbers. *Comput. Fluids* **29**, 639–667.

[9] MAGARVEY, R.H. & BISHOP, R.L. 1961 Transition ranges for three-dimensional wakes. *Can. J. Phys.* **39**, 1418–1422.

[10] MAGARVEY, R.H. & BISHOP, R.L. 1961 Wakes in liquid-liquid systems. *Phys. Fluids* **4**, 800–805.

[11] MAGARVEY, R.H. & MACLATCHY, C.S. 1965 Vortices in sphere wakes. *Can. J. Phys.* **43**, 1649–1656.

[12] MOUGIN, G. & MAGNAUDET, J. 2002 Path instability of a rising bubble. *Phys. Rev. Letters* **88**, 014502.

[13] NATARAJAN, R. & ACRIVOS, A. 1993 The instability of the steady flow past spheres and disks. *J. Fluid Mech.* **254**, 323–344.

[14] ORMIÈRES, D. & PROVANSAL, M. 1999 Transition to turbulence in the wake of a sphere. *Phys. Rev. Lett.* **83**, 80–83.

[15] PROSPERETTI, A. 2004 Bubbles. *Phys. Fluids* **16**, 1852–1865.

[16] SCHOUVEILER, L. & PROVANSAL, M. 2002 Self-sustained oscillations in the wake of a sphere. *Phys. Fluids* **14**, 3846–3854.

[17] TOMBOULIDES, A.G. & ORZAG, S.A. 2000 Numerical investigation of transitional and weak turbulent flow past a sphere. *J. Fluid Mech.* **416**, 45–73.

[18] VELDHUIS, C.H.J., BIESHEUVEL, A., VAN WIJNGAARDEN, L. & LOHSE, D. 2005 Motion and wake structure of spherical particles. *Nonlinearity* **18**, C1–C8.

[19] DE VRIES, A.W.G., BIESHEUVEL, A. & VAN WIJNGAARDEN, L. 2002 Notes on the path and wake of a gas bubble rising in pure water. *Int. J. Multiphase Flow* **28**, 1823–1835.

[20] WEAST, R.C. 1974 *Handbook of Chemistry and Physics*, 55th edn. CRC Press.

Chapter 6

General aspects of a single bubble rising in water

This chapter presents the general features of a single bubble ($1 \leq d_{eq} \leq 6$ *mm), rising in purified water. The smallest bubbles (*$d_{eq} \leq 1.72$ *mm) are oblate ellipsoids rising rectilinearly, whereas larger bubbles (*$1.72 \leq d_{eq} \leq 2.80$ *mm) are oblate ellipsoids in spiraling motion. For even larger bubbles (*$d_{eq} > 2.80$ *mm) shape oscillations set in and the path of the bubbles is strongly influenced by the shape oscillations. Right at the onset of shape oscillations (*$d_{eq} \approx 2.80$ *mm) the bubble is forced into a zigzagging motion.*

Comparison of the rise velocity and shape of the bubble with earlier research shows that the water used for the experiments is indeed pure, not contaminated with surfactants.

This chapter serves as a general introduction to single bubble motion. The next two chapters provide more details on bubbles without and with shape oscillations, respectively.

6.1 Introduction

The behavior of rising bubbles has been a research topic for many years. Haberman & Morton [6] and later Hartunian & Sears [7] have conducted numerous experiments in several liquids with different bubble sizes. A nice overview of bubble motion from small to large volume equivalent diameter (D_{eq}) is given by Lindt [9] (Table 6.1).

D_{eq}	Re	description
D_{eq} <0.08	Re <70	sphere, rectilinear path, C_D as for solid spheres
0.08< D_{eq} <0.12	70< Re <400	sphere, rectilinear path, C_D less than solid spheres
0.12< D_{eq} <0.15	400< Re <500	oblate spheroid, rectilinear motion
0.15< D_{eq} <0.48	500< Re <1100	oblate spheroid, helical motion
0.48< D_{eq} <0.70	1100< Re <1600	irregular oblate spheroid, almost rectilinear motion
0.70< D_{eq} <1.66	1600< Re <5000	transition from oblate spheroid to spherical cap, almost rectilinear motion
D_{eq} >1.66	Re >5000	spherical cap, rectilinear motion

Table 6.1: Overview of bubble motion. D_{eq} given in cm. Taken from Lindt [9].

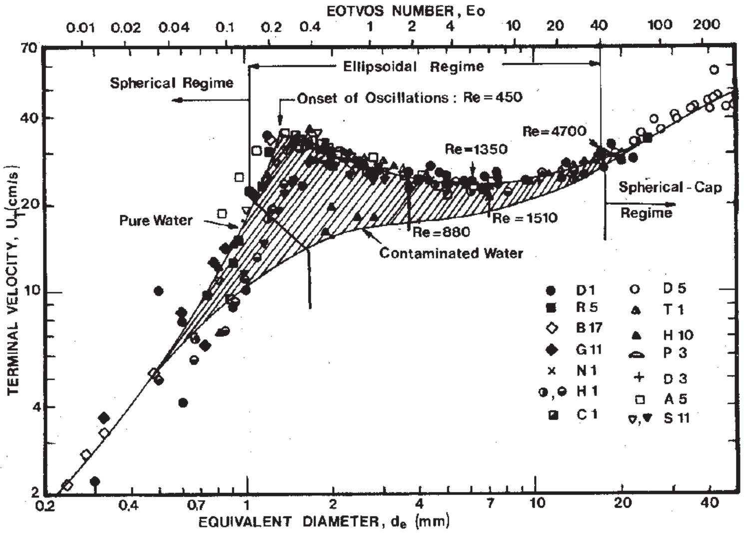

Figure 6.1: The terminal rise velocity as function of the bubble diameter and Eötvös number in water at 20^{o}C. Taken from Clift *et al.* [3].

Lindt extracted these data from a report by Rosenberg (1950). Here the Reynolds number is defined by

$$Re = \frac{U_v D_{eq}}{\nu}, \tag{6.1}$$

with U_v the vertical rise velocity of the bubble and ν the kinematic viscosity of the water. Clift *et al.* [3] provide an informative figure on the terminal rise velocity as function of the bubble diameter and Eötvös number (Figure 6.1). The Eötvös number is defined by

$$Eo = \frac{\Delta\rho D_{eq}^2 g}{\sigma}, \tag{6.2}$$

with $\Delta\rho$ the density difference between liquid and gas, g the gravitational acceleration, and σ the surface tension coefficient of the liquid-gas interface. Compared to the data of Lindt, their figure is less detailed with respect to the different regimes of bubble motion and shape, but it provides more information on the effect of surfactants in the water.

Small bubbles are spherical and rise rectilinearly. Thereafter, for increasing diameter, bubbles first become oblate spheroids, followed by a bifurcation to a helical path. When shape oscillations are triggered the bubble returns to an almost rectilinear motion. Finally the bubble has the form of a spherical cap rising rectilinearly. We are interested in the intermediate regime in which the bubble path deviates from rectilinear. What causes this deviation and what is the influence of shape oscillations? This research focuses on bubbles with an equivalent diameter between 1 and 6 millimeter. Hence, we start with fixed shaped bubbles in rectilinear motion and end with bubbles performing shape oscillations.

The dynamics of the bubble is strongly influenced by the properties of the fluid (density, viscosity, and surface tension). For smaller, spherical bubbles viscosity is most important in determining the rise velocity of the bubble whereas, in the case of ellipsoidal bubbles, surface tension is dominant. In the regime with ellipsoidal bubbles the Weber number is an important parameter providing the ratio between fluid inertia and surface tension

$$We = \frac{\rho U_v^2 D_{eq}}{\sigma}, \tag{6.3}$$

with ρ the density of the fluid. Moore [14, 15] calculated the Weber number as a function of the deformation of a bubble at large, but finite, Reynolds number. He assumed potential flow around an oblate ellipsoidal bubble rising rectilinearly. In his calculation he satisfied the balance between surface tension and pressure forces only at the stagnation point and at the intersection of the bubble surface with the horizontal midplane. More recently Benjamin [2] improved this calculation using a virial method satisfying the boundary condition on the entire bubble surface. In section 6.3 the experimental results are compared with the relations of Moore and Benjamin.

Bubble size and Reynolds number of the flow bifurcations are influenced by the purity of the water. Bel Fdhila & Duineveld [1] showed that surface active components attach to the bubble surface and migrate to the rear of the bubble. Above a certain critical concentration of surface active components the rise velocity decreases rapidly; for concentrations of the surface active components well above the critical concentration the rise velocity is equal to that of a solid sphere. Two mechanisms cause this decrease in rise velocity: firstly, at low surface-active concentration the front of the bubble is uncontaminated and the rear is covered with surface-active components, locally causing a drop in surface tension. The difference in surface tension between front and rear creates a Marangoni force which opposes the surface flow, and increases the drag coefficient [17]. Secondly, at higher concentrations of the surface-active agents the entire bubble is covered changing the boundary condition on the entire surface from no-shear to no-slip, increasing the drag on the bubble. We want to have reproducible results, study path instabilities, the effect of shape oscillations, and compare our results with potential flow theory. Therefore the bubble surface must satisfy a no-shear boundary condition and the use of purified water is necessary.

There is much discussion how to determine the purity of the water. Duineveld [5] studied the effect of surfactants in the water. Comparison with earlier research shows that in purified water the bubbles reach the highest rise velocity (see also figure 6.1) and therefore flow bifurcations occur at higher Reynolds numbers. Hence, comparison of these aspects in our experiments with those of Duineveld give a good indication of the purity of the water.

In section 6.2 the materials and methods are discussed, followed by the experimental results in section 6.3; here the relation between bubble path, shape and velocity will be discussed. Section 6.4 is left to conclusions.

6.2 Materials and methods

The experiments were conducted in a glass tank with a height of 0.50 m and a cross-section of 0.15 m × 0.15 m, filled with purified water with an electrical resistance of 18.2 MΩcm and less than 10 ppb organic particles. For comparison, some experiments have been performed in tap water. The temperature was maintained at 20 °C, giving a fluid density of 998 kg m^{-3} and a kinematic viscosity of 0.9810^{-6} m^2 s^{-1}. With an optical setup of lenses and mirrors two mutually perpendicular views of the rising bubbles were recorded at 500 or 1000 frames per second. More information on the experimental setup can be found in chapter 2.

After the bubble is produced (more details on the bubble generator can be found in a paper by Ohl [16]), it is pushed through a capillary to measure its volume. Several capillaries were used depending on the desired bubble size, resulting in a maximum volume error of 5% for the smallest bubbles dropping to 1% for the largest bubbles.

All bubbles are recorded 40 cm after release. This is well within the steady state regime of bubble motion, because the experiments showed no overall increase of the rise velocity as is the case in the transient state. Furthermore, experiments with solid spheres, see [8] and also chapter 5, show that the transient state is long (larger than 100 sphere diameters) for small Reynolds number. But in the case of high Reynolds number the spheres reach their final stage of motion already after a few sphere diameters. This can easily be understood, because the boundary layer thickness δ depends on the transient time t ($\delta \sim \sqrt{\nu t}$) and the Reynolds number ($\delta \sim D/\sqrt{Re}$). Therefore, the transient time for the boundary layer to fully develop depends on the ratio of the diameter and the velocity ($t \sim D/U$). So, the transient state is shorter for higher velocities.

Image analysis techniques result in a three-dimensional reconstruction of path, shape, and orientation of the bubble. This provides us with information on bubble velocity and aspect ratio, which is the ratio between the major and minor axis of an oblate ellipsoidal bubble. In chapter 7 the image analysis techniques will be discussed in more detail.

6.3 Experimental results

This section is divided in two parts: one on the path and the shape of the bubble and one on its rise velocity. In the figures the onset of path instability and shape instability are indicated with thin vertical or horizontal lines. To test the reproducibility of the experiments two data sets with purified water are presented marked with symbols ’+’ and ’o’; in case of tap water the symbol ’·’ is used.

6.3.1 Bubble path and shape

Figure 6.2(*a*) shows the dependance of the aspect ratio of the path (χ_{path}) on the bubble diameter. The aspect ratio of the path is extracted from the top view on the bubble path. A pure spiral has an aspect ratio of one, whereas a zigzag has an infinite aspect ratio; for rectilinearly rising bubbles no path aspect ratio can be

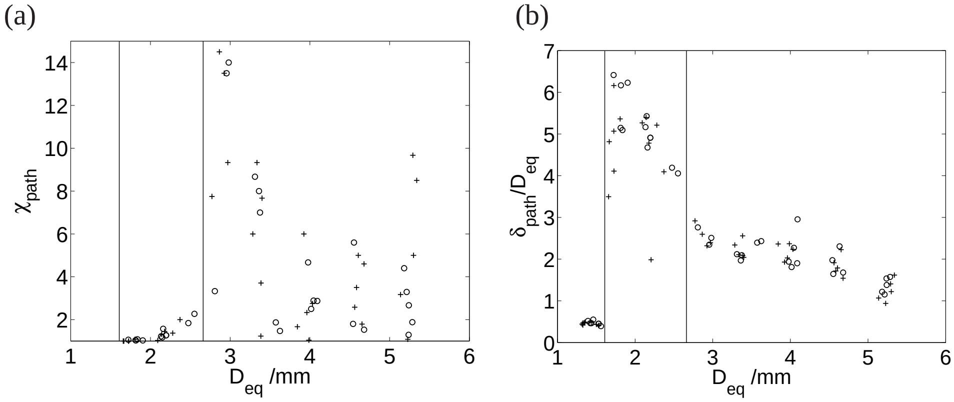

Figure 6.2: (*a*) χ_{path} versus D_{eq}; (*b*) δ_{path}/D_{eq} versus D_{eq}. '+ 'and 'o' represent two different data sets. The thin vertical lines indicate the onset of path instability (left line) and shape instability (right line).

defined.

After the first path bifurcation from rectilinear to helical at $D_{eq} \approx 1.72$ mm the aspect ratio remains one. The aspect ratio of the path increases rapidly when the shape oscillations set in at $D_{eq} \approx 2.80$ mm; the shape oscillations trigger a zigzagging motion. Recall that the bubbles are all in their final stage of motion. The literature (e.g. [12]) only mentions spiraling motion as final stage. Hence, the experiments show that shape oscillations drastically change this typical behavior. For larger bubble sizes the zigzagging motion disappears and a large scatter in the aspect ratio remains. We are now in the regime where we have so-called 'rocking' bubbles [10, 11]. More details on the effect of shape oscillations on the bubble motion will be discussed in chapter 8. The onset of shape oscillations for experiments in purified water and tap water is lower than the 4.8 mm found by Lindt [9]. Either Lindt performed experiments in even more contaminated water or he did not resolve the shape oscillations from his experimental observations. The latter hypothesis is the most plausible, because the shape oscillations (~50 Hz) can only be captured using high speed imaging, not available to him at that time.

Figure 6.2(*b*) shows the maximal horizontal displacement of the bubble, δ_{path}, as it can be observed in the reconstructed top view (XY-view), nondimensionalized with the equivalent diameter. For a bubble performing path oscillations this displacement will be measured within one period of the path oscillation; it is defined as

$$\delta_{path} = \sqrt{[\max(X) - \min(X)]^2 + [\max(Y) - \min(Y)]^2}, \qquad (6.4)$$

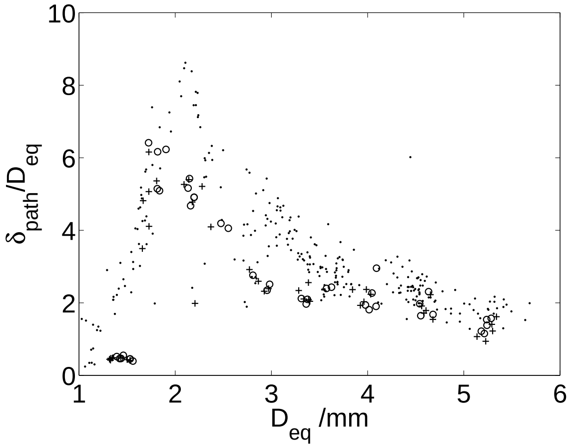

Figure 6.3: δ_{path}/D_{eq} versus D_{eq}. Experiments in purified water (o and +) and tap water (·).

with X and Y the horizontal displacements in X- and Y-direction, respectively. The nondimensionalized horizontal displacement is maximal for spiraling bubbles, right after the path instability. Further increasing the bubble size decreases the relative amplitude. When shape oscillations set in the amplitude remains almost constant; finally the motion will be almost rectilinear as was reported by Lindt [9]. It is well-known that surfactants increase the drag. Related to this the horizontal displacement of bubbles rising in purified water and in tap water are shown in figure 6.3. Bubbles in tap water have a larger horizontal displacement than bubbles rising in purified water. Energy is dissipated in horizontal motion, which links with a lower vertical rise velocity and therefore higher drag coefficient of bubbles rising in tap water as will become clear from figure 6.5. For larger bubble diameters these differences disappear. These observations agree with the findings of Clift *et al.* (see figure 6.1).

We saw that the bubble trajectory strongly depends on the bubble diameter; this is also the case for the bubble aspect ratio. Figure 6.4(*a*) shows an almost linear increase of the aspect ratio of the bubble (χ) with increasing equivalent diameter for rectilinearly rising bubbles. This agrees well with the data from Duineveld [4] and potential flow theory of Moore [15] for rectilinearly rising bubbles. The path instability sets in at an aspect ratio of 1.7, which is slightly smaller than 1.9 observed by Duineveld. At the onset of path instability our experimental results start to deviate from Moore's theory. The explanation is the lower rise velocity of non-rectilinearly rising bubbles which results in aspect ratios lower than predicted

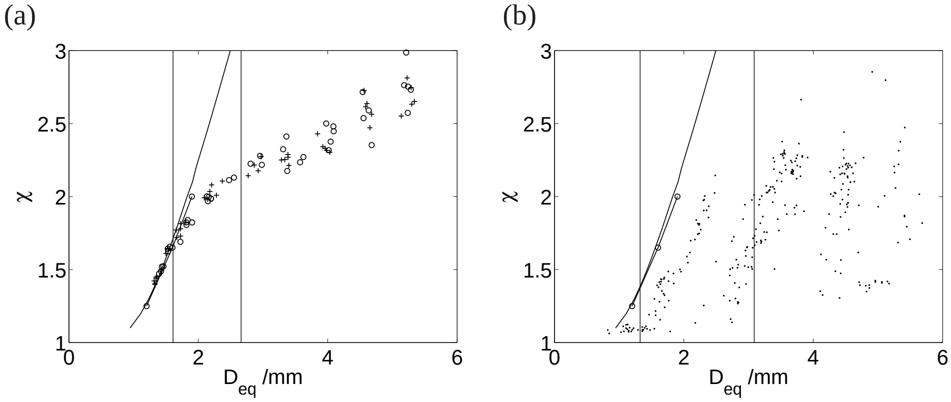

Figure 6.4: χ versus D_{eq} (*a*) purified water, '+' and 'o' represent two different data sets; (*b*) tap water. o—o taken from Duineveld [4], – Moore's theory. The thin vertical lines indicate the onset of path instability (left line) and shape instability (right line). The 'groups' in figure (*b*) are due to replacement of the capillary tube in the bubble generator for a larger tube (at 2.5 and 4 mm).

by Moore's theory. When shape oscillations set in at an aspect ratio of 2.2, the scatter of the aspect ratio increases.

The effect of surfactants can be seen in figure 6.4(*b*): for bubbles rising in tap water the aspect ratio is decreased in the entire range of bubble diameters, because of a lower surface tension and rise velocity of the bubble. Shape oscillations start at a slightly larger diameter ($D_{eq} \approx$ 3.0 mm). This is due to the lower aspect ratio; shape oscillations only appear above a certain critical aspect ratio and bubble diameter. The largest bubbles are so large that the bubble surface is already unstable at small aspect ratios. When shape oscillations set in there is a large scatter in the aspect ratio; some bubbles seem to reach the aspect ratio of uncontaminated bubbles. It is assumed that shape oscillations shed the surfactants, leaving an uncontaminated surface. Obviously, shape oscillations are not always strong enough to fully 'clean' the surface. The sudden drop in aspect ratio at a diameter of approximately 2.5 mm is due to a change in the experimental apparatus to generate the bubbles. Small bubbles are generated using a small capillary tube, whereas large bubbles, starting at approximately 2.5 mm diameter, are generated using a large capillary. The shape oscillations on the bubble are stronger in the case of a small capillary. Therefore a bubble pushed through a small capillary is probably cleaner than a bubble pushed through a large capillary; this results in a higher aspect ratio for the smaller bubbles. This phenomenon can again be seen at an equivalent diameter of 4 mm. Here the capillary has, again, been replaced by a larger capillary. Notice

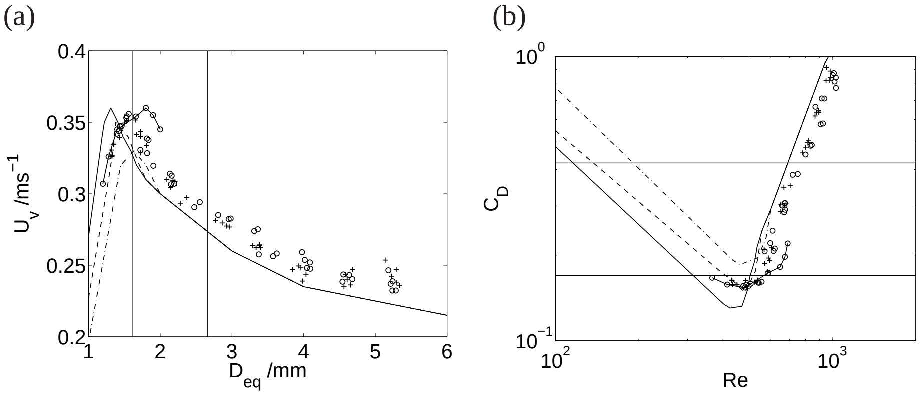

Figure 6.5: (*a*) U_v versus D_{eq}; (*b*) C_D versus Re. '+ 'and 'o' represent two different data sets. Three lines are taken from [13]: – water at 35^oC, - - water at 20^oC, $\cdot - \cdot$ water-glycerine mixture (10% by mass) at 20^oC. o—o taken from Duineveld [4]. The thin straight lines indicate the onset of path instability (left, respectively lower, line) and shape instability (right, respectively upper, line).

that for the experiments in purified water these replacements of the capillary tubes cannot be detected from the aspect ratio. Wu & Gharib [19] also reported this difference in bubble behavior depending on the way the bubble was generated. They assumed they performed experiments in purified water and therefore concluded that for one bubble size two behaviors would be possible: slow spherical bubbles and fast ellipsoidal bubbles. The present experiments suggest that they probably performed experiments in contaminated water; which was also suggested by Yang, Prosperetti & Takagi [20].

6.3.2 Bubble velocity

Figure 6.5(*a*) shows the dependance of the vertical rise velocity on the diameter of the bubble. The data of Duineveld [4] and Maxworthy [13] are included. The highest rise velocity ($U_v \approx 0.356$ m s^{-1}) is reached just before path instability sets in and agrees well with the maximum velocity ($U_v \approx 0.362$ m s^{-1}) measured by Duineveld. The path instability sets in at an equivalent diameter of 1.72 mm, this lies between the values of 1.62 mm determined by de Vries [18] and 1.81 mm by Duineveld [4], who both used purified water. The difference compared to the data of de Vries is due to his use of a temperature gradient to visualize the wake structures behind the bubbles. This leads to an averaged temperature of 28^{o}C, well above our 20^{o}C. The data of Maxworthy show that increasing the temperature decreases the ’critical’ diameter at which the path instability occurs, and increases the vertical rise velocity. The temperature used in our experiments (20^{o}C) is equal to that at which Duineveld’s experiments were done. We reach almost the same vertical rise velocity, but at a smaller bubble diameter. One might think this is caused by the data analysis method which detects the bubble contour in subsequent images. But previous comparison with data of Duineveld showed that a similar relation between bubble diameter and aspect ratio is detected. Vibrations in the system might trigger the path instability; therefore the effect of a water tank damped with and without air dampers has been investigated to see if there was any change in the position of the path instability. Although no change was detected our experiments might still possess more perturbations than the experiments of Duineveld. His experiments were conducted in a lab with a permanent concrete floor, whereas our lab is situated in a temporary building where low frequency vibrations are hardly damped. A second explanation is the possibility of a large scale recirculation in our water tank. After every experiment we waited 3 minutes for the water to come to rest, this might not be sufficient. Further research should investigate this more thoroughly.

Clift *et al.* showed that the drag experienced by the bubble is smallest in pure water, which is also reflected by Maxworthy’s experiments (see figure 6.5(*a*)); this can be related to the larger horizontal motion of the bubble in tap water (see figure 6.3). Now consider the drag coefficient

$$C_D = \frac{4}{3}\frac{D_{eq}g}{U_v^2}, \tag{6.5}$$

with g the gravitational acceleration of 9.81 m s^{-2}. Figure 6.5(*b*) shows the dependence of the drag coefficient on the Reynolds number. For rectilinearly rising bubbles our data overlaps the data of Maxworthy and Duineveld. The minima in the drag coefficient are equal. But for our spiraling bubbles the drag is larger than in Duineveld’s experiments because his bubbles still rise rectilinearly up to a bubble diameter of 1.82 mm.

Finally, we focus on the relation between the rise velocity and the shape of the bubble. Figure 6.6 shows the dependence of the Weber number on the aspect ratio. The relations of Moore [15] and Benjamin [2] are also plotted. At small aspect ratios there is a rather nice agreement between experiment and theory, but for increasing aspect ratio the deviation from theory becomes larger. Duineveld [4] ascribes this to overestimation of the deformation by theory. For identical equivalent diameter the aspect ratio found in the theory is larger than the aspect ratio found in experiments (see also figure 6.4); a larger aspect ratio increases the drag experienced

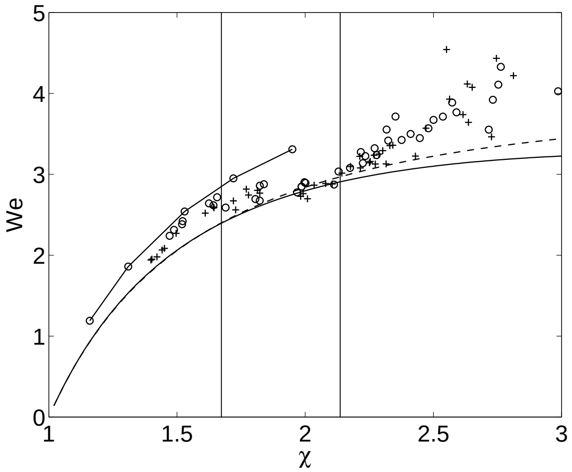

Figure 6.6: Weber number versus aspect ratio χ. '+ 'and 'o' represent two different data sets. o—o Duineveld's results [4], – Benjamin's relation [2], - - Moore's relation [15]. The thin vertical lines indicate the onset of path instability (left line) and shape instability (right line).

by the bubble (see also appendix B in chapter 7). In the experiments of Duineveld path instabilities set in at aspect ratios above 1.9 and Weber numbers larger than 3.3. Hence, all of Duineveld's data shown here are in the rectilinearly rising regime. Our experiments show a path instability at slightly lower values for the aspect ratio and Weber number, 1.7 and 2.7, respectively. As suggested before, this might be due to vibrations in our experimental setup or the presence of a large scale recirculation. After the onset of path instability, but before shape oscillations set in, the experimental and theoretical data are in better agreement. This is remarkable because the difference between the aspect ratio of the bubble in theory and in experiments is even larger for non-rectilinear rising bubbles (see figure 6.4). Hence, it seems that the overestimation of the deformation by theory, as suggested by Duineveld [4], is not the only reason for the difference between theory and experiment. A better explanation can be given in terms of the minimum radius of curvature of the bubble. For an oblate ellipsoid the radius of curvature is calculated in appendix C of chapter 7. The minimum radius of curvature (R_{min}) for an oblate ellipsoid is

$$R_{min} = D_{eq}\frac{\chi^{1/3}}{\chi^2+1}, \tag{6.6}$$

and is located at the equator of the ellipsoid. The theory of Moore provides a

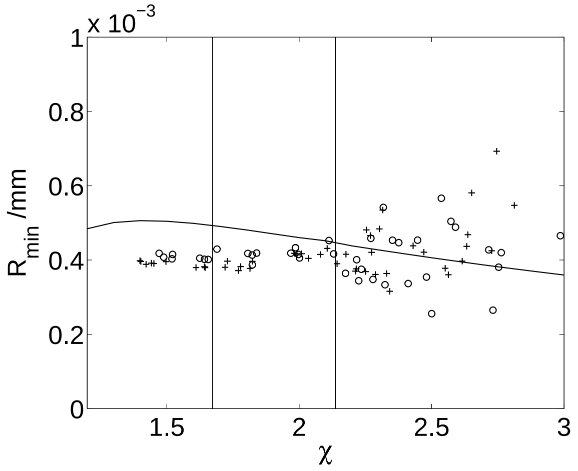

Figure 6.7: Minimum radius of curvature R_{min} versus aspect ratio χ. '+ 'and 'o' represent two different data sets. The solid line is the relation of Moore. The thin vertical lines indicate the onset of path instability (left line) and shape instability (right line).

relation between the equivalent diameter of the bubble and its aspect ratio (see also figure 6.4). Combining this relation with the relation for the minimum radius of curvature gives the solid line in figure 6.7. At the equator of the bubble the velocity at its surface reaches a maximum, resulting in a low pressure, hence a high pressure drop across the surface. This results in a small radius of curvature which is therefore seen to be related to the rise velocity of the bubble. Figure 6.7 shows that Moore's theory predicts bubble shapes which are in good agreement with respect to the minimum radius of curvature just before the onset of shape oscillations. That is the reason why in figure 6.6 at these aspect ratios the theoretical dimensionless velocity (the Weber number) is in such good agreement with experiments. When shape oscillations set in, the agreement is less because Moore assumed a bubble of fixed shape. So, with respect to the rise velocity, agreement in the radius of curvature at the equator of the bubble is more important than agreement in the aspect ratio of the bubble.

6.4 Conclusion

This chapter dealt with general aspects of single bubbles rising in purified water. The experiments clearly show the influence of shape oscillations on the motion of the bubble; the bubble path changes from a stable spiral into a pure zigzag at the bubble size where shape oscillations set in. The relative horizontal displacement of the bubble is maximal just before path instabilities set in. This results in the largest rise velocities, and therefore lowest drag, for these bubbles. These rise velocities are as high as has been measured by Duineveld. The critical diameter for the onset of path instabilities in our experiments is slightly lower than Duineveld finds. This might be caused by vibrations in our experimental setup which trigger these instabilities or large scale recirculations in the water tank. This smaller critical diameter gives rise to some deviation with respect to the results of Duineveld for the critical Weber numbers and aspect ratio for path and shape instabilities. But the agreements in rise velocity and drag experienced by the bubble justify the statement the experiments are conducted in purified water. Finally, it is shown that the minimum radius of curvature of the bubble shape is a better measure of the rise velocity of the bubble than the bubble aspect ratio.

In the next two chapters the behavior of rising bubbles will be examined in more detail. We saw the important influence of shape oscillations on the bubble dynamics. Therefore chapter 7 focusses on the bubbles without shape oscillations and chapter 8 on the bubbles with shape oscillations.

References

[1] BEL FDHILA, R. & DUINEVELD, P.C. 1996 The effect of surfactant on the rise of a spherical bubble at high Reynolds and Peclet numbers. *Phys. Fluids* **8**, 310–321.

[2] BENJAMIN, T.B. 1987 Hamiltonian theory for motion of bubbles in an infinite liquid. *J. Fluid Mech.* **181**, 349–379.

[3] CLIFT, R., GRACE, J.R. & WEBER, M.E. 1978 *Bubbles, Drops, and Particles*. Academic Press Inc.

[4] DUINEVELD, P.C. 1994 Bouncing and coalescence of two bubbles in water. PhD thesis, University of Twente, Enschede, the Netherlands.

[5] DUINEVELD, P.C. 1995 The rise velocity ans shape of bubbles in pure water at high Reynolds numbers. *J. Fluid Mech.* **292**, 325–332.

[6] HABERMAN, W.L. & MORTON, R.K. 1954 An experimental study of bubble moving in liquids. *Trans. ASCE* **387**, 227–252.

[7] HARTUNIAN, R.A. & SEARS, W.R. 1957 On the instability of small gas bubbles moving uniformly in various liquids. *J. Fluid Mech.* **3**, 27–47.

[8] JENNY, M., DUŠEK, J. & BOUCHET, G. 2004 Instabilities and transition of a sphere falling or ascending freely in a Newtonian fluid. *J. Fluid Mech.* **508**, 201–239.

[9] LINDT, J.T. 1972 On the periodic nature of the drag of a rising bubble. *Chem. Eng. Sci.* **27**, 1775–1781.

[10] LUNDE, K. & PERKINS, R.J. 1997 Observations on wakes behind spheroidal bubbles and particles. , vol. FEDSM97, p. 3530.

[11] LUNDE, K. & PERKINS, R.J. 1998 Shape oscillations of rising bubbles. *Appl. Sci. Res.* **58**, 387–408.

[12] MAGNAUDET, J. & EAMES, I. 2000 The motion of high-Reynolds-number bubbles in inhomogeneous flows. *Annu. Rev. Fluid Mech.* **32**, 659–708.

[13] MAXWORTHY, T., GNANN, C., KÜRTEN, M. & DURST, F. 1996 Experiments on the rise of air bubbles in clean viscous liquids. *J. Fluid Mech.* **321**, 421–441.

[14] MOORE, D.W. 1963 The boundary layer on a spherical gas bubble. *J. Fluid Mech.* **16**, 161–176.

[15] MOORE, D.W. 1965 The velocity of rise of distorted gas bubbles in a liquid of small viscocity. *J. Fluid Mech.* **23**, 749–766.

[16] OHL, C.D. 2000 Generator for single bubbles of controllable size. *Rev. of Scien. Instr.* **72**, 252–254.

[17] PALAPARTHI, R., PAPAGEORGIOU, D.T. & MALDARELLI, C. 2005 Theory and experiments on the stagnant cap regime in the motion of spherical surfactants-laden bubbles. *J. Fluid Mech.* **559**, 1–44.

[18] DE VRIES, A.W.G. 2001 Path and wake of a rising bubble. PhD thesis, University of Twente, Enschede, the Netherlands.

[19] WU, M. & GHARIB, M. 2002 Experimental studies on the shape and path of small air bubbles rising in clean water. *Phys. Fluids* **14**, L49–L52.

[20] YANG, B., PROSPERETTI, A. & TAKAGI, S. 2003 The transient rise of a bubble subject to shape or volume changes. *Phys. Fluids* **15**, 2640–2648.

Chapter 7

Motion of oblate ellipsoidal bubbles [‡]

The previous chapter introduced the general aspects of single bubble motion. In this chapter we focus on oblate ellipsoidal bubbles that rise without shape oscillations. Ellingsen & Risso [5] also studied bubble behavior in this regime. Their results will be compared with the results of our experiments.

A new mathematical method to calculate the bubble path, orientation and shape from the experimental data is introduced. This is followed by the calculation of the forces and torques acting on the bubbles. A link will be made with the vorticity structure behind the bubble and models for drag and lift experienced by the bubbles will be introduced. It is shown that the measured drag consists of a contribution related to viscous drag and a contribution induced instantaneously by the lift force. It seems that variations in the viscous contribution to the drag associated with the 'building-up' of the vorticity field by diffusion and convection, important at low Reynolds numbers, are negligible at high Reynolds numbers.

7.1 Introduction

Ellingsen & Risso [5] discuss the features of the flow around an ellipsoidal bubble of fixed shape rising in a quiescent liquid. They focus on a single bubble of 2.5 mm diameter, rising along a (flattened) helicoidal path. Several checks were made to ensure that their water was pure. The terminal rise velocity of the bubble is a good

---

[‡] adapted from: C.H.J. Veldhuis, A. Biesheuvel, & L. van Wijngaarden, *Motion of oblate ellipsoidal bubbles*, to be submitted to J. Fluid Mech. (2007)

indication for the purity of the water. Duineveld [4] performed experiments in purified water; the maximum rise velocities he found are the largest reported in the literature. Ellingsen & Risso's results for the terminal rise velocity of the bubble were in good agreement with the results of Duineveld.

In their paper they introduce some important research questions:
”...Do the observed trajectories correspond to transitory stage or to a stable final motion? Are shape oscillations present or not? What is the exact definition of zigzag and helical paths?...” They answer these questions for one bubble size; obviously answering these questions for a broad range of bubble diameters would give much more understanding, as will be shown in this chapter.

Ellingsen & Risso performed experiments with two high-speed cameras providing them with two side views of the bubble. They assumed the bubble to be an oblate ellipsoid of constant shape with its minor axis aligned with its trajectory, which has been confirmed by De Vries [12]. With respect to this constant shape and orientation the authors state:
”...owing to the constant relative orientation and shape of the bubble, the wake instability is the only possible cause of the path oscillations observed here. The prediction of the bubble motion thus requires taking into account the interaction between the bubble and the unsteady wake.” Later on the orientation of the wake behind the bubble will be discussed in more detail, providing a way to predict the forces acting of the bubble based on the wake structure behind it.

After an initial acceleration Ellingsen & Risso observe that the bubble starts oscillating in an almost plane zigzag. The plane zigzag progressively transforms into a flattened helix, which is the final stable trajectory. They explain this transition with two harmonic modes involved in the path oscillations. These modes have the same frequency but are $\pi/2$ out of phase. The primary mode was saturated, leading to a plane zigzag. The secondary mode was still increasing, leading to a transition from a plane zigzag to a helical trajectory. When the amplitude of the secondary mode is increasing the vertical velocity will decrease and finally become constant for a pure spiral.

Besides the path of the bubble Ellingsen & Risso also studied the liquid velocity induced by the bubble motion. They found two regions in the flow: potential flow in front of and next to the bubble and a long wake behind it. The flow in the wake consists of a quasi-steady part that spreads around the bubble trajectory and a part consisting of vortices that are generated at the bubble rear. These vortices are described by Lunde & Perkins [7] and Brücker [3]. About the wake vortices Ellingsen & Risso say: *”They have a strong influence on the flow just behind the bubble and on the hydrodynamic force that acts on it. They are the origin of the bubble path oscillations that cause the increase of the drag coefficient. ... Nevertheless, they do not induce large liquid velocities and their influence on the intermediate- and* *far-wake intensity is small. The velocity decay behind the bubble is predicted well by the axisymmetric wake around a rectilinear rising bubble provided the local orientation of the wake is taken parallel to the bubble trajectory.*"

In this chapter part of the work done by Ellingsen & Risso will be verified. Furthermore, by calculating the actual forces and torques acting on the bubbles this research will be extended in order to have a better understanding of bubble motion.

In section 7.2 a method to reconstruct the path, orientation and shape of the bubble will be introduced; equations will be derived from which the orientation and shape of the bubble easily follow. Section 7.3 discusses the experimental results. Here the forces and torques acting on the bubble expressed in a Frenet reference frame will be calculated. Furthermore several features of the wake behind the bubble will be discussed. In section 7.4 this wake will be linked to the forces acting on the bubble and a model for lift and drag will be introduced. Section 7.5 is left to conclusions. At the end of this chapter three appendices are included. Appendix A discusses the derivation of the general equations of motion to calculate forces and torques. This is follow by appendix B on the irrotational flow around oblate spheroids. We end with appendix C on the calculation of the surface of an oblate spheroid.

7.2 Reconstruction of path, orientation and shape

The reconstruction of the bubble path, orientation, and shape have been done by several researchers with slightly different methods. Ellingsen & Risso [5] reconstruct the bubble shape and orientation from two 2D projections of the bubble. They assume an oblate ellipsoid with its minor axis along the path of the bubble. The major axes are directly taken from the projections. They can only extract the minor axis of the bubble at those instances when the bubble velocity is vertical in one side view. The minor axis can then be extracted from the other side view. Assuming a bubble of constant volume with an oblate ellipsoidal shape they show they can correctly calculate the projected minor axis in the side views [5, fig.3]. The disadvantage of this method is, that they cannot continuously calculate the actual bubble shape; it is necessary for the bubble velocity to have a vertical component in one of the side views.

Luther, Rensen & Guet [8] and de Vries [12] calculate the bubble shape and orientation from two 2D, mutually perpendicular side views (projections) of one bubble, which they assume to be an oblate ellipsoid. They use a mathematical description of the bubble orientation based on a combination of rotation matrices which connect the laboratory frame to a frame attached to the bubble. They it-

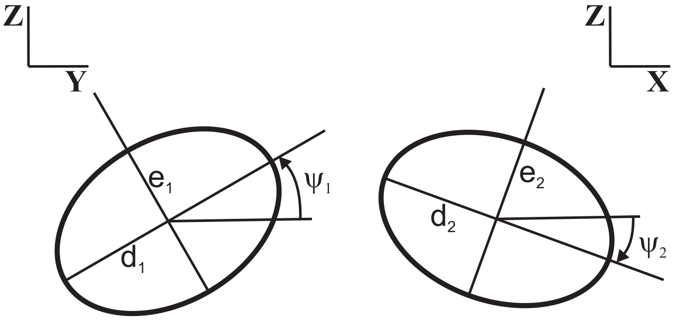

Figure 7.1: Two mutual perpendicular projections in a XYZ-laboratory frame. The angles are taken positive counterclockwise. The orientation of the side views of the bubble are arbitrary.

eratively calculate the bubble shape and orientation by assuming a certain bubble shape and orientation and calculate the projections onto the two side views and compare these projections with the real projections. By minimizing the error the iteration will converge to the correct representation of the bubble.

In this section a method is introduced which is also based on a mathematical description with rotation matrices, but the set of equation are solved explicitly, making this approach faster and more precise.

To reconstruct the bubble path, orientation and shape the digital images provided by the high speed camera have to be processed. Each digital image consists of two 2D, mutual perpendicular, side views (projections) of a single bubble (see figure 7.1). For a sphere the shape is known *a priori* and the position of the center can easily be extracted from the digital images. For a bubble only the position of the center and hence its path is known.

It is well-known that the bubble can be assumed to be an oblate ellipsoid, with major axes a and b (hence $a = b$) and minor axis c [4, 5, 13]. The aspect ratio of the bubble is defined by

$$\chi = \frac{a}{c} \geq 1. \tag{7.1}$$

The bubble orientation is defined by the rotation angles α, β, and γ, which will be explained in detail in figure 7.2. The projections of an ellipsoid are ellipses [5, 12]. From the two projections the axes and orientation angles of these ellipses can be extracted (see also figure 7.1):

- the long axes d_1 and d_2,
- the short axes e_1 and e_2, and

- the orientation angles ψ_1 and ψ_2 between the major axis and the horizontal plane.

The following discussion will give a procedure to reconstruct the shape and orientation of the bubble. The aim is to find the relations:

$$(d_1, d_2, e_1, e_2, \psi_1, \psi_2) \Longrightarrow (a, b, c, \alpha, \beta, \gamma)\,, \tag{7.2}$$

with the restriction that $a = b = d_1 = d_2$.

Consider an ellipsoid in an $x'y'z'$-frame with axes a, b, and c along the x'-, y'-, and z'-axis, respectively. The convention for the three rotation angles (α, β, and γ) can be found in figure 7.2. The first rotation, with angle γ, is around the c-axis, and results in the $x''y''z''$-frame. The c-axis is the symmetry axis; therefore γ is set to zero. The second rotation with angle β and the third rotation with angle α are around the y''-axis and x'''-axis, resulting in the $x'''y'''z'''$-frame and $x''''y''''z''''$-frame, respectively. Every rotation is governed by its unique rotation matrix $\mathbf{R}_z$, $\mathbf{R}_y$, and $\mathbf{R}_x$, respectively. Now denote the $\mathbf{x}''''$ as $\mathbf{X}$ and the matrix product of the three rotation matrices as $\mathbf{R}$. $\mathbf{X}$ is a vector in the laboratory frame; the coordinates of this vector can be taken directly from the two 2D side views, because these are the YZ- and XZ-projections. The relation between a vector in a frame with axes along the main axes of the ellipsoid and this vector in a frame fixed in the laboratory can be written as

$$\mathbf{X} = \mathbf{R}\mathbf{x}'. \tag{7.3}$$

For an oblate ellipsoid the rotation matrix $\mathbf{R}$ is

$$\mathbf{R} = \mathbf{R}_x\mathbf{R}_y\mathbf{R}_z = \begin{bmatrix} \cos\beta & 0 & \sin\beta \\ \sin\alpha\sin\beta & \cos\alpha & -\sin\alpha\cos\beta \\ -\sin\beta\cos\alpha & \sin\alpha & \cos\alpha\cos\beta \end{bmatrix}. \tag{7.4}$$

7.2.1 Calculation of the orientation

The minor axes $e_{1,2}$ in the two side views (figure 7.1) coincide with the projections of the real minor c-axis. Therefore, the orientation of the minor c-axis follows immediately for the two orientation angles ψ_1 and ψ_2. Consider a point (X_c, Y_c, Z_c) on the minor axis. The vector through this point and the origin expressed in laboratory frame coordinates is $\mathbf{R}\mathbf{e}_3$, with $\mathbf{e}_3$ the unit vector in z'-direction. Hence, this is the third column of the total rotation matrix $\mathbf{R}$:

$$\left\{ \begin{array}{c} X_c \\ Y_c \\ Z_c \end{array} \right\} = \left\{ \begin{array}{c} \sin\beta \\ -\sin\alpha\cos\beta \\ \cos\alpha\cos\beta \end{array} \right\}. \tag{7.5}$$

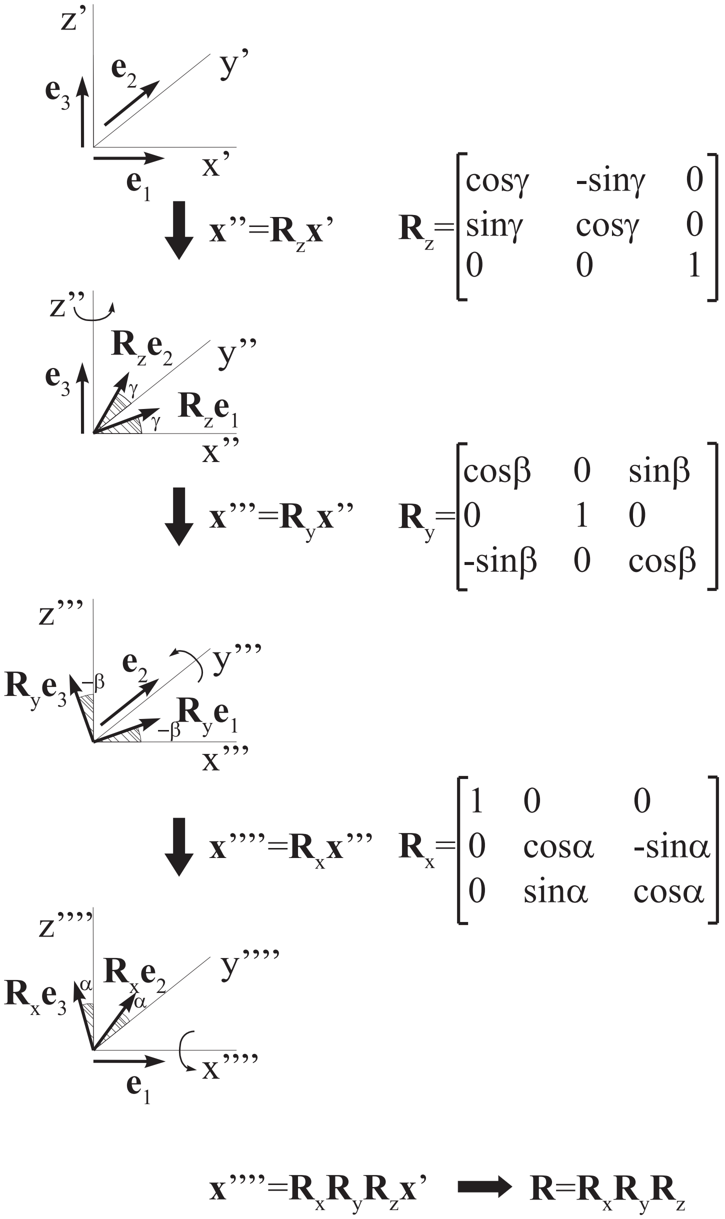

Figure 7.2: Representation of the axes, angles, and rotation matrices.

The orientation angles ψ_1 and ψ_2 are related to this point by

$$\tan\psi_1 = \frac{Y_c}{Z_c} = -\tan\alpha \quad \text{and} \quad \tan\psi_2 = \frac{X_c}{Z_c} = \frac{\tan\beta}{\cos\alpha}. \tag{7.6}$$

From these equations the angles α and β can be calculated, resulting in

$$\alpha = -\psi_1 \quad \text{and} \quad \beta = \tan^{-1}\left(\cos\psi_1 \tan\psi_2\right). \tag{7.7}$$

7.2.2 Calculation of the shape

For an oblate ellipsoid the axes d_1 and d_2 in the two side views should be equal. As long as this is true, the reconstruction is correct. For the two major axes it is assumed that $a = d_1$ and $b = d_2$. In contradiction to what is sometimes stated in the literature, the minor c-axis is not equal to the axes e_1 and e_2. These axes are projections of the oblate ellipsoid and therefore always larger than, or at most equal to, the minor c-axis.

The coordinates of the highest point on the ellipsoid (X_t, Y_t, Z_t) can be extracted from the two side views. This point is part of the ellipsoid and obeys the equation for an ellipsoid in the $x'y'z'$-frame:

$$\frac{x_t'^2}{a^2} + \frac{y_t'^2}{b^2} + \frac{z_t'^2}{c^2} = 1 \tag{7.8}$$

The axes a and b are known and the coordinates (x_t', y_t', z_t') in the body frame can be derived from the coordinates (X_t, Y_t, Z_t) in the laboratory frame by:

$$\mathbf{x'_t} = \mathbf{R}^{-1}\mathbf{X_t}. \tag{7.9}$$

Substituting this into the equation for the ellipsoid gives the minor axis c.

The two projections of the bubble in the digital images are detected using a threshold for the gray value at which the bubble rim is located. This procedure is calibrated with the known bubble volume from the capillary after the bubble generator; this leads to a maximum error of 1% in bubble volume. Now the bubble orientation and shape can be reconstructed from the digital images the experimental results are discussed in the next section.

7.3 Experimental results

Chapter 6 discussed the general features of single bubble motion. From the data presented in that chapter six representative experiments are selected. The equivalent diameter D_{eq}, aspect ratio χ, path frequency f_{path}, and Reynolds number Re

sub-figure	D_{eq}/mm	χ	Re	f_{path}/Hz	description
(*a*)	1.6	1.7	555	-	rectilinear path
(*b*)	1.8	1.8	640	4.7	spiral path
(*c*)	1.9	1.8	654	4.7	spiral path
(*d*)	2.1	2.0	720	5.2	flattened spiral path
(*e*)	2.6	2.1	818	5.7	flattened spiral path
(*f*)	2.8	2.2	859	6.7	zigzag path, shape oscillations

Table 7.1: Overview of experiments with oblate ellipsoidal bubbles presented in this chapter. The sub-figure numbers refer to the numbers of the sub-figures in sections 7.3.1 and 7.3.2. The last experiment shows an oscillating bubble as introduction to the next chapter.

for these experiments are given in table 7.1. In the next section the bubble path, orientation and shape are discussed, followed by a section on the forces and torques acting on these bubbles and a section on the wake structure behind the bubble. The regime of fixed bubble shape is limited to smaller bubbles and the size of the largest bubble presented in this chapter is just above the bubble size for the onset of shape oscillations.

7.3.1 Bubble path, orientation and shape

Figures 7.3 and 7.4 show the 3D paths and the top views of the bubble, respectively, where the gray values indicate the magnitude of the tangential velocity of a bubble. The smallest bubble rises in a straight path, while larger bubbles rise along a spiral with a constant velocity, which is maximal right after the path instability. The horizontal amplitude of the bubble motion is at its maximum for a pure spiral (see also figure 6.2(*b*)). For larger bubbles the path becomes flattened and the tangential velocity becomes unsteady and decreases; this is a characteristic feature just before the onset of shape oscillations. Right at the onset of shape oscillations the bubble rises along a zigzag path on which more details will be given in the next chapter.

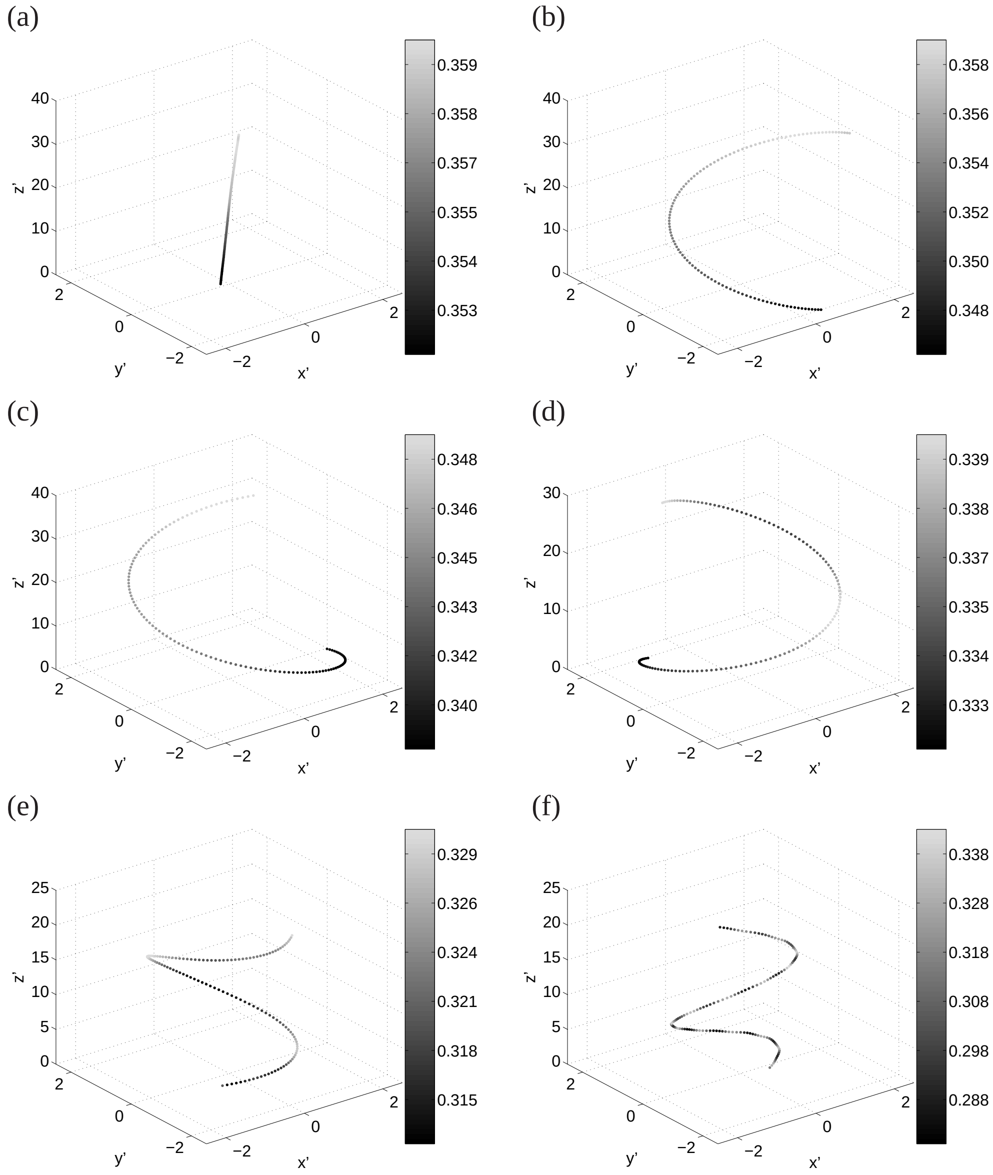

Figure 7.3: Measured trajectories of bubbles rising in water. The gray values represent the tangential velocity of the bubbles, with the numbers next to the codes giving the corresponding value in m s^{-1}. Axes are non-dimensionalized with the equivalent diameter. See table 7.1 for further details.

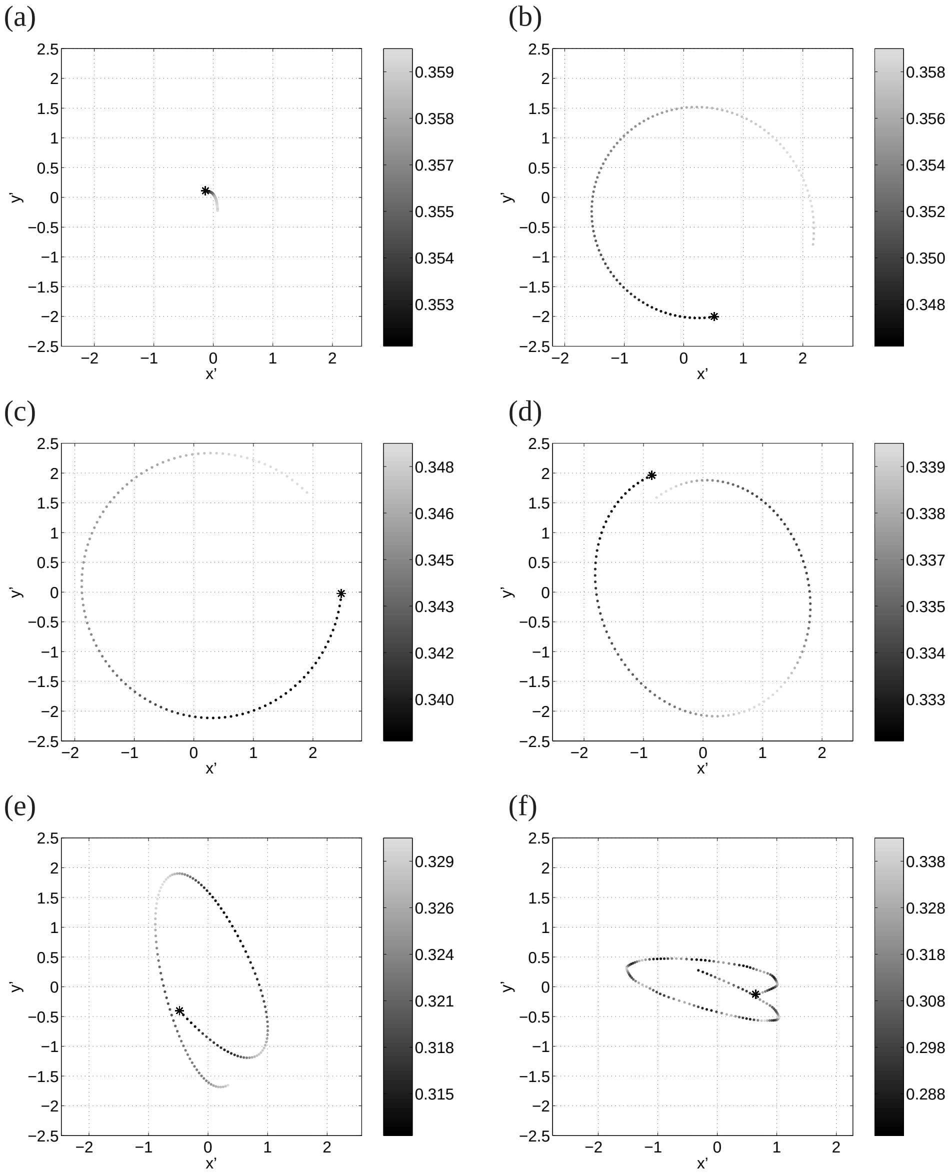

Figure 7.4: Top views of bubbles rising in water. The gray values represent the tangential velocity of the bubbles, with the numbers next to the codes giving the corresponding value in m s^{-1}. The * indicates the starting point of the trajectory. See table 7.1 for further details.

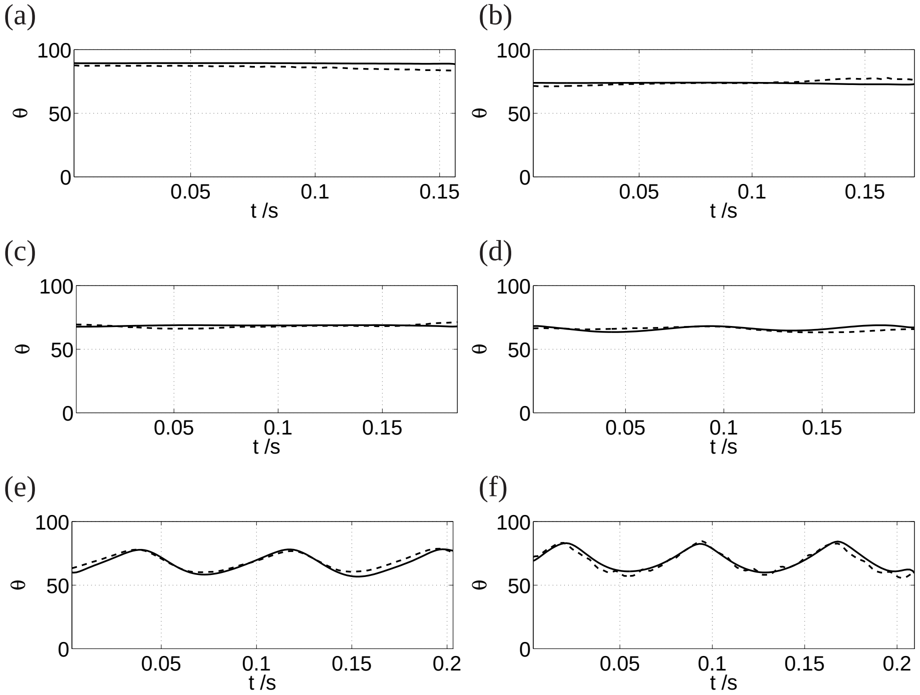

Figure 7.5: – Angle between the tangent and the horizontal plane, - - angle between the minor axis c and the horizontal plane. Angles are given in ^{o}. See table 7.1 for further details.

Figure 7.5 shows the angle between the tangent of the bubble trajectory and the horizontal plane, and the angle between the minor axis c and the horizontal plane. The minor axis coincides with the tangent, which has also been found by Ellingsen & Risso [5] and de Vries [12]. When the path instability sets in, the angle drops from 90^o for rectilinear motion to approximately 68^o. Further increase of the bubble size slightly decreases the angle.

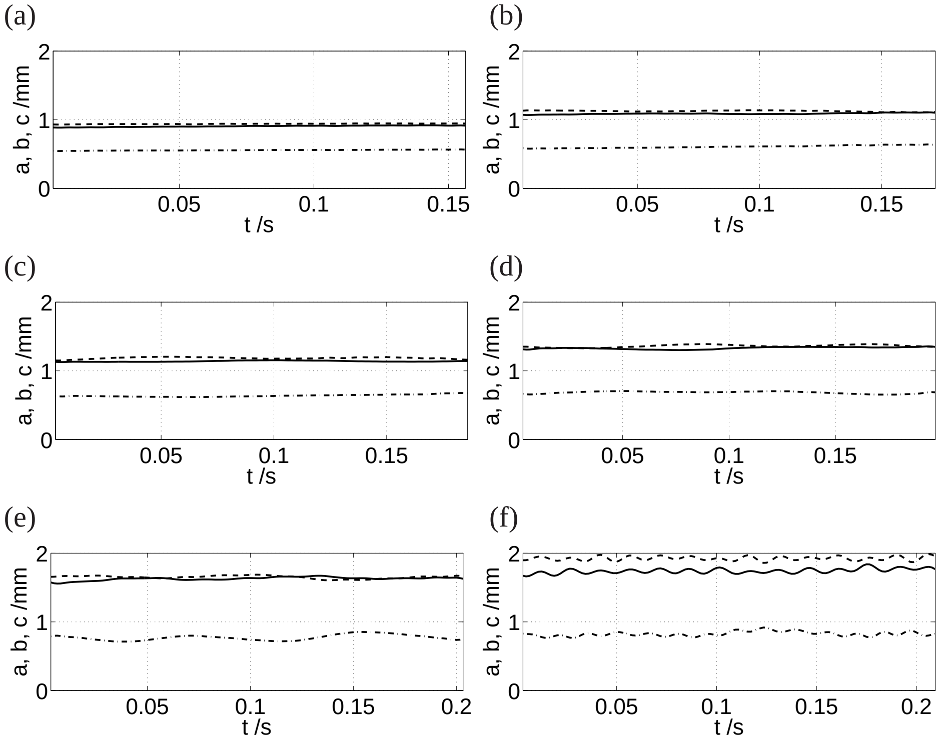

Figure 7.6: Shape of the bubble:– major axis a, - - major axis b, $\cdot - \cdot$ minor axis c. See table 7.1 for further details.

Figure 7.6 presents the axes a, b and c of the reconstructed bubble. The two major axis a and b are directly taken from the two major axes $d_{1,2}$ in the two side views. For convenience $a = d_1$ and $b = d_2$; so a breaking of axi-symmetry is directly detected from figure 7.6. The two major axes are constant and indeed equal, preserving axisymmetry as long as there are no shape oscillations. There is a symmetry breaking at the onset of shape oscillations ($d_1 \neq d_2$, hence $a \neq b$) as can be seen in figure 7.6(*f*). Therefore the reconstruction of bubble orientation and shape no longer holds in the regime of shape oscillations. Notice that all axes (a, b, and c) exhibit a low amplitude frequency equal to twice the frequency of the path oscillation. This is an artefact due to the bubbles moving in and out of focus of the digital camera.

7.3.2 Forces and torques acting on bubbles

The equations of motion with respect to a fixed laboratory frame XYZ for a massless bubble moving through a quiescent liquid are given by

$$\frac{\mathrm{d}\mathbf{I}}{\mathrm{d}t} = -\rho V \mathbf{g} + \mathbf{F}, \quad \frac{\mathrm{d}\mathcal{A}}{\mathrm{d}t} = \mathbf{T}. \tag{7.10}$$

Here $\mathbf{I}$ is the linear impulse of the irrotational fluid motion that would result if the motion of the bubble would be generated instantaneously from a state of rest; and in this respect $\mathcal{A}$ is the angular impulse. The density of the liquid is given by ρ; V is the volume of the bubble, and $\mathbf{g}$ the gravitational acceleration. The 'extraneous' force $\mathbf{F}$ and torque $\mathbf{T}$ are due to the presence of vorticity in the flow (see also chapter 4). To solve the equations of motion it is helpful to use a Frenet reference frame with unit vectors $\mathbf{t}$, $\mathbf{n}$, and $\mathbf{b}$, already discussed in chapter 4. Let $s(t)$ measure the distance travelled along the curve from some arbitrary initial instant. The translational velocity of the bubble in the Frenet frame is

$$\mathbf{U} = \frac{\mathrm{d}s}{\mathrm{d}t}\,\mathbf{t} = U\,\mathbf{t}, \tag{7.11}$$

and the angular velocity

$$\mathbf{\Omega} = \frac{\mathrm{d}s}{\mathrm{d}t}\,(-\tau\mathbf{t} + \kappa\mathbf{b}) \tag{7.12}$$

about the instantaneous position of its axes, with τ the torsion and κ the curvature of the curve. The momentum equations of the body now read

$$\left(\frac{\mathrm{d}\mathbf{I}}{\mathrm{d}t}\right)_F + \mathbf{\Omega}\times\mathbf{I} = -\rho V\mathbf{g} + \mathbf{F}, \tag{7.13}$$

$$\left(\frac{\mathrm{d}\mathcal{A}}{\mathrm{d}t}\right)_F + \mathbf{\Omega}\times\mathcal{A} + \mathbf{U}\times\mathbf{I} = \mathbf{T}, \tag{7.14}$$

where the first terms on the left-hand sides are the vectors formed by the rates of change of the components of the virtual linear momentum, respectively angular momentum, of the body with respect to the Frenet reference frame.

Figure 7.5 showed that the oblate ellipsoidal bubble is positioned with its minor axis along the tangential vector. Therefore it follows that

$$\mathbf{I} = AU\,\mathbf{t}, \tag{7.15}$$

where A is an element of the added mass tensor and is given in Lamb [6, art.114] for an oblate ellipsoid translating in the direction of its minor axis (see also (7.72) in appendix B).

$$A = \rho V M_z, \tag{7.16}$$

with

$$M_z(\chi) = \frac{(\chi^2-1)^{\frac{1}{2}} - \cos^{-1}\chi^{-1}}{\cos^{-1}\chi^{-1} - (\chi^2-1)^{\frac{1}{2}}/\chi^2}.$$

Here $\chi = a/c$, is the aspect ratio of the oblate ellipsoid. Remember that the bubble is without mass and axisymmetric around its minor axis. Therefore the angular impulse in the direction of the symmetry axis is zero. Hence, the angular impulse is

$$\mathcal{A} = QU\kappa\,\mathbf{b}, \tag{7.17}$$

where Q is an element of the added mass tensor for rotation. The element Q is given in Lamb [6, art.115] (see also (7.77) in appendix B).

$$Q = \tfrac{1}{5}\rho V R_x, \tag{7.18}$$

where

$$R_x(\chi) = \chi^{-\frac{4}{3}}(\chi^2-1)^{-1}\frac{(\gamma_0-\beta_0)}{2+[(\chi^2+1)/(\chi^2-1)](\beta_0-\gamma_0)}$$

with

$$\beta_0(\chi) = \frac{\chi^2\cos^{-1}\chi^{-1} - (\chi^2-1)^{\frac{1}{2}}}{(\chi^2-1)^{\frac{3}{2}}}, \qquad \gamma_0(\chi) = 2\,\frac{(\chi^2-1)^{\frac{1}{2}} - \cos^{-1}\chi^{-1}}{\chi^2(\chi^2-1)^{\frac{3}{2}}}.$$

In the Frenet reference frame the equations of motion reduce to

$$A\frac{\mathrm{d}U}{\mathrm{d}t} = F_D + \rho V g_t, \quad A\kappa U^2 = F_{L,n} + \rho V g_n, \quad F_{L,b} + \rho V g_b = 0, \tag{7.19}$$

$$T_t = 0, \quad Q\tau\kappa U^2 = T_n, \quad Q\frac{\mathrm{d}\kappa U}{\mathrm{d}t} = T_b. \tag{7.20}$$

In (7.19), F_D is the component of the vortex force in the tangential direction; the components in normal and bi-normal directions are $F_{L,n}$ and $F_{L,b}$, respectively. In (7.20) T_t, T_n, and T_b are the components of the torque in the three directions of the Frenet frame.

It should be mentioned that the reconstruction of these forces and torques has also been done without assuming the bubble minor axis to coincide with the tangent vector. Appendix A provides a detailed discussion of this second method. The advantage is that small deviations from the alignment of the minor axis with the tangent vector can be accounted for. After this more general reconstruction it turned out that the equations of motion from (7.19) and (7.20) indeed represent the dynamics of the bubble motion correctly.

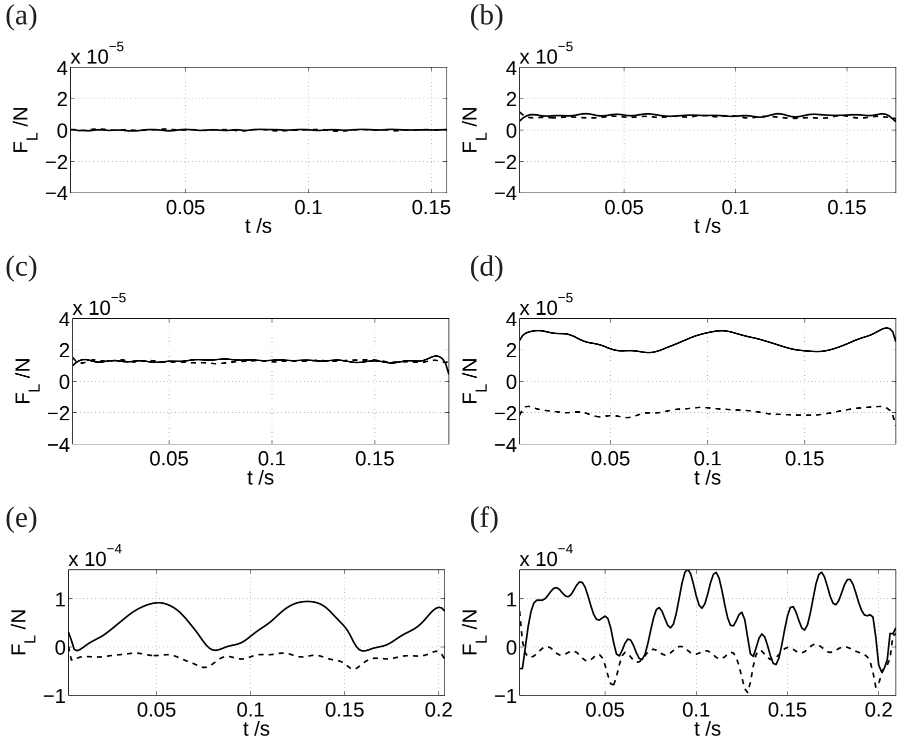

Figure 7.7: Lift force acting on the bubbles: – $F_{L,n}$, - - $F_{L,b}$. Notice the different scales of the F_L-axis. See table 7.1 for further details.

Lift and drag force

Figure 7.7 shows the components of the lift force acting on the bubble. For a bubble rising straight (figure 7.7(*a*)) the lift force is zero. For a bubble rising in a pure spiral (figures 7.7((*b*) and (*c*)) the lift force is non-zero and constant. The pitch and diameter of a pure spiral are constant; together with a constant velocity along the spiral this results in a constant lift force. For a flattened spiral (figures 7.7(*d*) and (*e*)) the lift force becomes unsteady. The lift force in the bi-normal direction tends to zero, which is the case for a pure zigzag, because the bi-normal is the vector normal to the zigzag-plane. The same features are still visible for a bubble with shape oscillations (figure 7.7(*f*)) except for the high frequency oscillations superimposed on the forces.

Figures 7.7 (*d*) to (*f*) show negative lift forces in the bi-normal direction. The reason for this is the counterclockwise trajectories compared to the clockwise trajectories in figures 7.7 (*b*) and (*c*) (see figure 7.4). In the case of a counterclockwise motion the bi-normal vector points in the positive Z-direction, whereas in clockwise direction the bi-normal vector points in the negative Z-direction.

Pure spiraling motion

The lift force in the normal and bi-normal direction are equal for the pure spirals (see figures 7.7 (*b*) and (*c*)). This can also be concluded from the analysis of the vortex structure behind the bubble which will be shown in section 7.4, where the vortex structure behind a spiraling bubble is analyzed in more detail.

Consider a spiraling bubble with a constant velocity in the Z-direction, an angle θ between the tangential direction and the horizontal XY-plane and a path radius R. The path curvature and torsion are given by

$$\kappa = \frac{\cos^2\theta}{R}, \quad \tau = \frac{\sin\theta\cos\theta}{R}. \tag{7.21}$$

For a spiral the normal is positioned in a horizontal plane. Using (7.19) and the experimental observation that $|F_{L,n}| = |F_{L,b}|$ leads to

$$U^2 = \rho g V \frac{R}{A\cos\theta}. \tag{7.22}$$

From appendix B it is known that A can also be written as $\rho V M_z$, with M_z the added mass factor, which is a function of the aspect ratio χ; hence,

$$U^2 = \frac{gR}{M_z\cos\theta}. \tag{7.23}$$

In the case of a spiral the velocity can also be written as:

$$U^2 = (2\pi)^2 \frac{f_{path}^2 R^2}{\cos^2\theta}, \tag{7.24}$$

where f_{path} is the path frequency. Combining (7.23) and (7.24) gives

$$(2\pi)^2 f_{path}^2 = \frac{g\cos\theta}{RM_z}. \tag{7.25}$$

The added mass coefficient M_z hardly varies and is approximately one for these bubbles. The possible spirals are limited to a select combination of path frequency, angle with the horizontal plane and the radius of the spiral.

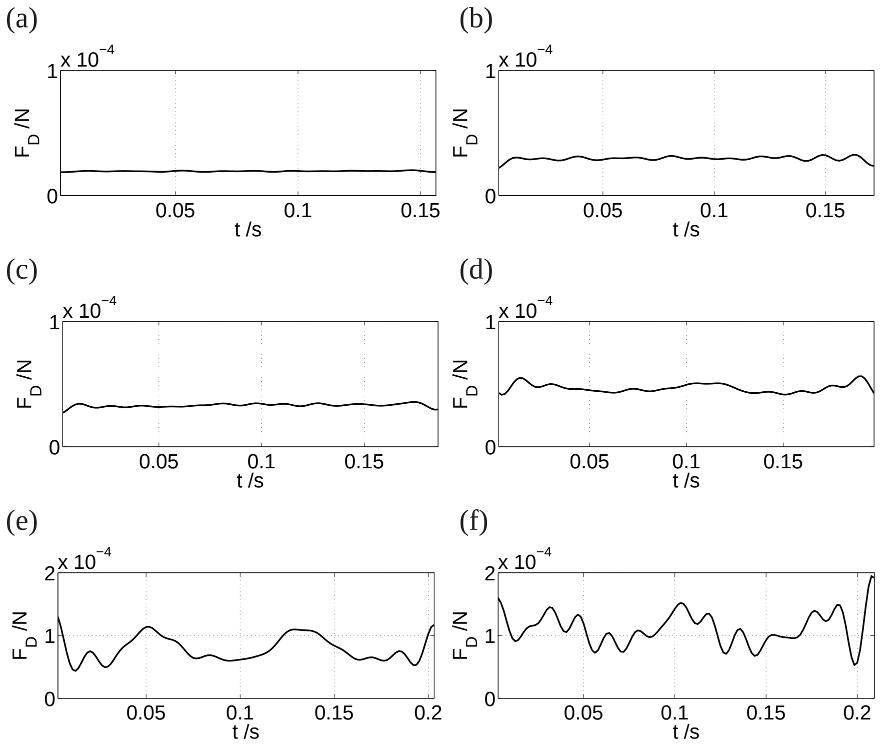

Figure 7.8: Drag force acting on the bubbles. Notice the different scales of the F_D-axis. See table 7.1 for further details.

Figure 7.8 shows the drag force acting on the bubble. The drag force increases with increasing bubble diameter. For the flattened spiraling motion the drag force becomes unsteady. For bubbles rising with shape oscillations the oscillations slightly change the bubble dynamics, but the general characteristics of non-oscillating bubbles remain.

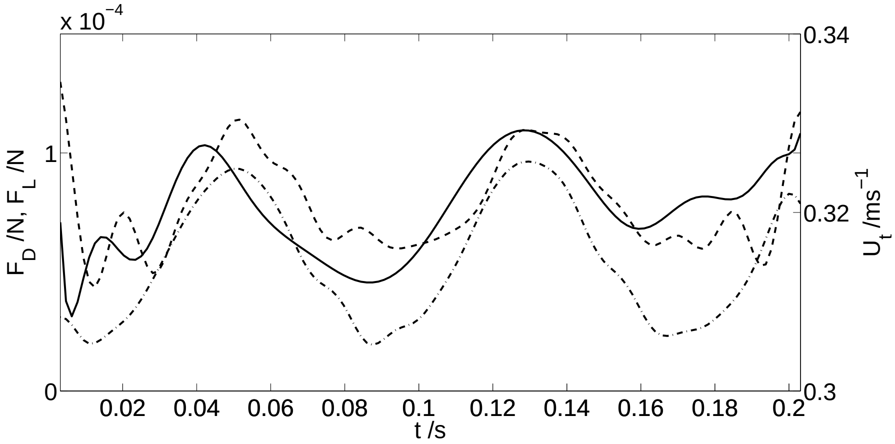

Figure 7.9: - - Drag force, and · — · lift force (left axis), and – tangential velocity (right axis). See table 7.1 for further details (sub-figure (*e*)).

Figure 7.9 shows the drag, lift, and velocity for the bubble from sub-figure (*e*) in the previous figures. As is also the case for rising light spheres (see chapter 4), the maxima for the drag and lift acting on the bubble do not coincide with maxima in the velocity at the outer positions of the bubble path; the drag force is out of phase with the velocity. Hence, the generally used drag relation

$$F_D \sim U^2 \tag{7.26}$$

is not suitable. In section 7.4 the drag will be studied in more detail and a model for it will be introduced that reflects this phase difference. For a more thorough discussion of the lift force in the case of pure zigzagging motion and on the phase difference between lift and velocity the reader is referred to section 4.4, dealing with rising light spheres.

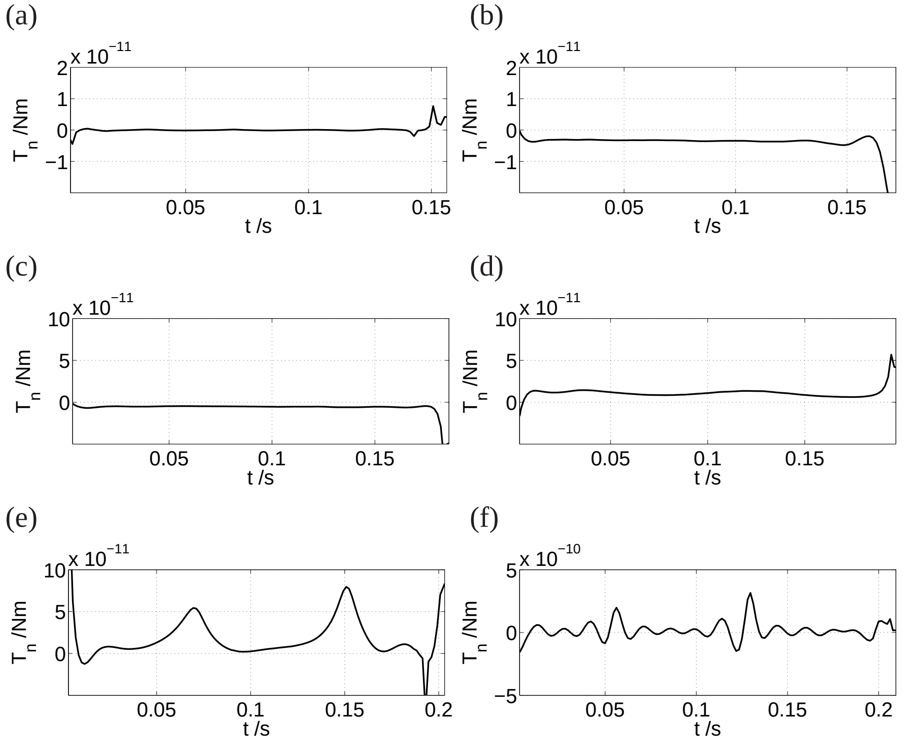

Figure 7.10: Torque acting on the bubbles around the normal. Notice the different scales of the T_n-axis. See table 7.1 for further details.

The torque

Figure 7.10 shows the torque around the normal vector, which is zero for a rectilinearly rising bubble. For the spiraling bubbles the torque is non-zero and constant and its sign depends on the clock- or counter-clockwise motion as was also the case for the lift force in the bi-normal direction (see figure 7.7). For the bubble rising along a flattened spiral the torque shows a peak right in between the maxima of the bubble path; this can also be seen in figure 7.12 (*a*) which shows the top view of the bubble path with the torque around the normal indicated by gray values. This behavior for a flattened spiral can be explained by looking at (7.20) and figure 7.11, which shows the curvatures κ and τ for the bubble from sub-figure (*e*). When the path is almost rectilinear, right in between the maxima of the bubble path, the curvature κ approaches zero and the torsion τ drops rapidly. For a pure zigzag the negative peak in the torsion will be infinite, because the normal vector will change

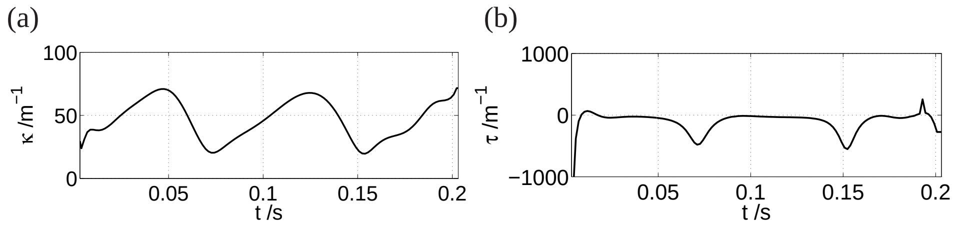

Figure 7.11: Path curvature and torsion for case (*e*). Figure (*a*) shows curvature κ and figure (*b*) shows torsion τ. See table 7.1 for further details (sub-figure (*e*)).

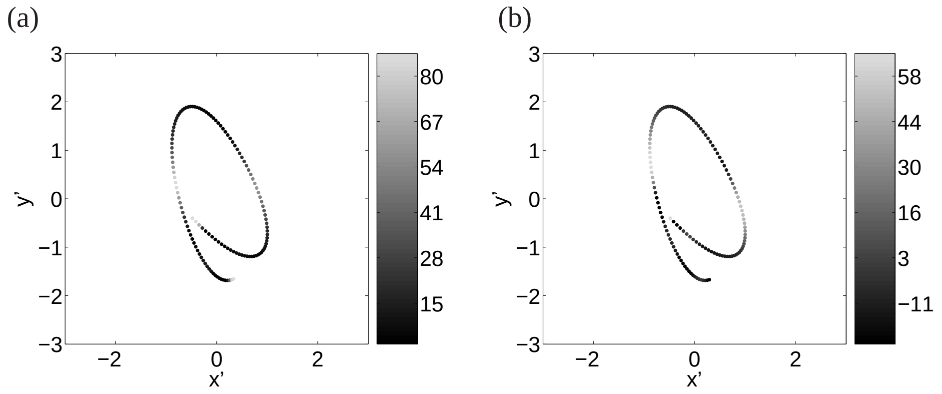

Figure 7.12: Top views of rising bubble for case (*e*). The gray values represent the torque in normal direction (figure (*a*)) and in bi-normal direction (figure (*b*)), respectively. The numbers next to the figure give the corresponding value in $\times 10^{-12}$Nm. See table 7.1 for further details (sub-figure (*e*)).

sign instantly when the zigzagging bubble passes the zigzag centerline. The same feature is still present for a bubble with shape oscillations, where the motion consists of a high frequency caused by shape oscillations and a low frequency equal to twice the path frequency (see figure 7.10 (*f*)).

Figure 7.13 shows the torque around the bi-normal vector, which remains zero as long as the motion is steady. In figure 7.13(*e*) the motion is unsteady; both the curvature and the velocity of the bubble are maximal at the outer positions of the flattened spiraling motion. The torque is related to the time derivative of the product of curvature and velocity (see (7.20)); it is therefore maximal between the position of maximum and minimum curvature, which can also be seen in figure 7.12 (*b*).

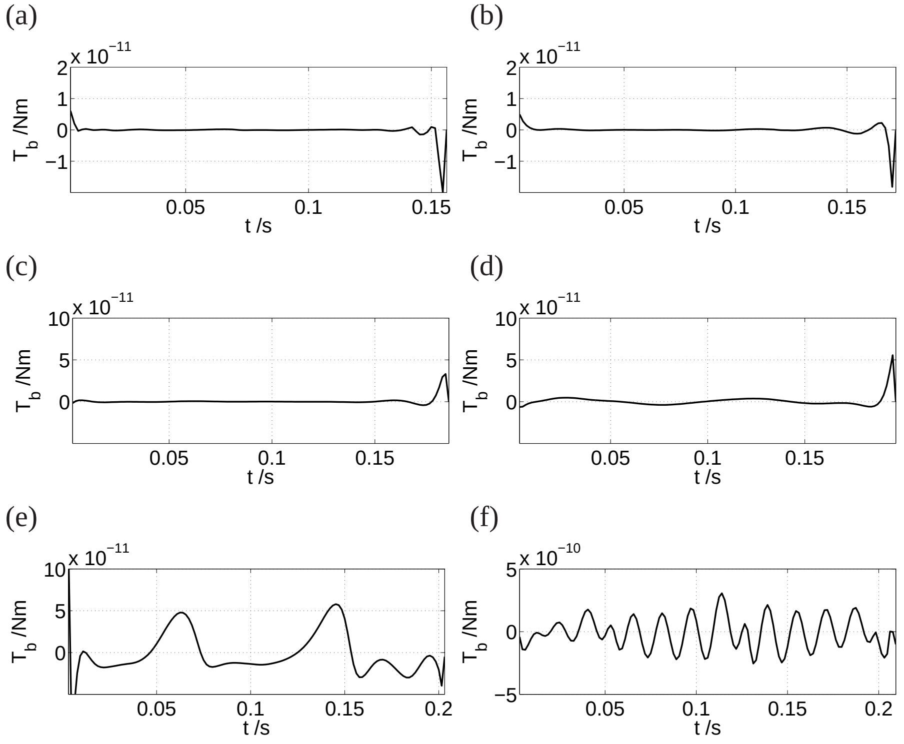

Figure 7.13: Torque acting on the bubbles around the bi-normal. Notice the different scales of the T_b-axis. See table 7.1 for further details.

For a bubble with shape oscillations (figure 7.13 (*f*)) this behavior is hardly visible; now the torque is dominated by the oscillations.

This section showed the calculated ’extraneous’ forces and torques acting on the bubbles, which are due to the vorticity in the flow. To understand the effect of this vorticity first the vorticity field behind the bubble is discussed in the next section. Thereafter the relation between the vorticity field and the calculated forces is analyzed.

sub-figure	D_{eq}/mm	χ	Re	description
(*a*)	1.3	1.4	546	rectilinear path
(*b*)	1.5	1.5	614	spiral path
(*c*)	2.0	1.6	797	spiral path
(*d*)	2.2	1.6	886	spiral path
(*e*)	2.5	1.8	980	flattened spiral path
(*f*)	2.8	1.9	1062	flattened spiral, shape oscillations

Table 7.2: Overview of Schlieren experiments with oblate ellipsoidal bubbles. The sub-figure numbers refer to the numbers of the sub-figures in section 7.3.3. The last experiment shows an oscillating bubble as introduction to the next chapter.

7.3.3 Bubble wake

The experiments described in the previous section have been done without using the Schlieren technique. In this way there is a better control of the water properties. In this section the wake of the bubble is our main interest. In order to visualize the wake structures a constant vertical temperature gradient of 1.0 Kcm^{-1} is imposed on the water in the water tank. The temperature in the recorded field of view (7 cm vertical distance) increases from 25^{o}C at the bottom to 32^{o}C at the top. This results in a difference in the viscosity of the water between top and bottom of approximately 14%. The density and surface tension are hardly effected by this change in temperature; 0.20% for the density and 1.5% for the surface tension. More details on the Schlieren technique can be found in chapter 2.

In this section the bubble wakes of six representative bubbles are shown. The bubble trajectories are more or less similar to the six bubbles presented in the previous sections. The path instability sets in at an equivalent diameter of 1.5 mm, which is lower than the 1.72 mm for the non-Schlieren experiments. The reason for this is the lower viscosity of the fluid as was also explained in chapter 6 with respect to the experimental data of de Vries [12]. Shape oscillations set in at 2.8 mm, which is in agreement with the non-Schlieren experiments. This was expected, because the shape oscillations are driven by surface tension, which is hardly affected by the temperature gradient.

Figure 7.14 shows the wake structures behind the bubble. The visibility of the wake strongly depends on the amount of distortion of the flow field. Therefore the wake is better visible for the larger bubbles. Increasing the temperature gradient might solve this problem, but this is hard to establish, because the temperature gradient is affected by the thermal conductivity of the system. The amount of heat at the top of the water tank was increased; this created a layer of warm water of almost constant temperature at the top of the water tank, but hardly affected the temperature gradient in the measurement section. Furthermore, a higher temperature gradient changes the water properties even more, leading to larger deviations in rise velocity compared to experiments without the use of Schlieren. De Vries performed a calculation to investigate the effect of the temperature gradient on the rise velocity of the bubble [12, Ch. 3, § 3, p. 10-23]. He used an empirical relation for the temperature dependent viscosity and solved the equations of motion with Levich's expression for the drag on the bubble (see also (7.80) in appendix B). He showed that not only the increase of the temperature influenced the rise velocity, through a drop in viscosity, but also the temperature gradient. In his calculation he simulated a 2 mm diameter bubble with an initial velocity of 0.328 ms^{-1} in a temperature field starting at 20 ^{o}C with a gradient of 1.1 Kcm^{-1}. The terminal rise velocity was 6% higher than the rise velocity for the case with a constant temperature of 28 ^{o}C.

Figure 7.14 shows that the straight rising bubbles have an axisymmetric wake. The wake becomes double-threaded when the path instability sets in. As stated before, the shape oscillations set in at an equivalent diameter of 2.8 mm. Already at an equivalent diameter of 2.5 mm the wake becomes unstable at the outer positions of the somewhat flattened bubble path; the shape of the bubble is not influenced by these instabilities in the wake. The presence of wake oscillations without shape oscillations suggests that the wake oscillations trigger shape oscillations when the bubbles are large enough, and not vice versa.

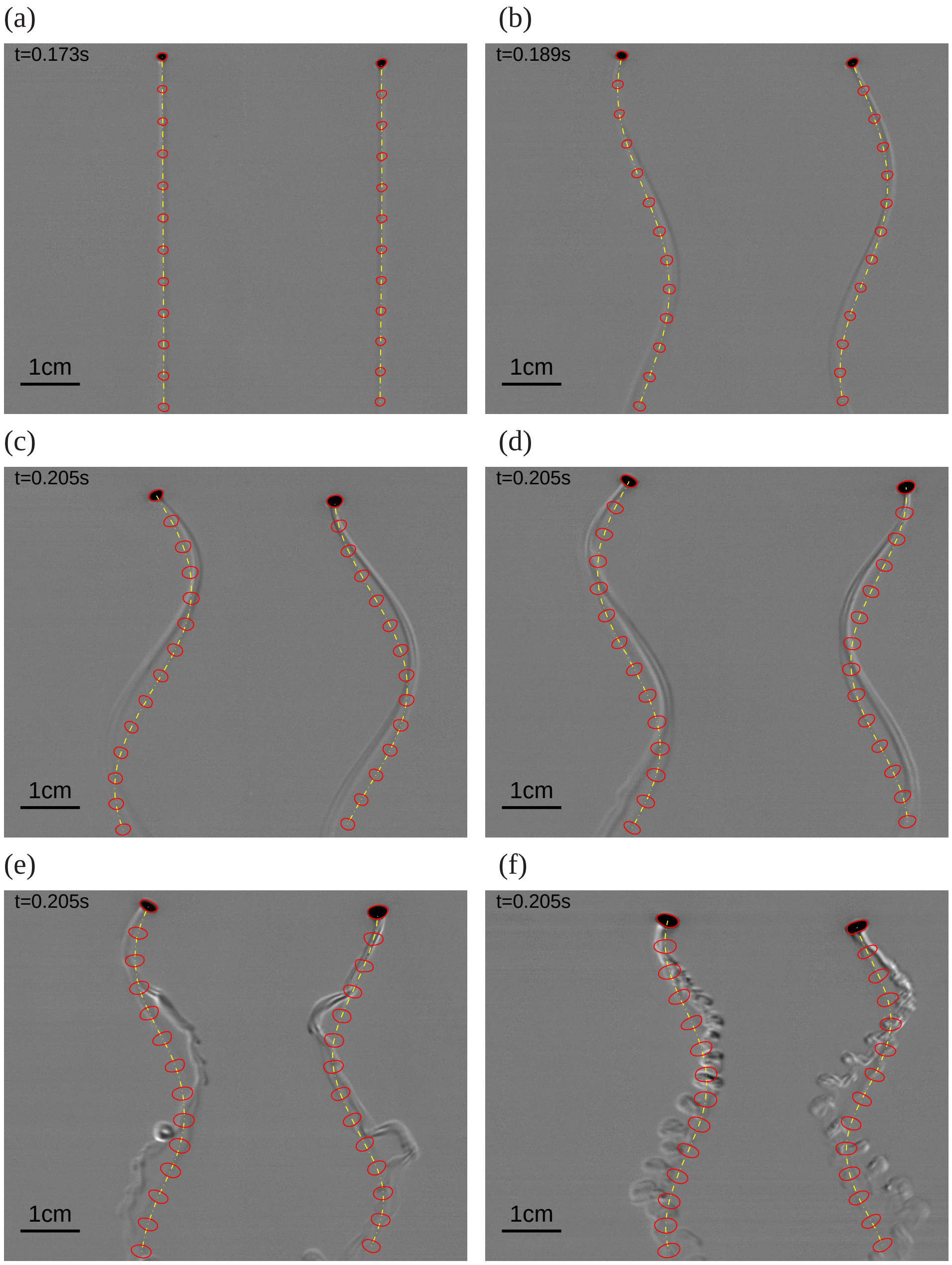

Figure 7.14: Stereoscopic Schlieren images of bubbles with their paths: dash-dotted line and bubble shape: solid line. Images are recorded with 640 frames/s. The bubble shapes are plotted every 10 frames, giving a time interval of 0.64 s between the bubble shapes. The elapsed time starting from the first bubble shape is indicated in the upper left corner. The Reynolds numbers are (*a*) 546, (*b*) 614, (*c*) 797, (*d*) 886, (*e*) 980, and (*f*) 1062. See table 7.2 for further details.

7.4 A model for lift and drag

This section deals with the influence of the vorticity field behind the bubble on the bubble motion. What is the relation between the structure and orientation of the vorticity field and the vortex flow forces acting on the bubble? In section 7.3.2 the vortex flow forces have been identified. Section 7.3.3 provided us with a clear view on the vorticity structure behind the bubble. With this knowledge a model is constructed for the vorticity behind the bubble and several aspects with respect to the generated forces are explained.

7.4.1 Vorticity structure behind the bubble

The Schlieren pictures reveal a double-threaded wake behind bubbles moving in a pure spiral. It is well-known that these two counter-rotating vortex threads give rise to a force perpendicular to a local plane immediately behind the bubble in which the two vortex threads are positioned, the vortex plane [e.g. 9]. We say 'local plane' because the vortex threads are curved and only locally a plane tangent to these vortex threads can be defined. To calculate the contribution of the force in the three main directions (tangential, normal and bi-normal) the orientation of the vortex plane and the strength of the vortex threads is necessary. Therefore the Schlieren images will be studied in more detail.

Consider a double-threaded wake behind a bubble. Depending on the angle between the vortex plane and the line of sight the distance between the two vortex threads varies between a maximum distance and zero (then the two vortex threads are overlapping in the particular view). Figure 7.15 shows a sequence of three images (A to C) of one side view of a spiraling bubble with two vortex threads accentuated by white lines. The sequence starts with a maximum distance between the two vortex threads and ends with zero distance. The middle image is taken when the bubble reached its outer position of the spiraling path in this side view. The left and right images are taken $\frac{1}{8}$ path oscillation period before and after, respectively.

Now consider figure 7.16, which gives a schematic top view on the bubble and its path. The positions A, B, and C are marked and the vortex threads are represented as circles or dots, depending on the clock or counter clockwise rotation of the vortex thread. The images of figure 7.15 were taken in YZ-direction. Recalling that in position A the distance between the two vortex threads was maximal and in position C zero, it is seen that the vortex plane is orientated under an angle ψ_1 of 45^o with the bi-normal.

The normal vector for a pure spiral is oriented in a horizontal plane towards the center of the spiral; the bi-normal vector is orientated along the spiral envelope.

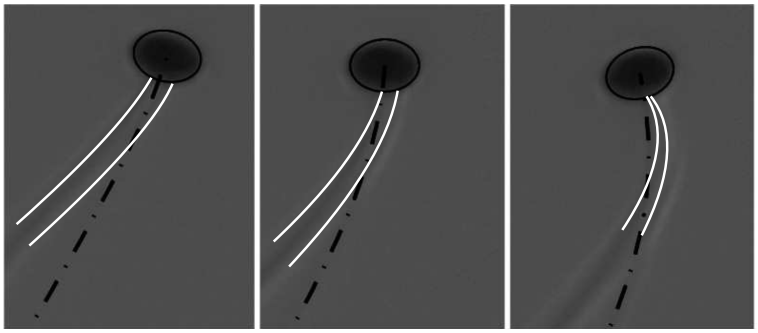

Figure 7.15: Spiraling bubble; left image: largest distance between vortex threads, middle image: smaller distance, right image: zero distance. The positions of the bubble in the images agree with positions A, B, and C in figure 7.16, respectively. The middle image is taken when the bubble reached its outer position of the spiraling path in this side view. The left and right images are taken $\frac{1}{8}$ path oscillation period before and after, respectively. The dash-dotted line marks the path of the bubble. The white lines are accentuated vortex threads.

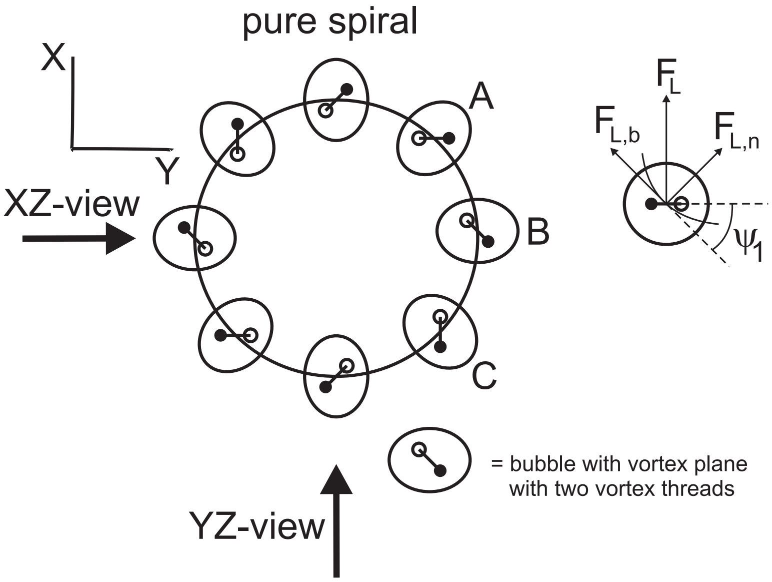

Figure 7.16: Sketch top view spiraling bubble. The positions A, B, and C correspond to the images in figure 7.15 from left to right, respectively. Right image: angle ψ_1 between the vortex plane and the bi-normal.

Because the angle ψ_1 is 45^o, the lift force in normal and bi-normal direction should be equal for a pure spiral. Recall figure 7.7 (*b*) and (*c*), which show that the lift forces in normal and bi-normal direction are indeed equal, confirming the observations with respect to the orientation of the two vortex threads.

The second orientation angle of the vortex plane ψ_2 is an angle between the vortex plane and the tangential direction. Although a direct link can be made with the analysis of the vortex structure behind rising light spheres in chapter 4, the present case differs in two aspects: (*i*) the bubble path is a spiral instead of more flattened spirals/zigzags for the rising spheres, (*ii*) the bubble wake consists of two stable vortex threads instead of the unstable, turbulent sphere wake. Therefore the approach to calculate the orientation angle ψ_2 is slightly different. Recall that, in chapter 4, this angle is called ψ_a.

The angle ψ_2 of the vortex plane with the tangent vector can be extracted from the last image of figure 7.15 in which the two vortex threads overlap. So in the YZ-view we have two overlapping vortex threads and in the XZ-view the distance between the two threads is maximal. Hence the normal vector of the vortex plane has no component in X-direction and the Y- and Z-component can easily be extracted from the YZ-view. Knowing the normal vector to the vortex plane, we can easily calculate the angle between the vortex plane and the tangent vector, by simply projecting the tangent vector onto the vortex plane. The angle ψ_2 can be calculated from

$$\mathbf{t} \cdot \mathbf{t_p} = |\mathbf{t}||\mathbf{t_p}| \cos \psi_2, \qquad (7.27)$$

where $\mathbf{t_p}$ is the projection of the tangent vector onto the vortex plane. The angle ψ_2 is 21^0.

7.4.2 Generated lift

Consider a vorticity field consisting of N closed vortex tubes. The force generated on the bubble by this vorticity field is [2]

$$F = -\rho \frac{d}{dt} \left(\sum_N \Gamma_N \int n_i dA_N \right), \qquad (7.28)$$

where Γ_N is the circulation and $\int n_i dA_N$ is the projected area in the i-direction of vortex tube N. Now assume the two vortex threads, which are connected at the moment they are generated, to resemble one closed vortex tube. The rate of change of the projected area in the direction normal to the vortex plane is

$$d \int n dA_N = lU dt, \qquad (7.29)$$

with l the distance between the vortex threads, which we assume to be constant and U is the velocity of the bubble in the direction of the vortex plane. Hence

$$U = U_t \cos\psi_2, \tag{7.30}$$

with U_t the tangential velocity of the bubble. The vortex flow force induced by two vortex threads is

$$F_\Omega = \rho_l \Gamma l U_t \cos\psi_2. \tag{7.31}$$

The circulation Γ can be estimated from the velocity induced by one vortex thread in the other vortex thread. Van Wijngaarden [14] studied the effect of trailing vortices behind bubbles on the bubble velocity. He gives an expression for the velocity induced by one vortex thread in the other, perpendicular to the vortex plane, as function of the distance x behind the bubble (his expression (3.13))

$$U_f = \frac{\Gamma}{4\pi l}\left(1 + \sqrt{1 + \frac{l^2}{x^2}}\right). \tag{7.32}$$

From the Schlieren images the induced velocity can be extracted from the motion of the vortex threads. Here we focus on the motion of the vortex threads some diameters behind the bubble. The distance between the vortex threads is approximately half the bubble diameter. Typically, l/x is approximately 0.02 and the induced velocity becomes

$$U_f \approx \frac{\Gamma}{2\pi l}, \tag{7.33}$$

as if the two vortex threads were infinite at both ends. Hence,

$$\Gamma \approx 2\pi U_f l, \tag{7.34}$$

where the distance l and the self-induced velocity U_f can be extracted from the Schlieren images. For a spiraling bubble of 1.9 mm diameter typical values are l =0.52 mm and U_f =3.0 cm/s, which is in nice agreement with De Vries [12], who gives 0.6 mm and 3.0 cm/s for a bubble of 2.0 mm diameter.

The lift force acting on the bubble is

$$F_l = F_\Omega \cos\psi_2. \tag{7.35}$$

Figure 7.17 shows the reconstructed lift force and the modelled lift force for a spiraling bubble: the agreement is clear.

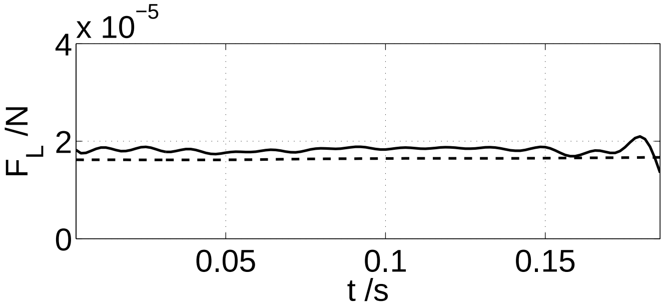

Figure 7.17: – measured lift, - - modelled lift. See table 7.1 for further details (subfigure (*c*)).

7.4.3 Lift-induced drag

The drag experienced by the bubble is related to vorticity in the boundary layer of the bubble, creating a viscous contribution to the drag. Furthermore the shed vorticity, consisting of the two vortex threads, can create a so-called ’lift-induced’ drag. Because the angle ψ_2 is non-zero the vortex flow force induced by the two vortex threads will have a component in tangential direction, this is the ’lift-induced’ drag (recall the discussion in chapter 4 on this subject). The lift-induced drag can be written as

$$F_{d,ind} = F_\Omega \cos\psi_2. \tag{7.36}$$

The two vortex threads will also induce a velocity in the boundary layer; they have an influence on the vorticity in the boundary layer and therefore on the viscous contribution to the drag. Typical velocities in the boundary layer are of the order of the bubble velocity. The previous section, on generated lift, showed that the velocities induced by the two vortex threads are of the order of 10% of the bubble velocity. Therefore it is assumed that the contribution of the velocity induced by the vortex threads in the boundary layer are negligible. The viscous contribution is modelled as if the boundary layer is equal to the boundary layer around a rectilinearly rising bubble. The viscous drag can now be modelled with Moore’s drag [10] and is given by a combination of (7.80), (7.81) and (7.83) in appendix B

$$F_{D,visc} = 6\pi\mu U^2 D_{eq} G(\chi) \tag{7.37}$$

with

$$G_z(\chi) = \frac{1}{3}\chi^{4/3}(\chi^2-1)^{3/2}\frac{(\chi^2-2)\sec^{-1}(\chi)+\sqrt{\chi^2-1})}{\left(\chi^2\sec^{-1}(\chi)-\sqrt{\chi^2-1}\right)^2}.$$

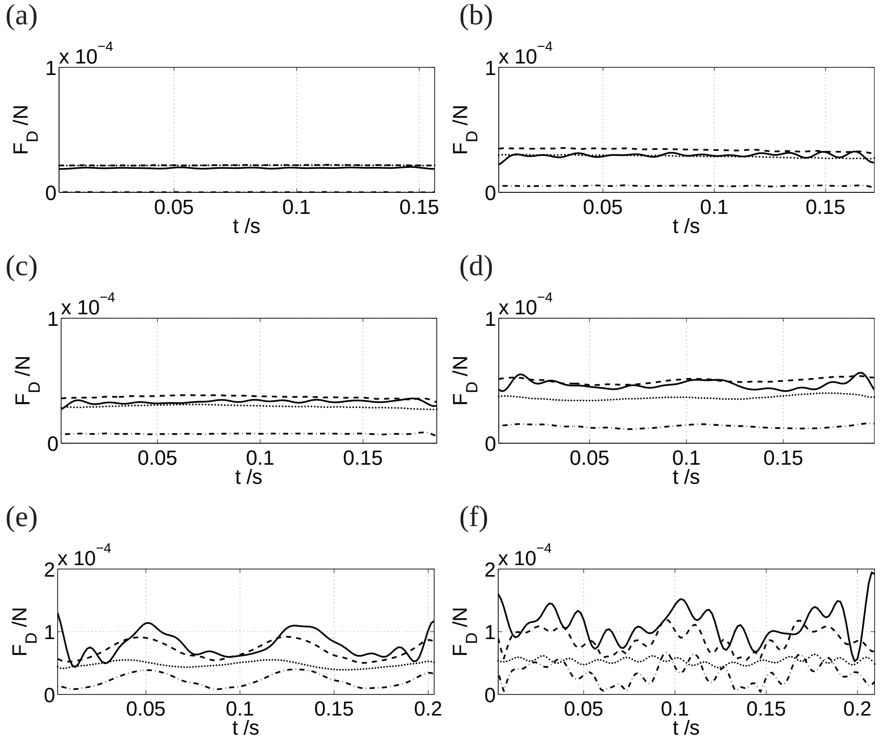

Figure 7.18: Drag force acting on the bubbles. – measured drag, - - modelled drag, · — · lift-induced drag, and ·· viscous drag. Notice the different scales of the F_D-axis. See table 7.1 for further details.

The total drag on the bubble can be modelled with

$$F_D = F_{D,visc} + F_{D,ind}. \tag{7.38}$$

The same approach can be used to estimate the drag on larger bubbles, for which the bubbles rise along more flattened spirals and thus the motion is unsteady. The Schlieren experiments showed that the angle ψ_2 varies from 21 to 24^o, which gives rise to a maximal difference of 2% in the lift-induced drag. Because the wake is not visualized in the non-Schlieren experiments the angle ψ_2 is set to 22.5^o.

Figure 7.18 shows the modelled drag (dashed lines) and its components the induced drag (dash-dotted line) and the viscous drag (dotted line). The agreement with the measured drag (the solid line) turns out to be rather good, even for the bubble with shape oscillations. For the purely spiraling bubbles the induced drag is approximately 20% of the modelled drag. The induced drag becomes more important when the bubble rises in an unsteady motion, because then the lift force, hence the induced drag, has large-amplitude oscillations.

While this approach to drag supports the view of the mechanisms that govern the generation of flow-induced forces on the bubbles, it also suggests that any variations in the viscous contribution to the drag associated with the ‘building-up’ of the vorticity field by diffusion and convection, and important at low Reynolds numbers, are negligible at high Reynolds numbers, as was also the case for light rising spheres (see chapter 4).

7.5 Conclusion

In this chapter we focussed on rising bubbles of fixed shape. The bubbles rise with their minor axis aligned with the path, as was also observed by Ellingsen & Risso [5]. Right after the onset of path instability the bubbles rise in a pure spiral, whereas for somewhat larger bubbles the path becomes flattened and the motion becomes unsteady. The largest bubble discussed in this chapter performed shape oscillations.

For the purely spiraling bubbles the lift forces in normal and bi-normal direction are equal, a feature which has not been reported before in an experimental study. Analysis of the orientation of the vortex plane behind a spiraling bubble confirms this equality of lift in normal and bi-normal direction. Implementing this feature into the equations of motion for a purely spiraling bubble gives a simple relation between the characteristics of the spiral and the shape of the bubble. Depending on the rotation, clock- or counterclockwise, the lift force in bi-normal direction is either positive or negative. Furthermore the lift in bi-normal direction vanishes for zigzagging bubbles.

Analysis of the vorticity structure behind spiraling bubbles reveals that the wake consists of two counter-rotating vortex threads, which account for the lift necessary to curve the bubble path. Analysis of the strength of these threads enables us to estimate the lift force. The estimate is in good agreement with the experiments.

The drag experienced by the bubble is unsteady when the bubble moves in a flattened spiraling motion and is out-of-phase with the bubble velocity. The general approach that the drag scales with the bubble velocity squared does not hold. The reason for this is the instantaneous vorticity contribution to the drag, the lift-induced drag. For all bubbles performing path oscillations the orientation of the plane through these threads immediately behind the bubble are measured and the lift-induced drag is calculated. It is shown that the measured drag can be modelled correctly with a contribution related to viscous drag and a contribution related to the lift-induced drag, which is induced instantaneously.

Appendix A: General equations of motion

This appendix deals with the calculation of the equations of motion for a rising oblate ellipsoidal bubble.

Impulsive wrench
Consider the general case of a body translating and rotating in a fluid in 3D [6]. The flow potential of such a system can be written as

$$\Phi = u\phi_1 + v\phi_2 + w\phi_3 + p\chi_1 + q\chi_2 + r\chi_3. \tag{7.39}$$

The linear and angular velocity of the body are

$$\mathbf{U} = (u, v, w)^T \text{ and } \mathbf{\Omega} = (p, q, r)^T . \tag{7.40}$$

The kinetic energy (T) of the system is

$$2T = (\mathbf{N}_T \cdot \mathbf{U}) \cdot \mathbf{U} + (\mathbf{N}_R \cdot \mathbf{\Omega}) \cdot \mathbf{\Omega} + (\mathbf{N}_{TR} \cdot \mathbf{U}) \cdot \mathbf{\Omega}. \tag{7.41}$$

Here the subscript $'T'$ denotes *translation* and $'R'$ *rotation*. The coefficients of the matrices are determined by the shape and position relative to the local coordinate frame.

The linear and angular impulse of the system are

$$\mathbf{I} = \left\{ \frac{dT}{du}, \frac{dT}{dv}, \frac{dT}{dw} \right\}^T = \mathbf{N}_T \cdot \mathbf{U} + \mathbf{N}_{TR} \cdot \mathbf{\Omega} \tag{7.42}$$

and

$$\mathcal{A} = \left\{ \frac{dT}{dp}, \frac{dT}{dq}, \frac{dT}{dr} \right\}^T = \mathbf{N}_R \cdot \mathbf{\Omega} + \mathbf{N}_{TR} \cdot \mathbf{U}. \tag{7.43}$$

For an oblate spheroid with main axes coinciding with the local frame the linear and angular impulse become

$$\mathbf{I} = \begin{bmatrix} A & 0 & 0 \\ 0 & A & 0 \\ 0 & 0 & C \end{bmatrix} \cdot \begin{Bmatrix} u \\ v \\ w \end{Bmatrix} \text{ and } \mathcal{A} = \begin{bmatrix} Q & 0 & 0 \\ 0 & Q & 0 \\ 0 & 0 & 0 \end{bmatrix} \cdot \begin{Bmatrix} p \\ q \\ r \end{Bmatrix} . \tag{7.44}$$

It is clear that the calculation of the impulse of an oblate spheroid can best be done in a frame rotated such that the three axes of the ellipsoid coincide with the axes of the local frame (see figure 7.2). The coefficients A, C, and Q can be calculated with (7.72), (7.74), and (7.77) in the next appendix.

Equations of motion

The equations of motion with respect to a frame XYZ fixed in the laboratory for a massless bubble rising through a quiescent liquid are described by

$$\frac{\mathrm{d}\mathbf{I}}{\mathrm{d}t} = -\rho V \mathbf{g} + \mathbf{F}, \quad \frac{\mathrm{d}\mathcal{A}}{\mathrm{d}t} = \mathbf{T}. \tag{7.45}$$

Here $\mathbf{I}$ is the linear impulse of the irrotational fluid motion that would result if the motion of the bubble would be generated instantaneously from a state of rest; and in this respect $\mathcal{A}$ is the angular impulse. The density of the liquid is given by ρ; V is the volume of the bubble, and $\mathbf{g}$ the gravitational acceleration. The 'extraneous' force $\mathbf{F}$ and torque $\mathbf{T}$ are due to the presence of vorticity in the flow

The linear and angular impulse are best calculated in a frame, rotating with the body (the $'x'y'z'$-frame in figure 7.2) as we saw in the previous discussion, but the equations of motion are related to the impulse in the XYZ-frame. The relation between a vector in XYZ-frame and $'x'y'z'$-frame is

$$\mathbf{X} = \mathbf{R} \cdot \mathbf{x}'. \tag{7.46}$$

The time derivative of this vector is

$$\begin{aligned} \frac{\mathrm{d}\mathbf{X}}{\mathrm{d}t} &= \mathbf{R} \cdot \frac{\mathrm{d}\mathbf{x}'}{\mathrm{d}t} + \frac{\mathrm{d}\mathbf{R}}{\mathrm{d}t} \cdot \mathbf{x}' \qquad (7.47) \\ &= \mathbf{R} \cdot \frac{\mathrm{d}\mathbf{x}'}{\mathrm{d}t} + \mathbf{R} \cdot \mathbf{R}^T \cdot \frac{\mathrm{d}\mathbf{R}}{\mathrm{d}t} \cdot \mathbf{x}' = \mathbf{R} \cdot \left(\frac{\mathrm{d}\mathbf{x}'}{\mathrm{d}t} + \mathbf{R}^T \cdot \frac{\mathrm{d}\mathbf{R}}{\mathrm{d}t} \cdot \mathbf{x} \right). \end{aligned}$$

As the rotation matrix is orthogonal the following holds

$$\frac{\mathrm{d}}{\mathrm{d}t}\mathbf{R} \cdot \mathbf{R}^T = 0 \rightarrow \mathbf{R} \cdot \frac{\mathrm{d}\mathbf{R}^T}{\mathrm{d}t} = -\frac{\mathrm{d}\mathbf{R}}{\mathrm{d}t} \cdot \mathbf{R}^T. \tag{7.48}$$

Hence the term $\mathbf{R}^T \cdot \frac{\mathrm{d}\mathbf{R}}{\mathrm{d}t}$ is an anti-symmetric matrix which consists of the angular velocities of the rotating body frame

$$\mathbf{R}^T \cdot \frac{\mathrm{d}\mathbf{R}}{\mathrm{d}t} = \begin{bmatrix} 0 & -\Omega_z & \Omega_y \\ \Omega_z & 0 & -\Omega_x \\ -\Omega_y & \Omega_x & 0 \end{bmatrix}. \tag{7.49}$$

Hence

$$\frac{\mathrm{d}\mathbf{X}}{\mathrm{d}t} = \mathbf{R} \cdot \left(\frac{\mathrm{d}\mathbf{x}'}{\mathrm{d}t} + \mathbf{\Omega} \times \mathbf{x}' \right), \tag{7.50}$$

where the angular velocity vector, in terms of the time derivatives of the rotation angles, is

$$\mathbf{\Omega} = \left(\dot{\alpha} \cos \beta, \dot{\beta}, \dot{\gamma} \sin \beta \right). \tag{7.51}$$

If the XYZ-frame and the $x'y'z'$-frame are overlapping at the time the time derivative is calculated, or for infinitesimal rotation, the rotation matrix $\mathbf{R}$ will be the identity matrix, resulting in

$$\frac{\mathrm{d}\mathbf{X}}{\mathrm{d}t} = \frac{\mathrm{d}\mathbf{x}'}{\mathrm{d}t} + \mathbf{\Omega} \times \mathbf{x}. \tag{7.52}$$

The time derivative of the linear impulse of the system can now be transformed from $x'y'z'$-frame to XYZ-frame by

$$\frac{\mathrm{d}\mathbf{I}_{XYZ}}{\mathrm{d}t} = \frac{\mathrm{d}\mathbf{I}_{x'y'z'}}{\mathrm{d}t} + \mathbf{\Omega} \times \mathbf{I}_{x'y'z'}. \tag{7.53}$$

Now the general form of the equations of motion in the $x'y'z'$-frame is

$$\frac{\mathrm{d}\mathbf{I}}{\mathrm{d}t} + \mathbf{\Omega} \times \mathbf{I} = -\rho V \mathbf{g} + \mathbf{F}, \tag{7.54}$$

$$\frac{\mathrm{d}\mathcal{A}}{\mathrm{d}t} + \mathbf{\Omega} \times \mathcal{A} = \mathbf{T}, \tag{7.55}$$

with $\mathbf{\Omega}$ the rotation of the bubble, hence the rotation of the $x'y'z'$-frame, and $\mathbf{U}$ the velocity of the bubble. Notice that the $\mathbf{U} \times \mathbf{I}$-term as it is present in the equations of Mougin & Magnaudet [11] only appears if one also accounts for a translation of the local axes. Finally the forces and torques are projected onto the Frenet frame, which was introduced in section 7.3.2.

In section 7.3.2 it is mentioned that the equations of motion are solved using the observation that the minor axis and the tangent vector coincide; this resulted in (7.19) and (7.20). That method and the method described in this appendix give identical results for the forces and torques; this justifies the assumption that the bubble minor axis and the tangent vector coincide.

Notice that for the oblate ellipsoidal bubble the angular velocity vector in terms of the time derivatives of the rotation angles (γ=0, because no rotation around the symmetry axis can be detected)

$$\mathbf{\Omega} = \left(\dot{\alpha} \cos \beta, \dot{\beta}, 0 \right) \tag{7.56}$$

is related to the angular velocity of the Frenet frame

$$\mathbf{\Omega} = \frac{\mathrm{d}s}{\mathrm{d}t}\left[-\tau\mathbf{t} + \kappa\mathbf{b}\right]. \tag{7.57}$$

Projecting $\dot{\alpha}\cos\beta$ and $\dot{\beta}$ onto the normal and bi-normal directions indeed results in a bi-normal contribution equal to $ds/dt\ \kappa$ only. Although the minor axis and the tangent vector coincide the rotation around the minor axis is not detected properly. This has no consequence for the bubble dynamics because the bubble is axisymmetric around this axis.

Appendix B: Irrotational flow around oblate spheroids

This appendix deals with the irrotational flow around oblate spheroids. First the ellipsoidal coordinate system will be introduced, followed by the velocity potential for the flow around oblate spheroids. From these flow potentials the virtual momentum and dissipation will be calculated.

Ellipsoidal coordinate system

An orthogonal coordinate system can be described by

$$x = (q_1, q_2, q_3), \quad y = (q_1, q_2, q_3), \quad z = (q_1, q_2, q_3)$$

$$h_i^2 = \left(\frac{\partial x}{\partial q_i}\right)^2 + \left(\frac{\partial y}{\partial q_i}\right)^2 + \left(\frac{\partial z}{\partial q_i}\right)^2, \quad \frac{\partial}{\partial q_i} = \frac{1}{h_i}\frac{\partial}{\partial q_i}, \quad i = 1, 2, 3. \tag{7.58}$$

Here, h_i are the so-called metric coefficients.

To describe the fluid motion around oblate spheroids an orthogonal system of coordinates (μ, θ, φ) is used; this system is related to a cartesian system (x, y, x) by

$$\begin{aligned} x &= k\cosh\mu\sin\theta\cos\varphi \\ y &= k\cosh\mu\sin\theta\sin\varphi \\ z &= k\sinh\mu\cos\theta, \end{aligned} \tag{7.59}$$

where μ is the variable perpendicular to the surface of the ellipsoid, θ the variable tangent to the surface, φ the angle around the symmetry axis, and $k = \sqrt{b^2 - c^2}$. Surfaces $\mu =$ constant, μ_0 say, are the family of oblate spheroids

$$\frac{x^2 + y^2}{b^2} + \frac{z^2}{c^2} = 1, \tag{7.60}$$

with major and minor axes given by

$$b = k\cosh\mu_0, \quad \text{and} \quad c = k\sinh\mu_0, \tag{7.61}$$

respectively; their ratio is

$$\chi = b/c = \coth\mu_0.$$

The metric coefficients h_μ, h_θ and h_φ for the ellipsoidal coordinates are

$$\begin{aligned} h_\mu &= h_\theta = k\big(\sinh^2\mu + \cos^2\theta\big)^{\frac{1}{2}} \\ h_\varphi &= k\cosh\mu\sin\theta. \end{aligned} \tag{7.62}$$

Velocity potential

The velocity potential Φ can be calculated from the Laplace equation:

$$\begin{aligned} &\frac{1}{k^2(\sinh^2\mu + \cos^2\theta)\cosh\mu}\frac{\partial}{\partial\mu}\left(\cosh\mu\frac{\partial\Phi}{\partial\mu}\right) \\ &+\frac{1}{k^2(\sinh^2\mu + \cos^2\theta)\sin\theta}\frac{\partial}{\partial\theta}\left(\sin\theta\frac{\partial\Phi}{\partial\theta}\right) + \frac{1}{k^2\cosh^2\mu\sin^2\theta}\frac{\partial^2\Phi}{\partial\varphi^2} = 0. \end{aligned} \tag{7.63}$$

Lamb [6] shows by separation of variables that elementary solutions which vanish at infinity have the form

$$\begin{aligned} \Phi(\mu,\theta,\varphi) \;=\; &\sum_{n=0}^{\infty}\sum_{m=0}^{n} c_{nm} Q_n^m(\sinh\mu) P_n^m(\cos\theta)\ \cos m\varphi \\ &+\sum_{n=0}^{\infty}\sum_{m=1}^{n} d_{nm} Q_n^m(\sinh\mu) P_n^m(\cos\theta)\ \sin m\varphi. \end{aligned} \tag{7.64}$$

Here $P_n^m(\cos\theta)$ denotes the associated Legendre function,

$$P_n^m(\cos\theta) = \sin^m\theta\,\frac{\mathrm{d}^m}{\mathrm{d}(\cos\theta)^m}P_n(\cos\theta) \tag{7.65}$$

with $0 < m \leq n$ and $P_n(\cos\theta)$ being the Legendre function of order n [1]. The functions $Q_n^m(\sinh\mu)$ follow from

$$Q_n^m(\sinh\mu) = \cosh^m\mu\,\frac{\mathrm{d}^m}{\mathrm{d}(\sinh\mu)^m}Q_n(\sinh\mu), \tag{7.66}$$

where the $Q_n(\sinh\mu)$ ('irregular Legendre functions of imaginary argument') are defined through the relations

$$\begin{aligned} &Q_0 = \cot^{-1}(\sinh\mu), \qquad Q_1 = 1 - \sinh\mu\ \cot^{-1}(\sinh\mu), \\ &Q_n = -\left(\frac{2n-1}{n}\right)\sinh\mu\, Q_{n-1} + \left(\frac{n-1}{n}\right) Q_{n-2}. \end{aligned} \tag{7.67}$$

Translation along the minor axis

Consider the steady motion of an oblate spheroid with velocity W in the direction of the z'-axis, which coincides with the minor axis. The velocity potential for the motion of the ellipsoid, in a fixed reference frame with the origin instantaneously coinciding with the center of the ellipsoid, is [6]:

$$\Phi(\mu,\theta) = c_{10}\left[1 - \sinh\mu\ \cot^{-1}(\sinh\mu)\right]\cos\theta; \tag{7.68}$$

where, if the body surface is assumed to be specified by $\mu = \mu_0$,

$$c_{10}(\mu_0) = -\frac{Wk}{\cot^{-1}(\sinh\mu_0) - \sinh\mu_0/[1+\sinh^2\mu_0]}.$$

Translation along a major axis

For the motion in the plane normal to the minor axis, say the x-direction, with velocity U the velocity potential is [6]:

$$\Phi(\mu,\theta,\varphi) = -c_{11}\cosh\mu\left[\frac{\sinh\mu}{1+\sinh^2\mu} - \cot^{-1}(\sinh\mu)\right]\sin\theta\cos\varphi; \tag{7.69}$$

with

$$c_{11}(\mu_0) = \frac{Uk}{\cot^{-1}(\sinh\mu_0) - [\sinh^2\mu_0 + 2]/\{\sinh\mu_0[1+\sinh^2\mu_0]\}}.$$

Rotation about a major axis

Consider the rotation of an oblate spheroid about one of its major axes, say with angular velocity Ω around the x-axis. The velocity potential turns out to be:

$$\begin{aligned} \Phi(\mu,\theta,\varphi) \quad = \quad & d_{21}\cosh\mu\left[3\sinh\mu\cot^{-1}(\sinh\mu) - 3 + \frac{1}{1+\sinh^2\mu}\right] \\ & \sin\theta\cos\theta\sin\varphi, \end{aligned} \tag{7.70}$$

with

$$d_{21}(\mu_0) = \frac{k^2\Omega}{[6\sinh^2\mu_0 + 3]\cot^{-1}(\sinh\mu_0) - 6\sinh\mu_0 - \sinh\mu_0/[1+\sinh^2\mu_0]}.$$

Virtual momentum

From the velocity potential the virtual momentum can be calculated.

Translation along the minor axis

The virtual momentum of the ellipsoid is defined as

$$I_{Bz} = -\rho\int W dV = -\rho\int \nabla_z\Phi dV = -\rho\int \Phi n_z \,\mathrm{d}S. \tag{7.71}$$

On substituting the solution (7.68) for the velocity potential Φ and the expressions given in appendix C for the area of the surface element dS and the z-component of the normal to the surface it is found that

$$I_{Bz} = \rho\mathcal{V}WM_z,$$

with

$$M_z(\chi) = \frac{(\chi^2-1)^{\frac{1}{2}} - \cos^{-1}\chi^{-1}}{\cos^{-1}\chi^{-1} - (\chi^2-1)^{\frac{1}{2}}/\chi^2}. \tag{7.72}$$

Here $\chi = b/c$, is the aspect ratio of the oblate spheroid. Notice that A mentioned in (7.19) is equal to $\rho V M_z$.

Translation along a major axis

The virtual momentum of the ellipsoid is now defined as

$$I_{Bx} = -\rho\int \Phi n_x \,\mathrm{d}S. \tag{7.73}$$

Substituting the solution (7.69) for the velocity potential and the expressions given in appendix C for the area of the surface element dS and the x-component of the normal to the surface this becomes

$$I_x = \rho\mathcal{V}UM_x,$$

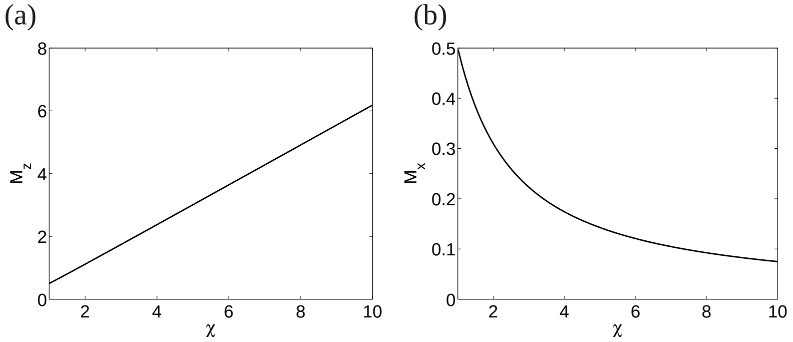

Figure 7.19: (*a*) $M_z(\chi)$ as function of χ, (*b*) $M_x(\chi)$ as function of χ.

with

$$M_x(\chi) = \frac{(\chi^2-1)^{\frac{1}{2}} - \chi^2\cos^{-1}\chi^{-1}}{\chi^2\cos^{-1}\chi^{-1} - [2\chi^2-1](\chi^2-1)^{\frac{1}{2}}}. \tag{7.74}$$

Figure 7.19 shows the plots of the factors M_z and M_x as a function of the aspect ratio of the bubble. The added mass increases with the aspect ratio for motion in the direction of the minor axis and decreases for motion in the direction of the major axis.

Rotation about a major axis

The virtual angular momentum of an ellipsoid rotating with angular velocity Ω about the x-axis is

$$A_x = -\rho\int \Phi\,[yn_z - zn_y]\,\mathrm{d}S. \tag{7.75}$$

Let a_e denote the equivalent radius of a sphere with equal volume, defined through

$$\mathcal{V} = \tfrac{4}{3}\pi a_e^3 = \tfrac{4}{3}\pi b^2 c. \tag{7.76}$$

Using the solution (7.70) for the velocity potential and the expressions given in appendix C for the area of the surface element dS and the y- and z-components of the normal to the surface one may then also write

$$A_x = \tfrac{4}{15}\pi\rho a_e^5\,\Omega\,R_x,$$

where

$$R_x(\chi) = \chi^{-\frac{4}{3}}(\chi^2-1)^{-1}\frac{(\gamma_0-\beta_0)}{2+[(\chi^2+1)/(\chi^2-1)](\beta_0-\gamma_0)} \tag{7.77}$$

with

$$\beta_0(\chi) = \frac{\chi^2 \cos^{-1}\chi^{-1} - (\chi^2-1)^{\frac{1}{2}}}{(\chi^2-1)^{\frac{3}{2}}}, \qquad \gamma_0(\chi) = 2\,\frac{(\chi^2-1)^{\frac{1}{2}} - \cos^{-1}\chi^{-1}}{\chi^2(\chi^2-1)^{\frac{3}{2}}}.$$

Notice that Q mentioned in (7.20) is equal to $\frac{1}{5}\rho V R_x$.

Dissipation

Irrotational flow can provide a good estimate for the force on a body at high Reynolds numbers, i.e. for sufficiently thin boundary layer. The dissipation in the fluid outside the boundary layer is now is dominant over the dissipation in the boundary layer. The dissipation D in the fluid can be calculated by

$$D = -\mu \int_A \nabla \mathbf{U}^2 \cdot \mathbf{n} \mathrm{d}A, \tag{7.78}$$

with ν the kinematic viscosity of the fluid. Substituting the velocity potential, the dissipation becomes:

$$D = -\mu \int_0^{\pi} \frac{1}{h_\mu}\frac{\partial}{\partial \mu}\left\{\left(\frac{1}{h_\mu}\frac{\partial \Phi}{\partial \mu}\right)^2 + \left(\frac{1}{h_\theta}\frac{\partial \Phi}{\partial \theta}\right)^2 + \left(\frac{1}{h_\phi}\frac{\partial \Phi}{\partial \phi}\right)^2\right\} h_\phi d\phi h_\theta \mathrm{d}\theta, \tag{7.79}$$

where h_i are the metric coefficients in an ellipsoidal coordinate system as defined in (7.62). In general the dissipation can be written as

$$D = 12\pi\mu U_i r_{eq} G_i(\chi), \;\; i = x, y, z. \tag{7.80}$$

Translation along a minor axis

For the motion along the minor axis we substitute the velocity potential (7.68) resulting in

$$G_z(\chi) = \frac{1}{3}\chi^{4/3}(\chi^2-1)^{3/2}\frac{(\chi^2-2)sec^{-1}(\chi) + \sqrt{\chi^2-1})}{\left(\chi^2 sec^{-1}(\chi) - \sqrt{\chi^2-1}\right)^2}. \tag{7.81}$$

This was already found by Moore [10].

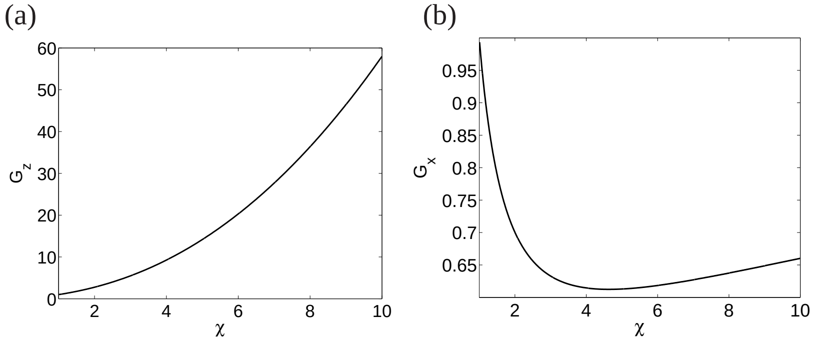

Figure 7.20: (*a*) $G_z(\chi)$ as function of χ, (*b*) $G_x(\chi)$ as function of χ.

Translation along a major axis

For the motion along the major axis we can proceed in a similar way. We substitute the velocity potential (7.69), resulting in

$$G_x(\chi) = \frac{2}{3}\chi^{-2/3}(\chi^2-1)^{3/2}\frac{(\chi^2-2)\sqrt{(}\chi^2-1)+\chi^4 sec^{-1}(\chi)}{\left((2\chi^2-1)\sqrt{\chi^2-1}-\chi^2 sec^{-1}(\chi)\right)^2}. \quad (7.82)$$

An expression which, to the authors' knowledge, has not been reported before.

Figure 7.20 shows the plots of the factors G_z and G_x as a function of the aspect ratio of the bubble. For the aspect ratio χ=1 the dissipation reduces to the spherical case. The higher the aspect ratio the higher the dissipation for motion in the direction of the minor axis will be. For the motion along the major axis there is a minimum. First the frontal surface area of the bubble decreases faster than the total surface of the bubble. Later the frontal surface area hardly increases and the dissipation is increased by an increase in total surface area, because the bubble becomes flatter.

Finally, for the steady motion of a single bubble the force experienced by the bubble at high Reynolds numbers can be calculated from the dissipation in the fluid by

$$F_D = DU. \quad (7.83)$$

Appendix C: Surface of an oblate spheroid

This appendix deals with the calculation of the surface of an oblate spheroid in ellipsoidal coordinates (μ, θ, φ).

Consider a point on the surface specified as

$$\mathbf{r} = \begin{cases} x &= b(\theta,\varphi)\sin\theta\,\cos\varphi \\ y &= b(\theta,\varphi)\sin\theta\,\sin\varphi \\ z &= c(\theta,\varphi)\cos\theta \end{cases}, \tag{7.84}$$

with

$$b(\theta,\varphi) = k\cosh\mu(\theta,\varphi), \qquad c(\theta,\varphi) = k\sinh\mu(\theta,\varphi).$$

The normal to a surface parameterized by θ and φ is, in cartesian co-ordinates,

$$\mathbf{n} = \frac{\mathbf{r}_\theta \times \mathbf{r}_\varphi}{|\mathbf{r}_\theta \times \mathbf{r}_\varphi|} = \frac{\mathbf{r}_\theta \times \mathbf{r}_\varphi}{\sqrt{EG - F^2}} \tag{7.85}$$

with

$$\begin{aligned} E &= \mathbf{r}_\theta \cdot \mathbf{r}_\theta, \\ F &= \mathbf{r}_\theta \cdot \mathbf{r}_\varphi, \\ G &= \mathbf{r}_\varphi \cdot \mathbf{r}_\varphi. \end{aligned}$$

It follows that

$$\begin{aligned} E &= b^2\cos^2\theta + c^2\sin^2\theta + 2(bb_\theta - cc_\theta)\sin\theta\cos\theta + b_\theta^2\sin^2\theta + c_\theta^2\cos^2\theta, \\ F &= (bb_\varphi - cc_\varphi)\sin\theta\cos\theta + b_\theta b_\varphi\sin^2\theta + c_\theta c_\varphi\cos^2\theta, \\ G &= b^2\sin^2\theta + b_\varphi^2\sin^2\theta + c_\varphi^2\cos^2\theta. \end{aligned} \tag{7.86}$$

The area of surface is

$$S = \int_0^{2\pi}\int_0^{\pi} \sqrt{EG - F^2}\,\mathrm{d}\theta\mathrm{d}\varphi \tag{7.87}$$

For our oblate ellipsoidal bubble this reduces to

$$S = 2\pi\int_0^{\pi}\sqrt{EG}d\theta = 2\pi\int_{-1}^{1} b\sqrt{E}\mathrm{d}\cos\theta. \tag{7.88}$$

The mean curvature H of the oblate ellipsoid is given by

$$2H = \frac{EN + GL}{EG}, \tag{7.89}$$

with E and G given above and

$$L = \mathbf{n}\cdot\mathbf{r}_{\theta\theta} = \frac{(\mathbf{r}_\theta \times \mathbf{r}_\varphi)\cdot\mathbf{r}_{\theta\theta}}{|\mathbf{r}_\theta \times \mathbf{r}_\varphi|}, \tag{7.90}$$

$$N = \mathbf{n} \cdot \mathbf{r}_{\varphi\varphi} = \frac{(\mathbf{r}_\theta \times \mathbf{r}_\varphi) \cdot \mathbf{r}_{\varphi\varphi}}{|\mathbf{r}_\theta \times \mathbf{r}_\varphi|}. \tag{7.91}$$

It is straightforward to show that

$$2H = -\frac{\sinh \mu_0 (1 + \sinh^2 \mu_0)^{\frac{1}{2}}}{k(\sinh^2 \mu_0 + \cos^2 \theta)^{\frac{3}{2}}} - \frac{\sinh \mu_0}{k(\sinh^2 \mu_0 + \cos^2 \theta)^{\frac{1}{2}} (1 + \sinh^2 \mu_0)^{\frac{1}{2}}}. \tag{7.92}$$

References

[1] Abramowitz, M. & Stegun, I.A. 1965 *Handbook of mathematical functions*. Dover Publications, New York, USA.

[2] Biesheuvel, A. & Hagmeijer, R. 2006 On the force on a body moving in a fluid. *Fluid Dyn. Res.* **38**, 716–742.

[3] Brücker, C. 1999 Structure and dynamics of the wake of bubbles and its relevance for bubble interaction. *Phys. Fluids* **11**, 1781–1796.

[4] Duineveld, P.C. 1995 The rise velocity ans shape of bubbles in pure water at high Reynolds numbers. *J. Fluid Mech.* **292**, 325–332.

[5] Ellingsen, K. & Risso, F. 2001 On the rise of an ellipsoidal bubble in water: oscillatory paths and liquid-induced velocity. *J. Fluid Mech.* **440**, 235–268.

[6] Lamb, H. 1932 *Hydrodynamics*, 6th edn. Cambridge University Press, USA.

[7] Lunde, K. & Perkins, R.J. 1997 Observations on wakes behind spheroidal bubbles and particles. , vol. FEDSM97, p. 3530.

[8] Luther, S., Rensen, J. & Guet, S. 2004 Bubble aspect ratio and velocity measurement using a four-point fiber-optical probe. *Exp. Fluids* **36**, 326–333.

[9] Magnaudet, J. & Eames, I. 2000 The motion of high-Reynolds-number bubbles in inhomogeneous flows. *Annu. Rev. Fluid Mech.* **32**, 659–708.

[10] Moore, D.W. 1965 The velocity of rise of distorted gas bubbles in a liquid of small viscocity. *J. Fluid Mech.* **23**, 749–766.

[11] Mougin, G. & Magnaudet, J. 2002 Path instability of a rising bubble. *Phys. Rev. Letters* **88**, 014502.

[12] DE VRIES, A.W.G. 2001 Path and wake of a rising bubble. PhD thesis, University of Twente, Enschede, the Netherlands.

[13] DE VRIES, A.W.G., BIESHEUVEL, A. & VAN WIJNGAARDEN, L. 2002 Notes on the path and wake of a gas bubble rising in pure water. *Int. J. Multiphase Flow* **28**, 1823–1835.

[14] VAN WIJNGAARDEN, L. 2005 Bubble velocities induced by trailing vortices behind neighbours. *J. Fluid Mech.* **541**, 203–229.

Chapter 8

Motion of bubbles with shape oscillations [‡]

The previous chapter dealt with bubbles of fixed ellipsoidal shape. In this chapter larger bubble diameters will be considered which cause shape oscillations to set in. Literature, mainly the work by Lunde & Perkins [11], will be discussed and the present experimental results will be compared with their results.

For bubble sizes right at the onset of shape oscillations the stable spiraling motion changes into a pure zigzagging motion. This is due to a coupling with the non-axisymmetric mode (2,2) shape oscillation. Larger bubbles rise in more or less spiral paths. Finally multiple shape oscillations force the bubble into an erratic path. All bubbles show an axisymmetric mode (2,0) shape oscillation which is coupled with velocity oscillations and therefore with oscillations in the wake.

The analytical method to calculate shape oscillations on spherical bubbles (e.g. [2, 7]) is extended to shape oscillations on ellipsoidal bubbles. The limiting case for aspect ratio one is calculated correctly but the method results in deviations from numerical calculations by Meiron [13] for higher aspect ratios. A correct closure of the model is still in progress. A similar approach has been used to derive an analytical expression for volume oscillations on oblate ellipsoidal bubbles as function of the aspect ratio. Evaluation of this expression at several aspect ratios provides frequencies which agree with numerical data of Strasberg [19].

[‡] adapted from: C.H.J. Veldhuis, A. Biesheuvel, & L. van Wijngaarden, *Shape oscillations on ellipsoidal bubbles*, to be submitted to J. Fluid Mech. (2007)

8.1 Introduction

Lindt [8] is one of the first to report on bubbles performing shape oscillations. Following the regime with an oblate spheroid in helical motion Lindt finds oblate spheroids with shape oscillations in almost rectilinear motion starting at an equivalent diameter of 4.8 mm (see figure 6.1). In chapter 6 we already saw that shape oscillations in our experiments start at 2.8 mm for purified water and 3.0 mm for tap water. The difference with Lindt's findings is attributed to the lack of time resolution in his experimental data, because no high speed imaging was available to him.

Lunde & Perkins [11] also studied the shape oscillations on ellipsoidal rising bubbles. They provide an overview of bubble experiments for diameters of 2.4, 3.02, 3.52, 4.32, and 5.16 mm. They used stereoscopic high speed imaging (up to 500 frames/s) and extracted two major axes (d_1 and d_2) from their digital images. These axes are identical to the axes d_1 and d_2, defined in figure 7.1. Lunde & Perkins distinguish between axisymmetric and non-axisymmetric shape oscillations. Therefore they perform a Fourier analysis on the product of the two measured axes ($d_1 \cdot d_2$) and their ratio (d_1/d_2). For axisymmetric shape oscillations the axes will change in phase; the product of the two axes will amplify the oscillations, whereas their ratio will cancel the oscillations. For non-axisymmetric shape oscillations the axes will change out of phase; therefore their ratio will amplify the oscillations.

Lunde & Perkins analyzed the acceleration of the bubble along its path and showed a clear interaction between oscillations of the acceleration and axisymmetric shape oscillations; this is in agreement with de Vries *et al.* [20]. They studied the effect of oscillations in the aspect ratio on the velocity of the bubble and showed that only by taking into account these oscillations the rise velocity of the bubble can be modelled properly.

Comparison with numerical work of Meiron [13] suggests that the axisymmetric and non-axisymmetric frequencies detected by Lunde & Perkins are of mode (2,0) and (2,2), respectively. They state that the axisymmetric mode (2,0) 'travels' from pole to pole and the non-axisymmetric mode (2,2) 'travels' around the equator. Assuming the bubble to be an oblate ellipsoid and the oscillations to be capillary waves, Lunde & Perkins give approximate expressions for mode (2,0) and (2,2), respectively

$$f_{2,0} = \frac{1}{2\pi}\sqrt{\frac{16\sqrt{2}\chi^2}{(\chi^2+1)^{3/2}}}\sqrt{\frac{\sigma}{\rho_l r_{eq}^3}} \quad \text{and} \quad f_{2,2} = \frac{1}{2\pi}\sqrt{\frac{8}{\chi}}\sqrt{\frac{\sigma}{\rho_l r_{eq}^3}}, \tag{8.1}$$

where σ is the surface tension coefficient. Note that these expressions do not reduce to the frequency of a spherical bubble ($\chi = 1$). Comparison with results from Meiron [13] shows that these expressions are accurate within 8% for $1.5 < \chi < 3.5$. The bubbles examined by Lunde & Perkins and the experiments discussed in this report lie well within this range.

Lunde & Perkins also investigated the wake of bubbles. They stated that the vortex shedding frequency is equal to twice the path frequency (approximately constant at 6.5 Hz for a wide range of bubble diameters). This idea follows from dye-injection experiments with zigzagging ellipsoidal particles which shed large amounts of vorticity at the outer positions of the zigzag. Lunde & Perkins did not analyze the bubble wake in uncontaminated fluids, where the bubbles have a no-shear boundary condition. As will become clear from the Schlieren experiments in purified water (see section 8.2.2), the bubble wake is completely different and the vortex shedding frequency is not equal to twice the path frequency, but much higher.

In section 8.2 the experimental results will be presented and compared with the literature; new insights with respect to the relation between path, shape and wake of the bubble will be discussed. In section 8.3 an analytical method to calculate shape oscillations on an oblate ellipsoidal bubble will be discussed. Section 8.4 is left to conclutions. At the end of this chapter two appendices are included. Appendix A discusses the calculation of the surface of an oblate spheroid to second order. This is follow by appendix B on the calculation of the volume oscillation frequency of an oblate spheroid.

8.2 Experimental results

In chapter 6 the general features of single bubble motion are discussed. From these data six representative experiments are selected. The equivalent diameter D_{eq}, aspect ratio χ, path frequency f_{path}, and Reynolds number Re for these experiments are given in table 8.1.

In the next section the bubble path, orientation, and shape will be discussed followed by a section on the wake structure behind the bubble, and finally a section on the interaction between path, shape and wake oscillations.

8.2.1 Bubble path, orientation and shape

Figure 8.1 shows the 3D bubble path with gray values indicating the bubble velocity for the six representative bubbles; figure 8.2 shows the top view in this respect.

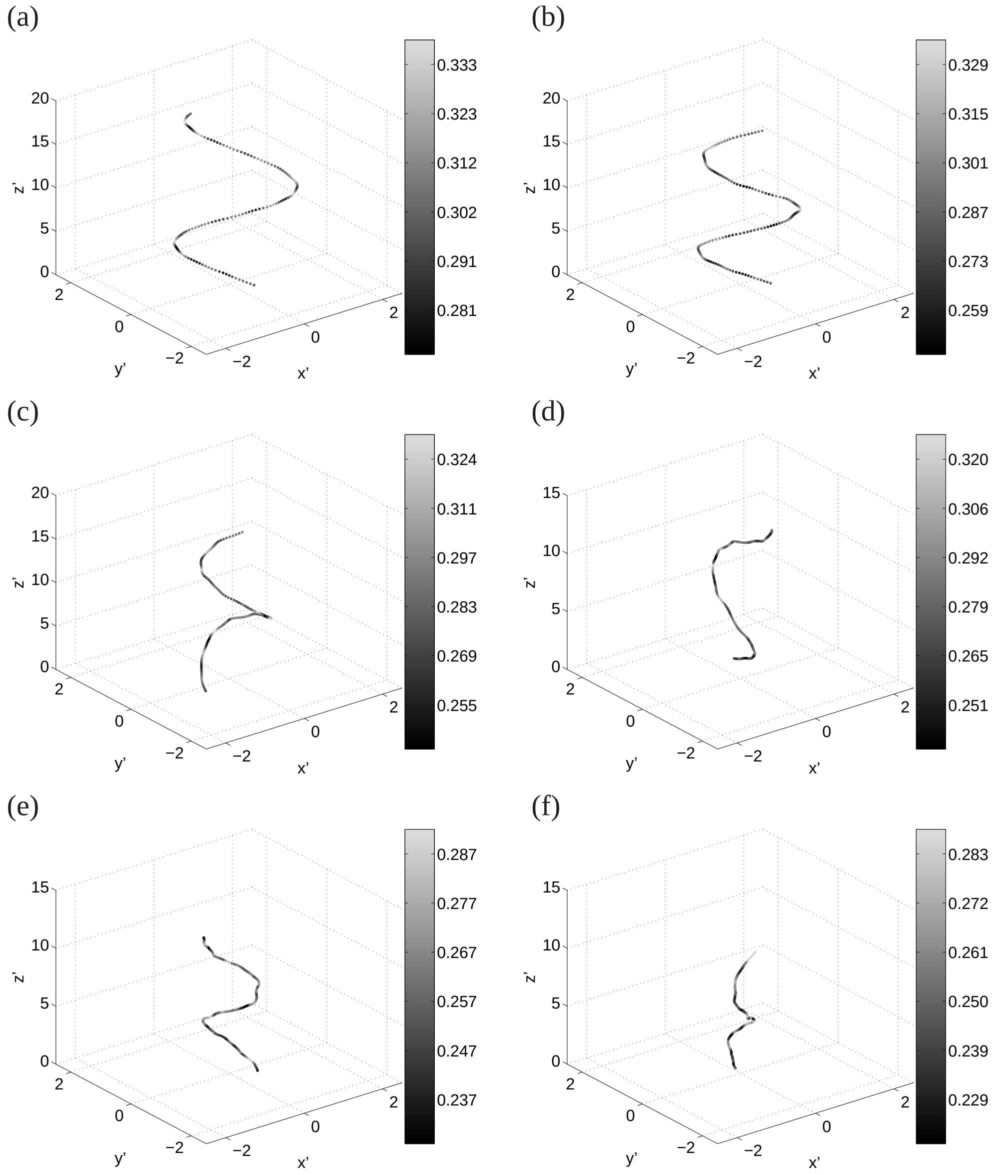

Figure 8.1: Measured trajectories of bubbles rising in water. The gray values represent the tangential velocity of the bubbles, with the numbers next to the codes giving the corresponding value in m s^{-1}. Axes are non-dimensionalized with the equivalent diameter. See table 8.1 for further details.

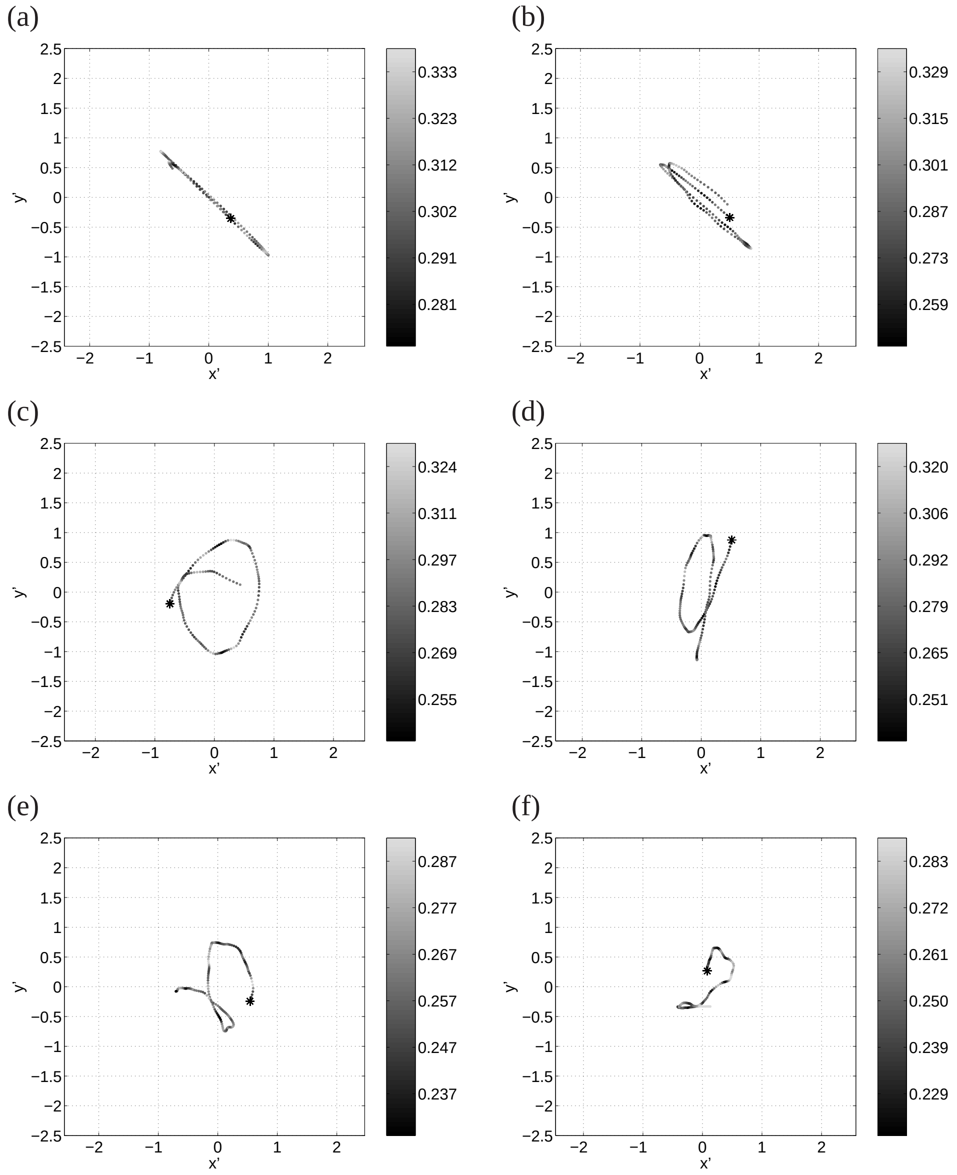

Figure 8.2: Top views of bubbles rising in water. The gray values represent the tangential velocity of the bubbles, with the numbers next to the codes giving the corresponding value in m s^{-1}. The '*' indicates the starting point of the trajectory. See table 8.1 for further details.

sub-figure	D_{eq}/mm	χ	Re	f_{path}/Hz	path
(*a*)	3.0	2.2	899	6.7	zigzag
(*b*)	3.4	2.2	973	7.0	zigzag
(*c*)	3.6	2.3	1018	5.5	spiral
(*d*)	4.0	2.4	1096	6.5	flattened spiral
(*e*)	4.5	2.7	1162	6.2	tilted flattened spiral
(*f*)	5.2	2.8	1305	5.2	chaotic

Table 8.1: Overview of experiments with bubbles with shape oscillations presented in this chapter. The sub-figure numbers refer to the numbers of the sub-figures in section 8.2.1.

In chapter 6 several reasons were given for these bubbles to have reached their final stage of motion. The first two bubbles, (*a*) and (*b*), are purely zigzagging bubbles. Hence, in contrast to what has been stated in the literature [12, 17], a zigzagging path can be a stable solution for the rising bubble. The reason for this zigzagging motion will become clear when the shape oscillations of the bubble are discussed.

Increasing the bubble size changes the bubble path into a curve of, roughly, spiral form (figures 8.2(*c*) and (*d*)). The largest bubbles (figures 8.2(*e*) and (*f*)) are so-called rocking bubbles for which the motion is more random. In all cases the velocity has large oscillations. The characteristic high velocities at the outer positions of the zigzag or flattened spiral, as has been reported in chapter 7 for bubbles without shape oscillations, are hardly visible.

Figure 8.3 shows projections of bubble shape and path onto the vertical XZ and YZ-plane. Whereas the smallest bubbles still resemble an ellipsoid with small amplitude shape oscillations and a minor axis aligned with the bubble path, the largest bubbles experience large amplitude shape oscillations and their basic shape is far from ellipsoidal. It is clear that the reconstruction of bubble shape and orientation, as presented in chapter 6, is not valid in this regime. But still a small and a large axis can be detected in each projection ($e_{1,2}$ and $d_{1,2}$, respectively, see also figure 7.1). Hence, an analysis of the bubble shape oscillation frequencies, in the sense of Lunde & Perkins as described in the introduction, is possible.

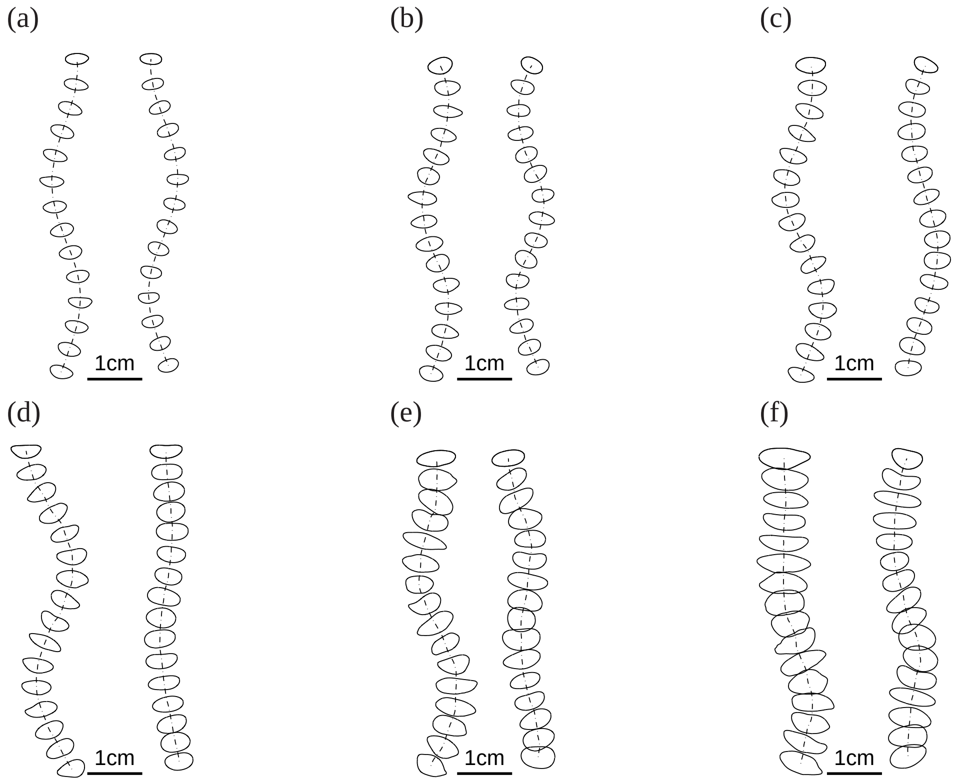

Figure 8.3: Stereoscopic images of bubbles with their paths and shapes. Images are recorded with 640 frames/s. The bubble shapes are plotted every 10 frames, giving a time interval of 0.64 s between the bubble shapes. See table 8.1 for further details.

Relation between oscillations in shape and velocity

Figure 8.4 presents normalized power spectra of the tangential velocity of the bubble, the product of the two major axes and their ratio. The power spectra are normalized with their average value. On the vertical axis in figure 8.4 $|FFT|$ means

$$|\mathcal{F}(f(t))| \, / \, \overline{|\mathcal{F}(f(t))|},$$

with $\mathcal{F}$ the Fast Fourier Transform of a function $f(t)$. Before the Fourier transform is calculated, the average of $f(t)$ is subtracted. Now the power spectrum does not show any pronounced peaks equal to the inverse of the duration of an experiment. The typical duration of an experiment is approximately 0.2 s. The path frequency is approximately 5-7 Hz; hence, the period of path oscillation varies between 0.14 and 0.2 s. Therefore the path frequency cannot be detected in the normalized power

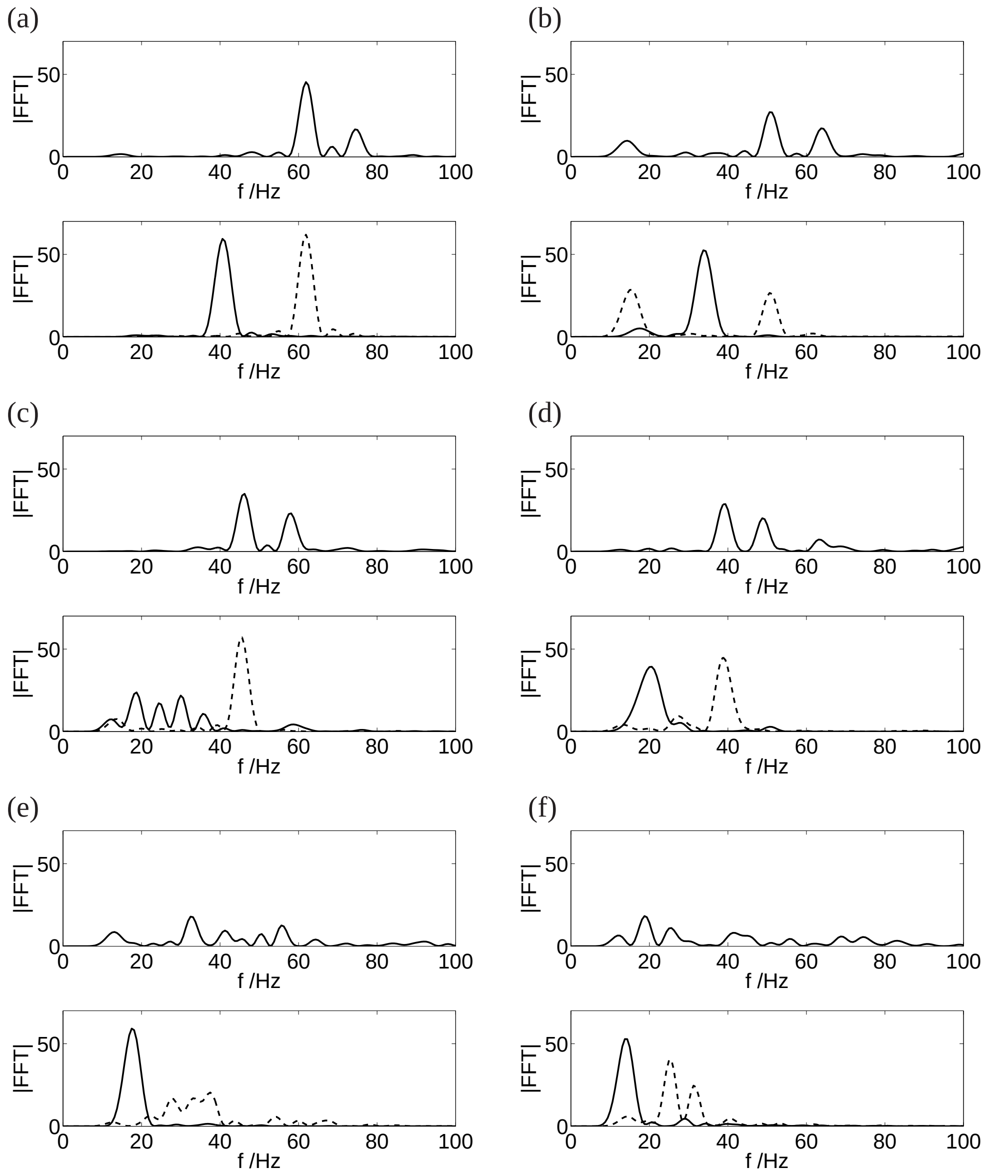

Figure 8.4: Normalized power spectra of tangential velocity and shape. Upper plot: $|FFT\ U_t|$, Lower plot: – $|FFT\ d_1/d_2|$ and - - $|FFT\ d_1 d_2|$. See table 8.1 for further details.

spectra in figure 8.4.

At the onset of shape oscillations there are only two basic modes. Meiron [13] calculated the frequency of shape oscillation modes (n, m), with $n = 2, 3, ..$ and $m = 0, .., n$, using a linear stability analysis. Comparison of our experiments with his results shows that the two basic modes are the axisymmetric mode (2,0) and the non-axisymmetric mode (2,2), as was also found by Lunde & Perkins and with respect to the axisymmetric mode by de Vries *et al.* [20]. For larger bubbles multiple frequencies are present, which cannot be linked with frequencies of higher modes ($n > 2$) calculated by Meiron, because frequencies for mode 3 and higher are larger than approximately 150 Hz. It is more likely that the other frequencies are caused by non-linear effects.

For the smaller bubbles there is a clear coupling between the frequency of the tangential velocity and the axisymmetric shape oscillation. The larger the bubble the more frequencies appear, and the more random the bubble path becomes. But the coupling between the mode (2,0) shape oscillation and the tangential velocity remains. This coupling can be understood by recalling that the mode (2,0) implies an oscillation of the bubble aspect ratio. Therefore the added mass and drag are influenced, leading to an effect on the velocity of the bubble [20]. This becomes clear by looking at the momentum balance in tangential direction which states

$$\rho V \frac{d}{dt}\left(M_z(\chi)U\right) \approx \rho V g_t + 6\pi\mu U D_{eq} G_z(\chi) + F_{D,ind}. \tag{8.2}$$

Here, the added mass coefficient M_z is given in (7.72) in appendix B of chapter 7. The second term on the right hand side is the viscous contribution to the drag $F_{D,visc}$, where G_z is given by (7.81) in appendix B of chapter 7. Figures 7.19 and 7.20 in this appendix show the dependence of added mass and drag on the aspect ratio. Typical variations in the aspect ratio are of the order of 20% leading to variations in added mass and drag coefficients of approximately 8% and 4%, respectively. De Vries *et al.* [20] studied the effect of oscillations in drag and added mass on the rise velocity of a bubble. From experiments they extracted the shape of the bubble. This enabled them to calculate the drag and added mass coefficients and solve (8.2) with a Runge-Kutta scheme. They showed that oscillations in the calculated rise velocity of the bubble only agree with oscillations in the experimentally measured rise velocity if added mass is taken into account. For the relatively large bubble studied, the effect of the drag is much less than the effect of the added mass.

Relation between oscillations in shape and path

Figure 8.4 shows that the velocity of the bubble is not influenced by the non-axisymmetric mode, because this mode does not change the aspect ratio and therefore the added mass and drag. But there is an influence on the bubble path, which

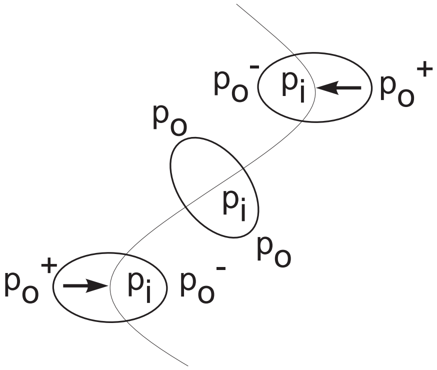

Figure 8.5: Bubble along a zigzag path. Arrows indicate direction of force due to pressure difference.

becomes clear when figures 8.2 and 8.4 are compared. The non-axisymmetric shape oscillation is clearly present in figures 8.4(*a*) and (*b*); the path of the bubble is a zigzag, as can be seen in figures 8.2(*a*) and (*b*). For the third bubble (figure 8.4(*c*)) the non-axisymmetric shape oscillation is less pronounced; the bubble path is a spiral. The fourth bubble shows a non-axisymmetric shape oscillation, although the peak is less pronounced than for the bubbles in (*a*) and (*b*). The bubble now performs a flattened spiraling motion. Obviously there is an interaction between the bubble path and the non-axisymmetric shape oscillation; the zigzag path can be directly coupled to the presence of non-axisymmetric shape oscillations. The reason for this interaction is the breaking of the axisymmetry of the system in case of a zigzagging motion. A spiraling path is axisymmetric and does not give rise to non-axisymmetric shape oscillations, as is shown by the bubble in figure 8.4(*c*). A zigzagging motion forces the bubble to have a non-axisymmetric shape. Figure 8.5 schematically shows a bubble aligned with a zigzag path. In order to move along a zigzag curve an effective horizontal force has to be present. Therefore the pressure outside the bubble on the two sides will be different (p_o^+ and p_o^-). The positions of p_o^+ and p_o^- change depending on the location on the zigzag curve. This leads to a local difference in curvature, because $p_i - p_o = \sigma \nabla \cdot \mathbf{n}$, with p_i the pressure inside, p_o the local pressure outside the bubble and $\nabla \cdot \mathbf{n}$ the local curvature, and the bubble axisymmetry breaks. For a spiraling bubble this axisymmetry is far less pronounced because of the larger radius of curvature of the path compared to the zigzagging path. Furthermore the curvature of the spiral path is steady, in contrast to the unsteady zigzagging motion. Therefore the presence of non-axisymmetric shape oscillations is expected for zigzagging bubbles and not for spiraling ones.

D_{eq}/mm	$f_{2,0}/Hz$	$f_{2,2}/Hz$	f_{path}/Hz	$f_{2,2}/f_{path}$	path
3.0	61.8	40.6	6.7	6.0	zigzag
3.4	50.7	34.0	7.0	4.9	zigzag
3.6	45.5	-	5.5	-	spiral
4.0	39.0	20.5	6.5	3.2	flattened spiral
4.5	-	17.5	6.2	2.8	tilted flattened spiral
5.2	-	14.0	5.2	2.7	chaotic

Table 8.2: Relation between shape oscillations and bubble path. ’-’ Means no distinct frequency detected.

Table 8.2 summarizes the frequencies for the six bubbles in figure 8.4. The frequency of the mode (2,2) oscillation is linked with a multiple of the path oscillation frequency. The better the ’fit’ of these frequencies, the flatter the bubble path. Notice that the path frequency of zigzagging bubbles is slightly higher than the path frequency of spiraling bubbles. It seems that the non-axisymmetric shape oscillations are able to change and ’lock-in’ the path frequency.

8.2.2 Bubble wake

In this section the wakes of four representative bubbles are shown. The development in bubble motion is similar to that of the six bubbles presented in the previous section. Table 8.3 shows the relevant parameters for these experiments.

Figure 7.14(*a*) to (*e*) presented the wake behind bubbles of fixed shape. In figure 7.14 (*f*) shape oscillations set in. Figure 8.6 starts with the bubble in figure 7.14 (*f*) and continues with Schlieren images of larger bubbles. At the onset of shape oscillations the unsteady wake is rather structured. The wake consists of regions of concentrated vorticity, which are shed at a specific frequency. Increasing the bubble diameter destabilizes the wake. The single vortex shedding frequency disappears and no specific frequencies are detected any longer. This is in agreement with the Fourier analysis of the bubble shape and velocity, which shows multiple frequencies for larger bubble diameters (see figure 8.7). Notice again the coupling between mode (2,0) and the velocity. Furthermore, the non-axisymmetric mode (2,2) is strongest when the bubble performs a zigzagging motion (figures 8.7(*b*) and (*c*)) as was also the case for the non-Schlieren experiments.

sub-figure	D_{eq}/mm	χ	Re	path
(*a*)	2.8	2.1	1062	spiral
(*b*)	3.5	2.2	1197	zigzag
(*c*)	3.9	2.3	1289	zigzag
(*d*)	5.5	2.7	1674	chaotic

Table 8.3: Overview of Schlieren experiments of bubbles with shape oscillations. The sub-figure numbers refer to the numbers of the sub-figures in section 8.2.2.

From the Schlieren images the wake frequency can be extracted. The largest bubbles have a highly irregular wake consisting of multiple frequencies. Therefore the wake frequency cannot be detected for bubble diameters larger than 3.5 mm. Table 8.4 shows the wake frequencies for seven bubbles with shape oscillations. We clearly see the wake oscillation frequency decreasing with increasing bubble diameter. In the next section we will see how the wake oscillations are coupled with oscillations in velocity and shape.

D_{eq}/mm	2.8	2.9	3.1	3.1	3.3	3.4	3.5
f_{wake}/Hz	74	65	65	54	48	45	46

Table 8.4: Wake frequencies for several bubble diameters.

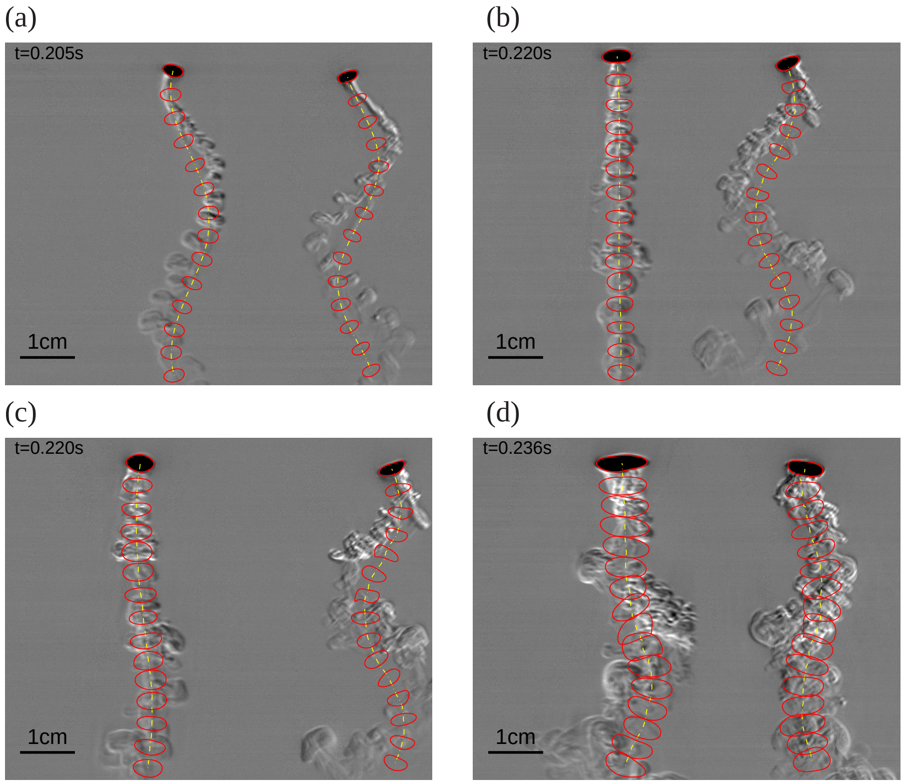

Figure 8.6: Stereoscopic Schlieren images of bubbles with their paths: dash-dotted line and bubble shape: solid line. Images are recorded with 640 frames/s. The bubble shapes are plotted every 10 frames, giving a time interval of 0.64 s between the bubble shapes. The elapsed time starting from the first bubble shape is indicated in the upper left corner. The Reynolds numbers are (*a*) 1062, (*b*) 1197, (*c*) 1289, and (*d*) 1674. See table 8.3 for further details.

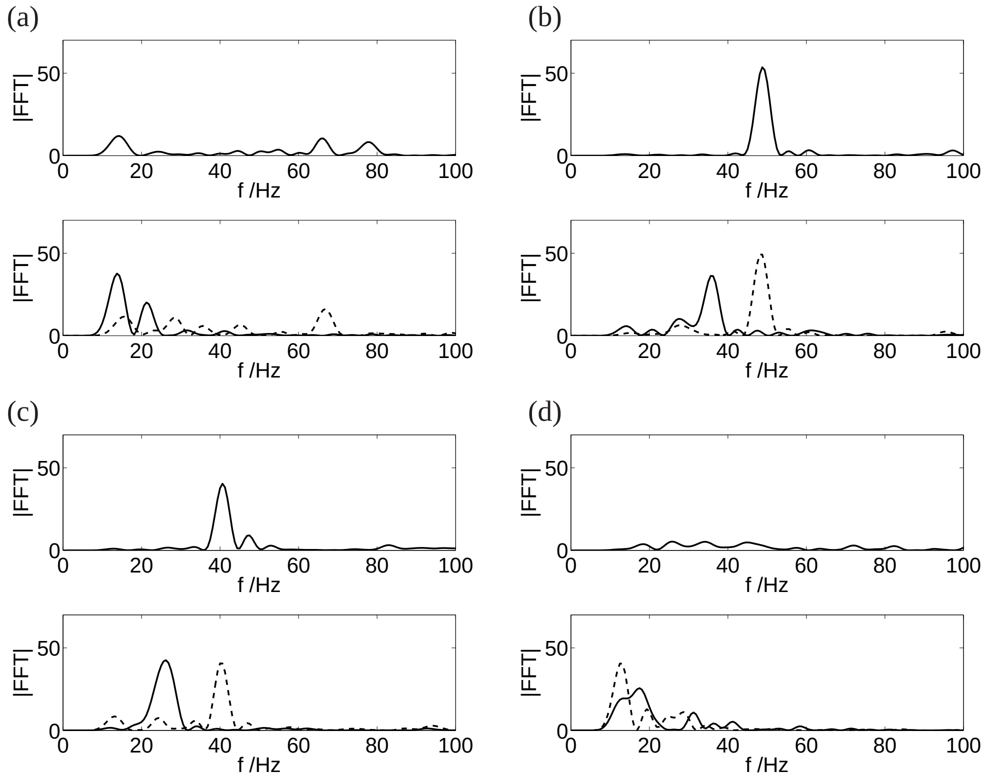

Figure 8.7: Normalized power spectra of tangential velocity and shape. Upper plot: $|FFT\ U_t|$, Lower plot: – $|FFT\ d_1/d_2|$ and - - $|FFT\ d_1 d_2|$. See table 8.3 for further details.

8.2.3 Interaction of path, shape, and wake oscillations

The bubble path, shape and wake and their oscillations are discussed; this section focusses on the interaction between these aspects.

Shape oscillations frequency versus bubble diameter
Figure 8.8(*a*) shows the oscillation frequencies of shape, velocity, and wake versus the equivalent bubble diameter for bubbles rising in purified water. These data agree well with the experimental data of Lunde & Perkins [11] (see figure 8.8(*c*)). They performed a series of five experiments at six bubble diameters and averaged the results over these five experiments; therefore their scatter is much smaller. Lunde & Perkins performed some experiments to visualize the wake structure, but detailed information is never obtained. They recorded zigzagging ellipsoidal particles where vorticity is shed at the outer positions of the zigzagging path. Therefore the wake frequency is assumed to be twice the path frequency [10]. The present Schlieren experiments show a different view of the wake dynamics of bubbles; the frequencies are higher than twice the path frequency and are given in the previous section and also plotted in figure 8.8(*a*) with '*'. There is a match between axisymmetric shape oscillations and oscillations in the wake. This is due to the change in momentum of the bubble when the axisymmetric shape oscillation changes the bubble aspect ratio. Any change in velocity and shape modifies the production of vorticity at the bubble surface; these variations will be visible in the wake. One might think that the shape oscillations are directly coupled with the wake oscillations and not indirectly through the bubble velocity. Figure 7.14(*e*) suggests otherwise; here wake instabilities for a bubble performing a flattened spiral occur before shape oscillations are present, suggesting that wake oscillations are triggered by velocity oscillations rather than shape oscillations. It seems that any shape oscillation first has to trigger velocity oscillations before there will be any effect on the wake; this effect can also be observed for bubbles rising in tap water as we will see now.

Figure 8.8(*b*) shows the oscillation frequency of shape and velocity for bubbles rising in tap water. There is a large scatter in the shape oscillation frequency; this is due to surfactants which can lower the surface tension down to 1/3 of the surface tension in ultra clean water. For every experiment in tap water it is not precisely know what the amount of surfactants is on the bubble surface; this leads to differences in aspect ratio, bubble velocity and oscillation frequencies (see also chapter 6). Generally, the aspect ratio of the bubble is lower in tap water; therefore the critical bubble diameter above which shape oscillations are triggered increases. In many cases the most important frequency is twice the path frequency (approximately 6.5 Hz). The mode (2,0) shape oscillations is still detected, but the coupling between the axisymmetric mode (2,0) and the oscillations in the velocity of the

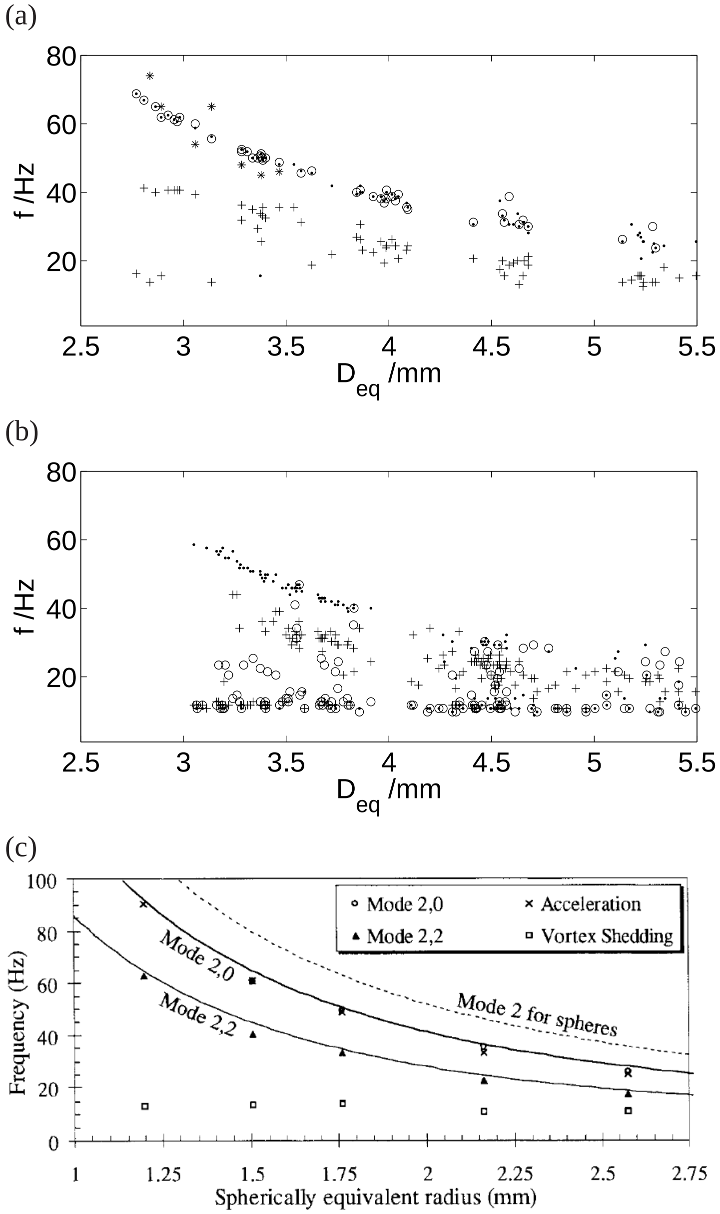

Figure 8.8: Figures (*a*) and (*b*) show the measured frequencies versus bubble diameter: * the wake, o the velocity, · the shape oscillations mode (2,0), and + mode (2,2). Figure (*a*) for purified water, and figure (*b*) for tap water. Figure (*c*) gives the frequency of acceleration, shape oscillations (mode (2,0) and mode (2,2)), and wake versus the equivalent radius. The lines resemble the model in (8.1). Figure (*c*) is taken from Lunde & Perkins [11], with permission of R.J. Perkins and Springer Science.

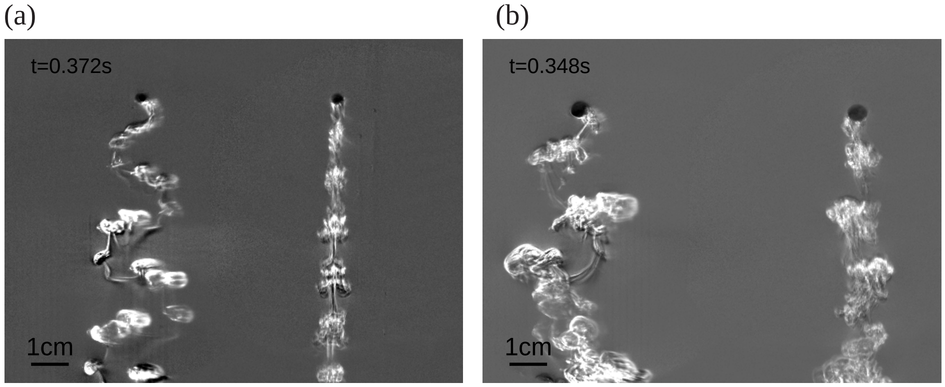

Figure 8.9: Schlieren images of a 3 mm (figure (*a*)) and a 3.5 mm (figure (*b*)) zigzagging bubble rising in tap water. Clearly visible are the periodic bursts of vorticity at the outer positions of the zigzagging motion. In between the bursts a stable double-threaded vortex structure is present. The elapsed time starting from the moment the bubble appears in the images is indicated in the upper left corner.

bubble is no longer present. At first this might look odd, because the idea was that axisymmetric shape oscillations change added mass and drag and therefore bubble velocity. But surfactants in the tap water change the boundary condition on the bubble surface from no-shear to no-slip which results in a larger drag. Whereas in the no-shear case the added mass is dominant, in the no-slip case the drag is dominant. Therefore shape oscillations no longer trigger oscillations in bubble velocity in tap water. This might also explain the low vortex shedding frequency found by Lunde & Perkins, which is based on experiments in contaminated water. The vortex shedding is coupled with the oscillations in the velocity and is therefore only twice the path frequency. Figure 8.9 gives an example of a zigzagging bubble in tap water; the vortex shedding is periodic in bursts at the outer position of the zigzag, and therefore it is equal to twice the path frequency. This vortex structure is clearly different from the vortex structures of bubbles rising in purified water. So, again, we see that the vortex shedding frequency is uncoupled from the shape oscillation and there is only a coupling between vortex shedding and oscillations in the velocity. In the case of free-shear surfaces shape oscillations trigger oscillations in the velocity and therefore the vortex shedding frequency is also affected.

Shape oscillation frequency versus bubble aspect ratio
Figure 8.10 shows the experimental data for the frequency of the shape oscillations versus the aspect ratio of the bubble. Figure 8.10(*a*) shows the data for bubbles

rising in purified water and figure 8.10(*b*) for tap water, where the bubble aspect ratio is smaller, because of surfactants.

Meiron [13] performed a numerical simulation based on potential flow to calculate the eigenmodes of an oscillating ellipsoidal bubble. Actually, the paper was a reaction on an earlier paper from Hartunian & Sears [5] who claimed that shape oscillations on a flattened spheroid would lead to instability of the bubble path. Their linear stability analysis showed unstable eigenmodes of the spherical base shape. Meiron repeated their calculation but he performed a stability analysis perturbing a bubble with ellipsoidal base shape. He found no unstable eigenmodes and concluded that inviscid theory does not provide a mechanism for path instability. His research also led to a relation for the dependence of the frequency of a mode on the aspect ratio of the base shape; mode (2,0) and (2,2) are presented in figure 8.10 ('o-.-o'- and 'o—o'-line, respectively). The experiments show frequencies which are lower than Meiron's prediction. This might be caused by the assumption of an oblate ellipsoidal bubble in both Meiron's calculations and the analysis of the experiments. In the experiments the bubbles do not have a for-aft symmetry; the bubble is slightly flatter at the front. Therefore, by assuming an oblate ellipsoidal shape, the aspect ratio is slightly underestimated, leading to a lower frequency compared with Meiron's calculations. But still after a small shift of the experimental data towards a higher aspect ratio (15% being the maximum error in the aspect ratio) the difference with Meiron's results remains. Probably the remaining difference is due to effects of viscosity which are not account for by Meiron. Lunde & Perkins's expressions from (8.1) are also plotted in figure 8.10. For mode (2,0) the agreement with the experiments is much better. For mode (2,2) Lunde & Perkins' model agrees well with both the experimental data and Meiron's results.

Notice that the large scatter in the non-dimensionalized frequency for bubbles rising in tap water is again due to surfactants; now the surface tension is taken equal for all experiments. If the surface tension is known for every individual experiment the scatter would be much less.

We see that the rather simple model of Lunde & Perkins is in better agreement with experimental data than the extensive numerical calculation of Meiron. In order to better understand the difference we will focus on the calculation of shape oscillation frequencies of ellipsoidal bubbles. In the next section the well-known calculation of the shape oscillation frequency of a spherical bubble will be discussed. Following a similar approach the shape oscillation frequencies of an oblate ellipsoidal bubble will be calculated and compared with Meiron's results.

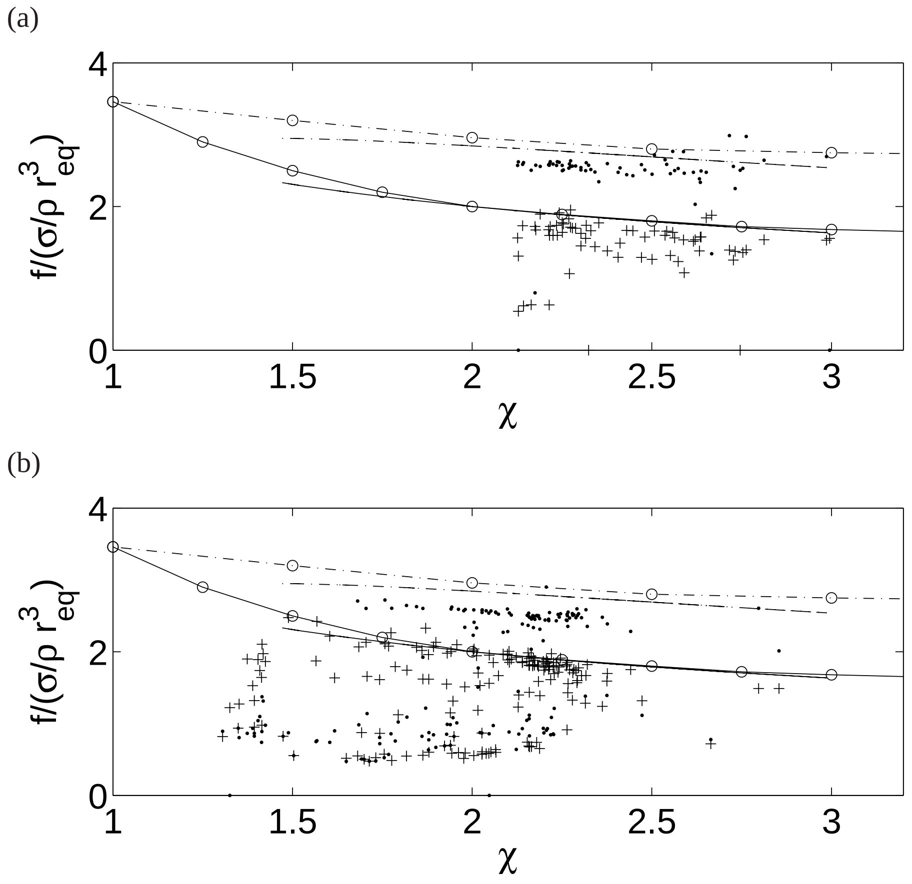

Figure 8.10: The non-dimensionalized frequency, with f in rad s^{-1} for the shape oscillations versus the aspect ratio of the bubble: · experimental values for mode (2,0), + experimental values for mode (2,2), o-·-o Meiron's mode (2,0), o—o Meiron's mode (2,2), -·- Lunde & Perkins's mode (2,0), and – Lunde & Perkins's mode (2,2) taken from (8.1). Figure (*a*) for purified water and figure (*b*) for tap water.

8.3 Calculating shape oscillations

The calculation of shape oscillations of a spherical bubble in an inviscid liquid under the action of capillary forces has been the subject of many papers. Rayleigh [16] originally analyzed the oscillations of spherical droplets in a gas. But a similar approach can be used for a spherical gas bubble in a liquid. In his approach he calculates the surface energy and the kinetic energy in the system in spherical coordinates (r, θ, ϕ). Substituting these energies in Lagrange's equation provides the equations of motion. For oscillations of the form

$$\exp i(n\theta + m\phi) \exp i\omega_{n,m}t,$$

the eigenfrequencies of the system are

$$\omega_{n,m}^2 = (n+1)(n-1)(n+2)\frac{\sigma}{\rho a^3}. \tag{8.3}$$

Here σ is the surface tension coefficient, ρ is the density of the liquid, a is the radius of the undisturbed bubble, and n and m are the modes of the oscillation. There is no difference between the frequency of the axisymmetric mode $(n, 0)$ $(n = 1, 2, ...)$ and the non-axisymmetric mode (n, m) $(n = 1, 2, ...$ and $m = 1, 2, ...)$ for a spherical bubble. This equation is valid when the density of the surrounding fluid is much larger than the density inside the bubble. Lamb [7] had a different approach; he used the dynamic boundary condition to close the system and found the same result as Rayleigh.

More recent studies [2, 4, 9, 13, 18] repeated these calculations with different approaches, leading to identical expressions for the frequency of shape oscillations of a spherical bubble. These calculations are all based on spherical bubbles. So, with respect to rising bubbles, these equations will only hold for small Weber numbers. For higher Weber numbers one should have an ellipsoidal base shape in order to treat the oscillations as sufficiently small, so that linearized theory can be used. To the authors' knowledge the calculation of shape oscillations on ellipsoidal shaped bubbles was only carried out by Meiron [13]. He used a similar method as Lamb, but now for a base shape which is consistent with the Weber number. He was not able to analytically calculate the equivalent of (8.3) for an ellipsoidal bubble, but calculated it numerically. Figure 8.10 shows the dependence of the non-dimensional frequency on the aspect ratio of the bubble for mode 2 oscillations. At an aspect ratio of one the frequencies are equal to the frequencies on a spherical bubble. The overall tendency is a decreasing frequency for increasing aspect ratio.

The aim of this section is to derive the analogue of (8.3) for the case of an ellipsoidal bubble. Before we start with the ellipsoidal bubble, let us study the eigenfrequencies for a spherical bubble. The method of Rayleigh will be used to calculate the surface and kinetic energy of the system.

8.3.1 Shape oscillations on a spherical bubble

The velocity potential Φ of the irrotational fluid motion outside the gas bubble satisfies Laplace's equation; in spherical polar co-ordinates (r, θ, φ),

$$\frac{1}{r^2}\frac{\partial}{\partial r}\left(r^2\frac{\partial\Phi}{\partial r}\right)+\frac{1}{r^2\sin\theta}\frac{\partial}{\partial\theta}\left(\sin\theta\frac{\partial\Phi}{\partial\theta}\right)+\frac{1}{r^2\sin^2\theta}\frac{\partial^2\Phi}{\partial\varphi^2}=0. \tag{8.4}$$

A solution associated with standing waves on the fluid-gas interface is

$$\begin{aligned}\Phi(r,\theta,\varphi,t) \quad = \quad & \sum_{n=0}^{\infty} r^{-(n+1)}\left(\sum_{m=0}^{n} c_{nm}(t)P_n^m(\cos\theta)\,\cos m\varphi\,+\right. \\ & \left.\sum_{m=1}^{n} d_{nm}(t)P_n^m(\cos\theta)\,\sin m\varphi\right).\end{aligned} \tag{8.5}$$

Here $P_n^m(\cos\theta)$ denotes the associated Legendre function (e.g. Abramowitz & Stegun [1]) and $c_{nm}(t)$ and $d_{nm}(t)$ are shape modes of the potential. The velocity potential must satisfy the kinematic condition that at the bubble surface the normal component of the fluid velocity equals the normal velocity of the bubble surface. Write the equation for the bubble surface as

$$r = R(\theta, \varphi, t),$$

then this condition becomes

$$\frac{\partial R}{\partial t}+\left(\frac{1}{r}\frac{\partial\Phi}{\partial\theta}\right)\left(\frac{1}{r}\frac{\partial R}{\partial\theta}\right)+\left(\frac{1}{r\sin\theta}\frac{\partial\Phi}{\partial\varphi}\right)\left(\frac{1}{r\sin\theta}\frac{\partial R}{\partial\varphi}\right)=\frac{\partial\Phi}{\partial r}, \tag{8.6}$$

to be satisfied at $r = R(\theta, \varphi, t)$.

In order to linearize the boundary condition assume that

$$R(\theta, \varphi, t) = a + \zeta(\theta, \varphi, t),$$

where ζ is small. On using that the disturbance potential must also be small, the kinematic condition becomes

$$\frac{\partial\zeta}{\partial t}=\frac{\partial\Phi}{\partial r}, \tag{8.7}$$

to be satisfied at $r = a$.

At this point Lamb [7] introduces the linearized dynamic boundary condition. Therefore it is necessary to calculate the curvature of the bubble to first order. Rayleigh's approach uses the surface energy and kinetic energy. The advantage is that the curvature of the bubble does not have to be calculated, but the disadvantage is that the kinetic energy is of second order in the disturbance potential. Hence, the surface energy should also be calculated to second order. Here care must be taken because the oscillations cause a second order contribution to the volume of the bubble, which has to be accounted for in the surface energy.

The instantaneous volume of the bubble is given by

$$V = \tfrac{1}{3}\int_0^{2\pi}\int_0^{\pi} R^3 \sin\theta \,\mathrm{d}\theta\mathrm{d}\varphi = \tfrac{1}{3}\int_0^{2\pi}\int_0^{\pi} [a_0+\zeta]^3 \sin\theta \,\mathrm{d}\theta\mathrm{d}\varphi, \tag{8.8}$$

where the 'time-dependent radius' $a_0(t)$ and the 'undisturbed radius' a can be different. Linearizing the bubble volume gives

$$V = \tfrac{4}{3}\pi a_0^3\left[1 + 3\overline{\zeta}/a_0 + 3\overline{\zeta^2}/a_0^2\right], \tag{8.9}$$

with

$$\overline{\zeta} = \frac{1}{4\pi}\int_0^{2\pi}\int_0^{\pi} \zeta \sin\theta \mathrm{d}\theta\mathrm{d}\varphi \quad \text{and} \quad \overline{\zeta^2} = \frac{1}{4\pi}\int_0^{2\pi}\int_0^{\pi} \zeta^2 \,\sin\theta\mathrm{d}\theta\mathrm{d}\varphi.$$

Let the disturbance of the radius ζ be

$$\begin{aligned}\zeta(\theta,\varphi,t) \quad &= \quad \sum_{n=2}^{\infty}\Bigg\{\sum_{m=0}^{n} a_{nm}(t)P_n^m(\cos\theta)\,\cos m\varphi \\ &\qquad + \sum_{m=1}^{n} b_{nm}(t)P_n^m(\cos\theta)\,\sin m\varphi\Bigg\},\end{aligned} \tag{8.10}$$

where $a_{nm}(t)$ and $b_{nm}(t)$ are surface modes. From the orthogonality properties of spherical harmonic functions (e.g. Lamb [7]) it follows that

$$\overline{\zeta} = 0 \quad \text{and} \quad \overline{\zeta^2} = \sum_n\sum_m \left(a_{nm}^2 + b_{nm}^2\right)\frac{1}{2n+1}\frac{(n+m)!}{(n-m)!}. \tag{8.11}$$

There is no first order contribution to the volume. We are interested in the surface energy due to shape oscillations and not due to changes in volume. Avoiding a mean source term in the velocity potential requires a small correction to the 'undisturbed radius' of 'second order'

$$a_0(t) = a\left[1 - \overline{\zeta^2}/a^2\right], \tag{8.12}$$

where the radius a is related to $V(t) = \frac{4}{3}\pi a^3$. This correction needs to be taken into account when calculating the surface energy. The instantaneous area of the surface of the bubbles is given by

$$S = \int_0^{2\pi} \int_0^{\pi} \sqrt{1 + \left(\frac{1}{R}\frac{\partial R}{\partial \theta}\right)^2 + \left(\frac{1}{R\sin\theta}\frac{\partial R}{\partial \varphi}\right)^2}\, R^2 \sin\theta \, \mathrm{d}\theta \mathrm{d}\varphi. \tag{8.13}$$

Hence, the linearized surface energy is

$$\begin{aligned} S &= 4\pi a_0^2 \left[1 + \overline{\zeta^2}/a_0^2\right] + 2\pi \left[\overline{\left(\frac{\partial \zeta}{\partial \theta}\right)^2 + \left(\frac{1}{\sin\theta}\frac{\partial \zeta}{\partial \varphi}\right)^2}\right] \\ &= 4\pi a^2 \left[1 + \tfrac{1}{2}(n-1)(n+2)\overline{\zeta^2}/a^2\right] \end{aligned} \tag{8.14}$$

from which the excess surface energy associated with the oscillations is found to be

$$\begin{aligned} \sigma\left(S - 4\pi a^2\right) &= 2\pi a^2 (n-1)(n+2)\,\sigma \\ &\quad \sum_n \sum_m \frac{a_{nm}^2 + b_{nm}^2}{a^2} \frac{1}{2n+1} \frac{(n+m)!}{(n-m)!}. \end{aligned} \tag{8.15}$$

The kinetic energy of the fluid can be calculated from the expression

$$T = -\tfrac{1}{2}\rho \int \Phi \nabla \Phi \cdot \mathbf{n} \, \mathrm{d}S. \tag{8.16}$$

The linearized kinetic energy is

$$\begin{aligned} T &= -\tfrac{1}{2}\rho\, a^2 \int_0^{2\pi} \int_0^{\pi} \left\{\Phi \frac{\partial \Phi}{\partial r}\right\}_{r=a} \sin\theta \, \mathrm{d}\theta \mathrm{d}\varphi \\ &= 2\pi \frac{n+1}{a^{2n-1}} \sum_n \sum_m \frac{c_{nm}^2 + d_{nm}^2}{a^2} \frac{1}{2n+1} \frac{(n+m)!}{(n-m)!}. \end{aligned} \tag{8.17}$$

Substituting the expression for the velocity potential (8.5) and the expression for the disturbance of the radius (8.10) into the kinematic condition (8.7) requires that

$$c_{nm} = -\frac{a^{n+2}}{n+1} \frac{\mathrm{d}a_{nm}}{\mathrm{d}t} \quad \text{and} \quad d_{nm} = -\frac{a^{n+2}}{n+1} \frac{\mathrm{d}b_{nm}}{\mathrm{d}t}. \tag{8.18}$$

Finally, consider the a_{nm} and b_{nm} as independent generalized coordinates, we can substitute the expressions (8.15) and (8.17) in Lagrange's equation. For generalized coordinate a_{nm} this is

$$\frac{d}{dt}\frac{\partial L}{\partial \dot{a}_{nm}} - \frac{\partial L}{\partial a_{nm}} = 0, \tag{8.19}$$

with

$$L = T - \sigma\left(S - 4\pi a^2\right),$$

and $\dot{a}$ representing the time derivative of a. The ‘equation of motion’ for a typical ‘coordinate’ a_{nm} then becomes

$$\frac{\mathrm{d}^2 a_{nm}}{\mathrm{d}t^2} - (n+1)(n-1)(n+2)\frac{\gamma}{\rho\, a^3}\, a_{nm} = 0, \tag{8.20}$$

by which the eigenfrequency from (8.3) is recovered.

8.3.2 Shape oscillations on an ellipsoidal bubble

Now we follow an identical approach for the shape oscillations of an ellipsoidal bubble. First look at the surface energy and kinetic energy to second order, then calculate the second order contribution to the volume of the bubble.

Appendix B in chapter 7 provides general information on the flow around oblate spheroids in an ellipsoidal coordinate system. Let the bubble surface in an ellipsoidal coordinate system be specified by

$$\mu = \mu(\theta, \varphi, t),$$

where μ is the variable perpendicular to the surface of the ellipsoid, θ the variable tangent to the surface and φ the angle around the symmetry axis. Surfaces $\mu =$ constant form a family of oblate spheroids.

The kinematic boundary condition becomes

$$\begin{aligned} \frac{\partial \mu}{\partial t} &+ \frac{1}{k^2(\sinh^2\mu + \cos^2\theta)}\,\frac{\partial \Phi}{\partial \theta}\,\frac{\partial \mu}{\partial \theta} \\ &+ \frac{1}{k^2\cosh^2\mu\,\sin^2\theta}\,\frac{\partial \Phi}{\partial \varphi}\,\frac{\partial \mu}{\partial \varphi} = \frac{1}{k^2(\sinh^2\mu + \cos^2\theta)}\,\frac{\partial \Phi}{\partial \mu}, \end{aligned} \tag{8.21}$$

to be satisfied on $\mu = \mu(\theta, \varphi, t)$. Suppose that without the shape oscillations the bubble has an oblate spheroidal shape $\mu = \mu_0$; the corresponding ratio of axes is $\chi = \coth \mu_0$. Let the perturbed surface of the bubble be given by

$$\mu(\theta, \varphi, t) = \mu_0 + \zeta(\theta, \varphi, t),$$

where ζ is small. Linearizing the kinematic boundary condition one obtains

$$\begin{aligned} \frac{\partial \zeta}{\partial t} &- \frac{1}{k^2(\sinh^2\mu_0 + \cos^2\theta)}\,\frac{\partial \Phi'}{\partial \mu} = \\ & \frac{1}{k^2(\sinh^2\mu_0 + \cos^2\theta)}\left(\frac{\partial^2 \Phi_0}{\partial \mu^2}\,\zeta - \frac{\partial \Phi_0}{\partial \theta}\,\frac{\partial \zeta}{\partial \theta}\right), \end{aligned} \tag{8.22}$$

to be satisfied on $\mu = \mu_0$; here we have set

$$\Phi(\mu, \theta, \varphi, t) = \Phi_0(\mu, \theta) + \Phi'(\mu, \theta, \varphi, t), \tag{8.23}$$

where Φ_0 denotes the undisturbed velocity potential and Φ' a small disturbance to it.

The undisturbed velocity potential Φ_0 forces the bubble to have an oblate ellipsoidal shape. We now set $\Phi_0 = 0$ and retain the oblate ellipsoidal shape by assuming a certain aspect ratio. With a constant surface tension a sphere is the only equilibrium shape in a quiescent liquid. A variable surface tension along the surface can make an ellipsoidal shape an equilibrium one. This implies that the surface tension has to change with the angle θ, which will be discussed later on. The linearized kinematic boundary condition now reduces to

$$\frac{\partial \zeta}{\partial t} - \frac{1}{k^2(\sinh^2\mu_0 + \cos^2\theta)}\,\frac{\partial \Phi'}{\partial \mu} = 0. \tag{8.24}$$

If the flow potential takes the form

$$\Phi'(\mu, \theta, \varphi, t) = \sum_{n=0}^{\infty}\sum_{m=0}^{n} c_{nm} Q_n^m(\sinh\mu) P_n^m(\cos\theta)\cos m\varphi \tag{8.25}$$

this corresponds to

$$\zeta(\theta, \varphi, t) = \sum_{n=2}^{\infty}\sum_{m=0}^{n} \frac{a_{nm}}{k^2(\sinh^2\mu_0 + \cos^2\theta)} P_n^m(\cos\theta)\cos m\varphi \tag{8.26}$$

with

$$c_{nm} = \frac{1}{\{\mathrm{d}Q_n^m/\mathrm{d}\mu\}_{\mu_0}}\,\frac{\mathrm{d}a_{nm}}{\mathrm{d}t}.$$

The shape oscillation frequency will be calculated for the axisymmetric modes only. Hence $m = 0$ and the φ-dependence vanishes.

Surface energy

Following the notation given in Kuipers & Timman [6] the surface area is

$$S = \int_0^{2\pi}\int_0^{\pi} \sqrt{EG - F^2}\,\mathrm{d}\theta\mathrm{d}\varphi. \tag{8.27}$$

Expressions for E, G, and F are given in appendix C of chapter 7. For our oblate ellipsoidal bubble this reduces to:

$$S = 2\pi\int_0^{\pi} \sqrt{EG}\mathrm{d}\theta = 2\pi\int_{-1}^{1} b\sqrt{E}\mathrm{d}\cos\theta, \tag{8.28}$$

with

$$E = b^2\cos^2\theta + c^2\sin^2\theta + 2\left(bb_\theta - cc_\theta\right)\sin\theta\cos\theta + b_\theta^2\sin^2\theta + c_\theta^2\cos^2\theta.$$

and

$$\begin{aligned} b &= k\cosh\mu, \\ c &= k\sinh\mu. \end{aligned}$$

Appendix A gives the detailed calculation of the surface to second order. The surface energy is

$$\begin{aligned} \sigma S = 2\pi\sigma k^2 \int_{-1}^{1} \quad & \left[\cosh\mu_0\left(\sinh^2\mu_0 + \cos^2\theta\right)^{1/2}\right] + \\ & \left[\left(\sinh^2\mu_0 + \cos^2\theta\right)^{-1/2}\cosh^2\mu_0\sinh\mu_0\zeta + \right. \\ & \left. \sinh\mu_0\left(\sinh^2\mu_0 + \cos^2\theta\right)^{1/2}\zeta\right] + \\ & \left[\frac{1}{2}\left(\sinh^2\mu_0 + \cos^2\theta\right)^{-1/2}\cosh\mu_0\right. \\ & \left(\sinh^2\mu_0 + \cosh^2\mu_0\right)\zeta^2 + \\ & \frac{1}{2}\left(\sinh^2\mu_0 + \cos^2\theta\right)^{1/2}\cosh\mu_0\zeta_\theta^2 - \\ & \frac{1}{2}\left(\sinh^2\mu_0 + \cos^2\theta\right)^{-3/2}\cosh^3\mu_0\sinh^2\mu_0\zeta^2 + \\ & \left(\sinh^2\mu_0 + \cos^2\theta\right)^{-1/2}\cosh\mu_0\sinh^2\mu_0\zeta^2 + \\ & \left.\frac{1}{2}\left(\sinh^2\mu_0 + \cos^2\theta\right)^{1/2}\cosh\mu_0\zeta^2\right] \mathrm{d}\cos\theta. \end{aligned} \tag{8.29}$$

Here the first term between brackets ([..]) is the zeroth order, the second term the first order, and the third term the second order contribution to the surface energy.

The excess surface energy is the second order contribution to the surface energy. In the spherical case the first order contribution to the surface energy vanishes; later in this section we will see this is also the case for the ellipsoidal bubble if we allow for a variable surface tension over the bubble surface.

Kinetic energy

The kinetic energy of the fluid is

$$T = -\frac{1}{2}\rho\int_V \left|\nabla\Phi\right|^2 dV = -\rho\pi k\cosh\mu_0\int_{-1}^{1}\Phi\Phi_\mu \mathrm{d}\cos\theta. \tag{8.30}$$

Using the expression for the kinematic boundary condition (8.24) and the flow potential Φ' (8.25) the kinetic energy is

$$T = -\rho\pi k \cosh\mu_0 \int_{-1}^{1} \sum_n \left[\frac{da_n}{dt} Q_n P_n \bigg/ \frac{dQ_n}{d\mu}\right] \sum_n \left[\frac{da_n}{dt} P_n\right] \mathrm{d}\cos\theta. \quad (8.31)$$

Using the orthogonality conditions for the Legendre polynomials the kinetic energy for every mode can be written as

$$T = -\rho\pi k \cosh\mu_0 Q_n \left(\frac{\mathrm{d}Q_n}{\mathrm{d}\mu}\right)^{-1} \frac{2}{2n+1} \left(\frac{\mathrm{d}a_n}{\mathrm{d}t}\right)^2. \quad (8.32)$$

Volume of an ellipsoidal bubble

The volume of an oblate ellipsoidal bubble is:

$$\begin{aligned} V &= \int_0^{\mu}\int_0^{\pi}\int_0^{2\pi} h_\mu h_\theta h_\varphi d\mu d\theta d\varphi = \\ & 2\pi k^3 \int_{-1}^{1} \left(\frac{1}{3}\sinh^3\mu + \cos^2\theta \sinh\mu\right) \mathrm{d}\cos\theta. \end{aligned} \quad (8.33)$$

To second order the volume is

$$\begin{aligned} V = 2\pi k^3 \int_{-1}^{1} & \left(\frac{1}{3}\sinh^3\mu_0 + \cos^2\theta\sinh\mu_0\right) + \\ & \cosh\mu_0 \left(\sinh^2\mu_0 + \cos^2\theta\right)\zeta + \\ & \left(\frac{1}{2}\sinh^3\mu_0 + \sinh\mu_0\cosh^2\mu_0 + \frac{1}{2}\cos^2\theta\sinh\mu_0\right)\zeta^2 \mathrm{d}\cos\theta. \end{aligned} \quad (8.34)$$

The second order volume correction to the surface energy can be calculated using several approaches which are used in the spherical case. Two will be discussed here: firstly the idea of Rayleigh [16] will be followed; this approach was also discussed earlier in this section. Secondly, the approach of Benjamin [2] will be discussed.

Volume correction according to Rayleigh
Considering the expression for the perturbation ζ (8.26), now the first order contribution to the volume is zero. Hence the volume is

$$\begin{aligned} V &= \frac{4}{3}\pi k^3 \sinh\mu_0 \cosh^2\mu_0 + \\ & 2\pi k^3 \int_{-1}^{1} \left(\frac{1}{2}\sinh\mu_0\left(\sinh^2\mu_0 + \cos^2\theta\right) + \sinh\mu_0\cosh^2\mu_0\right)\zeta^2 \mathrm{d}\cos\theta. \end{aligned} \quad (8.35)$$

We now define an effective $\tilde{k}$ by $V = \frac{4}{3}\pi\tilde{k}^3 \sinh\mu_0 \cosh^2\mu_0$. Here k and the 'undisturbed' $\tilde{k}$ can be different. Avoiding a mean source term in the velocity potential requires a small correction to the undisturbed $\tilde{k}$ of second order

$$\begin{aligned} k &= \tilde{k} - \frac{1}{2}\frac{\tilde{k}}{\sinh\mu_0\cosh^2\mu_0} \\ &\quad \int_{-1}^{1}\left(\frac{1}{2}\sinh\mu_0\left(\sinh^2\mu_0+\cos^2\theta\right)+\sinh\mu_0\cosh^2\mu_0\right)\zeta^2 \mathrm{d}\cos\theta. \end{aligned} \tag{8.36}$$

The surface energy scales with k^2. Therefore we write

$$\begin{aligned} k^2 &= \tilde{k}^2 - \frac{\tilde{k}^2}{\sinh\mu_0\cosh^2\mu_0} \\ &\quad \int_{-1}^{1}\left(\frac{1}{2}\sinh\mu_0\left(\sinh^2\mu_0+\cos^2\theta\right)+\sinh\mu_0\cosh^2\mu_0\right)\zeta^2 \mathrm{d}\cos\theta. \end{aligned} \tag{8.37}$$

The volume correction to the surface energy (σS_{Ray}) consists of the second order contribution to k^2 and the zeroth order surface energy contribution (see (8.29)), i.e.

$$\begin{aligned} \sigma S_{Ray} &= 2\pi\sigma\frac{\tilde{k}^2}{\sinh\mu_0\cosh^2\mu_0} \\ &\quad \int_{-1}^{1}\left(\frac{1}{2}\sinh\mu_0\left(\sinh^2\mu_0+\cos^2\theta\right)+\sinh\mu_0\cosh^2\mu_0\right)\zeta^2 \mathrm{d}\cos\theta \\ &\quad \int_{-1}^{1}\left(\cosh\mu_0\left(\sinh^2\mu_0+\cos^2\theta\right)^{1/2}\right)\mathrm{d}\cos\theta. \end{aligned} \tag{8.38}$$

Volume correction according to Benjamin

Benjamin [2] assumes a second order contribution to the spherical radius

$$R(\theta,t) = a + \zeta(\theta,t) + \delta(t), \;\; \delta(t) \sim O(\epsilon^2). \tag{8.39}$$

For the ellipsoidal case this would be

$$\mu(\theta,t) = \mu_0 + \zeta(\theta,t) + \delta(t), \;\; \delta(t) \sim O(\epsilon^2). \tag{8.40}$$

The volume to second order gives

$$\begin{aligned} V &= 2\pi k^3 \int_{-1}^{1}\left[\left(\frac{1}{3}\sinh^3\mu_0 + \cos^2\theta\sinh\mu_0\right) + \right. \\ &\quad \cosh\mu_0\left(\sinh^2\mu_0+\cos^2\theta\right)\delta + \\ &\quad \left.\left(\frac{1}{2}\sinh^3\mu_0 + \sinh\mu_0\cosh^2\mu_0 + \frac{1}{2}\cos^2\theta\sinh\mu_0\right)\zeta^2\right]\mathrm{d}\cos\theta. \end{aligned} \tag{8.41}$$

Notice there is an extra second order contribution due to δ. For the volume to be constant δ must statisfy

$$\begin{aligned}\delta \;&=\; -\int_{-1}^{1}\left(\frac{1}{2}\sinh^3\mu_0+\sinh\mu_0\cosh^2\mu_0+\frac{1}{2}\cos^2\theta\sinh\mu_0\right)\zeta^2 d\cos\theta\\ &\left[\int_{-1}^{1}\cosh\mu_0\left(\sinh^2\mu_0+\cos^2\theta\right)\mathrm{d}\cos\theta\right]^{-1}. \qquad (8.42)\end{aligned}$$

Now the extra second order contribution to the surface energy (σS_{Ben}) to account for a constant volume is

$$\begin{aligned}\sigma S_{Ben} = 2\pi\sigma k^2\delta\int_{-1}^{1}&\left[\left(\sinh^2\mu_0+\cos^2\theta\right)^{-1/2}\cosh^2\mu_0\sinh\mu_0+\right.\\ &\left.\sinh\mu_0\left(\sinh^2\mu_0+\cos^2\theta\right)^{1/2}\right]\mathrm{d}\cos\theta. \qquad (8.43)\end{aligned}$$

So, for the volume correction one can choose between (8.38) and (8.43).

Variable surface tension

We assumed $\Phi_0 = 0$ and an oblate ellipsoidal shape. Because there is no flow around the bubble the pressure is equal outside the bubble; this would imply a spherical bubble. We adjust the surface tension according to the curvature of the ellipsoid in order to match the equal pressure difference along the surface.

We know

$$\sigma\nabla\cdot\mathbf{n} = \Delta P, \qquad (8.44)$$

for a spherical bubble this becomes

$$\sigma_0\frac{2}{a_{eq}} = \Delta P, \qquad (8.45)$$

with a_{eq} the equivalent radius. Hence, for constant pressure difference, the surface tension for an ellipsoidal bubble is

$$\sigma(\theta) = \frac{2\sigma_0}{a_{eq}\nabla\cdot\mathbf{n}}. \qquad (8.46)$$

Using appendix C in chapter 7 this becomes

$$\sigma(\theta) = \sigma_0\left[2\frac{\sqrt{\chi^2-1}}{\chi^{2/3}}\frac{\left(\sinh^2\mu_0+\cos^2\theta\right)^{3/2}}{\sinh\mu_0\cosh\mu_0+\frac{\sinh\mu_0}{\cosh\mu_0}\left(\sinh^2\mu_0+\cos^2\theta\right)}\right]. \qquad (8.47)$$

Using this expression the first order contribution to the surface energy (8.29) becomes zero.

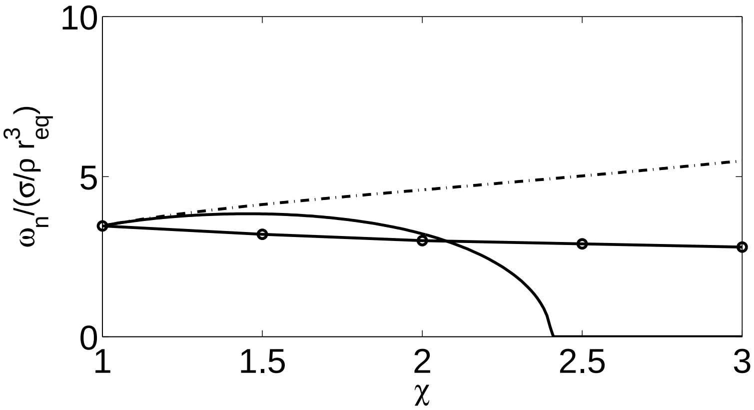

Figure 8.11: The non-dimensional frequency for the shape oscillations of mode (2,0) versus the aspect ratio of the bubble. – the result using (8.38) for the volume correction, ·-· the result using (8.43) for the volume correction, and o–o Meiron's result.

Shape oscillation frequency

Averaged over an oscillation period the surface energy and kinetic energy are equal. The second order part of the surface energy can be taken from (8.29). An extra second order surface contribution follows from the volume correction in (8.38) or (8.43). The kinetic energy, which is already of second order, is given in (8.32). The oscillation frequency follows from

$$\omega_n^2 = \frac{\langle \sigma S \rangle}{\langle T \rangle}. \tag{8.48}$$

For every mode the energies can be calculated separately as a function of the aspect ratio of the undisturbed oblate ellipsoidal bubble. Figure 8.11 shows the axisymmetric shape oscillations of mode 2 as a function of the aspect ratio. The spherical case is correct, but for higher aspect ratio the results deviate for the calculation of Meiron and experiments (see figure 8.10). What is also striking is the different results using the volume correction following Rayleigh's approach or Benjamin's approach. Both approaches have a similar positive slope at χ=1, but deviate at larger aspect ratios.

To the authors' knowledge Meiron's results can only partially be verified with an analytical approach of Feng [3], who studied the change of shape and volume oscillation frequencies for a small deviation from the spherical shape. For a mode 2 shape oscillation he found the following relation

$$\omega_2 = \omega_{2,sph}\left[1 - 0.0658U^2\right] \quad U \ll 1, \tag{8.49}$$

with $\omega_{2,sph}$ the shape oscillation frequency of the spherical bubble and U the bubble velocity. The frequencies decrease as the velocity around the bubble, and therefore the aspect ratio, increases. He explained this as follows: *"The phenomenon may be mainly caused by an overall reduction in the surface restoring force, because of the quiescent expansion of the bubble volume and reduction in the pressure...*" So, our calculation seems to be incorrect. This might be due to the assumption to set the undisturbed potential Φ_0 to zero and vary the surface tension to come to the correct ellipsoidal ground shape of the bubble. In further research we might have to take into account contributions of Φ_0 to the surface energy, but this complicates the calculations substantially.

The results of our calculation suggest that the surface energy is not calculated correctly for aspect ratios larger than one. Therefore a hypothetical case is tested where the kinetic energy is calculated according to (8.32) and the surface energy is set to the value of a spherical bubble. Hence it can be calculated from (8.15), which has to be slightly changed because the disturbance ζ has the unit of meter in the spherical calculation, whereas it has no unit in the ellipsoidal calculation. The frequency resulting from this approach is

$$\omega_n^2 = \frac{\langle \sigma S \rangle}{\langle T \rangle} = \frac{\sigma}{\rho a_{eq}^3} \frac{\chi^{2/3}}{\sqrt{\chi^2 - 1}} \frac{(n-1)(n+2)}{\cosh \mu_0} \frac{\mathrm{d}Q_n}{\mathrm{d}\mu} Q_n^{-1}. \tag{8.50}$$

Surprisingly this expression yields the same frequencies as the numerical calculations of Meiron for $n = 1, 2, 3, ...$. So, it seems that the second order surface energy does not change for changing aspect ratio if we assume Meiron's results to be correct; this is remarkable and cannot be explained this at this moment.

The results of the calculations in this section give rise to many questions, but also give new insight in the shape oscillations on ellipsoidal bubbles; it could therefore serve as a basis for further research.

The approach to take the average of the kinetic energy and the surface energy in order to calculate oscillation frequencies can also be used to calculate volume oscillation frequencies. In appendix B an analytical expression for the volume oscillation frequency of an oblate ellipsoidal bubble is derived using this approach.

8.4 Conclusion

The previous chapter dealt with bubbles of fixed ellipsoidal shape. In the present chapter the bubble diameter is increased and shape oscillations set in. For bubble sizes just after the onset of shape oscillations two modes are found: an axisymmetric mode (2,0) and a non-axisymmetric mode (2,2). For larger bubbles, besides modes (2,0) and (2,2), more shape oscillation modes are detected.

The bubble motion is affected by the shape oscillations. The mode (2,0) is linked with the bubble velocity. For bubble sizes right at the onset of shape oscillations, the stable spiraling motion changes into a pure zigzagging motion because the mode (2,2) forces the bubble to rise in a zigzag when this mode is a multiple of the path frequency. Larger bubbles rise in more or less spiraling paths, but now with large variations in velocity. Finally, multiple oscillations force the bubble into an erratic path.

Wake oscillations link with velocity oscillations and therefore the mode (2,0) oscillations. Experiments in tap water reveal that shape oscillations remain the same as in purified water, but velocity oscillations are no longer linked with shape oscillations, they drop to twice the path frequency as do the wake oscillations. In the previous chapter we observed wake instabilities behind bubbles without shape oscillations. Thus wake oscillations are not coupled with shape oscillations; this coupling is only through oscillations in the velocity.

The analytical method to calculate shape oscillations on spherical bubbles (e.g. [2, 7]) is extended to shape oscillations on ellipsoidal bubbles by calculating the surface and kinetic energies of an oscillating bubble. The limiting case for aspect ratio one is calculated correctly but the method results in deviations from the numerical theory by Meiron [13] for higher aspect ratios. Surprisingly when the second order surface energy is assumed to be equal to the value of the spherical case for all aspect ratios our results are identical to those of Meiron. This is a remarkable finding which should be investigated thoroughly in further research.

Appendix A: Surface of an oblate spheroid to second order

This appendix deals with the calculation of the surface of an oblate spheroid to second order. The result can be used to calculate the surface energy in the calculation of the shape oscillation frequency of an oblate spheroid.

From appendix C in chapter 7 we know that the area of surface of an oblate ellipsoidal bubble is

$$S = 2\pi \int_0^{\pi} \sqrt{EG}d\theta = 2\pi \int_{-1}^{1} b\sqrt{E}\mathrm{d}\cos\theta, \tag{8.51}$$

with

$$E = b^2\cos^2\theta + c^2\sin^2\theta + 2(bb_\theta - cc_\theta)\sin\theta\cos\theta + b_\theta^2\sin^2\theta + c_\theta^2\cos^2\theta,$$

and

$$b(\theta,\varphi) = k\cosh\mu(\theta,\varphi), \qquad c(\theta,\varphi) = k\sinh\mu(\theta,\varphi).$$

In oblate ellipsoidal coordinates (μ, θ, φ) we assume the bubble surface to be given by

$$\mu(\theta,\varphi,t) = \mu_0 + \zeta(\theta,\varphi,t),$$

where ζ is small. Now calculate the surface to second order in ζ.

$$\begin{aligned}
b &= k\cosh(\mu+\zeta) = k\cosh\mu_0 + k\sinh\mu_0\zeta + \frac{1}{2}k\cosh\mu_0\zeta^2, \\
c &= k\sinh(\mu+\epsilon\zeta) = k\sinh\mu_0 + k\cosh\mu_0\zeta + \frac{1}{2}k\sinh\mu_0\zeta^2, \\
b_\theta &= k\sinh(\mu+\epsilon\zeta)\zeta_\theta = k\sinh\mu_0\zeta_\theta + k\cosh\mu_0\zeta\zeta_\theta, \\
c_\theta &= k\cosh(\mu+\zeta)\zeta_\theta = k\cosh\mu_0\zeta_\theta + k\sinh\mu_0\zeta\zeta_\theta, \\
bb_\theta &= k^2\cosh\mu_0\sinh\mu_0\zeta_\theta + k^2\left(\sinh^2\mu_0 + \cosh^2\mu_0\right)\zeta\zeta_\theta, \\
cc_\theta &= k^2\cosh\mu_0\sinh\mu_0\zeta_\theta + k^2\left(\sinh^2\mu_0 + \cosh^2\mu_0\right)\zeta\zeta_\theta, \\
bb_\theta - cc_\theta &= 0, \\
b^2 &= k^2\cosh^2(\mu+\zeta) = k^2\cosh^2\mu_0 + \\
&\quad 2k^2\cosh\mu_0\sinh\mu_0\zeta + k^2\left(\sinh^2\mu_0 + \cosh^2\mu_0\right)\zeta^2, \\
c^2 &= k^2\sinh^2(\mu+\zeta) = k^2\sinh^2\mu_0 + \\
&\quad 2k^2\cosh\mu_0\sinh\mu_0\zeta + k^2\left(\sinh^2\mu_0 + \cosh^2\mu_0\right)\zeta^2, \\
b_\theta^2 &= k^2\sinh^2\mu_0\zeta_\theta^2, \\
c_\theta^2 &= k^2\cosh^2\mu_0\zeta_\theta^2.
\end{aligned}$$

Hence,

$$\begin{aligned}
E &= b^2\cos^2\theta + c^2\sin^2\theta + b_\theta^2\sin^2\theta + c_\theta^2\cos^2\theta \\
&= k^2\left[\left(\sinh^2\mu_0 + \cos^2\theta\right) + 2\cosh\mu_0\sinh\mu_0\zeta + \right. \\
&\quad \left.\left\{\left(\sinh^2\mu_0 + \cosh^2\mu_0\right)\zeta^2 + \left(\sinh^2\mu_0 + \cos^2\theta\right)\zeta_\theta^2\right\}\right]. \\
E^{1/2} &= k\left[\left(\sinh^2\mu_0 + \cos^2\theta\right)^{1/2} + \frac{1}{2}\left(\sinh^2\mu_0 + \cos^2\theta\right)^{-1/2}\right. \\
&\quad \left\{2\cosh\mu_0\sinh\mu_0\zeta + \left(\sinh^2\mu_0 + \cosh^2\mu_0\right)\zeta^2 + \left(\sinh^2\mu_0 + \cos^2\theta\right)\zeta_\theta^2\right\} - \\
&\quad \left.\frac{1}{2}\left(\sinh^2\mu_0 + \cos^2\theta\right)^{-3/2}\cosh^2\mu_0\sinh^2\mu_0\zeta^2\right].
\end{aligned}$$

Now the area of surface to second order is

$$\begin{aligned} S = 2\pi k^2 \int_{-1}^{1} \quad & \left[\cosh\mu_0 \left(\sinh^2\mu_0 + \cos^2\theta\right)^{1/2}\right] + \\ & \left[\left(\sinh^2\mu_0 + \cos^2\theta\right)^{-1/2} \cosh^2\mu_0 \sinh\mu_0 \zeta + \right. \\ & \left. \sinh\mu_0 \left(\sinh^2\mu_0 + \cos^2\theta\right)^{1/2} \zeta\right] + \\ & \left[\frac{1}{2}\left(\sinh^2\mu_0 + \cos^2\theta\right)^{-1/2} \cosh\mu_0 \right. \\ & \left(\sinh^2\mu_0 + \cosh^2\mu_0\right) \zeta^2 + \\ & \frac{1}{2}\left(\sinh^2\mu_0 + \cos^2\theta\right)^{1/2} \cosh\mu_0 \zeta_\theta^2 - \\ & \frac{1}{2}\left(\sinh^2\mu_0 + \cos^2\theta\right)^{-3/2} \cosh^3\mu_0 \sinh^2\mu_0 \zeta^2 + \\ & \left(\sinh^2\mu_0 + \cos^2\theta\right)^{-1/2} \cosh\mu_0 \sinh^2\mu_0 \zeta^2 + \\ & \left. \frac{1}{2}\left(\sinh^2\mu_0 + \cos^2\theta\right)^{1/2} \cosh\mu_0 \zeta^2\right] \mathrm{d}\cos\theta. \end{aligned} \tag{8.52}$$

Here the first term between brackets ([..]) is the zeroth order, the second term the first order, and the third term the second order contribution to the surface.

Appendix B: Oblate spheroid with volume oscillations

For a spherical bubble the frequency of volume oscillation has been calculated by Minnaert [15]. For the ellipsoidal bubble an expression for the frequency will be calculated and compared with the results of Strasberg [19] . Therefore the reader is referred to Milne-Thomson [14, p. 543, example 34], where the potential is given for an ellipsoid with volume oscillation

$$\Phi = -\frac{1}{6}abc\left(\frac{\dot{a}}{a} + \frac{\dot{b}}{b} + \frac{\dot{c}}{c}\right)\int_{\lambda}^{\infty} \frac{\mathrm{d}\lambda}{[(a^2+\lambda)(b^2+\lambda)(c^2+\lambda)]^{1/2}}. \tag{8.53}$$

The relation between λ and the aspect ratio $\chi = \frac{a}{b}$ is

$$\sqrt{a^2+\lambda} = \frac{b\chi}{\chi^2-1} \text{ and } \sqrt{b^2+\lambda} = \frac{b\chi^2}{\chi^2-1}. \tag{8.54}$$

For an oblate ellipsoid the flow potential becomes

$$\Phi = -\frac{1}{6}a^2 b\left(\frac{2\dot{a}}{a} + \frac{\dot{b}}{b}\right)\sqrt{\chi^2-1}\left[\frac{2\arctan\sinh\mu - \pi}{b\chi}\right]. \tag{8.55}$$

Assume that the axis behave like

$$\begin{aligned} a &= a_0(1+\epsilon\cos(\omega t)), \\ b &= b_0(1+\epsilon\cos(\omega t)), \end{aligned} \tag{8.56}$$

with ϵ a small constant. The potential energy is

$$E_{pot} = p_\infty(V-V_0) - \int_{V_0}^{V} p\mathrm{d}V. \tag{8.57}$$

The volume can be written as

$$V = \frac{4}{3}\pi a_0^2 b_0 (1+\epsilon\cos(\omega t))^3. \tag{8.58}$$

Hence,

$$V - V_0 = \frac{4}{3}\pi a_0^2 b_0 \left[3\epsilon\cos(\omega t) + 3\epsilon^2\cos^2(\omega t) + \epsilon^3\cos^3(\omega t)\right]. \tag{8.59}$$

If we assume adiabatic behavior, we can say

$$pV^\gamma = p_\infty V_0^\gamma \Rightarrow p = p_0\left(\frac{V_0}{V}\right)^\gamma, \tag{8.60}$$

with γ is the ratio of the heat capacities. Hence,

$$\begin{aligned} -\int_{V_0}^{V} p\mathrm{d}V &= -\frac{p_\infty V_0}{1-\gamma}\left[\left(\frac{V_0}{V}\right)^{\gamma-1} - 1\right] \\ &= -p_\infty V_0\left[3\epsilon\cos(\omega t) + \frac{3}{2}(2-3\gamma)\epsilon^2\cos^2(\omega t) + O(\epsilon^3)\right]. \end{aligned} \tag{8.61}$$

The potential energy now becomes

$$E_{pot} = \frac{9}{2}p_\infty V_0 \gamma \epsilon^2 \cos^2\omega t. \tag{8.62}$$

The kinetic energy is

$$T = -\frac{1}{2}\rho\int_V |\nabla\Phi|^2\, dV = -\rho\pi k\cosh\mu_0 \int_{-1}^{1} \Phi\Phi_\mu \mathrm{d}\cos\theta. \tag{8.63}$$

Substituting the flow potential from (8.55) in this equation yields

$$T = \frac{\rho\pi}{\sqrt{a_0^2 - b_0^2}}\left\{\pi - 2\arctan(\sinh(\mu_0))\right\} a_0^4 b_0^2 \omega^2 \sin^2(\omega t)\epsilon^2. \tag{8.64}$$

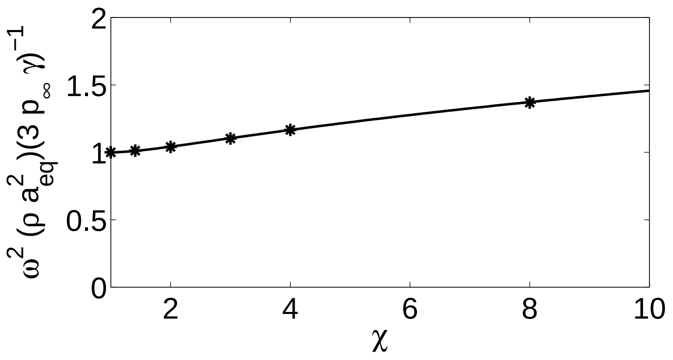

Figure 8.12: The non-dimensionalized frequency of the volume oscillations as function of the aspect ratio of the bubble. – Equation (8.65) and * data taken from Strasberg [19].

Taking the time averaged energies over an oscillation period and taking the potential energy to be equal to the kinetic energy the volume oscillation frequency as function of the aspect ratio is

$$\omega^2 = \left(3\frac{p_\infty\gamma}{\rho a_{eq}^2}\right)\frac{\sqrt{\chi^2-1}}{\chi^{2/3}}\frac{1}{\cot^{-1}\left(\frac{1}{\sqrt{\chi^2-1}}\right)}. \tag{8.65}$$

The frequency is increasing with the aspect ratio. Figure 8.12 shows that this equation gives similar values for the volume oscillation frequency as Strasberg [19].

References

[1] ABRAMOWITZ, M. & STEGUN, I.A. 1965 *Handbook of mathematical functions*. Dover Publications, New York, USA.

[2] BENJAMIN, T.B. 1989 Note on shape oscillations of bubbles. *J. Fluid Mech.* **203**, 419–424.

[3] FENG, J.Q. 1992 The oscillations of a bubble moving in an inviscid fluid. *J. Appl. Math.* **52**, 1–14.

[4] FENG, Z.C. & LEAL, L.G. 1997 Nonlinear bubble dynamics. *Annu. Rev. Fluid Mech.* **29**, 201–243.

[5] HARTUNIAN, R.A. & SEARS, W.R. 1957 On the instability of small gas bubbles moving uniformly in various liquids. *J. Fluid Mech.* **3**, 27–47.

[6] KUIPERS, L. & TIMMAN, R. 1963 *Handboek der Wiskunde*. Scheltema & Holkema, Amsterdam, the Netherlands.

[7] LAMB, H. 1932 *Hydrodynamics*, 6th edn. Cambridge University Press, USA.

[8] LINDT, J.T. 1972 On the periodic nature of the drag of a rising bubble. *Chem. Eng. Sci.* **27**, 1775–1781.

[9] LONGUET-HIGGINS, M.S. 1989 Monopole emission of sound by asymetric bubble oscilations. Part 1. Normal modes. *J. Fluid Mech.* **201**, 525–541.

[10] LUNDE, K. & PERKINS, R.J. 1997 Observations on wakes behind spheroidal bubbles and particles. , vol. FEDSM97, p. 3530.

[11] LUNDE, K. & PERKINS, R.J. 1998 Shape oscillations of rising bubbles. *Appl. Sci. Res.* **58**, 387–408.

[12] MAGNAUDET, J. & EAMES, I. 2000 The motion of high-Reynolds-number bubbles in inhomogeneous flows. *Annu. Rev. Fluid Mech.* **32**, 659–708.

[13] MEIRON, D.I. 1989 On the stability of gas bubbles rising in an inviscid fluid. *J. Fluid Mech.* **198**, 101–114.

[14] MILNE-THOMSON, L.M. 1996 *Theoretical Hydrodynamics*, 5th edn. Dover Publications, New York, USA.

[15] MINNAERT, M. 1933 On musical air bubbles and sounds of running water. *Phil. Mag.* **16**, 235–248.

[16] RAYLEIGH, LORD 1879 On the capillary phenomena of jets. *Proc. R. Soc. Lond.* **29**, 71–97.

[17] SAFFMAN, P.G. 1956 On the rise of small air bubbles in water. *J. Fluid Mech.* **1**, 249–275.

[18] SHAW, S.J. 1994 Surface mode deformations on an oscillating bubble. In *Bubble Dynamics and Interface Phenomena* (ed. J.R. Blake et al. (eds.)), pp. 355–363. Kluwer Academic Publishers, the Netherlands.

[19] STRASBERG, M. 1953 The pulsation frequency of nonspherical gas bubbles in liquids. *J. Acoust. Soc. Am.* **25**, 536–539.

[20] DE VRIES, J., LUTHER, S. & LOHSE, D. 2002 Induced bubble shape oscillations and their impact on the rise velocity. *Eur. Phys. J. B* **29**, 503–509.

Chapter 9

Conclusions and outlook

In chapter 1 several aspects on solid sphere and bubble motion were discussed which continue to raise many questions in the research community. This thesis addressed several of these aspects and answered some of the open research questions, which were related to the different motions, shapes and wake structures of these bodies, the forces acting on these bodies and the interacting between path, wake and shape instabilities. This chapter will provide a general discussion of the previous conclusions in each chapter and will focus on recommendations for future research on sphere and bubble motion.

Chapter 3 focused on flow visualizations of the wake behind solid spheres moving under the action of gravity. This research revealed differences with the wakes behind spheres held fixed, studied by Schouveiler & Provansal [15] and Johnson & Patel [7]. The wake behind some heavy falling spheres clearly shows hairpin vortices shedding from the sphere surface, whereas the wake behind other falling spheres and rising spheres is not dominated by vortex shedding. There is a continuous formation of vorticity into two vortex threads of opposite-signed vorticity. These threads cross and kinks are formed on these threads that finally develop into hairpin vortex like structures. Hence, with respect to the wake structure to be developed, the sphere-fluid density ratio is important. The experiments presented in this thesis show that rising spheres are more susceptible to instabilities in the wake and their path is influenced by these instabilities. For all spheres the double-threaded wake structure seems to be a basic feature, even for large Reynolds numbers. Chapter 5 investigated the effect of the density ratio on both sphere path and wake more thoroughly.

In chapter 4 the proposal, given originally by Karamanev & Nikolov [9], to replace the standard drag relation by $C_D(Re) = 0.95$, for spheres with a density ratio $\rho_s/\rho < 0.3$ and $Re > 130$, was examined. The experiments with spheres for which $\rho_s/\rho \approxeq 0.02$ showed a rather poor agreement with this proposal. This is consistent with the view that it is more appropriate to replace the standard drag curve by a series of curves parameterized by the value of ρ_s/ρ. Each of these curves starting off from the standard drag curve at a higher Reynolds number than 130, namely between $Re = 205.8$ and $Re = 211.9$. These values are directly related to the work of Dušek [6] who found that the onset of path instability for freely moving spheres depends on the density ratio and occurs between $Re = 205.8$ and $Re = 211.9$. For any individual case above these Reynolds numbers a substantial difference may be found between the measured drag and the drag given by the standard drag relation. This difference is largest for light spheres, because these spheres do not rise along any preferred path once path oscillations set in. It was proposed, and verified with experiments, that the drag force consists of (i) a viscous contribution that may be estimated from the standard drag curve by evaluating the Reynolds number using the actual value of the velocity, and (ii) an inertial contribution that arises essentially by the same mechanisms that cause the lift-induced drag on airplane wings.

The study on freely rising spheres is connected with work done on vortex-induced vibrations, especially with studies of the motion of elastically mounted and tethered spheres. The description of the origin of the lift force on such spheres in Govardhan & Williamson [4] is essentially similar to the one presented in this thesis. It would be interesting to combine their DPIV measurements of the sphere wakes with the simple model of the drag force. It may even be possible to estimate the vortex-flow forces experienced by the spheres on using the expressions derived by Kambe [8] and Howe [5].

In chapter 5 the numerical work of Dušek and co-workers [6] was verified. Their work is the first to give a detailed analysis of the instabilities and transitions in the motion of spheres moving freely under the action of gravity. The observations made in this thesis agree very well with their description of the quite distinct features of sphere motion in different regimes of the $(G, \rho_s/\rho)$ parameter space.

The Schlieren flow visualizations did not recover the finding of Dušek *et al.* on the absence of a bifid wake behind the spheres after the path instability has set in. In all the pictures the wake consists, entirely or in part, of two counter-rotating vortices as can also be seen in earlier studies on the wake structures of freely moving spheres in chapter 3.

Dušek *et al.* [6] showed that the transient state for freely moving spheres can be rather long; hence the Schlieren experiments presented in this thesis, carried out in a small tank of 50 cm in height, might be carried out in this transient state.

Therefore an enlargement of the water tank in the Schlieren setup is an important issue for future research. Furthermore, the Schlieren technique limits the field of view to the diameter of the largest lens, 10 cm. To capture low frequency wake oscillations, as were found by Dušek *et al.*, this field of view should be enlarged.

Chapters 3 to 5 clearly show the importance of the sphere and fluid properties when looking at sphere motion. The study of Dušek *et al.* and the present experimental verification make clear that the motion of spheres can be completely different depending on the value of the parameters sphere-fluid density ratio ρ_s/ρ and Galileo number G. This will also have its effect on the wake behind the sphere and the drag experienced by it. The use of one ’standard’ drag curve for all spheres, which only depends on the Reynolds number, is therefore incorrect. Future research should provide drag curves parameterized by G and ρ_s/ρ (or Re and G or ρ_s/ρ and Re) to account for this difference in sphere motion.

Chapter 6 showed the general aspects of single bubble motion. The bubble path changes from a stable spiral into a pure zigzag when shape oscillations set in. The bubbles reach rise velocities as high as measured by Duineveld [2]; this is also reflected in the low drag coefficients. This justifies the statement that the experiments were carried out in ultra clean water. It is shown that the minimum radius of curvature of the bubble shape is a better measure for the rise velocity of the bubble than the bubble aspect ratio, as was put forward by Duineveld.

Chapter 7 focussed on bubbles that rise without shape oscillations. The bubbles rise with their minor axis aligned with the path, as was also observed by Ellingsen & Risso [3]. Right after the onset of path instability the bubbles rise in a pure spiral, whereas for somewhat larger bubbles the path becomes flattened and the motion becomes unsteady.

For the purely spiraling bubbles the lift force in normal and bi-normal direction are equal; a feature which has not been reported before in an experimental study. Only numerical work by Mougin & Magnaudet [14] shows identical results. Analysis of the orientation of the vortex plane behind a spiraling bubble confirms this equality of lift in normal and bi-normal direction. Implementing this feature into the equations of motion for a purely spiraling bubble yields a simple relation between the characteristics of the spiral and the shape of the bubble; this shows that only a limited number of combinations of spiral frequency, pitch, and radius is possible.

Analysis of the vorticity structure behind spiraling bubbles reveals that the wake consists of two counter-rotating vortex threads, which account for the lift necessary to curve the bubble path. Analysis of the strength of these threads enables us to estimate the lift force; the estimate is in good agreement with the experiments. Furthermore it is shown that the measured drag can be modelled with a contribution related to viscous drag and a contribution induced by the lift force, the lift-induced drag, which is induced instantaneously. This model for drag is similar to the case of spheres moving through a liquid, as discussed in chapter 4.

In chapter 8 the bubble diameter is increased and shape oscillations set in. For bubble sizes just after the onset of shape oscillations two shape oscillation modes are found: an axisymmetric mode (2,0) and a non-axisymmetric mode (2,2), as was also found by Lunde & Perkins [11]. For larger bubbles, besides frequencies for modes (2,0) and (2,2), more frequencies are detected. These frequencies cannot be linked with higher modes and are probably due to non-linear effects.

The bubble motion is affected by shape oscillations; the frequency of mode (2,0) is linked with the frequency of bubble velocity oscillations. For bubble sizes right at the onset of shape oscillations the stable spiraling motion changes into a purely zigzagging motion, because the mode (2,2) forces the bubble to rise in a zigzag when this mode is a multiple of the path frequency. Larger bubbles rise in more or less spiraling paths, but now with large variations in velocity. Finally multiple oscillations force the bubble into an erratic path.

Wake oscillations link with velocity oscillations and therefore the mode (2,0) oscillations. Experiments in tap water reveal that shape oscillations remain the same as in purified water, but velocity oscillations are no longer linked with shape oscillations, they drop to twice the path frequency as do the wake oscillations. In chapter 7 it is observed that wake instabilities can be present behind bubbles without shape oscillations; hence, the wake oscillations are not coupled with shape oscillations, this coupling is only through oscillations in the velocity.

It would be interesting to study the forces and torques acting on bubbles performing shape oscillations. It is possible to reconstruct the 3D bubble shape, orientation and path from two perpendicular views on the bubble if the bubble is an oblate ellipsoid. But when shape oscillations set in this reconstruction is no longer valid. Hence, a third view on the bubble is necessary. Positioning a camera on top of the water tank to capture the top view of the bubble would solve this problem. Of course, bubbles moving in and out of focus of the top camera are now problems which have to be solved.

To better understand the shape oscillations the analytical method to calculate shape oscillations on spherical bubbles [e.g. 1, 10] was extended to shape oscillations on ellipsoidal bubbles. The limiting case for aspect ratio one is calculated correctly, but the method results in deviations from the results of numerical work by Meiron [12] for higher aspect ratios. Future research should focus on a correct closure of the model, which should be compared with experimental results on shape oscillation frequencies. Further analysis of this comparison should provide a better understanding of the difference between our experimental results and the theory of Meiron [12] as we saw in figure 8.10.

Recapitalizing all results, we see that there are remarkable agreements between the motion of spheres and bubbles. Although the boundary conditions are different, the effect of the generated vorticity at the surfaces of these bodies on their motion is similar; in both cases we see wake structures consisting of two vortex threads. And the drag experienced by these bodies moving at high Reynolds numbers can both be modelled correctly with a viscous contribution and a contribution related to lift. The orientation of the vortex plane (i.e. the angle between the vortex plane and the horizontal plane) which is related to the lift induced drag varies between 21 and 24^o for a bubble and between 25 and 38^o for a sphere. Further research should provide more information of the dependance of this angle on the sphere-fluid density ratio. Does an even lighter sphere give smaller vortex plane angles? Or is this angle more dependent on the amount of vorticity produced at the surface? Related to this is the relative contribution of the lift-induced drag to the total drag experienced by the body. For a bubble the lift induced-drag is approximately 23-29 % of the total drag. For a sphere this percentage is 21-26 %. These percentages are more or less equal, but the vortex plane angle is larger for a sphere. A larger vortex plane angle would imply a larger lift-induced drag. Why is the relative contribution of the lift-induced drag to the total drag in the case of a sphere not higher than in the case of a bubble? The reason is the boundary condition, which is a no-slip boundary condition for a sphere compared to a no-shear condition for a bubble. Therefore the relative contribution of the lift-induced drag to the total drag might be smaller. An important subject for further research would be to investigate the dependence of the relative contribution of the lift-induced drag to the total drag on the sphere-fluid density ratio and the boundary condition.

Besides the differences in boundary condition and density there is a difference in shape. Therefore it would be interesting to study ellipsoidal particles. Some experiments with flattened polystyrene spheres are carried out. These experiments showed that the aspect ratio of the ellipsoidal particle cannot be fully controlled; also the axisymmetry after the sphere is flattened might be lost. Figure 9.1 shows the angle θ between the path of an ellipsoidal particle and the horizontal plane and the angle between the minor axis of the particle and the horizontal plane for a particle rising along a zigzag path through water. We clearly see that the particle is not always aligned with its path; when the particle rises straight up the particle is aligned with its path and both angles are 90^o, but when the particle moves through the symmetry axis of the zigzag path the particle ’overshoots’ the path. The angle between the minor axis and the horizontal plane is larger than the angle of the path

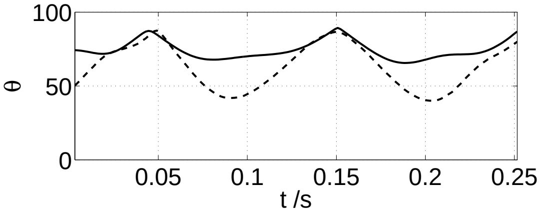

Figure 9.1: – Angle between the tangent and the horizontal plane, - - angle between the minor axis and the horizontal plane for an ellipsoidal particle ($\rho_s/\rho \approxeq 0.02$, D_{eq}=5.9 mm, and $\chi = 1.4$.). Angles are given in ^{o}.

with the horizontal plane. Now the ellipsoidal particle is no longer aligned with its path inertial forces perpendicular to the path of the particle are generated. This is, because the added mass tensor no longer is a diagonal matrix.

All flattened spheres that were tested had a small non-axisymmetry of about 2-5%. This caused the particle always to move in a zigzag. Probably a spiral path can be only be observed for perfectly axisymmetric ellipsoids. This is related to the observed zigzag paths for bubbles with non-axisymmetric shape oscillations as we saw in chapter 8.

It would be interesting to study the drag experienced by these ellipsoids. Before one could test the drag model as it is presented in this thesis it is necessary to have an expression for the viscous contribution to the drag. For spheres the standard drag curve is used and for bubbles Moore's drag is used. In future research the viscous drag could be measured using heavy ellipsoidal particles or ellipsoidal particles held fixed. Finally a study of the wake structures behind ellipsoidal particles has to be conducted to provide information of the orientation of the vortex plane behind the particle. In this research it is important to focus on the effect of the density ratio; for small density ratios a comparison could be made with numerical work of Mougin & Magnaudet [13] on ellipsoidal bubbles. Furthermore the work of Dusek *et al.* [6] could be extended to ellipsoidal particles.

References

[1] BENJAMIN, T.B. 1989 Note on shape oscillations of bubbles. *J. Fluid Mech.* **203**, 419–424.

[2] DUINEVELD, P.C. 1994 Bouncing and coalescence of two bubbles in water. PhD thesis, University of Twente, Enschede, the Netherlands.

[3] ELLINGSEN, K. & RISSO, F. 2001 On the rise of an ellipsoidal bubble in water: oscillatory paths and liquid-induced velocity. *J. Fluid Mech.* **440**, 235–268.

[4] GOVARDHAN, R.N. & WILLIAMSON, C.H.K. 2005 Vortex-induced vibration of a sphere. *J. Fluid Mech.* **53**, 11–47.

[5] HOWE, M.S. 1995 On the force and moment on a body in an incompressible fluid, with application to rigid bodies and bubbles at high and low Reynolds numbers. *Q. J. Mech. Appl.* **48**, 401–426.

[6] JENNY, M., DUŠEK, J. & BOUCHET, G. 2004 Instabilities and transition of a sphere falling or ascending freely in a Newtonian fluid. *J. Fluid Mech.* **508**, 201–239.

[7] JOHNSON, T.A. & PATEL, V.C. 1999 Flow past a sphere up to a Reynolds number of 300. *J. Fluid Mech.* **378**, 19–70.

[8] KAMBE, T. 1987 A new expression of the force on a body in viscous vortex flow and asymptotic pressure field. *Fluid Dyn. Res.* **2**, 15–23.

[9] KARAMANEV, D.G. & NIKOLOV, L.N. 1992 Free rising spheres do not obey Newton's law for free settling. *AIChE J.* **38**, 1843–1846.

[10] LAMB, H. 1932 *Hydrodynamics*, 6th edn. Cambridge University Press, USA.

[11] LUNDE, K. & PERKINS, R.J. 1998 Shape oscillations of rising bubbles. *Appl. Sci. Res.* **58**, 387–408.

[12] MEIRON, D.I. 1989 On the stability of gas bubbles rising in an inviscid fluid. *J. Fluid Mech.* **198**, 101–114.

[13] MOUGIN, G. & MAGNAUDET, J. 2002 Path instability of a rising bubble. *Phys. Rev. Letters* **88**, 014502.

[14] MOUGIN, G. & MAGNAUDET, J. 2006 Wake-induced forces and torques on a zigzagging/spiralling bubble. *J. Fluid Mech.* **567**, 185–194.

[15] SCHOUVEILER, L. & PROVANSAL, M. 2002 Self-sustained oscillations in the wake of a sphere. *Phys. Fluids* **14**, 3846–3854.

Summary

Bubble and particle laden flows are important in a wide range of industrial and geophysical processes. This broad application field stimulated bubbly and particle laden flow research. In the upper limit research focuses on dense, highly laden flows, which provides overall statistical properties of such flows. In the lower limit the research addresses the problem of single bubble and particle behavior, providing a more fundamental knowledge of the hydrodynamic forces acting on bodies. This thesis focuses on both single solid particle and bubble behavior.

Chapter 2 discusses the experimental Schlieren setup which is used to visualize wake structures behind rising and falling spheres and rising bubbles in quiescent water. The advantage of the Schlieren technique compared to other flow visualization techniques, like PIV and dye-injection, is the ability to visualize the entire 3D flow field without contaminating the water. The last being important for the visualization of wake structures behind bubbles rising in purified water.

Chapter 3 shows that the wake structures behind solid spheres rising or falling freely in liquids under the action of gravity show remarkable differences to the wake structures observed behind spheres held fixed. The wake behind some falling spheres consists of hairpin vortices shedding from the sphere surface. The wake behind other falling spheres and behind rising spheres are not dominated by vortex shedding, but consist of two continuous vortex threads of opposite-signed vorticity. These threads cross and kinks are formed on these threads, that finally develop into hairpin vortex like structures. Furthermore, the double-threaded wake structure seems to be a basic feature, even for large Reynolds numbers.

Related to these differences in sphere dynamics is the research of Karamanev and co-workers (Karamanev and Nikolov 1992; Karamanev, Chavarie & Mayer 1996; Karamanev 2001) on the behavior of spheres rising freely in a Newtonian fluid with a sphere-fluid density ratio less than 0.3. They propose to replace, for these spheres, the standard relation for the drag coefficient C_D as a function of the Reynolds number Re by $C_D = 0.95$ for $Re > 130$. In chapter 4 it is shown that this is not supported by our experiments. It is shown, that the drag force consists of (i) a viscous contribution that may be estimated from the standard drag curve by

evaluating the Reynolds number using the actual value of the velocity, and (ii) an inertial contribution that arises essentially by the same mechanisms that cause the lift-induced drag on airplane wings.

The two parameters controlling the rise or fall velocity are the sphere-fluid density ratio ρ_s/ρ and the Galileo number G. Jenny, Dušek & Bouchet (2003) studied the instability and the transition of the motion of solid spheres in this $(G, \rho_s/\rho)$ parameter space numerically. They showed that the parameter space may be divided into regions with distinct features of the sphere trajectories; furthermore an asymmetry around a density ratio of one is found. In chapter 5 an experimental investigation is presented in which the interesting conclusions of their study are verified. The experiments agree well with what was observed in their numerical study. However, our flow visualizations of the wakes of the spheres always show a double-threaded wake. This contradicts the conclusion of Jenny, Dušek & Bouchet, namely the absence of a bifid wake structure.

In chapter 6 the general features of single bubbles ($1 \leq d_{eq} \leq 6$mm), rising in purified water, are studied. The smallest bubbles are oblate ellipsoids rising rectilinearly. Larger bubbles are oblate ellipsoids in spiraling motion. For even larger bubbles shape oscillations set in, strongly influencing the bubble path. Comparison of the rise velocity and shape of the bubble with earlier research shows that the used water is indeed pure, not contaminated with surfactants.

Chapter 7 focuses on oblate ellipsoidal bubbles that rise without shape oscillations. It is shown that the measured drag on the bubble consists of a contribution related to viscous drag and a contribution related to the lift acting on the bubble, which is induced instantaneously. It seems that variations in the viscous contribution to the drag associated with the ‘building-up’ of the vorticity field by diffusion and convection, important at low Reynolds numbers, is negligible at high Reynolds numbers. This is also the case for solid spheres.

Chapter 8 focuses on larger bubbles for which shape oscillations set in. For bubble sizes right at the onset of shape oscillations the stable spiraling motion changes into a pure zigzagging motion. This is due to a coupling with the non-axi-symmetric mode (2,2) shape oscillation. Larger bubbles rise in more or less helicoidal paths. Finally, multiple shape oscillations force the bubble into an erratic path. All bubbles show an axi-symmetric mode (2,0) shape oscillation which is coupled with velocity oscillations and therefore with oscillations in the wake.

An analytical method to calculate shape oscillations on ellipsoidal bubbles is presented. The limiting case for aspect ratio one is calculated correctly but the method results in deviations from numerical theory by Meiron (1989) for higher aspect ratios.

Samenvatting

Stromingen met bellen en deeltjes zijn belangrijk in vele industriële en geofysische processen. Dit grote toepassingsgebied heeft het onderzoek naar stromingen met bellen en deeltjes gestimuleerd. Aan de ene kant richt het onderzoek zich op de stroming met een grote dichtheid van bellen of deeltjes. Dit geeft de statistische eigenschappen van zulke stromingen. Aan de andere kant wordt er gekeken naar het gedrag van één bel of deeltje. Dit geeft een fundamenteel inzicht in de hydrodynamische krachten, die werken op deze lichamen. Dit proefschrift richt zich op het gedrag van één deeltje van vaste vorm of één bel.

In hoofdstuk 2 wordt een experimentele Schlieren opstelling besproken, die gebruikt is voor de visualisatie van vorticiteitsstructuren achter opstijgende en vallende sferische deeltjes en opstijgende bellen in stilstaand water. Het voordeel van de Schlieren techniek ten opzichte van andere stromingsvisualisatietechnieken, zoals PIV en inkt-injectie, is, dat Schlieren het gehele 3D stromingsveld visualiseert zonder het water te vervuilen. Dit is vooral van belang voor onderzoek naar het gedrag van bellen in zuiver water.

Hoofdstuk 3 laat zien, dat de vorticiteitsstructuren achter sferische deeltjes van vaste vorm (het zog), die opstijgen of vallen, opmerkelijke verschillen vertonen met deeltjes, die vastgehouden worden. Het zog achter sommige vallende deeltjes bestaat uit zogenaamde 'hairpin' vortices, die afgeschud worden van het oppervlak van het deeltje. Het zog achter andere vallende deeltjes en opstijgende deeltjes bestaat uit twee continue vortexdraden van tegengestelde vorticiteit. Deze vortexdraden kruizen, waarna lussen ontstaan, die uiteindelijk overgaan in structuren, die lijken op 'hairpin' vortices. Verder valt op, dat de dubbele vortexstructuur een standaard eigenschap is voor het zog van deeltjes, zelfs voor hoge Reynolds-getallen.

Gerelateerd aan deze verschillen in de dynamica van deeltjes is het onderzoek van Karamanev en collega's (Karamanev and Nikolov 1992; Karamanev, Chavarie & Mayer 1996; Karamanev 2001) over het gedrag van opstijgende deeltjes in een Newtoniaanse vloeistof voor een deeltje-vloeistof dichtheidsverhouding kleiner dan 0.3. Zij stellen voor om de standaard relatie voor de weerstandscoëfficiënt C_D als functie van het Reynolds-getal te vervangen door $C_D = 0.95$ voor $Re > 130$.

In hoofdstuk 4 wordt aangetoond, dat onze experimenten dit gedrag niet bevestigen. De weerstand blijkt te bestaan uit twee bijdragen (i) een viskeuze bijdrage, die afgeschat kan worden met de standaard weerstandsrelatie, gebruikmakend van het actuele Reynolds-getal, en (ii) een bijdrage, die voortkomt uit dezelfde mechanismen als lift-geïnduceerde weerstand op vliegtuigvleugels.

De twee parameters, die de stijg- of valsnelheid controleren zijn de dichtheidsverhouding tussen deeltje en vloeistof ρ_s/ρ en het Galileo-getal G. Jenny, Dušek & Bouchet (2003) bestudeerden de instabiliteit en transitie van de beweging van vaste deeltjes in deze $(G, \rho_s/\rho)$-parameterruimte. Zij toonden aan, dat de parameterruimte opgedeeld kan worden in regimes met specifieke eigenschappen voor de paden, die de deeltjes doorlopen. De parameterruimte laat duidelijk een asymmetrie zien rond een dichtheidsverhouding van één. Hoofdstuk 5 toont een experimenteel onderzoek waarin de interesante conclusions van hun onderzoek worden geverifiëerd. De experimenten komen goed overeen met de bevindingen in hun numerieke onderzoek. Echter, de visualisaties van het zog achter de deeltjes laat altijd een dubbeldraads zog zien. Dit spreekt de conclusie van Jenny, Dušek & Bouchet, over het ontbreken van een dubbeldraads zog, tegen.

In hoofdstuk 6 worden de algemene eigenschappen van een bel ($1 \leq d_{eq} \leq 6$mm) opstijgend in zuiver water bestudeerd. De kleinste bellen zijn afgeplatte ellipsoiden, die recht omhoog gaan en grotere bellen volgen een spiraalpad. Nog grotere bellen vertonen vormoscillaties, die het pad sterk beïnvloeden. Vergelijking van de opstijgsnelheid en de belvorm met eerder onderzoek toont aan, dat het gebruikte water inderdaad zuiver is.

Hoofdstuk 7 richt zich op afgeplatte ellipsoiden zonder vormoscillaties. Het blijkt dat de weerstand, die werkt op de bel, afhangt van de viskeuze weerstand en een bijdrage geïnduceerd door de liftkracht werkend op de bel. Variaties in de viskeuze bijdrage door opbouw van het vorticiteitsveld door diffusie en convectie zijn verwaarloosbaar voor hoge Reynolds-getallen.

Hoofdstuk 8 richt zich op grotere bellen met vormoscilaties. Voor belgroottes net na het ontstaan van vormoscilaties gaat de spiraalbeweging over in een zigzagbeweging. Dit komt door een koppeling met de niet-axisymmetrisch mode (2,2) vormoscillatie. Bij nog grotere bellen zorgen meerdere vormoscillaties ervoor dat de bel opstijgt in een grillig pad. Alle bellen vertonen een axisymmetrische mode (2,0) vormoscillatie, die is gekoppeld aan oscillaties in de snelheid van de bel en daardoor ook aan oscillaties in het zog achter de bel.

Een analytische methode voor het berekenen van vormoscillaties op een afgeplatte ellipsoidale bel is behandeld. Het limietgeval voor een afplattinggraad van één, een bolvormige bel, wordt met deze methode correct berekend. Echter, voor grotere afplattingsgraden treden er afwijkingen op ten opzichte van de numerieke berekeningen van Meiron (1989).

Acknowledgements

The research described in this thesis is part of the research program of the ”Stichting voor Fundamenteel Onderzoek der Materie”(FOM), which is financially supported by the ”Nederlandse Organisatie voor Wetenschappelijk Onderzoek” (NWO). It was carried out at the Physics of Fluids research group of the faculty of Science and Technology of the University of Twente. I gratefully acknowledge the support of these institutions.

Carrying out scientific work and finally finishing a PhD thesis is sometimes a struggle. This starts when you start to study at the university. After you followed the first couple of lectures you might start to think ”What am I doing here? This is not what I was educated for at high school!”. As top of the bill, you start doing research as a PhD student. Every PhD student knows this is indeed sometimes an even harder struggle. I could not have achieved as much as I did by finishing this PhD thesis without the support of many people during those years. At this point I would like to thank everybody that contributed to it. Some people I would like to thank in particular.

First of all, I would like to thank my promotor Detlef Lohse for giving me the opportunity to carry out this PhD work. His enthusiasm and bright look on physics inspired me a lot.

I want to thank my supervisors Arie Biesheuvel and Leen van Wijngaarden for all the invaluable scientific discussions we had and their patience when explaining numerous aspects of theoretical hydrodynamics. But also our non-scientific conversations made my PhD period even more worthwhile.

I would like to thank Andrea Prosperetti for giving me the opportunity to visit his research group at the Johns Hopkins University in Baltimore, USA. Following his lectures on Convection were challenging and inspiring. We discussed a lot on the ”never ending story” of shape oscillations on ellipsoidal bubbles. This gave me a much better understanding of several mathematical techniques that can be used to solve many of the encountered problems.

I thank Rob Hagmeijer for his help with the calculations to reconstruct bubble orientation and shape. His mathematical approach clarified numerous aspects and improved the reconstruction model.

I want to thank the master students Harmke van Aken, Peter van Oostrum, and Marike Aalbers for all the effort they put in performing experiments and exploring new research fields. Parts of their results are included in this thesis.

I am grateful to Michel Versluis and Claus-Dieter Ohl who guided me through the world of experimental science. Without their help the Schlieren setup would not do its job as well as it does now.

Many thanks go to the technicians Gert-Wim Bruggert, (late) Henni Scholten, and Martin Bos. Without them I could not have performed all the experiments. I thank Bas Benschop for all the help with computer related problems. I thank Joanita Leferink for all the administrative work. Not only their support, but also the conversations with real ”Tukkers” gave me a lot of relaxation and inspiration.

I would like to thank my office mate Francisco Fontenele Araujo Jr. for solving almost all my LaTeX problems. I thank my office mate Jos de Jong for solving numerous Matlab problems and problems with my computer. But most of all, I want to thank them for all the lively discussion on world politics, philosophical matters, and research in general. It was great fun having them as my office mates.

I thank all the members of the Physics of Fluids group for their scientific input and the lively discussions during the coffee breaks and other social events.

Special thanks go to my family, Lilian and Jeroen, Ilse and Frans, Karine and John and, above all, my parents Johan and Femi for all their support and understanding during all those years of education and the final years as a PhD student.

Finally, I thank Juliëtte for her love and patience. It has been a hard time lately, especially with a stubborn guy like me.

Christian Veldhuis
Enschede, December 2006

About the author

Christian Veldhuis was born on February 21, 1978, in Hengelo, the Netherlands. He graduated from high school (VWO) at ”De Grundel” in Hengelo in 1996. Until the summer of 1997 he worked as a car polisher at ”Reuvekamp autowassalon” in Hengelo. In August 1997 he started to study Mechanical Engineering at the University of Twente in Enschede. He did his traineeship at BMW in Munich, Germany. In November 2002 he obtained his master degree with prof. dr. ir. H.W.M. Hoeijmakers on a numerical study of cavitating flows. In February 2003 he joined the Physics of Fluids group of prof. dr. D. Lohse as a PhD student.